Thesis presented to obtain the degree of
DOCTOR OF THE ECOLE POLYTECHNIQUE
Specialization: Physics
by
Igor FAVORSKIY



Optical pumping in Silicon thin films

Defended on 29 November 2013 in front of the jury:

Prof. Franco CICCACCI	Referee
Prof. Xavier MARIE	Referee
Prof. Luca PERFETTI	Examiner
Prof. Matthieu VERSTRAETE	Invited
Dr. Yves LASSAILLY	Supervisor
Dr. Jacques PERETTI	Supervisor

Thesis prepared at the Laboratoire de Physique de la Matière Condensée

To my family

Acknowledgments

A PhD thesis in experimental physics is clearly a teamwork effort. I would like to thank those who contributed to the results presented below, as well as all with whom I worked during these years.

First of all, I am indebted to my scientific advisors, Jacques Peretti and Yves Lassailly, who not only offered me a unique opportunity to work on a state of the art spintronics project, but also contributed immensely in its success. Yves, at the beginning you said that the operation of the Mott detector would be particularly complicated and delicate. By carefully following the experimental protocols we were able to successfully operate this setup during all the three years, and more than that, managed to extract a rich set of experimental data. Jacques and Yves, I want to thank you for your great help and availability during the experimental part of the work, as well as during the drafting and defense preparation. I am sincerely grateful to Alistair Rowe, who welcomed me in Laboratoire de Physique de la Matière Condensée during my master thesis, and then actively participated in the supervision of my PhD work. Alistair, I would like to express my special thanks for the clarity of your explanations and advices, as well as for our fruitful work on the modelling of strained Silicon.

I would like to thank a lot Franco Ciccacci, Xavier Marie, Luca Perfetti for agreeing to participate in the jury, as well as for the important and interesting discussions, which allowed reviewing and improving certain parts of the manuscript. Also, I would like to express my gratitude to Lucio Martinelli for setting up and assistance during the operation of the key components of the experimental setup (Ti:Sapphire laser, Babinet-Soleil compensator, automatic liquid nitrogen filling system). Lucio, you always managed to find an original approach to each particular experimental problem, which inevitably led to its resolution. I thank Georges Lampel for his help in setting up the Mott detector, as well as for the detailed explanations he provided to me on the subject of optical pumping in nuclear magnetic resonance experiment and the analytical calculation of the initial polarization. I would like to acknowledge the effort of André Wack, who designed and manufactured a number of mechanical components, namely those of the sample introduction chamber. Although I was able to bring this project only to an intermediate stage, the obtained in the present work conclusions clearly show that the implementation of such a chamber will be an essential requirement for further investigations. Many thanks to Oleg Tereshenko for careful reading of the experimental chapters, and valuable scientific discussions on the analysis of the sample preparation procedures. I am thankful to my predecessor Frederic Roux for his huge work on the automation of the Mott detector, which greatly facilitated the experimental part of my thesis, and for the detailed information that he had provided in his thesis and auxiliary documents.

I am very thankful to Matthieu Verstaete, Momar Diakhate and all the Nanomat team of the Liege University for the project they have undertaken on the modeling of optical orientation in Silicon. You provided to me an excellent introduction to ab initio numerical methods, as well as an opportunity to apply this knowledge performing a series of calculations on the

server of your group. Personally, I would like to thank you for a very warm welcome during my two visits to Liege. Thanks to Lucia Reining, Fabien Bruneval and Igor Reshetnyak for valuable scientific discussions on the optical pumping and spin diffusion process. I would like to acknowledge the effort of the worldwide Abinit community, resulted in excellent software.

I would like to thank Vladimir Sabelnikov for our discussion on the state of the art modelling of spin-polarized electron distributions. Obviously, the future developments in this direction will constitute an important step towards the interpretation of the experimental data presented below. Many thanks to Evgeny Chelnokov for his great help in the description of two-photon optical pumping and laser operation in the pulsed mode and to Denis Grebenkov for his valuable advice on statistical analysis of a counting experiment.

I was happy to work in the team of the Laboratoire de Physique de la Matière Condensée. I thank Anne-Marie Hernecq for her help in ordering the instrumentation components, François Ozanam, Audrey Lemarechal and Michel Rosso for backing up the administrative part of the dissertation, Denis Coupvent-Desgraviers and Julien Monguillon for promptly addressing the IT issues, as well as for their assistance in setting up the numerical calculations. I would like to thank all the members of the laboratory for their professionalism, openness and excellent work atmosphere.

From the personal point of view, I would like to acknowledge the great contribution of my family: wife and daughter for their constant support and commitment, the parents of my wife, who helped a lot during their visits to France and in fact enabled the intensive work during the last year of the thesis, as well as my parents for their great implication in my education from childhood.

Abstract

Silicon is a potentially promising material for spintronics due to its long spin relaxation time. At the same time, classical approaches to the study of the conduction electrons' polarization, such as luminescence, are ineffective for Silicon due to the weak spin-orbit interaction and indirect-bandgap structure. In the present work, the polarization of the conduction electrons is studied by means of spin-resolved low-energy electron photoemission spectroscopy. The Silicon surface is activated to negative electron affinity by Cesium and Oxygen adsorption so that electron emission can be achieved with photon excitation very close to the band gap (1.12 eV at 300 K). We use a tunable laser which allows a systematic measurement of the polarization spectra from the absorption onset up to energies above the Γ_2^- band. We measured spin polarization spectra on Silicon-on-insulator films of different thicknesses. Based on the obtained data, band structure parameters such as direct band gap and the spin-orbit splitting are evaluated. However, contrary to expectations, when diminishing the Silicon film thickness, even below the value of the spin diffusion length, the electron polarization remains close to zero ($-0.4\,\%$), much lower than the theoretically predicted values of the initial polarization ($-20\,\%$), thus bringing into question their straightforward interpretation. A theoretical investigation was performed on the basis of an ab initio band structure model in order to calculate the full spin polarization spectra. These calculations are still on-going but predictions for strained Silicon confirm that this material should be an interesting candidate for further spin polarization studies.

Keywords: optical pumping, photoemission, spin, Silicon, band structure

Résumé

Grâce à un long temps de vie de spin, le silicium est un matériau prometteur pour l'électronique de spin. Mais les approches classiques d'étude de la dynamique de spin basées sur la luminescence polarisée ne peuvent pas être utilisées dans ce matériau à cause du faible couplage spin-orbite et du gap indirect. Dans ce travail, nous avons étudié la polarisation de spin des électrons de conduction créée en condition de pompage optique par spectroscopie de photoémission. La surface du silicium est activée en affinité négative par dépôt de césium et d'oxygène de sorte que les électrons photoexcités avec une énergie proche du gap peuvent émis dans le vide. Nous utilisons un laser accordable qui permet de mesurer systématiquement le spectre de polarisation pour des énergies d'excitation allant du seuil d'absorption jusqu'à la bande Γ_2^- au-dessus du gap direct. Nous avons obtenus les spectres de polarisation à partir de couches minces SOI d'épaisseurs différentes. A partir de ces résultats, nous déterminons la valeur de paramètres importants de la structure de bande comme le gap direct ou l'énergie du couplage spin-orbite. Cependant, contrairement aux prédictions, lorsque l'épaisseur de la couche de silicium diminue jusqu'à des valeurs inférieures à la longueur de diffusion de spin, la polarisation en spin des électrons émis reste proche de zéro ($-0.4\,\%$), remettant en cause l'interprétation directe des valeurs théoriques de la polarisation initiale égale à $-20\,\%$. Une approche théorique a donc été développée sur la base d'un modèle ab initio de structure de bande pour déterminer les spectres de polarisation en spin. Ces calculs sont encore en cours, mais les résultats déjà obtenus sur la structure électronique du silicium sous contrainte indiquent une piste intéressante pour les études futures.

Mots clés : pompage optique, photoemission, spin, silicium, structure de bandes

Contents

Contents **7**

List of Symbols **13**

List of Abbreviations **15**

1 Introduction **17**

2 Some aspects of electronic structure and spin physics in semiconductors **19**
2.1 Optical pumping in direct band gap semiconductors 19
2.1.1 Band structure of GaAs 20
2.1.2 Initial polarization in an OP experiment 20
2.2 Optical pumping in Silicon 22
2.2.1 Crystallographic properties of Silicon 23
2.2.2 Band structure of Silicon 23
2.2.3 Initial polarization in an OP experiment 27
2.3 Proposed approach 28
2.3.1 Experimental: polarized photoemission 28
State of the art 28
Contribution of the present work: increasing the spin to electron lifetime ratio 31
2.3.2 Theoretical: full Brillouin zone calculation of OP 32
State of the art 32
Contribution of the present work: energy-resolved ab initio model 35

3 Experimental details **37**
3.1 Introduction 37
3.2 Experimental setup 37
3.2.1 Light excitation 38
Light sources 38
Modulation of light polarization 39
Convention on circular polarization 41
3.2.2 Low-energy electrostatic electron spectrometer 43
3.2.3 Mott polarimeter 44
Electron spot adjustment criteria 45
Electron beam rotation in longitudinal magnetic field 46

Spin-orbit coupling 51
Effective spin scattering asymmetry calibration 52
3.2.4 Coil calibration 55
3.3 Studied Silicon samples 55
3.3.1 Sample holder 58
3.3.2 Cathode preparation 58
Activation of a p-type semiconductor to negative electron affinity 58
Studied crystal orientations 60
Experimental protocol 61
Oxygen exposure 63
3.3.3 Stability of Silicon on insulator structure 63
Excitation with high optical density 63
Successive annealings 65
3.3.4 Internal stress 65
3.3.5 Quantum yield-based estimation of escape probability and diffusion length 66
3.4 Electron distribution curves (EDCs) measurements 67
3.4.1 Energy reference 68
Dependence of EDC(V_{cath}) on the settings of the electron optics 68
Energy calibration 68
Comparison of onsets of direct and indirect transitions 69
3.4.2 Determination of thresholds 70
Analysis of individual EDC 70
Alignment of EDCs with the same energy 73
Precision of high-energy threshold determination 73
3.4.3 Temperature variations of thresholds 75
3.4.4 Slope of the low-energy onset 76
3.4.5 Features on EDCs: interpretation and detection 77
3.5 Polarized energy distribution curves (PEDCs) measurements 79
3.5.1 Characteristic regimes observed on PEDC 79
3.5.2 Acquisition protocol 80
3.5.3 Correction of spurious instrumental asymmetries 81
3.5.4 Precision of the polarization measurements 83
3.5.5 Polarization at the high-energy threshold 85
3.5.6 EDC-averaged polarization 86
3.5.7 Magnetic moment 87
3.6 Conclusion 87

4 Experimental results 89
4.1 Introduction 89
4.2 Excitation near $\epsilon_{g,X}$ indirect gap ($\Gamma_5^+ \rightarrow \Gamma_4^-$) 89
4.2.1 Energy of the absorption onset 89
4.2.2 Light interference in SOI structure 90
Experiment 90
Model 90

Comparison 91
4.2.3 Polarization of ballistic electrons 92
4.2.4 EDC-averaged polarization 93
4.2.5 Possible reasons for the low observed polarization 96
Non-uniform angular sensitivity of the photoemission setup 97
Insufficient sensitivity to the ballistic electrons 98
Depolarization in the BBR and CsO - covered surface 99
4.2.6 Conclusion 100
4.3 Excitation near $\epsilon_{g,\Gamma}$ first direct gap ($\Gamma_5^+ \to \Gamma_4^-$) 101
4.3.1 Analysis of features in EDCs 101
Structure diagrams 101
4.3.2 Electron momentum relaxation in Cs surface layer 104
4.3.3 Difference between the contributions of the direct and indirect optical transitions 107
4.3.4 PEDCs 107
4.3.5 Polarization of ballistic electrons 108
4.3.6 Negative contribution to the HE threshold polarization 110
4.3.7 Average polarization of hot electrons 112
4.3.8 EDC-averaged polarization - comparison with [Bona1985] 115
4.4 Excitation near $\epsilon_{g,\Gamma}^2$ second direct gap ($\Gamma_5^+ \to \Gamma_2^-$) 116
4.4.1 Polarization of ballistic electrons 116
4.4.2 EDC-averaged polarization 117
4.4.3 Polarization of Cs surface layer 118
4.5 Conclusion 119

5 Two-photon optical pumping 121
5.1 Introduction 121
5.2 Operation of the electron optics in the regime of high electron flux 122
5.2.1 Description 122
5.2.2 Influence of the excitation mode on polarization 123
Continuous excitation 123
Pulsed excitation 124
5.2.3 Methods of distortion minimization under pulsed irradiation 124
5.2.4 Interpretation 125
5.2.5 Conclusion 126
5.3 Fundamental (infra-red) range 126
5.3.1 Number of particles per pulse 126
5.3.2 Analysis of peaks on pulsed EDCs 126
5.3.3 Photocathode $I_{\text{cath}}(V_{\text{cath}})$ curve 130
5.3.4 Polarization of two-photon absorption peak 131
5.3.5 High affinity quadratic photocurrent dependence 133
5.4 Second harmonic (visible-ultraviolet) range 134
5.5 Third harmonic (ultraviolet) range 135
5.5.1 Possibility of second harmonic generation above ϕ_{Si} 135
5.6 Relative intensities of one and two-photon processes 136

5.7 Two-photon cross-section 137
5.8 Conclusion 138

6 Theoretical and modeling aspects of the optical pumping and spin diffusion 139
6.1 Introduction 139
6.2 Light absorption in semiconductor 139
6.2.1 Fermi's golden rule 139
6.3 Analytical model 140
6.3.1 Semiconductor wave functions at $k = 0$ 140
6.3.2 Calculation principle 142
6.3.3 Polarization of virtual state for near-indirect gap excitation 144
6.3.4 First direct gap 145
6.3.5 Second direct gap 147
6.4 Numerical models 147
6.4.1 Indirect transitions 147
6.4.2 Direct transitions 149
6.5 Calculation algorithm 152
6.5.1 Comparison of ab-initio and empirical pseudopotential models 154
6.6 Calculation of band structure of strained Silicon 155
6.7 Perspectives 156
6.7.1 Carrier injection 156
6.7.2 Spin injection 156
Polarization of selected transitions 156
Spectrum versus excitation energy 157
6.7.3 Improvements in the model 157
Temperature dependence 157
New features 157
6.8 Energy and spin relaxation 158
6.8.1 Dynamics of the population of spin-polarized electrons 158
Electron lifetime 158
Spin relaxation mechanisms 158
Spin relaxation times 159
6.8.2 Diffusion equations 160
Accounting for the emission at the boundary 163
Numerical results 163
6.8.3 Modeling of conduction electrons energy distributions 164
Fokker-Plank approach 164
Langevin approach 166
6.9 Conclusion 167

7 Conclusions and future work 169
7.1 Conclusions 169
7.2 Future work 170
7.2.1 New sample types 170
Selective optical pumping 170

Photoemission from ultra-thin Silicon films 171
Spin-polarized surface states on Si 171
Other materials 171
7.2.2 Improvements of the experimental setup 172
Sample introduction chamber 172
Further investigation of two-photon optical pumping 172
In situ calibration of the energy scale of the spectrometer 173
Angular resolution of the spectrometer 173
7.2.3 Use of other experimental techniques 174
Magneto-optical measurement 174
Investigation of Cs-O deposition on (1 1 1) surface 174

A Averaging in a counting experiment 175
A.1 Bernoulli variables 175
A.2 Independent Poisson variables 176
A.3 Normalized asymmetry 177
A.4 Conclusion 178

B Density functional theory 179
B.1 Kohn-Sham scheme 179
B.1.1 Hohenberg-Kohn theorem 179
B.1.2 Local density approximation 180
B.1.3 Gradient-corrected approximations 181
B.2 Pseudopotentials 181
B.3 Calculated quantities 182
B.4 Approximations based on many-body perturbation theory 182
B.5 Quantum chemistry packages 184

C Comparative convergence study of different pseudopotentials 187
C.1 Combination of `scGW` and $\texttt{DFT}_{\texttt{SO}}$ eigenenergies 187
C.2 SCF convergence for different pseudopotentials 190
C.2.1 Convergence on `ecut` and `ngkpt` 190
C.3 Convergence on GW model parameters 192
C.3.1 Number of scGW cycles 193
C.3.2 MLWF interpolation parameters 194

List of Figures 194

List of Tables 202

Bibliography 205

List of Symbols

D electron diffusion coefficient
I_{Faraday} photocurrent, collected on Faraday cup (after the energy selector)
I_{cath} photocurrent
L_e electron diffusion length
L_s spin diffusion length
P_i initial polarization created by optical pumping
T_1 spin-lattice (longitudinal) relaxation time. Characteristic time for a spin population to return to equilibrium
T_2 spin-spin (transverse) relaxation time. Characteristic time of decay of spin coherence in perpendicular magnetic field
V_{cath} voltage applied to the photocathode
- $V_{\text{cath}}^{\text{CB}}$ voltage corresponding to minimum of conduction band
- $V_{\text{cath}}^{\text{HE}}$ voltage corresponding to high-energy threshold on spectra
- $V_{\text{cath}}^{\text{LE}}$ voltage corresponding to low-energy threshold on spectra

V_{foil} high voltage applied to the gold foil in the Mott detector
Δ_{SO}^{c} spin-orbit splitting of conduction band
Δ_{SO} spin-orbit splitting
χ electron affinity
ϵ_d dielectric constant
ϵ kinetic energy of electrons above ϵ_{CB}
- ϵ_{CB} minimum of conduction band
- ϵ_{F} Fermi level
- ϵ_{HE} energy corresponding to high-energy threshold on spectra
- ϵ_{LE} energy corresponding to low-energy threshold on spectra
- ϵ_{VB} maximum of valence band
- ϵ_{ph} phonon energy

$\epsilon_{g,L}^{\text{direct}}$ L direct gap of Silicon
$\epsilon_{g,L}$ L indirect gap of Silicon
$\epsilon_{g,X}$ fundamental gap of Silicon
$\epsilon_{g,\Gamma}^{2}$ second direct gap of Silicon
$\epsilon_{g,\Gamma}$ first direct gap of Silicon
$\hbar$ reduced Plank constant
$\langle P \rangle$ EDC-averaged polarization
$\mathcal{A}$ asymmetry

$\mathcal{P}_X$ matrix element of the coupling $\langle S_C|p_x|X\rangle$
$\mathcal{P}$ matrix element of the coupling $\langle Y_C|p_x|Z\rangle$
π linearly polarized light
σ^+ right/clockwise (from the point of view of the source) circularly polarized light
σ^- left/counter-clockwise (from the point of view of the source) circularly polarized light
τ_{escape} electron dwell time in crystal before their escape to vacuum
τ_e conduction electron lifetime
τ_m momentum relaxation time
τ_s spin lifetime
c speed of light in vacuum
d sample thickness (for bulk Silicon), or thickness of active layer of Silicon on insulator (SOI) structure
e elementary charge
$h\nu$ photon energy of the incident laser radiation
h Plank constant
m_e electron mass

List of Abbreviations

1PA	one-photon absorption	1PA
2PA	two-photon absorption	2PA
ARPES	angle-resolved photoemission spectroscopy	
BBR	band bending region	
BZ	Brillouin zone	
DFT	density functional theory	DFT
DOS	density of states	
DSP	degree of spin polarization	
EDC	electron distribution curve	N
EPM	empirical pseudopotential model	
ESR	electron spin resonance	
GGA	generalized gradient approximation	
GW	the GW approximation of Hedin	
HE	high-energy threshold of (P)EDC	
HGH	Hartwigsen Goedecker Hutter pseudopotential	
IR	infrared	IR
KS	Kohn-Sham	
LA	longitudinal acoustic phonon	
LDA	local density approximation	
LE	low-energy threshold of (P)EDC	
LEED	low-energy electron diffraction	
LO	longitudinal optical phonon	
MLWF	maximally localized Wannier functions	
NEA	negative electron affinity	

NMR	nuclear magnetic resonance	
OP	optical pumping	
PAW	projector-augmented wave	
PDF	probability density function	
PE	photoemission	
PEDC	polarized electron distribution curve	P
PEEM	photoemission electron microscopy	
QMC	quantum Monte Carlo	
SCF	self-consistent field method	
SDC	spin distribution curve	S
SHG	second harmonic generator	
SNR	signal to noise ratio	SNR
SOI	Silicon on insulator	
TA	transverse acoustic phonon	
THG	third harmonic generator	
TO	transverse optical phonon	
UHV	ultra-high vacuum	
UV	ultraviolet	UV

Chapter 1

Introduction

A major event in the history of spin physics of semiconductors was the discovery of optical pumping in Silicon. [Lampel1968a]. It was shown that under illumination with circularly polarized light, the excited conduction electrons acquire a preferential spin orientation. This phenomenon was detected by observing the dynamic nuclear polarization of ^{29}Si nuclei induced by their interaction with spin-polarized electrons.

Then, the focus shifted to direct-gap materials due to their accessibility to the optical methods of injection and detection of spin polarization [Parsons1969; Garwin1974; Pierce1975]. In recent years, the scientific community has again turned to the study of spin in Silicon, but usually using transport measurement techniques [Appelbaum2007; Jansen2012]. In fact, Silicon presents important advantages for a spin-based information processing technology:

- The mainstream electronics technology is designed for Silicon.
- Its spin relaxation time τ_s is longer than in other widely used semiconductors. Indeed, the $\tau_s \approx 10^{-10}$ s for both GaAs and Ge at room temperature [Oh2009; Hanbicki2012], whereas for Si $\tau_s \approx 10^{-8}$ s [Fabian2007]. Such difference is explained by higher spin-orbit coupling effect in heavy elements. Since the atomic mass Z_{Si} is lower than Z_{Ge}, Z_{Ga}, Z_{As}, the spin-orbit coupling, and as consequence the spin relaxation rate due to Elliot-Yafet mechanism is lower in Silicon rather than in other materials cited above. Furthermore, the absence of Dyakonov-Perel mechanism due to the inversion symmetry of Silicon crystal accentuates the difference of spin relaxation times.

Thus, Silicon has a number of properties suitable for spin-based electronics, but the experimental investigation of them remains a challenging issue, mainly because the use of optical injection and detection techniques is complicated. The reasons are related to the indirect band structure which results in an unfavorable ratio of spin lifetime τ_s to electron lifetime τ_e:

$$\frac{\tau_s}{\tau_e} \approx 10^{-3} \ll 1 \tag{1.1}$$

resulting in very low polarization in steady-state regime, and low luminescence efficiency. The problem is accentuated by weak spin-orbit coupling, requiring the use of finely tuned optical excitation. From the theoretical point of view, the indirect band structure makes the calculation of initial polarization a difficult problem, because in the latter one should account for several mutually vanishing contributions: that of valence band and conduction

band mechanisms of an indirect transition, that of different phonon modes and conduction valleys.

In this context the present work addresses the following issues:

- Given the discrepancies in the theoretical results on optical pumping in Silicon, a detailed experimental investigation is required for further analysis of the subject.
- The absence (incomplete) of an optical pumping calculation which would account for both direct and indirect transitions in Silicon motivates the development of more complete numerical models. Indeed, the existing models are developed to describe either the average polarization, or the quantities of interest for the luminescence measurements (such as contributions to luminescence spectrum from different phonon modes). There is up to now no theoretical description of the initial polarization spectrum as function of incident photon energy and of kinetic energy of photoemitted electrons.

Thus the optical pumping in Silicon is still an open issue.

In the first chapter of this thesis the basics of optical pumping in direct-gap materials and Silicon are recalled. From this analysis, arguments are developed to support our experimental approach. In chapter 3 the experimental setup, measurement techniques and studied samples are described. We have in particular studied Silicon thin films in order to reduce the photoelectron dwell time in the material. The third and fourth chapters of the dissertation are devoted to the experimental results. In the third chapter we present the results of spectroscopic and polarimetric measurements for different combinations of parameters (energy of incident laser light, temperature, sample thickness). The polarization for near indirect gap excitation is about 0.4 % whatever the sample thickness, i.e. the escape depth, whereas it reaches 10 % for near direct gap excitation. Transitions away from the zone center provide a negative contribution to the polarization spectrum. The analysis of the polarization spectrum evolution as a function of excitation energy allows to determine direct transitions energies at Γ and L points. In the fourth chapter we discuss preliminary results on a new approach consisting in carrying out spectroscopic measurements using pulsed radiation, which opens up the perspective of measuring properties of two-photon optical pumping. The problem of saturation of electron spectrometer was identified, and needs to be resolved in order to attain the mentioned above perspective. The fifth chapter of the thesis is dedicated to a review of existing models of optical pumping in Silicon and presents the ongoing work for the ab initio modeling of the process. The comparison of our experimental data with recent numerical calculations provides important insights relative to spin physics of conduction electrons in Silicon. The last chapter briefly summarizes the conclusions made in this study and the proposed perspectives for further development of the subject.

Chapter 2

Some aspects of electronic structure and spin physics in semiconductors

Since the majority of semiconductors are non-magnetic materials, in order to study the properties of electron spin it is first necessary to create an out-of-equilibrium spin-polarized electron population. The most widely used methods are optical pumping and electrical injection from a ferromagnetic material.

Then electron spin polarization has to be detected, every detection method is characterized by its own time and space scale. For instance, the use of electric field can alter the diffusion process, so the measurement becomes sensitive to the drift rather than diffusion length [Luber2006].

In the first group of detection methods the spin polarization is analyzed in the material where it was created. It contains nuclear magnetic resonance (NMR), electron spin resonance (ESR), magneto-optical and luminescence measurements. In this case the important time scale is intrinsic to the material, such as electron and spin lifetimes.

In the second group of experimental techniques, the electrons are extracted from Silicon into vacuum (photo-, thermo-, electro- emission) or to another material (electrical detection). Here, the important timescale is the time electron takes to escape from the creation material to the point where its spin is analyzed.

In the present work we focus on the process of optical pumping. As we will see in the following, the different analysis techniques do not provide the same sensitivity to the initial polarization of photo-electrons. We will discuss here this problem and give the main reasons that led us to study spin-resolved photoemission of Silicon thin films.

2.1 Optical pumping in direct band gap semiconductors

Generally speaking, the optical pumping is the light-induced excitation of electrons from lower to higher energy level. In semiconductors and gazes, the circularly polarized light produces spin-polarized population of photoelectrons in the conduction band. This results from a transfer of angular moment from the photons to the photoexcited electrons which originate from spin-orbit interaction. This process is also called optical spin orientation.

Since the work on GaSb [Parsons1969] and on GaAs [Zakharchenya1971; Garwin1974], III-

V semiconductors became the materials of choice for optical pumping experiments. In fact, their large spin-orbit splitting allowed to easily obtain high spin polarization, and direct band gap facilitated both optical injection and detection. The results obtained on these materials led to the identification of the main mechanisms of spin relaxation in polar semiconductors [Elliott1954; Dyakonov1971; Bir1975].

2.1.1 Band structure of GaAs

GaAs is the archetype of direct gap semiconductors. Its crystal structure is of zinc blend type (represented in the left panel of fig. 2.1).

The spin-orbit coupling is the interaction of a particle with non-zero spin (here of an electron), when it is moving in an electric field, in particular in the electric field of the atoms of the crystal lattice. The effect of this interaction on the band structure of GaAs consists in and splitting of valence band into quadruplet of heavy and light holes, and double degenerate split-off band (left part of fig. 2.2). As a result, the valence states are no more pure spin states and optical transition selection rules on orbital variables will produce excitation of photoelectrons with preferential spin orientation.

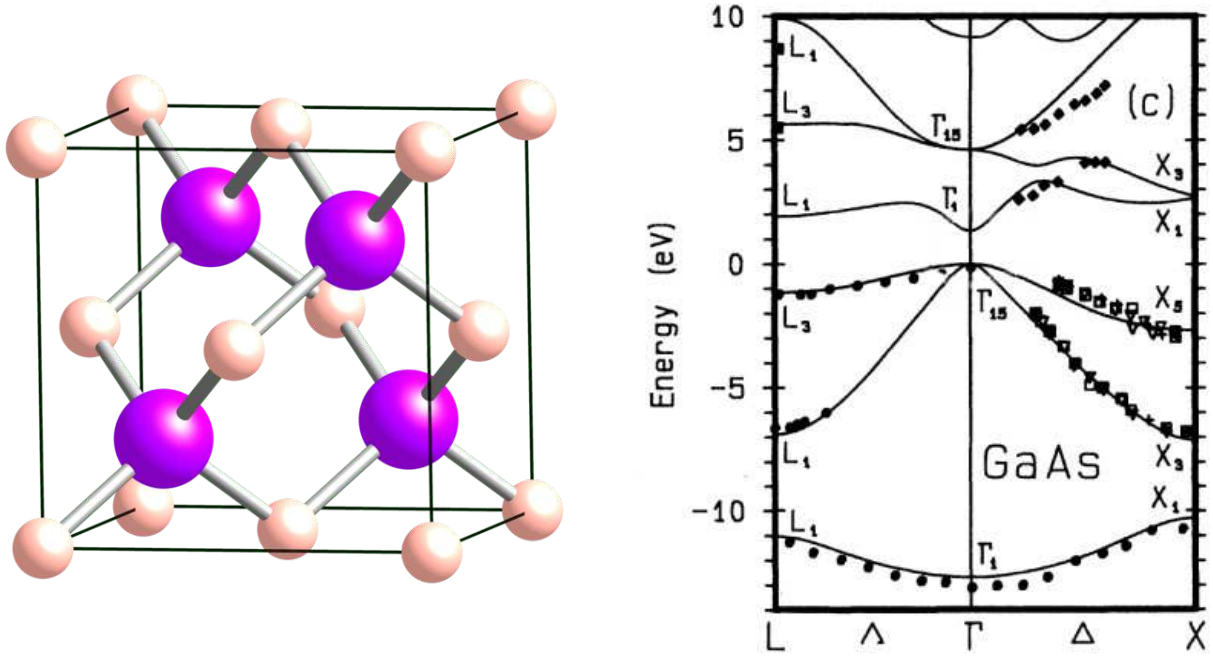


Figure 2.1: Zinc blende crystal lattice (left), band structure of GaAs [Rohlfing1993] (right)

2.1.2 Initial polarization in an OP experiment

In the process of interband optical absorption of a photon with energy $h\nu > E_G$ in the semiconductor, an electron in the conduction band and a hole in the valence band are generated.

The symmetry of states at $k = 0$ together with the use of corresponding Clebsh-Gordon coefficients allows to calculate the transition probabilities induced by circularly polarized

light (fig. 2.2) [Garwin1974]. When the excitation energy $h\nu \in [\epsilon_g, \epsilon_g + \Delta_{\mathrm{SO}}]$, only the transitions from heavy- and light-hole bands are involved, and the spin-polarized population of photoelectrons is created in the conduction band. The initial polarization of photoelectrons in this regime is obtained as

$$P_i = \frac{1-3}{1+3} = -\frac{1}{2} \tag{2.1}$$

Here the minus sign indicates that the spin polarization is opposite to the angular momentum of absorbed photons.

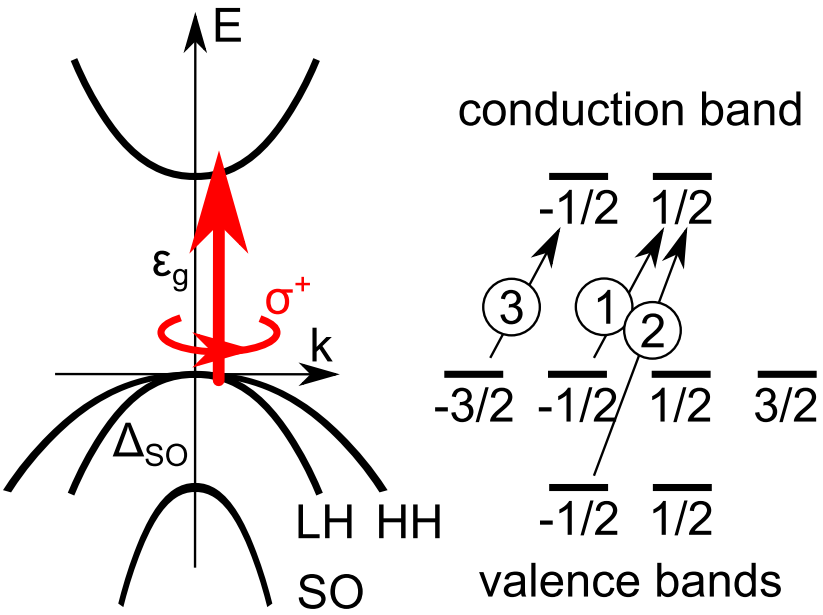


Figure 2.2: Left: Direct optical transition at the center of Brillouin zone of GaAs. Valence bands are denoted as: HH (heavy hole band), LH (light hole band), SO (split-off band). Right: Transition probabilities in an atomic-like model under σ^+-circularly polarized light excitation. The fractions denote the projection of total orbital angular momentum m_j of states at $k = 0$, the circled numbers are the transition intensities [Dyakonov2008].

When $h\nu > \epsilon_g + \Delta_{\mathrm{SO}}$, the overall polarization vanishes due to the positive contribution of electrons photoexcited from split-off band fig. 2.3. The excitation within $[\epsilon_g, \epsilon_g + \Delta_{\mathrm{SO}}]$ results in a selection of electrons with given spin polarization.

The photoexcited carriers live some time τ_e before recombination, which may be radiative (i.e., accompanied by emission of photons, which constitute the luminescence signal), or non-radiative. In direct-band gap semiconductors, like GaAs, the recombination is predominantly radiative with a rather short lifetime of the order of $\tau_e = 10^{-9}\,\mathrm{s}$ at 300 K [Luber2006] and spin lifetime $\tau_s = 10^{-10}\,\mathrm{s}$ [Zerrouati1988]. As we can see, for GaAs the ratio

$$\frac{\tau_s}{\tau_e} \approx 10^{-1} \tag{2.2}$$

is two orders of magnitude greater than the similar ratio for Silicon (eq. (1.1)).

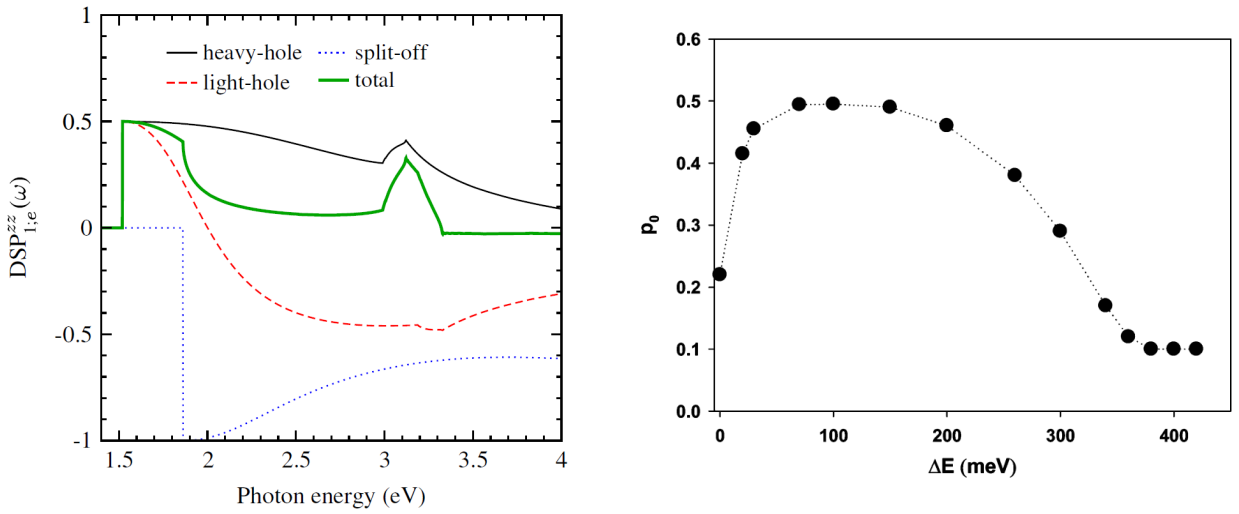


Figure 2.3: Numerically calculated dependence of the initial polarization (denoted as degree of spin polarization (DSP) in theoretical articles) on the excitation energy in GaAs, for σ^- excitation [Rioux2012] (left). Same dependence, measured by two-photon spin-polarized spectroscopy [Miah2009] (right).

The recombination of electrons with holes obeys the same selection rules as the excitation of electron-hole pairs. Therefore, the recombination of polarized electrons also produces circularly polarized light. The degree of circular polarization of the luminescence under excitation in optical pumping condition is given by:

$$P_{\mathrm{PL}} = P_i P_{\mathrm{el}} = {P_i}^2 \frac{\tau_s}{\tau_e} \tag{2.3}$$

where τ_s is the spin lifetime, τ_e is the conduction electron lifetime, and P_{el} is the steady-state electron spin polarization.

When the initial photoelectron polarization P_i is known (which is the case for GaAs under near band gap excitation), the effectively measured steady-state polarization provides important conclusions about the dynamics of spin-polarized electrons population. Using eq. (2.3) one indeed obtains the ratio of τ_s/τ_e. If such experiment is combined with the measurement of the spin depolarization in transverse magnetic field (Hanle effect, first discovered in atoms [Hanle1924] in atoms, later in semiconductors [Parsons1969], and recently reviewed in [Dyakonov2008]), both the spin relaxation time and photoelectron lifetime can be determined. Note that, if τ_e can be independently measured, then the measurement of Hanle effect allows the determination of the electron g-factor [Hermann1977].

2.2 Optical pumping in Silicon

As we just have seen in the previous section, in direct band gap III-V compounds like GaAs, all the conditions are fulfilled for an easy access to conduction electron spin physics by means of optical techniques. Indeed, the band structure (with large spin-orbit splitting and

direct band gap) plus the symmetry of the electronic states near the Γ point allows optical orientation of photoelectron spin with a high degree of polarization ($P_i = -0.5$) according to the very simple scheme of fig. 2.2. Moreover, another consequence of the direct band gap is the efficient radiative recombination with a rather short electron lifetime which makes easy the determination of the electron spin polarization from the detection of the photoluminescence polarization, thus providing access to spin dynamics and intrinsic quantities like the effective electron Lande factor.

In Silicon, the situation is much less favorable mainly because of the indirect nature of the band gap. It is even surprising that optical pumping was discovered in Silicon and still determining the electron spin orientation under optical excitation remains a challenging issue both from the theoretical and from the experimental point of view.

2.2.1 Crystallographic properties of Silicon

Silicon possesses the crystallographic structure of diamond. Direct lattice is face-centered cubic, with lattice parameter of $a = 5.43\,\text{Å}$ at $300\,\text{K}$. Its group of point symmetry is O_h^7, which contains, in particular the inversion symmetry. An important consequence is that the Dyakonov-Perel mechanism which plays an important role in spin relaxation in noncentrosymmetric semiconductors, such as GaAs [Dyakonov1986], is absent in Silicon.

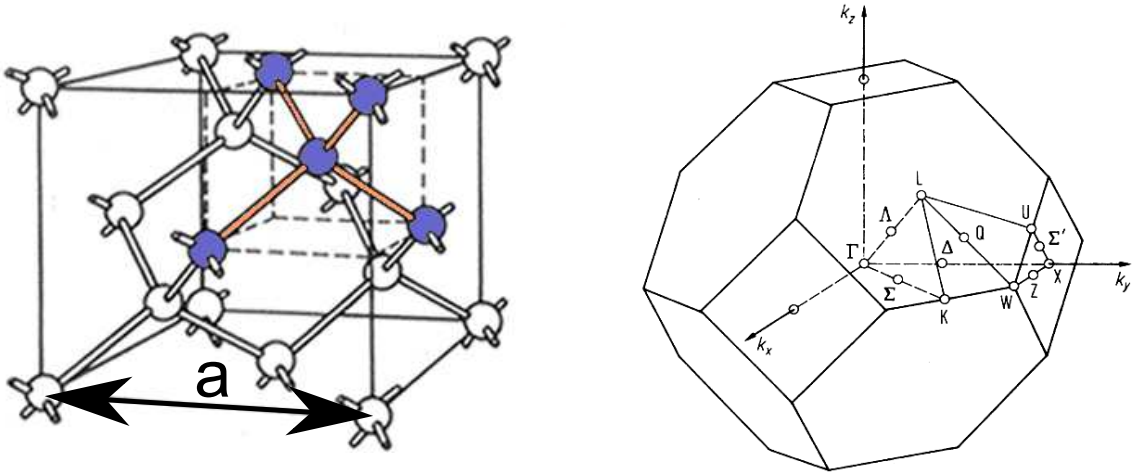


Figure 2.4: Silicon crystal lattice in real (left) and reciprocal (right) spaces

The reciprocal lattice is body-centered cubic with lattice parameter of $\frac{4\pi}{a}$. The first Brillouin zone (or Wigner-Seitz cell in the reciprocal space) is a truncated octahedron (the left panel in fig. 2.4). Table 2.1 recalls the position of high symmetry points of reciprocal lattice. In particular, the minimum of the lowest conduction band is achieved in six equivalent directions, also called valleys.

2.2.2 Band structure of Silicon

Silicon possesses an indirect band structure (fig. 2.5), i.e. the maximum of the highest valence band and the minimum of the lowest conduction band are located in different points

Point	Position	Degeneracy	Axis
Γ (the center of the Brillouin zone)	$k_0(0,0,0)$	1	
X	$k_0(1,0,0)$	6	Δ
L	$k_0(\frac{1}{2},\frac{1}{2},\frac{1}{2})$	8	Λ
K	$k_0(\frac{3}{4},\frac{3}{4},0)$	12	Σ

Table 2.1: Most important symmetry points of the reciprocal lattice. Degeneracy is the number of equivalent directions in which these points are found. $k_0 = \frac{2\pi}{a}$

of reciprocal space. As a result, the absorption and recombination of electrons between the valence band and the conduction band are indirect (phonon-assisted) processes. An immediate consequence is that the lifetime of electrons in the conduction band is very long, typically 10^{-5} s.

Another particularity of Silicon is the low spin-orbit coupling. The spin-orbit splitting at Γ is around $\Delta_{SO} = 44\,\text{meV}$ for the valence band [Nishino1974] and $\Delta^c_{SO} = 30 - 40\,\text{meV}$ for the conduction band [Wepfer1971].

In literature the symbols $\Gamma_n^{\pm}$ from fig. 2.5 are often used to designate the bands only in vicinity of the Brillouin zone (BZ) center (Γ point). However, in the present work the symbols $\Gamma_n^{\pm}$ by convenience denote the corresponding bands all over the BZ.

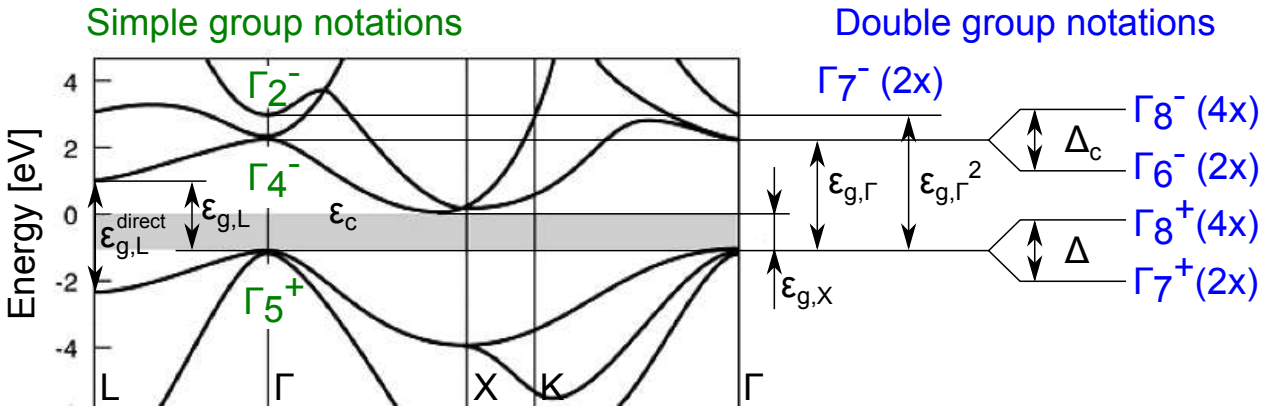


Figure 2.5: Silicon band structure along high symmetry directions calculated by non-local pseudopotential method [Chelikowsky1976]. Bands are labeled according to [Koster1963]. The numbers in parentheses indicate the degeneracy of bands. The energy reference is taken at the minimum of the conduction band which is located at $k_0(0.83, 0, 0)$

The constant energy surfaces of valence bands can be described by spherical approximation only for wave vector $k \approx 0$. As shown in left panel of fig. 2.6, starting from $k/k_0 \gtrsim 0.025$ a strong anisotropy of constant energy surfaces (and, as consequence, of effective masses) takes place. The conduction band minimum is located away from Γ point, which implies the anisotropy of effective masses even at the minimum point itself.

For large values of wavevector k, the heavy and light holes bands are quasi-parallel along the directions X and L, with the distance between them of about 20 meV (the left panel in fig. 2.6).

Outside the center of Brillouin zone, the lowest conduction band Γ_6^- bends down with a curvature which is similar to that of valence bands (the right panel in fig. 2.6). In fact, there is still few experimental evidence about the effective mass of this band. The conduction band Γ_6^- and the valence band Γ_8^+ are parallel over almost the entire Brillouin zone along the direction Λ, and about the half of the Brillouin zone along the direction Δ.

All the three bands represented in fig. 2.6 are two-fold degenerate. In particular, away from the center of zone the Γ_8^- band should also split into two distinct two-fold bands. However, the latter splitting is not reflected in the right panel of fig. 2.6 since it is not accounted for in the model proposed by Chelikowsky and Cohen.

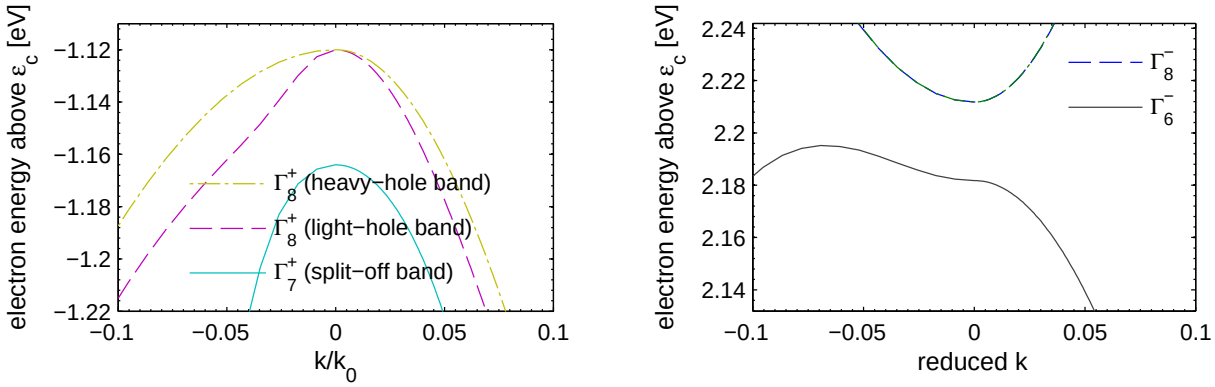


Figure 2.6: Zoom near Γ point: Γ_5^+ valence band (left), Γ_4^- conduction band (right). Negative values of k correspond to Λ direction, positive values to Δ direction. The bands are calculated by 30 band k.p method [Richard2004b].

Band gaps In the present work the five lowest band gaps, which are represented in table 2.2, will be of importance.

The values of the lowest optical band gaps in Silicon are measured by means of optical techniques. Spectroscopic ellipsometry allows to measure both real and complex parts of the dielectric function ϵ_d (fig. 2.7). Its imaginary part $\Im(\epsilon_d)$ corresponds to the absorption

Name	Symbol	Energy	Initial state		Final state	
			Point	Band	Point	Band
Fundamental	$\epsilon_{g,X}$	1.12 eV	Γ	Γ_5^+	$k_0(0.83,0,0)$	Γ_4^-
Indirect L	$\epsilon_{g,L}$	2.25 eV	Γ	Γ_5^+	L	Γ_4^-
Direct L	$\epsilon_{g,L}^{\text{direct}}$	3.39 eV	L	Γ_5^+	L	Γ_4^-
First direct	$\epsilon_{g,\Gamma}$	3.35 eV[a]	Γ	Γ_5^+	Γ	Γ_4^-
Second direct	$\epsilon_{g,\Gamma}^2$	4.17 eV	Γ	Γ_5^+	Γ	Γ_2^-

Table 2.2: Calculated parameters of lowest band gaps in Silicon [Richard2004b]

[a]Instead of $\epsilon_{g,\Gamma}(0\,\text{K}) = 3.4\,\text{eV}$, the room temperature value $\epsilon_{g,\Gamma}(300\,\text{K}) = 3.3\,\text{eV}$ is taken.

spectrum of the material. A direct optical transition is reflected in $\Im(\epsilon_d)$ by the contribution:

$$\Im(\epsilon_d) \propto \left(\frac{h\nu}{\epsilon_g}\right)^{-2} \sqrt{\left(\frac{h\nu}{\epsilon_g}\right) - 1}\ \mathbb{I}_{h\nu>\epsilon_g} \tag{2.4}$$

where $h\nu$ is the energy of incident photons, ϵ_g is a direct band gap ($\epsilon_{g,\Gamma}$ or $\epsilon^2_{g,\Gamma}$ of Silicon). According to this equation, the transition starts to absorb once the photon energy $h\nu$ exceeds the gap ϵ_g. Thus, the peaks observed in the left bottom panel of the fig. 2.7 corresponds to optical transitions. It also follows from eq. (2.4) that $\Im(\epsilon_d)$ is more sensitive to the band gap compared to $\Re(\epsilon_d)$.

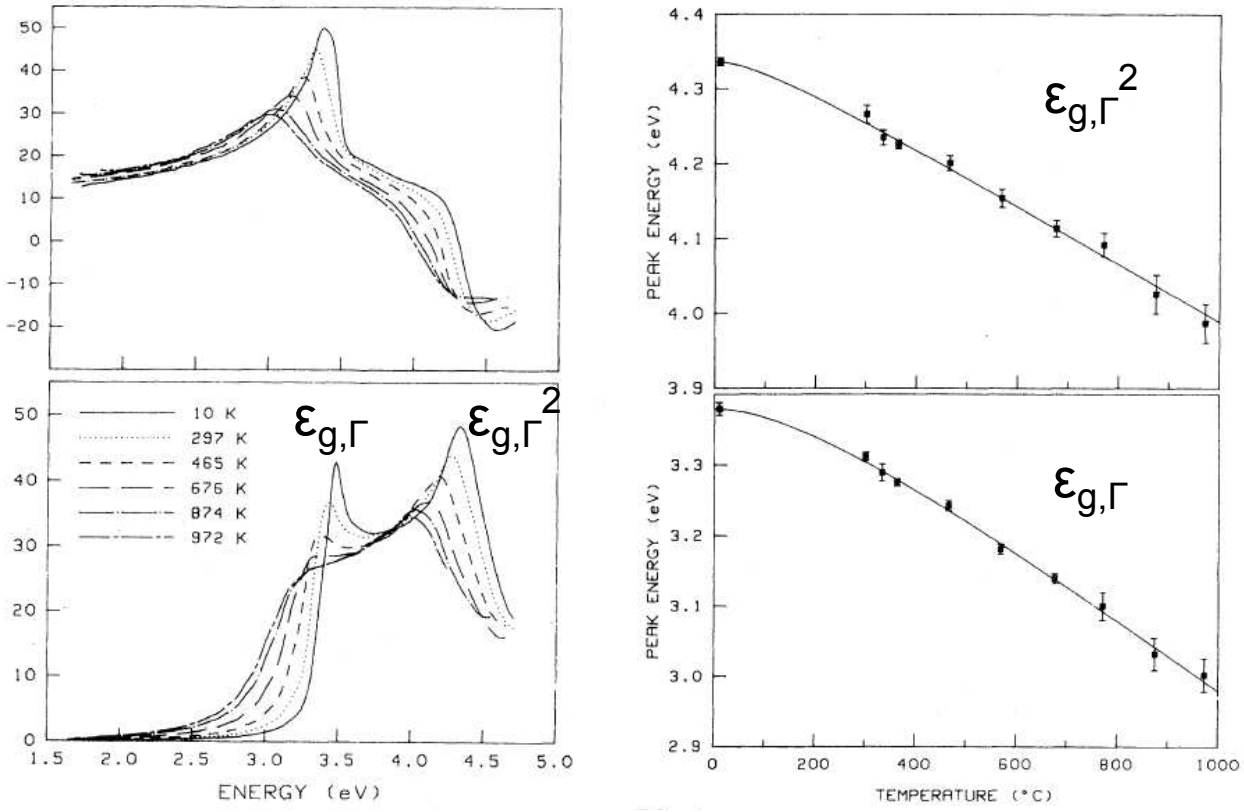


Figure 2.7: Real (top panel) and imaginary (bottom panel) parts of dielectric function of Si for different temperatures measured by ellipsometry [Jellison1983] (left). Temperature variation of peaks on $\Im(\epsilon_d)$. The experimental data is fitted with the empirical relation of Varshni (right).

In general, the band gap of semiconductors reduces with increasing temperature, due to the crystal expansion and interaction with phonons [Boulanger2011]. In particular, this relationship holds for the band gaps of Silicon (see table II of [Lautenschlager1987]), which constitutes the indication that the distance between conduction and valence bands increases with decreasing temperature throughout the entire BZ. The temperature variation of the

fundamental band gap of Silicon is given by [Bludau1974]:

$$\epsilon_{g,X}(T[\mathrm{K}]) = \begin{cases} 1.17 + 1.059 \times 10^{5} T - 6.05 \times 10^{-7} T^2 & \text{for } 0\,\mathrm{K} < T \leq 190\,\mathrm{K} \\ 1.1785 - 9.025 \times 10^{-5} T - 3.05 \times 10^{-7} T^2 & \text{for } 150\,\mathrm{K} < T \leq 300\,\mathrm{K} \end{cases} \tag{2.5}$$

The right panel of fig. 2.7 represents the temperature variation of the peaks observed on $\Im(\epsilon_d)$. The top and bottom curves provide the temperature dependence of $\epsilon^2_{g,\Gamma}$ and $\epsilon_{g,\Gamma}$ respectively. Note that the thermal expansion of Silicon generates no additional structure. The values for 300 K are $\epsilon_{g,\Gamma} = 3.28\,\mathrm{eV}$ and $\epsilon^2_{g,\Gamma} = 4.23\,\mathrm{eV}$

The left panels of fig. 2.7 shows not only the change in transition energies with temperatures but also the increasing linewidth which in fact corresponds to the decreasing electron lifetime τ_e. Indeed, τ_e decreases with increasing temperature because of increasing phonon population which leads to an increase in the number of collisions between electrons and phonons.

Table 2.3 summarizes the results of different measurements of Si band gaps and valence band spin-orbit splitting. One should note that both the measurement of absorption spectrum and photoreflectance spectrum are sensitive to surface induced effects due to shallow probed layer, and thus may differ from the results on bulk material. The work of [Ortega1993] is characterized by comparatively low energy resolution. So, for instance, the measured value of fundamental gap $\epsilon_{g,X}(300\,\mathrm{K}) = 1.25\,\mathrm{eV}$ was significantly different from well established $\epsilon_{g,X}(300\,\mathrm{K}) = 1.12\,\mathrm{eV}$. The detection of exciton and phonon structures on absorption spectrum allows to determine the value of spin-orbit splitting with excellent precision of 0.3 meV [Nishino1974].

One can note that the typical variation of direct gap

$$\epsilon_{g,\Gamma}(0\,\mathrm{K}) - \epsilon_{g,\Gamma}(300\,\mathrm{K}) = 3.4\,\mathrm{eV} - 3.3\,\mathrm{eV} = 100\,\mathrm{meV} \tag{2.6}$$

is two times higher than the variation of the indirect band gap

$$\epsilon_{g,X}(0\,\mathrm{K}) - \epsilon_{g,X}(300\,\mathrm{K}) = 1.17\,\mathrm{eV} - 1.125\,\mathrm{eV} = 45\,\mathrm{meV} \tag{2.7}$$

For the 115 K, which is the typical low temperature considered in the experimental part of the present work, we take the values $\epsilon_{g,X}(115\,\mathrm{K}) = 1.162\,\mathrm{eV}$ and $\epsilon_{g,\Gamma}(115\,\mathrm{K}) = 3.382\,\mathrm{eV}$. The position of L-valley is deduced from the value of $\epsilon_{g,\Gamma}$, applying a temperature-independent energy shift of $-1.10\,\mathrm{eV}$ [Richard2004b].

2.2.3 Initial polarization in an OP experiment

The initial electron polarization created by direct optical transition in the center of Silicon BZ can be calculated similarly to the case of GaAs. Considering the symmetry of states of Silicon, one obtains (fig. 2.8):

$$\begin{cases} P_i(\Gamma_8^+ \to \Gamma_6^-) = \dfrac{1(-\frac{\hbar}{6}) + 3(\frac{\hbar}{6})}{(\hbar/2)(1+3)} = \dfrac{1}{6} & \text{(2.8a)} \\ P_i(\Gamma_8^+ \to \Gamma_8^-) = \dfrac{2(-\frac{3\hbar}{6}) + 2(\frac{\hbar}{6})}{(\hbar/2)(2+2)} = -\dfrac{1}{3} & \text{(2.8b)} \\ P_i(\Gamma_7^+ \to \Gamma_8^-) = \dfrac{1(-\frac{3\hbar}{6}) + 3(-\frac{\hbar}{6})}{(\hbar/2)(1+3)} = -\dfrac{1}{2} & \text{(2.8c)} \end{cases}$$

Temperature	$1.8 - 10\,\mathrm{K}$	$190\,\mathrm{K}$	$300\,\mathrm{K}$
$\epsilon_{g,\Gamma}$	$3.365\,\mathrm{eV}^a$		$3.05\,\mathrm{eV}^h$
	$3.4\,\mathrm{eV}^b$		$3.28\,\mathrm{eV}^c$
			$3.28\,\mathrm{eV}^d$
			$3.294\,\mathrm{eV}^e$
			$3.33\,\mathrm{eV}^a$
$\epsilon_{g,L}^{\mathrm{direct}}$	$3.45\,\mathrm{eV}^b$		$3.36\,\mathrm{eV}^d$
$\epsilon_{g,\Gamma}^2$	$4.18\,\mathrm{eV}^a$	$4.135\,\mathrm{eV}^f$	$4.1\,\mathrm{eV}^h$
	$4.185\,\mathrm{eV}^f$		$4.23\,\mathrm{eV}^c$
Δ_{SO}	$0.04\,\mathrm{eV}^b$		
	$0.044\,\mathrm{eV}^f$		
	$0.0441\,\mathrm{eV}^g$		

[a] electroreflectance [Daunois1978]
[b] wavelength modulation spectroscopy [Zucca1970]
[c] ellipsometry [Jellison1983]
[d] electroreflectance [Grover1974]
[e] electroreflectance [Kondo1976]
[f] photoreflectance [Aspnes1972]
[g] absorption spectrum [Nishino1974]
[h] inverse photoemission [Ortega1993]

Table 2.3: Experimental measurements of Silicon band structure parameters

The details of this calculation will be discussed further in section 6.3 of chapter 6.

However, a similar calculation of indirect optical transitions is more complex since it requires calculating the effects of electron-phonon coupling.

2.3 Proposed approach

2.3.1 Experimental: polarized photoemission

State of the art

The polarized photoemission refers to the measurement of spin polarization of electrons emitted from sample by photoelectric effect. In the case of spectroscopic measurement the kinetic energy of electrons is also analyzed. Photoemission spectroscopy allows to separate the electrons with different history in crystal. In other words, in the measured spectrum the contributions of ballistic electrons and the electrons which have undergone collisions are resolved. A characteristic feature of this method is its applicability to the study of the properties of both the electrons at the bottom of the conduction band and at the high-energy bands.

Let us concentrate on the photoemission process from bulk Silicon under optical pumping (OP) conditions. For the electron inside the crystal, one should consider three processes:

1. Free travel between two collisions, characterized by free mean path, τ_m.

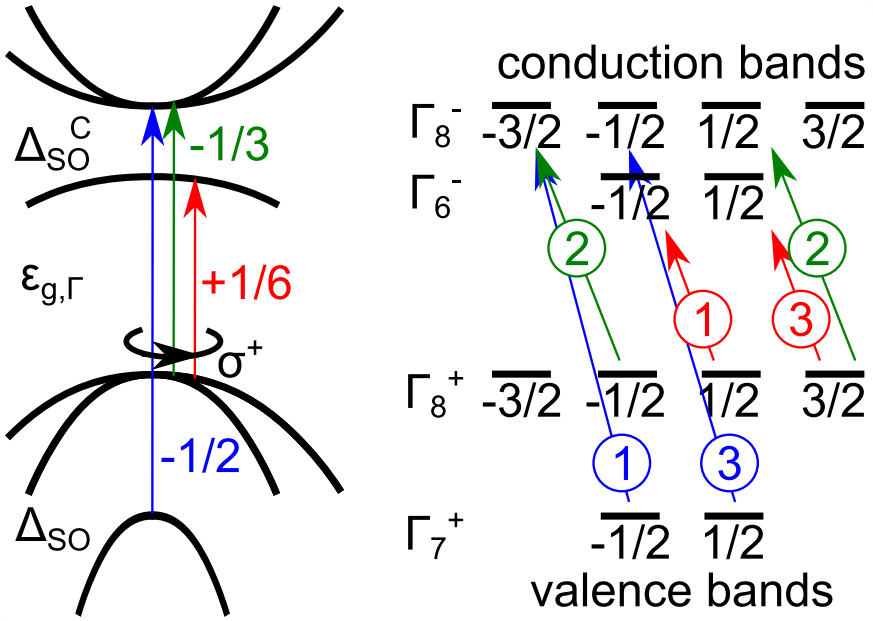


Figure 2.8: A direct optical transition at the center of Brillouin zone of Si. The spin-orbit interaction-induced splittings of valence and conduction band are denoted as Δ_{SO} and Δ_{SO}^{c} respectively (left). Calculation of corresponding initial polarization under σ^+-circularly polarized light excitation. The fractions denote m_j orbital moment of states at $k = 0$, the circled numbers are the transition intensities (right).

The energy dependence of the inelastic mean free path is characterized by so called 'universal' curve, valid for metals and semiconductors (fig. 2.9). One can note that few information is available on mean free path lower than 5 eV. Furthermore, according to a classical model for low energies

$$l = \left(\frac{1}{\epsilon - \epsilon_F} \right)^2 \tag{2.9}$$

mean free path diverges at ϵ comparable with ϵ_F. For energies above 10^2 eV the dependence of the mean free path is proportional to $\epsilon^{\frac{1}{2}}$.

2. The diffusion of conduction photoelectron until its recombination back to valence band. This process is equivalently characterized by the electron lifetime τ_e or by its diffusion length

$$L_e = \sqrt{D\tau_e} \tag{2.10}$$

with the diffusion coefficient D given by Einstein relation $D = \frac{\mu k_B T}{q}$.

3. Photoemission of conduction electrons into vacuum.

Ballistic and hot electrons experience only the processes 1 and 3, whereas for thermalized electrons the free travel between collisions appears as a part of a diffusion process on a larger time scale. Another important length scale to be considered is the depth of space charge region, which is about 10 nm.

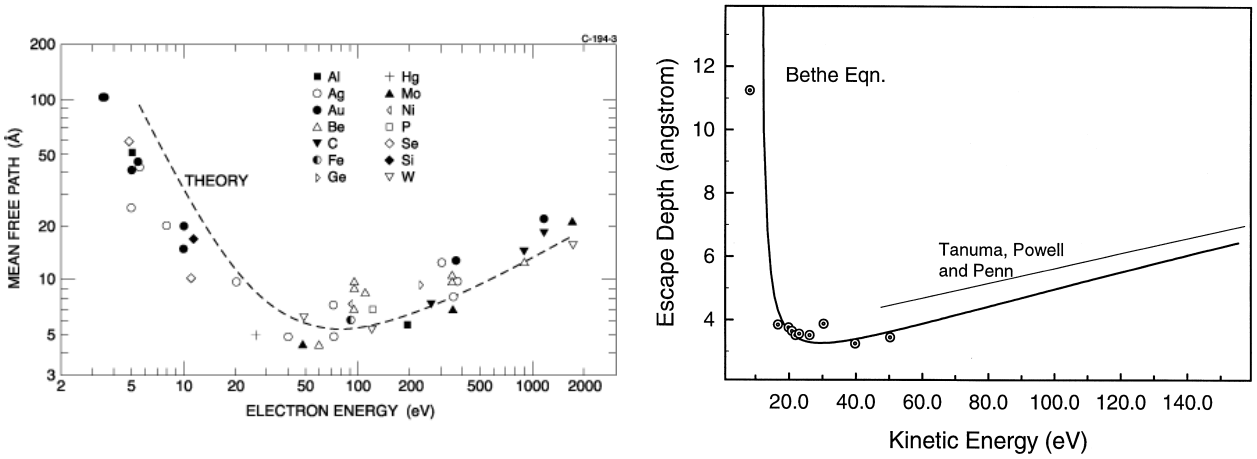


Figure 2.9: Electron mean free path dependence on kinetic energy [Briggs1983] (left), the same curve for Silicon [Pi2000] (right)

Let us denote the spin relaxation time by T_1. In fact, the discussed earlier spin lifetime τ_s is defined via

$$\frac{1}{\tau_s} = \frac{1}{T_1} + \frac{1}{\tau_e} \tag{2.11}$$

The eq. (6.47) can be interpreted as follows: the decay of polarization can occur either due to the spin relaxation, or due to the recombination of electrons back into the valence band. Given the eq. (6.47), the ratio of spin and electron lifetimes can be rewritten as

$$\frac{\tau_s}{\tau_e} = \frac{T_1}{T_1 + \tau_e} \tag{2.12}$$

Since in Silicon $\tau_e \gg T_1$, τ_s is essentially close to T_1.

Two regimes of photoemission should be distinguished:

- In the case when the absorption length α^{-1} exceeds the sample thickness d: $\alpha^{-1} > d$, or equivalently $h\nu < h\nu_{\text{critical}}$ (regime of weak injection) [Drouhin1985]

$$P_{\text{el}} = P_i \frac{T_1}{T_1 + \tau_{\text{escape}}} \tag{2.13}$$

where
Here the escape time is of the same order of magnitude as electron lifetime. Indeed the absorption depth is long enough to suppose that creation takes place throughout the sample volume. The mean distance traveled by electrons before their escape from crystal is on the same order of magnitude as the diffusion length. Consequently the ratio of ballistic to thermalized electrons in this regime is weak. It is generally considered that the electrons thermalize quickly and then diffuse towards surface [Martinelli1970]. The diffusion of electrons is also the reason for the power 1/2-dependence of electron polarization on the ratio of lifetimes.

- In the case when the absorption length is lower than the sample thickness: $\alpha^{-1} < d$, or equivalently $h\nu > h\nu_{\text{critical}}$ (regime of strong injection), the photoemission experiment allows to replace the lifetime by an escape time of electrons in a vacuum:

$$P_{\text{el}} = P_i \sqrt{\frac{T_1}{T_1 + \tau_{\text{escape}}}} \tag{2.14}$$

  Since the absorption coefficient is an increasing function of excitation energy $h\nu$, for fixed d this regime can also be characterized by $h\nu > h\nu_{\text{critical}}$.

For the considered in the present work SOI samples $d \approx 10^{-6}\,\text{m}$, which results in $h\nu_{\text{critical}} \approx 2.5\,\text{eV}$.

The measurement of the distributions of electron kinetic energy from Silicon was previously performed by [Ebina1972; Lassailly1990; Roux2008]. The polarimetry of photoelectrons is a commonly used technique, applied to various types of samples. The polarization of electrons photoemitted from bulk Silicon was measured by [Bona1985; Roux2008]. Semiconductor materials with lower symmetry (e.g. strained or low-dimensional structures) often yield higher spin polarization. So the polarization of 60% from Ge/GeSi/Si(1 0 0) nanostructure was recently reported [Bottegoni2011].

The inverse polarized photoemission is a similar technique for measurement the conduction states. However, its application is associated with problem of low cross section, and as a consequence, high total charge [Yoshida2012]. Combined with angular resolution, the photoemission (direct or inverse) gives access to the electron dispersion curves along different direction.

The polarized photoemission is the most natural technique for studying the properties of hot electrons. In fact, besides the general limitation of luminescence reflected by eq. (2.3), the luminescence of hot electrons is also characterized by very weak signal level. As for magnetic resonance approach, it is also insensitive to the hot electrons.

Contribution of the present work: increasing the spin to electron lifetime ratio

For semiconductors, where, like in Silicon,

$$\frac{\tau_s}{\tau_e} \approx 10^{-3}\,\text{s} \ll 1 \tag{2.15}$$

a commonly used experimental approach consists in increasing this ratio via the reduction of the effective lifetime of conduction electrons. In order to increase the polarization obtained by OP with circularly polarized light, following ways of reducing τ_e were considered:

- In the context of NMR, the enhancement of nuclear polarization by factor of 30 was achieved with the introduction of deep recombination centers at concentration of $n_{\text{Au}} = 3 \times 10^{16}\,\text{cm}^{-3}$ [Bagraev1978].
- Roux tested similar approach with lower concentration $n_{\text{Au}} = 10^{14}\,\text{cm}^{-3}$ for increasing the initial polarization of conduction electrons detected by polarized photoluminescence. However, no polarization above the detection limit was observed.

Methods proposed in [Verhulst2004] are related to the increase of the nuclear polarization under linearly polarized irradiation (so called Overhauser effect), and are not directly applicable for increasing the electronic polarization under circularly polarized light excitation.

In a photoemission experiment on bulk Silicon [Roux2008], the major difficulty is to discriminate between initial polarization P_i and the way it is relaxed, governed by eq. (2.15). In fact, in such experiment a non-zero polarization is only measured in vicinity of the first direct gap. As for the excitation energy near the fundamental gap, the obtained polarization is close to zero. Since no electron energy-resolved theoretical calculation of $P_i(h\nu \approx \epsilon_{g,X})$ is available, it is not possible to discriminate between

- Low initial polarization $P_i(h\nu \approx \epsilon_{g,X})$
- Presence of significant spin relaxation

In the case of the low initial polarization, it is legitimate to suppose that electrical injection can provide interesting results. However, the spin-LED measurements, where 30% spin-polarized electrons was electrically injected in Silicon from a ferromagnetic material, and the degree of circular polarization of the photoluminescence was measured, reveal very low polarization of nearly 3% [Jonker2007]. Similarly to spin-LED measurements, the photoemission is another possible approach which allows to partially lift off the limitation induced by low initial polarization P_i, since the characteristic for luminescence ${P_i}^2$ is replaced by P_i.

The guideline to the experimental part of our work is to reduce the sample thickness in order to replace τ_e by (lower) escape time, and thus to limit the ratio τ_s/τ_e. In particular, the present study is aimed is to check whether the use of thin layer of Silicon ($d \lesssim L_s$) results in an increase of the observed polarization under OP conditions with near $\epsilon_{g,X}$ light excitation.

2.3.2 Theoretical: full Brillouin zone calculation of OP

As we have seen in section 2.2.3, the analytical model of initial polarization provides only a limited description of optical pumping mechanisms in Silicon. In fact, in order to estimate the initial polarization below the direct band gap, a full Brillouin zone calculation of both the band structure and phonon dispersion relationships should be performed.

State of the art

The determination of the main band gaps (optical transition onsets) is crucial for interpreting optical pumping experiments. But in fact, a successful complete calculation of optical pumping relies on a precise description of the band structure and electronic states all over the BZ. The ability to reproduce the experimentally measured band gaps is a prerequisite of such the description. Thus, as a preliminary step for the construction of complete OP model, it is of interest to assess the precision of different numerical methods. The fundamental concepts of density functional theory (DFT), such as local density approximation (LDA) and the GW approximation of Hedin (GW), are recalled in appendix B.

DFT A non-local pseudopotential method [Chelikowsky1976] yields the gap values in good agreement with the experimental: $\epsilon_{g,X} = 1.17\,\mathrm{eV}$, $\epsilon_{g,\Gamma} = 3.43\,\mathrm{eV}$, $\epsilon^2_{g,\Gamma} = 4.17\,\mathrm{eV}$,

$\epsilon_{g,L} = 2.15\,\text{eV}$, $\epsilon_{g,L}^{\text{direct}} = 3.37\,\text{eV}$. This paper is used as a reference for a number of later experimental works.

Boulanger calculated the thermal variation of band gaps with use of Gruneisen parameters within the framework of LDA, in good agreement with experimentally observed variation. For $T = 0\,\text{K}$ the calculation via GW yields $\epsilon_{g,X} = 1.15\,\text{eV}$ and $\epsilon_{g,\Gamma} = 3.19\,\text{eV}$. Energy-only self-consistent GW results in $\epsilon_{g,\Gamma} = 3.42\,\text{eV}$, whereas the full self-consistent GW overestimates the direct gap as $\epsilon_{g,\Gamma} = 3.48\,\text{eV}$ [Boulanger2011]. Using GW method with self-consistency on quasiparticle part of the Green's function, an indirect band gap of Silicon $\epsilon_{g,X} = 1.2\,\text{eV}$ is obtained [Shishkin2007].

The use of all-electron one-shot GW for Si, which is often considered as a reference for pseudopotential calculations, results in $\epsilon_{g,X} = 1.19\,\text{eV}$, whereas the direct gaps are less concordant with the experimental data ($\epsilon_{g,\Gamma} = 3\,\text{eV}$, $\epsilon_{g,\Gamma}^2 = 4.3\,\text{eV}$) [Ishii2010]. In this work the L gap is given by $\epsilon_{g,L} = 2.09\,\text{eV}$ and $\epsilon_{g,L}^{\text{direct}} = 3.32\,\text{eV}$.

[Krasovskii1999] presented an original combination of k.p and plane wave method for half space. However, the energies are much higher than the energy of the lower conduction bands of Silicon studied in the present work. The same research group described carrier injection in the regime of direct transitions within one-step photoemission model [Krasovskii2010].

Marini and Del Sole have shown that modeling excitons with Bethe-Salpeter equation results in absorption spectrum in good agreement with experimental results from [Lautenschlager1987]. The eigenenergies for Silicon are not explicitly given [Marini2003].

k.p method The k.p method provides a quazi-analytical description of the band structure based on a number of adjustable input parameters, which include in particular the eigenenergies at Γ. The result of a k.p calculation is the eigenenergies in the whole Brillouin zone. Thus, it makes sense to consider as an output of k.p calculation only the parameters requiring the points distinct from Γ (such as $\epsilon_{g,X}$, $\epsilon_{g,L}$, $\epsilon_{g,L}^{\text{direct}}$). As for parameters at $\epsilon_{g,\Gamma}$, $\epsilon_{g,\Gamma}^2$, they should be directly compared with the source data for the k.p model. To date the most precise k.p model of Silicon is the 30 band description which has been developed in [Richard2004a; Richard2004b]. The band structure parameters, calculated within this model, are given in table 2.2.

Phonon dispersion The phonons represent an integral part of optical transitions with excitation energies below the direct bang gap. In this section we present the main phonon modes in Silicon crystal. So, fig. 2.10 shows the phonon dispersion curves calculated by DFT. Since the Silicon primitive cell contains $N = 2$ atoms, there exists one longitudinal acoustic mode and two transverse acoustic modes, as well as $3(N-1) = 3$ optical modes.

As one can see in the fig. 2.11, the amplitude of peaks in absorption spectrum is very different for different phonon modes. For instance, the amplitude of longitudinal optical (LO) phonon peak is comparable with that of two-phonon peak implying transverse optical (TO) phonons. As will be discussed in chapter 6, the polarization of indirect optical transitions depends heavily on the phonon mode. Thus, the total polarization is in fact determined by relative intensities of phonon-assisted transitions, similar to that shown in fig. 2.11.

In Silicon, four types of phonons are distinguished, with typical energies of Γ given in table 2.4. As illustrated by third column of the table, the phonon energies can be precisely reproduced within pseudopotential numerical models.

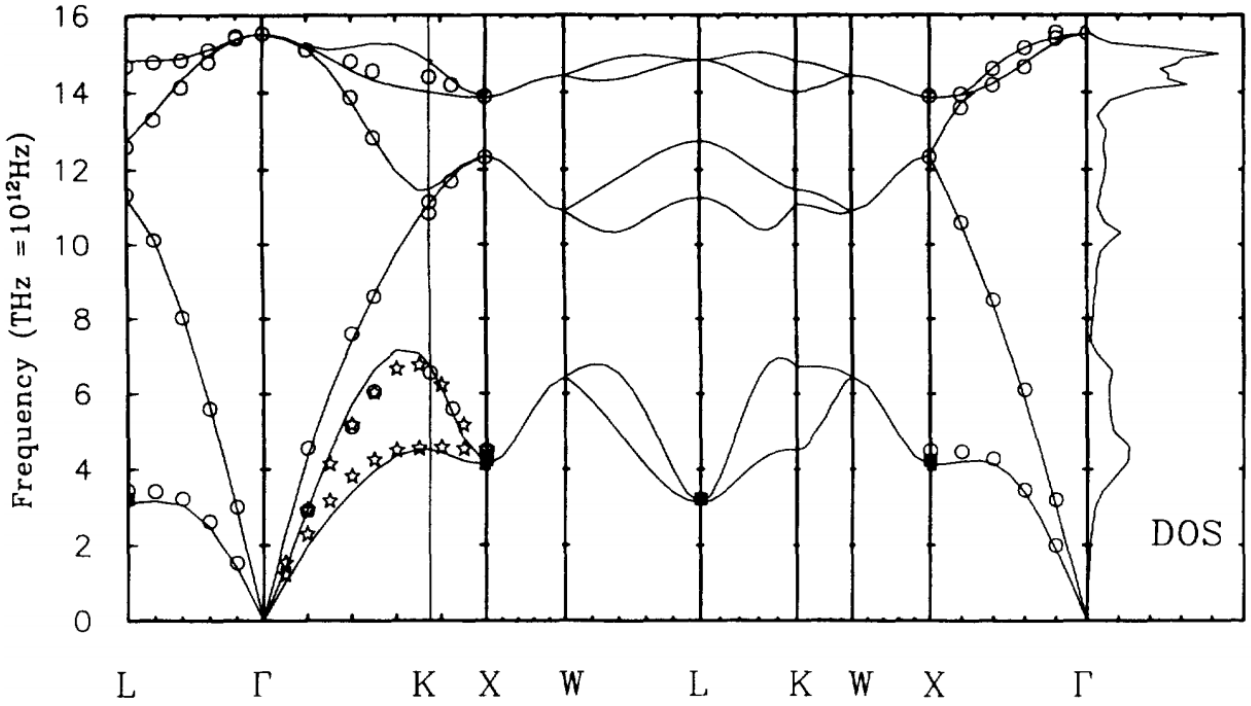


Figure 2.10: Dispersion of phonons in Silicon. $100\,\mathrm{cm}^{-1} = 12.7\,\mathrm{meV}$ [Giannozzi1991]. Experimental data are taken from [Nilsson1972]

Phonon mode	Experiment [Nishino1974]	Calculation [Cheng2011a]
Transverse optical (TO)	57.5 meV	57 meV
Longitudinal optical (LO)	55 meV	53 meV
Transverse acoustic (TA)	18.5 meV	19 meV
Longitudinal acoustic (LA)	46.3 meV	43 meV

Table 2.4: Energies of phonon modes at Γ

Optical pumping calculations Recent numerical calculations, which will be discussed in details in chapter 6, supply a more complete yet still partial response to the question of initial polarization. The existing numerical calculations of optical pumping in Silicon can be divided in two categories:

- Those considering near-indirect gap excitation [Li2010; Cheng2011a]. In these calculations the initial polarization is calculated as a sum of the transition probabilities over all admissible indirect transitions.
- Those considering only direct optical transitions [Nastos2007].

However, all of them describe only the energy-averaged polarization, which is well suited for the comparison with the luminescence spectrum, but not with the data obtained via the polarized photoemission.

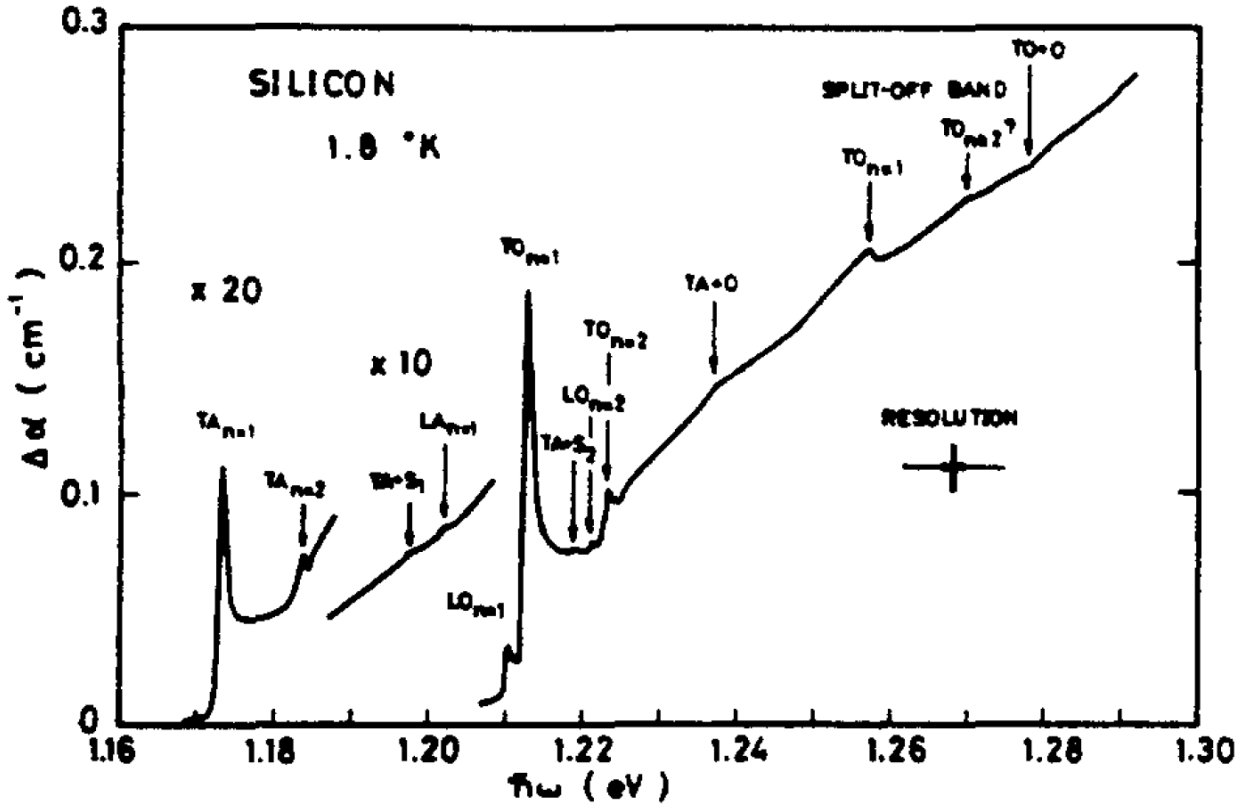


Figure 2.11: Absorption spectrum at 1.8 K with contributions of different phonon modes [Nishino1974]. The dots represent the neutron spectroscopy data from [Nilsson1972]

Contribution of the present work: energy-resolved ab initio model

In order to enable in-depth comparison with the photoemission data on OP in Silicon, an initial polarization model should include following features, none of them being present in the existing calculations:

- Initial polarization calculated as a function of both excitation energy $h\nu$ and electron kinetic energy ϵ
- k-point resolution: transitions from different regions of Brillouin zone are to be calculated separately
- Consideration of both indirect and direct optical transitions within the same computational framework

The initiation of the development of such a theoretical description is the second objective of the present work.

Chapter 3

Experimental details

3.1 Introduction

In this chapter we give an overview of the experimental setup for measuring the electron polarization under circularly polarized light excitation. We focus on the experimental techniques, such as the calibration of the Babinet-Soleil compensator and the Mott polarimeter. In section section 3.3 we describe the considered sample types, the photocathode preparation procedure, and characterize the photoemission yield of the studied samples.

In the following sections we present the measurable quantities, such as electron distribution curve (EDC) and polarized electron distribution curve (PEDC), and propose original methods of their analysis. We analyze the temperature dependence of the thresholds on the EDCs, and present the interpretation of features observed in this type of spectra.

3.2 Experimental setup

The experimental setup, which operates under ultra-high vacuum (UHV) conditions, consists of sample preparation and Mott detector chambers interconnected by the tube containing the electron spectrometer. The sample, acting as a photocathode, is mounted on a holder which allows sample heating up to 1500 K and cooling down to liquid nitrogen temperature. In the optical pumping configuration, a quartz window allows sample illumination at normal incidence. The circularly polarized light is produced by a linearly-polarized laser followed by the Babinet-Soleil compensator (the left panel of fig. 3.1). The extracted photoelectrons are energy-analyzed by the spectrometer and injected in a Mott polarimeter where their spin polarization is measured.

In order to achieve the activation of photocathodes to negative electron affinity with a sufficient stability the working pressure should not exceed 5×10^{-10} Torr. In particular, the cathodes are especially sensitive to partial pressures of O_2 and H_2O.

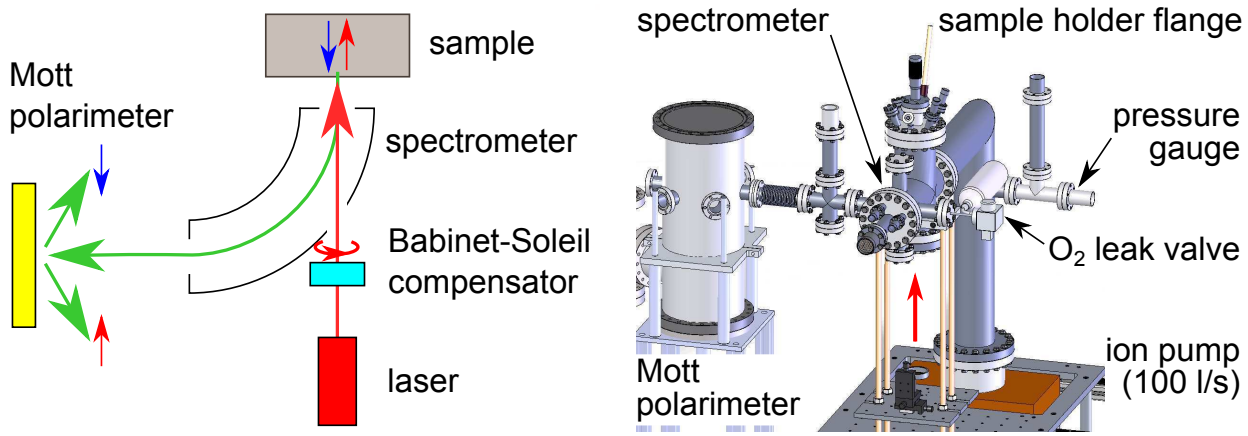


Figure 3.1: Setup operation principle (left), schematic view of UHV chamber (right)

3.2.1 Light excitation

Light sources

The objective of the present work is to study optical pumping in Silicon in an energy range which starts from the fundamental band gap $\epsilon_{g,X} \approx 1.12\,\text{eV}$ at room temperature and extends beyond the direct gap $\epsilon_{g,\Gamma} \approx 3.3\,\text{eV}$. Thus we have made use of different classes of light sources:

- Laser diodes:
  - Infrared (IR) $\lambda = 785.2\,\text{nm}$, $h\nu = 1.579\,\text{eV}$. This light source is usually used during the cesiation procedure in order to monitor the variation of the photocurrent.
  - Red $\lambda = 641\,\text{nm}$, $h\nu = 1.934\,\text{eV}$
  - Green $\lambda = 531.4\,\text{nm}$, $h\nu = 2.333\,\text{eV}$
- Kr+ laser which provide about 10 different lines from the near IR to the near ultraviolet (UV).
- Pulsed Ti:Sapphire laser, followed by the second harmonic generator (SHG) or the third harmonic generator (THG). Three ranges of photon energy should be distinguished:
  - Fundamental range: IR light, $\lambda = 680 - 1060\,\text{nm}$, $h\nu = 1.17 - 1.82\,\text{eV}$
  - SHG range: visible - near-UV light, $\lambda = 340 - 530\,\text{nm}$, $h\nu = 2.34 - 3.65\,\text{eV}$
  - THG range: UV light, $\lambda = 267 - 353\,\text{nm}$, $h\nu = 3.54 - 5.47\,\text{eV}$

The choice of pulsed rather than continuous Ti:Sapphire laser was guided by the requirement to cover not only IR but also UV part of the spectrum, which is achievable with SHG/THG provided that pulsed radiation is used.

The Ti:Sapphire laser is used either in continuous or in low-power pulsed modes. Because this laser has been designed for use in pulsed mode, the operation resulted in a continuous mode power fluctuations in the long-term (more than a day) measurements, probably induced by temperature variations. A drift in wavelength of the order of the few nm was observed for some acquisitions lasting more than several days.

It should be noted that even at the optimum tuning of the pulsed mode, the radiation output always contains a continuous component. For a good tuning of the laser employed in the present work,

$$\frac{I_{\text{continuous}}}{I_{\text{pulsed}}} \approx 10^{-4} - 10^{-6} \tag{3.1}$$

however, this ratio may be substantially higher for the pseudo-pulsed modes.

The laser is designed for pulse generation mode TEM00, which is localized in the spot center. Continuous radiation components usually correspond to higher modes. Thus continuous components may have an uneven distribution in the plane traverse to the beam propagation direction. The latter fact was confirmed experimentally. If the $(\boldsymbol{e}_x, \boldsymbol{e}_y, \boldsymbol{e}_z)$ is a Cartesian coordinate system, and laser light propagates along $\boldsymbol{e}_z$, it is likely that $\frac{I_{\text{continuous}}(x,y)}{I_{\text{pulsed}}(x,y)}$ can take higher values on the periphery of the beam.

The Ti:Sapphire laser can generate an output beam with a power up to 3 W. According to the table 3.1, the SHG in the femtosecond regime yields up to $0.5 - 1$ W of average optic power in the near UV, which corresponds to 25 kW and 25 MW of peak power respectively in the case of 100 ps and 100 fs pulses at the rate $F_{\text{pulse}} = 80$ MHz. The energy per pulse is about 2.5 µJ for both regimes. The power is adjusted with help of a linear polarizer tilted with respect to the linear polarization direction at the exit of the laser.

Wavelength is measured using an Ocean Optics USB spectrometer, and later with Jobin-Yvon H25, with typical precision of ±1 nm.

Measurements of laser power are made using a bolometer with a bandwidth of the order of $F_{\text{bolometer}} = 10$ Hz. Thus, the measured values correspond to the pulsed radiation power averaged over about

$$\frac{F_{\text{pulse}}}{F_{\text{bolometer}}} \approx 10^7 \text{ pulses}$$

both in the picosecond and the femtosecond regimes.

Modulation of light polarization

Usually in similar experiments a Pockels cell is used to modulate the laser light polarization. However, in our case a long optical path would make the alignment process with the Pockels cell more difficult, so the use of the Babinet-Soleil compensator was preferred to generate circularly polarized light. In order to change between σ^+ and σ^-, the mobile wedge of the Babinet-Soleil compensator is mounted on a piezomotor (PI C866) with the typical precision of 0.1 µm which corresponds to a precision of about 0.2 Å in the fig. 3.4. The Babinet-Soleil compensator is rotated by 45° with respect to the axis of initial linear polarization of the laser.

	Picosecond	Femtosecond
SHG	10%	30%
THG	3%	10%

Table 3.1: Maximum conversion efficiency of high-harmonic generator

Before the polarization measurement, the displacement of the compensator corresponding to σ^+ and σ^- need to be calibrated. This is achieved with the help of the Glan–Thompson prism, which is installed after the Babinet-Soleil compensator to ensure light extinction when the polarization is crossed. Then the photocurrent dependence on the position of the mobile wedge is recorded. This dependence consists of dark and bright fringes, with interfringe distance proportional to $\lambda/2$. The transmitted intensity I follows the law:

$$I = I_0 \sin^2 \phi/2 \tag{3.2}$$

where I_0 is the incident intensity, and ϕ is the phase shift induced by different thicknesses of fixed and mobile wedge.

In fig. 3.2 the transmitted intensity dependence on piezomotor position for excitation at 374 nm is shown. The maximum of piezomotor excursion is 18 mm. On the basis of this data, precise estimations of period and zero order are obtained. These two quantities are plotted as a function of excitation energy in fig. 3.3.

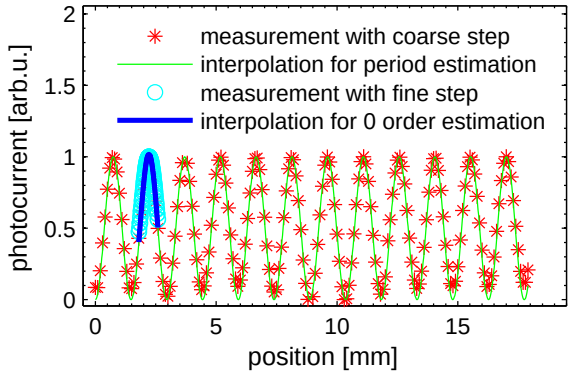


Figure 3.2: Example of Babinet-Soleil calibration for $h\nu = 3.32\,\mathrm{eV}$

The interpolation of intensity variation period (denoted by T) yields

$$T[\mathrm{mm}] = 4.614 \times 10^{-3} h\nu[\mathrm{nm}] - 2.479 \times 10^{-1} \tag{3.3}$$

and the zero order position O

$$O = 2.16\,\mathrm{mm} \pm 0.15\,\mathrm{mm} \tag{3.4}$$

where 0.15 mm is the standard deviation of measurements shown in the right panel of fig. 3.3.

The position of $O+T/4$ corresponds to σ^+ light, and $O-T/4$ to σ^- (the detailed definition of circular polarization is given further in section 3.2.1).

One should note that by definition the zero order position is wavelength-independent. Fluctuations in the estimation of zero order position (the right panel in fig. 3.3) are likely due to the fact that this value accounts for the deviation from the linear polarization at the laser output, which appears on the optical path. For measurements implying high harmonic generation (wavelengths shorter than 600 nm) the additional possibility of polarization distortion is introduced by non-linear optical components. So in order to keep the polarization

as circular as possible, the calibration of the zero order was carried out before each measurement. The error bar of each individual point in the right panel of fig. 3.3 does not exceed 0.1 mm and cannot explain the observed high level of scattering of the zero order position.

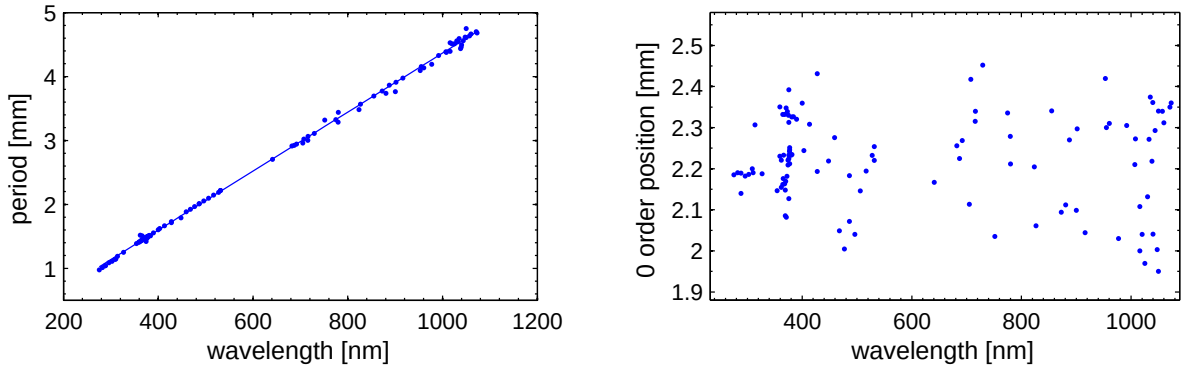


Figure 3.3: Results of the Babinet-Soleil calibration for all measurements: period of intensity variation from fig. 3.2 (left), 0 order position (right)

The convention on circular polarization is crucial for the determination of the polarization sign in optical pumping experiments. As consequence, it is important to know the direction of linear polarization just before the Babinet-Soleil compensator. The light is horizontally polarized at the output of the Ti:Sapphire laser. When arriving after several deflections to the horizontal plane of Babinet-Soleil compensator, the linear polarization is orientated along with $\boldsymbol{e}_x$ both for the fundamental and second harmonic optical lines (fig. 3.4). The third harmonic light is polarized along with $\boldsymbol{e}_y$, reversing the convention for σ^+. The vectors $\boldsymbol{e}_x$ and $\boldsymbol{e}_y$ correspond to the north-south and east-west directions in the laboratory and the setup itself is oriented along with north-south direction in order to minimize the electron beam deflection in the magnetic field of the Earth.

Convention on circular polarization

Let $(\boldsymbol{e}_x, \boldsymbol{e}_y, \boldsymbol{e}_z)$ be the right Cartesian coordinates with $\boldsymbol{e}_z$ orthogonal to the sample and $\boldsymbol{e}_x$ is aligned with south-north direction. The incident laser beam propagates along $\boldsymbol{e}_z$ direction (fig. 3.4).

Denote

$$\boldsymbol{e}_+ = \frac{\boldsymbol{e}_x + i\boldsymbol{e}_y}{\sqrt{2}}, \ \boldsymbol{e}_- = \frac{\boldsymbol{e}_x - i\boldsymbol{e}_y}{\sqrt{2}} \tag{3.5}$$

For a circularly polarized light (which exact polarization is detailed below), the vector potential $\boldsymbol{A}(t, z)$ is given by

$$\boldsymbol{A}(t, z) = A_0 \exp[i(kz - \omega t)]\boldsymbol{e}_+ \tag{3.6}$$

where A_0 is a complex constant.

$$\boldsymbol{A}(t, 0) = \frac{A_0}{\sqrt{2}} \left(\exp\left(-i\omega t\right) \boldsymbol{e}_x + \exp\left[-i\left(\omega t - \frac{\pi}{2}\right)\right] \boldsymbol{e}_y \right)$$

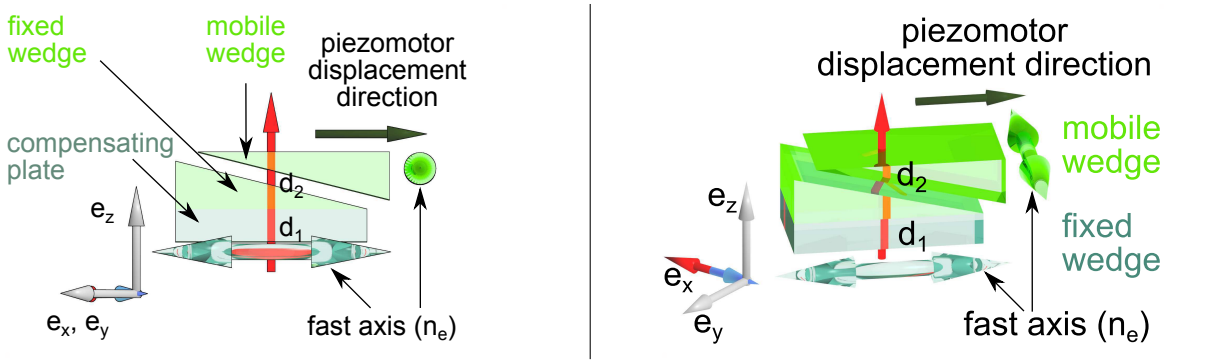


Figure 3.4: The location of axis of the Babinet-Soleil compensator, and the direction of the mobile wedge displacement, which leads to σ^+ if shifted by the value given in eq. (3.11). Incident laser radiation is linearly polarized along $\boldsymbol{e}_x$. The orientation of fast axis was double-checked with help of a calibrated quarter-wave plate.

It can be easily verified that the quantity

$$Re[\boldsymbol{A}(t,0)] = \frac{Re[A_0]}{\sqrt{2}}\left(\cos\left(-\omega t\right)\boldsymbol{e}_x + \cos\left(-\omega t + \frac{\pi}{2}\right)\boldsymbol{e}_y\right)$$

rotates counter-clockwise in $(\boldsymbol{e}_x, \boldsymbol{e}_y)$ plane when facing the light source, and at the same time

$$\arg[A_x(t,0)] - \arg[A_y(t,0)] = -\frac{\pi}{2} \tag{3.7}$$

The electric field is given by

$$\boldsymbol{E}(t,z) = -\frac{\partial \boldsymbol{A}}{\partial t} = i\omega A_0 \exp(i(kz - \omega t))\boldsymbol{e}_+ \tag{3.8}$$

$Re[\boldsymbol{E}(t,z)]$ follows the same sense of rotation as $Re[\boldsymbol{A}(t,z)]$.

The electron polarization is determined by the combination of light polarization and light propagation direction, i.e. by the chirality, denoted by σ^+ or σ^-. It should be noted that the rotation of the electric field vector in the counter-clockwise sense in the plane $(\boldsymbol{e}_x, \boldsymbol{e}_y)$ corresponds both

- To σ^+ light, propagating along $\boldsymbol{e}_z$
- To σ^- light, propagating along $-\boldsymbol{e}_z$

The electric field of the incident light before compensator, which is linearly polarized along the $\boldsymbol{e}_x$, is given by

$$\boldsymbol{E}(z,t) = \exp\left(i\left(\frac{2\pi z}{\lambda} - \omega t\right)\right) E\boldsymbol{e}_x \tag{3.9}$$

In the anisotropic medium we decompose the electric field in the basis of slow and fast axes of the fixed wedge ($\boldsymbol{o}_1 = \frac{\boldsymbol{e}_x - \boldsymbol{e}_y}{\sqrt{2}}, \boldsymbol{e}_1 = \frac{\boldsymbol{e}_x + \boldsymbol{e}_y}{\sqrt{2}}$). After propagating through wedges we obtain (the gap between wedges does not induce any phase difference and is omitted):

$$\boldsymbol{E}(d_1{+}d_2,t) = \frac{E}{\sqrt{2}}\left(\exp\left(i\left(\frac{2\pi(n_o d_1 + n_e d_2)}{\lambda} - \omega t\right)\right)\boldsymbol{o}_1 + \exp\left(i\left(\frac{2\pi(n_e d_1 + n_o d_2)}{\lambda} - \omega t\right)\right)\boldsymbol{e}_1\right)$$

The phase difference between x and y components is

$$\begin{aligned}\arg E_x(d_1+d_2,t) - \arg E_y(d_1+d_2,t) &= \arg(\boldsymbol{E}(d_1+d_2,t)\cdot\boldsymbol{o}_1) - \arg(\boldsymbol{E}(d_1+d_2,t)\cdot\boldsymbol{e}_1) \\ &= \frac{2\pi}{\lambda}((n_o d_1 + n_e d_2) - (n_e d_1 + n_o d_2)) = \frac{2\pi}{\lambda}(d_1-d_2)(n_o-n_e)\end{aligned} \tag{3.10}$$

For quartz $n_e - n_0 > 0$, thus the displacement of the mobile wedge (fig. 3.4) to the right corresponds to

$$d_1 - d_2 = \frac{\lambda}{4(n_e-n_o)} > 0 \tag{3.11}$$

and

$$\arg E_x(d_1+d_2,t) - \arg E_y(d_1+d_2,t) = -\frac{\pi}{2}$$

which is σ^+-polarized light according to the definition introduced in eq. (3.7).

3.2.2 Low-energy electrostatic electron spectrometer

The electron spectrometer is of cylindrical deflector type [Jost1981], and is described in details elsewhere [Drouhin1982; Drouhin1986; Roux2008]. Here we recall the main features: it is made of two 90° electrostatic deflection selectors coupled by a decelerating electron optics (the left panel in fig. 3.5). Only electrostatic components are used in the spectrometer in order to avoid the distortion of the spin polarization of electrons. An accelerating transport optics project analyzed electrons from the exit slit of the analyzer into the Mott polarimeter used for spin detection. The spectrometer resolution can be set in the range $20-100$ meV. Most of the measurements in the present study are performed at the resolution of 40 meV.

The photoelectrons with energy above the vacuum level (abbreviated as VL in the right panel in fig. 3.5) are extracted from the photocathode. With circularly polarized light excitation a longitudinal spin polarization of the emitted electrons is expected. The first 90° deflector (rotator) is needed to transform the longitudinal spin polarization of the emitted electron beam into a transverse polarization required for Mott scattering. The electrons are then decelerated and energy-analyzed in the second deflector (selector). To measure the EDC, electrons are collected on an electrode which acts as a Faraday cup. An EDC is obtained by varying the negative bias V_{cath} applied to the photocathode, while other potentials (i.e. the selection potential) are maintained fixed.

As can be seen from the fig. 3.5, to select the photoelectrons with kinetic energy in vacuum ϵ^{vac}, the following cathode potential should be applied

$$eV_{\text{cath}} = \epsilon^{\text{vac}} + \phi_{\text{cath}} - \phi_{\text{Au}} \tag{3.12}$$

The electron affinity χ relates ϵ^{vac} with the electron kinetic energy in the crystal ϵ:

$$\epsilon^{\text{vac}} = \epsilon - \chi \tag{3.13}$$

If the surface states form a continuum, we can redefine the minimum of conduction band at the surface as the beginning of this interval, which could result in slightly lower affinity, compared to the case where the surface states are not considered.

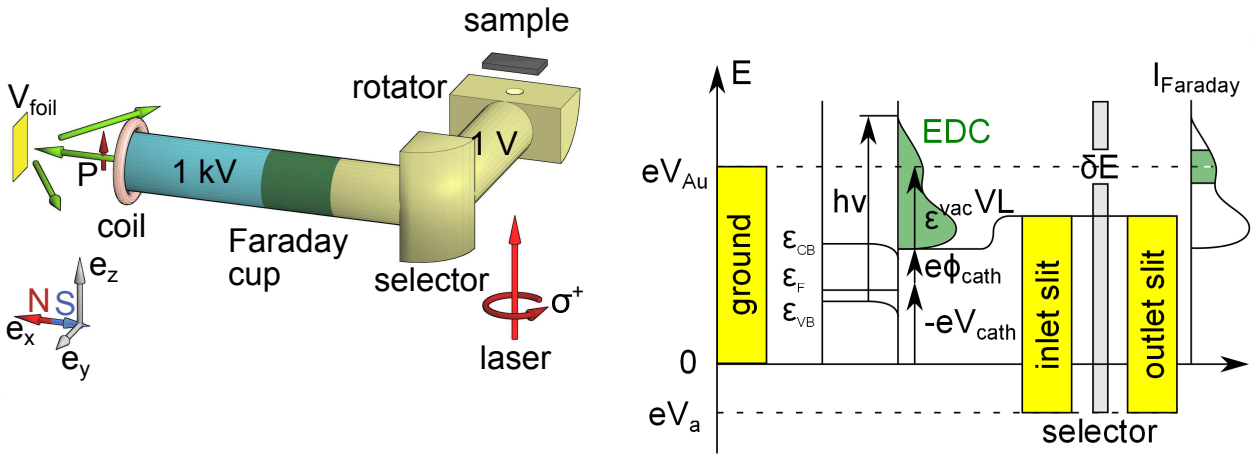


Figure 3.5: Schematic view of the electron optics. The sample faces the entrance slit of the rotator which is coupled to the selector by a decelerating electron optics. The selected electrons are either detected on a Faraday cup for EDC's measurements, or accelerated in a transport optics and projected into the Mott polarimeter. The P_z component of spin polarization is measured (left). Operation of the electron spectrometer: The bias voltage V_{cath} is applied to the cathode. The electrons which have a zero kinetic energy in the zero potential of the grounded gold electrode are selected. The electron optics potentials remain constant at the positive bias V_a. The conduction band minimum, the Fermi level and the valence band maximum are denoted as ϵ_{CB}, ϵ_F, ϵ_{VB} respectively (right). δE is the band pass energy of the spectrometer which can be chosen in the range $20 - 80\,\text{meV}$

At the same time,

$$\phi_{\text{cath}} - \chi = \epsilon_{\text{CB}} - \epsilon_{\text{F}} \approx \epsilon_{g,X} \tag{3.14}$$

where $\epsilon_{g,X}$ is the indirect band gap of Silicon.

Injecting eq. (3.13) and eq. (3.14) into eq. (3.12), we deduce

$$eV_{\text{cath}} = \epsilon + \epsilon_{g,X} - \phi_{\text{Au}}$$

Taking $\phi_{\text{Au}} = 4.8\,\text{eV}$ [Fomenko1966], and $\epsilon_{g,X} = 1.12\,\text{eV}$ the difference between cathode potential and electron energy in crystal can be estimated:

$$eV_{\text{cath}} = \epsilon + \epsilon_{g,X} - \phi_{\text{Au}} \approx \epsilon - 3.7\,\text{eV} \tag{3.15}$$

According to eq. (3.15), the minimum of the conduction band should appear for $eV_{\text{cath}} \approx -3.7\,\text{eV}$. A typical spectrum, which illustrates the relationships above, is denoted by EDC in the right panel of fig. 3.5.

3.2.3 Mott polarimeter

To measure the electron spin polarization, electrons are reaccelerated by a transport optics to the 1 kV potential of the outer cylinder of the Mott polarimeter chamber and further

injected in the Mott polarimeter. At the end of the transport optics an external coil is used to produce a magnetic field parallel to the electron velocity. Since electron spin polarization is transverse, precession around the magnetic field allows reversion of the polarization. In this way we can reverse the direction of polarization of the beam from $+\boldsymbol{P}$ to $-\boldsymbol{P}$ either by manipulating the light polarization between σ^+ and σ^- or by applying a magnetic field. This allows us to eliminate instrumental asymmetries.

In the cylindrical Mott polarimeter electrons are accelerated by a high voltage V_{foil} (typically $30 - 100\,\text{kV}$) toward an auto-supported gold film. The gold is chosen as scatterer for its chemical passivity and high atomic mass, implying strong spin-orbit coupling. In our experiment we use $1\,\mu\text{m}$-thick gold foil. A luminescent screen can be moved at the gold foil position for beam visualization. Once scattered by the foil electrons are collected by the right and the left detectors in two symmetric scattering directions.

In order to measure only elastically scattered electrons, a bias V_b is applied to the electrodes at the detectors entrance (the right panel in fig. 3.6). The choice of this bias represents a balance between electron flux (the higher V_b, the more electrons are collected) and the spin selectivity (since secondary electrons created in Au film do not contribute to the spin asymmetry), described by the figure of merit, which will be discussed in details further in eq. (3.30).

Electron spot adjustment criteria

The following criteria are used for tuning the electron optics:

1. Beam position. In an ideal situation, the image of the electron beam should be aligned with respect to the mirror symmetry plane of the Mott detector. In principle, this can be achieved by centering the spot on the fluorescent screen, which is located approximately in the symmetry plane of the detectors. At the same time, taking into account the small size of the fluorescent screen (8 mm) compared to 150 mm of the distance to the detectors, the angular asymmetry due to the centering inaccuracy is low, and is comparable to the asymmetry introduced by the finite size of the beam itself. Furthermore the centers of the entrance of the Mott detector and of the screen do not necessarily match horizontally (as shown in the right panel of fig. 3.7), or vertically (as the latter is mounted on a vertical translation). Thus the guideline is to keep the **spot entirely inside the Mott inlet aperture**.
2. Beam shape. A well-focused beam should form an **image of the vertical slit of the selector** (a rectangle of $0.5\,\text{mm} \times 3\,\text{mm}$).
3. Invariance in magnetic field. In order to limit instrumental asymmetry due to beam misalignment, the ideally obtained spots with and without longitudinal magnetic field should possess similar spatial distribution and intensity. However, since the application of magnetic field causes beam rotation, the only practical possibility is to **superpose the centers of spots** with and without magnetic field.

A successful tuning of the electron optics requires a compromise between all the parameters above. It was verified that the changes in sample position do not influence the shape of the spot on the gold foil.

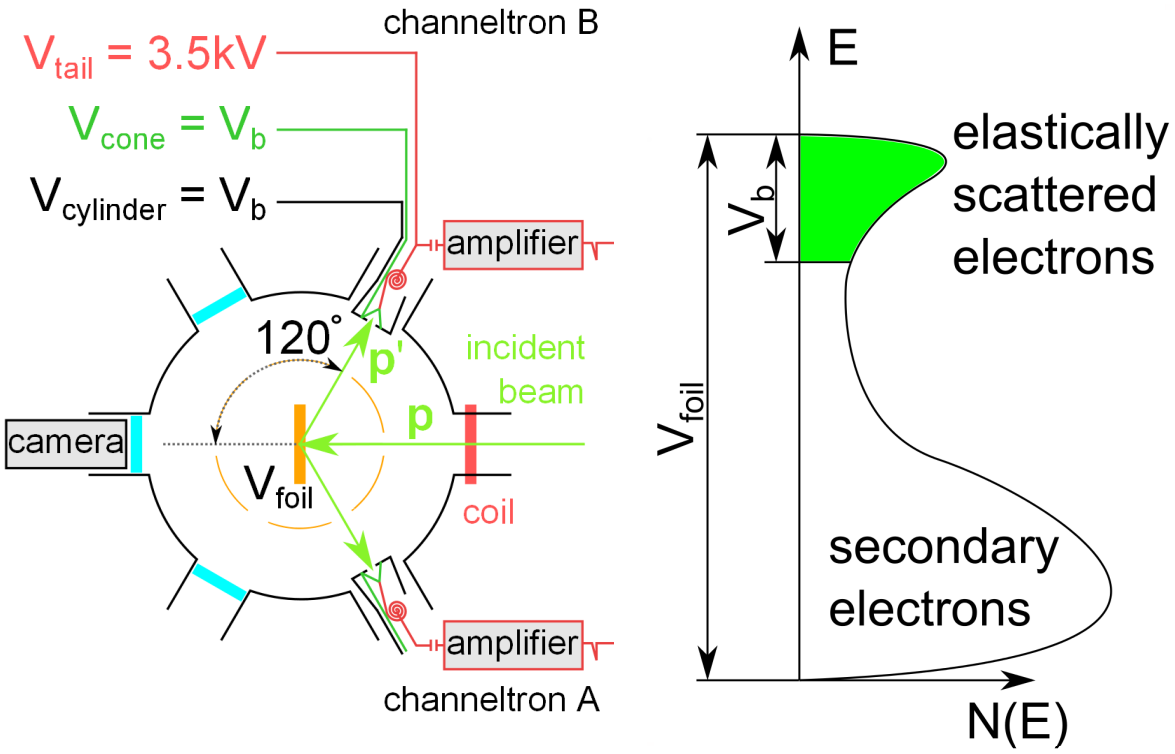


Figure 3.6: Top view of the Mott detector chamber. Electrons are accelerated by V_{foil}, and those which scatter at $\pm 120°$, pass through cone-shaped apertures and enter in the retarding fields V_b. $\boldsymbol{p}$ and $\boldsymbol{p}'$, the momentum vectors of the incident and scattered electron beams, define the scattering plane (left). Selection of the ballistic electrons in the Mott detector. Only the electrons that have suffered small inelastic energy losses on scattering are detected (right).

Electron beam rotation in longitudinal magnetic field

Experimental observations

Ideally electrons should move along the direction of the magnetic field and their polarization should be perpendicular to it. In this case electron trajectories remain unchanged and polarization precesses about the field with the frequency $\omega = \frac{eB}{m}$.

However, in the presented experimental setup the magnetic field of the coil which is used to flip spins by 180° also induces beam rotation by 97.5° (fig. 3.8). Furthermore, when the magnetic field is off both in figs. 3.7 and 3.8 one can note a slight tilt

$$\alpha_{\text{off}} = 5.5° \tag{3.16}$$

of the spot with respect to the horizontal plane. This tilt does not depend on the potential of electrodes, and is probably due to the action of horizontal component of the Earth's magnetic field. In fact, the acceleration optics is not magnetically screened. The south-north

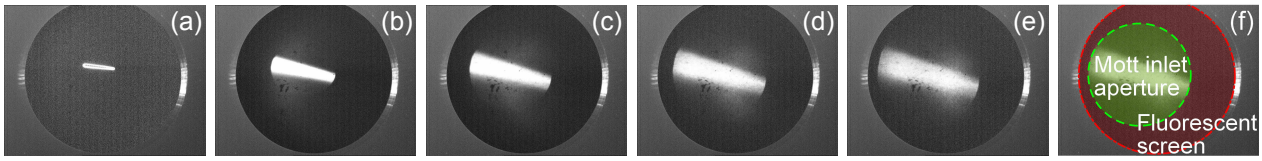


Figure 3.7: Spot size dependence on accelerating voltage (20 kV, 40 kV, 60 kV, 80 kV and 100 kV). The round inlet aperture of Mott detector can be seen in e and f images. It is artificially colored in f image

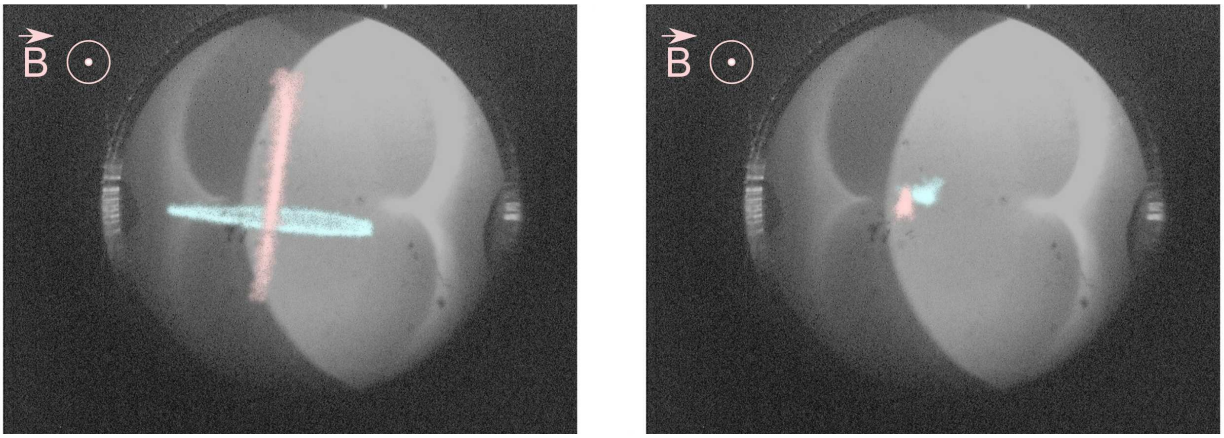


Figure 3.8: Superimposed images of the electron spot with (red vertical line) and without (blue horizontal line) magnetic field. On the left HT=60 kV, $h\nu = 2.38$ eV, resolution 40 meV, on the right HT=60 kV, $h\nu = 3.425$ eV, resolution 30 meV. The size of spots depends mostly on the potentials on electrodes. The magnetic field is perpendicular to the image.

orientation of this part of optics is aimed to minimize the electron beam deflection. The rotation of the beam image as a whole indicates that electrons possess the same angular velocity and rotation radius of about 1 mm.

In principle, the effect of the geomagnetic field may be compensated by using one or more large radius coils. However, as will be shown below, the effect of the Earth's magnetic field on polarization is insignificant.

An important question is why the beam that has a vertical cross-section at the selector outlet slit takes a horizontal form on the fluorescent screen. In the general case, a beam rotation could be caused by

- presence of a spurious longitudinal magnetic field, which may also perturb the measurements of the spin polarization
- deformation induced by an electrostatic field. Given the homogeneity of the magnetic field in the plane perpendicular to the beam propagation direction, the spot deformation can be explained by
  - non-homogeneity of the electric field (i.e. action of the Einzel lenses)
  - non-uniform initial distribution of velocities of electrons

Let us focus on the last hypothesis. The variation of v_y can be explained for instance by a non-zero divergence of the electron beam. Suppose that electrostatic lens focus the beam at the selector entrance. In this situation, as it can be seen in fig. 3.9, the variance of the velocity at the exit is equivalent to the variance at the inlet slit. v_z component remains unchanged during the passage of the selector, but variance along this axis can be caused by the above described mechanism during the passage of the rotator (first 90° deflector in fig. 3.5). Thus, in the real situation the velocity dispersion may take place along both $\boldsymbol{e}_y$ and $\boldsymbol{e}_z$.

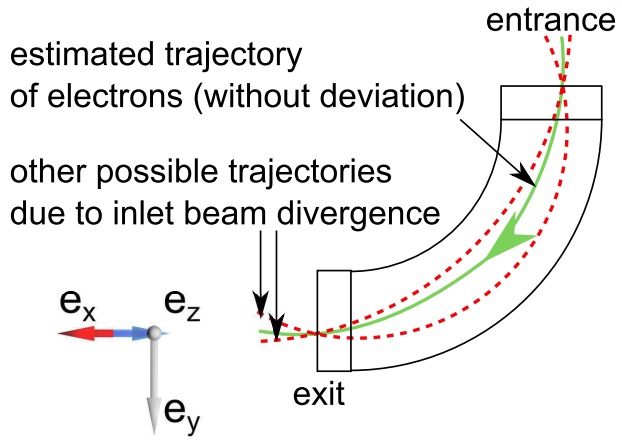


Figure 3.9: Planned (green line) and other possible (red dashed lines) electron trajectories in the selector. The electrons are polarized along $\boldsymbol{e}_z$

Theoretical description

In order to model and interpret these phenomena, we define a Cauchy problem on electron position $\boldsymbol{r}(t) = (x(t), y(t), z(t))$:

$$\begin{cases} m_0 \dfrac{d^2\boldsymbol{r}(t)}{dt^2} = e\dfrac{d\boldsymbol{r}(t)}{dt} \times \boldsymbol{B}(\boldsymbol{r}) + e\boldsymbol{E}(\boldsymbol{r}) & \text{(3.17a)} \\ \boldsymbol{r}(t=0) = \boldsymbol{r}^0 & \text{(3.17b)} \\ \dfrac{d\boldsymbol{r}}{dt}(t=0) = \boldsymbol{v}^0 & \text{(3.17c)} \end{cases}$$

The problem is reduced into a system of two first order ordinary differential equations, which is easily resolved with the explicit Euler scheme.

Here the magnetic field $\boldsymbol{B}(\boldsymbol{r}) = (B_{\text{Earth}}\cos(64°) + B_{\text{coil}}(x), 0, B_{\text{Earth}}\sin(64°))$ accounts for the magnetic inclination of 64°. The experimental value of 5.7 mT is taken for the magnetic field in the center of the coil (see section 3.2.4). The coil diameter is 5 cm, which is significantly larger than the typical diameter of electron optics (1 cm). Thus, the expression for the field on the symmetry axis of the coil provides a good description of the induced magnetic field in the electron optics.

The electric field $\boldsymbol{E}(\boldsymbol{r}) = (E_{\text{transport}}(x), 0, 0)$ is calculated as a gradient of potentials on transverse electrodes of transport optics, using the exact description of its geometry. In order

to keep the model simple, we do not consider either the Einzel lenses, or the electrostatic deflectors. The effect of the first ones on the solution represented in fig. 3.10 would probably result in the focusing of the beam, thus resulting in more vertical spot when the coil magnetic field is applied. The deflectors are likely to induce a rigid shift of the spot without inducing much shape deformation.

The spin precession frequency is given by $\omega = \gamma B$, where the gyromagnetic ratio $\gamma = \frac{eg_e}{2m_0} = 1.7609 \times 10^{11} \frac{\text{rad}}{\text{s T}}$. The Cauchy problem on polarization direction $\boldsymbol{e}_P(t)$ following the electron trajectory $\boldsymbol{r}(t)$ is given by

$$\begin{cases} \dfrac{d\boldsymbol{e}_P(t)}{dt} = -\gamma \boldsymbol{e}_P(t) \times \boldsymbol{B}(x) & \text{(3.18a)} \\ \boldsymbol{e}_P(t=0) = \boldsymbol{e}_z & \text{(3.18b)} \end{cases}$$

Results

As shown in left panel in fig. 3.10, the vertical component of the Earth's magnetic field induces a non-zero horizontal velocity even if the initial distribution is aligned with $\boldsymbol{e}_x$. In turn, the horizontal component enables the interaction of electron with the coil magnetic field and thus further distortion of the trajectory. This phenomenon may be accentuated even more in the real situation due to the electric fields not considered in the model. The right panel of fig. 3.10 represents the tilt in the spot in the presence of the coil magnetic field.

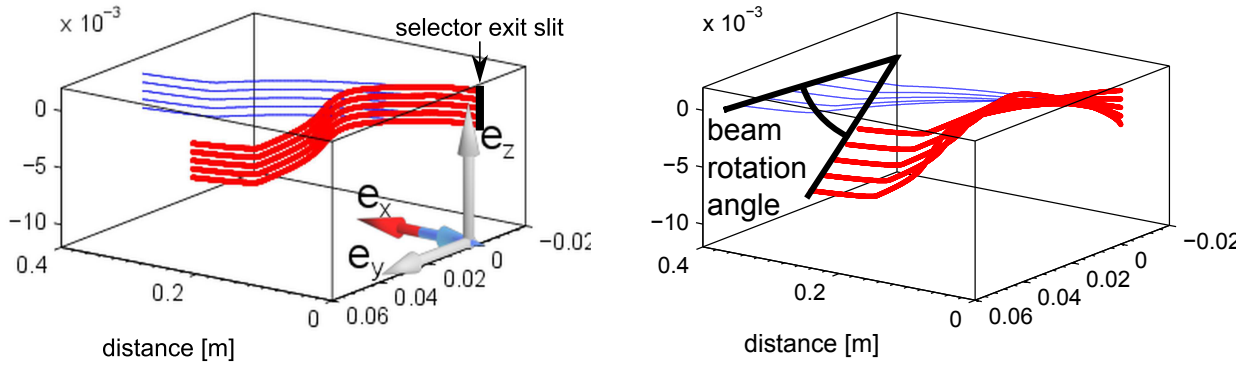


Figure 3.10: The calculated electron trajectories with (red points) and without (blue lines) the coil magnetic field. Electrons propagate along $\boldsymbol{e}_x$ (i.e. south-north) direction, and the presence of electric and magnetic fields leads to weak deviations in (y, z) plane. Left and right panels correspond to initial velocity distribution $(v_x, 0, 0)$ and $(v_x, v_y, 0)$ respectively. The projections are represented further in fig. 3.11

Using the model given in eq. (3.17) it is found that the initial velocity distribution varying along $\boldsymbol{e}_y$ describes the experimental data better rather than the distribution varying along $\boldsymbol{e}_z$. Such the spatial variation is given by

$$\boldsymbol{v}^0 = \left(v_x^0, v_y^0 \frac{z}{d_s}, 0\right), \text{ where } z \in [-d_s, d_s] \text{ with selector slit height } d_s = 1.5\,\text{mm} \qquad \text{(3.19)}$$

The left panel in fig. 3.10 corresponds to initial velocity aligned with $\boldsymbol{e}_x$:

$$\boldsymbol{v}^0 = \left(v_x^0, 0, 0\right) \tag{3.20}$$

The initial velocity components are taken as

$$v_x^0 = \sqrt{\frac{20\,\mathrm{eV}}{m_0}} = 1.8 \times 10^6\,\mathrm{m/s}, \quad v_y^0 = \sqrt{\frac{2\,\mathrm{eV}}{m_0}} = 6 \times 10^5\,\mathrm{m/s}$$

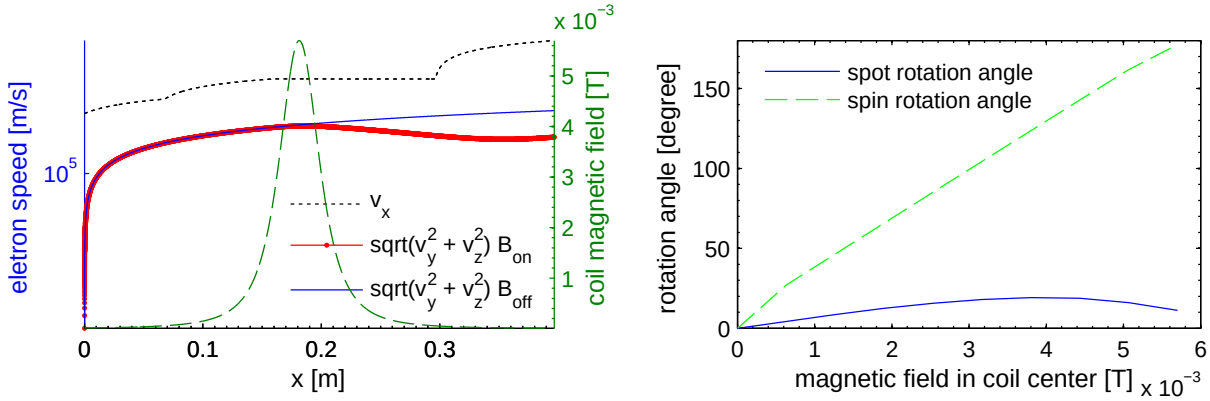


Figure 3.11: Longitudinal and transverse components of electron speed and magnetic field of the coil (left), spot rotation angle (right). The discontinuities of v_x correspond to the positions of accelerating electrodes.

The numerical solution allows for an estimation of the transit time of the transport optics, which is about 35 ns.

Equation (3.18) allows one to calculate the polarization direction at the moment of collision with the gold foil (table 3.2). As one can see in the first column, the action of the horizontal and vertical components of the Earth's magnetic field respectively result in some deviation of the polarization direction from vertical axis, but at the same time have no significant effect on the measured value of the polarization.

The right panel in fig. 3.11 shows that the spin rotation angle is essentially linear with the applied magnetic field, as well as increasing part of spot rotation angle. Thus, in the real situation we can estimate spin rotation angle as the double of spot rotation angle. In particular, the deviation of the spin polarization without magnetic field is about twice larger than the observed spot tilt, i.e. about 10°. The latter value is in reasonable agreement with modeled zero coil field value of $\theta = 7°$ from table 3.2.

The following processes are correctly described in the framework of this model:

- The beam without the coil magnetic field rotates from a vertical selector slit to almost horizontal screen image
- The change in the image tilt under the magnetic field of the coil is described qualitatively. However
  - No decrease in spot rotation angle similar to that represented in the right panel of fig. 3.11 is experimentally observed.

	θ	ϕ	P_z
B_{off}	7°	1°	0.992
B_{on}	177°	3°	-0.999

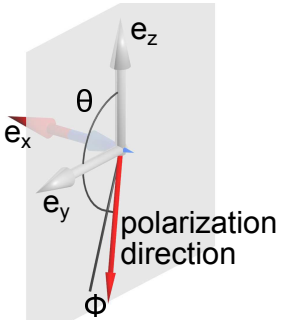


Table 3.2: The direction of the polarization vector of the electron in the moment of contact with the screen. θ is the angle in $(\boldsymbol{e}_y, \boldsymbol{e}_z)$ plane, Φ is the angle between polarization vector and its projection on $(\boldsymbol{e}_y, \boldsymbol{e}_z)$ plane.

  - Maximum rotation angle is significantly lower than the experimentally observed value of 90°.

- The angles of the spin polarization tilt taken from table 3.2, which are calculated based on the experimentally measured coil magnetic field, are in good agreement with the observed values.

Figure 3.10 suggests that the effect of the coil magnetic field exceeds considerably the effect of the Earth's magnetic field. Thus it is likely that the latter deviates the beam only by a small angle, such as the angle given by eq. (3.16), but cannot explain the 90° rotation of the beam.

It should be noted that the presence of a spurious magnetic field would lead to the rotation of the polarization direction, which could be compensated by the magnetic field of the coil. The fact that the measured electron polarization is symmetric with respect to the coil magnetic field (represented further in fig. 3.15, section 3.2.4) leads to the conclusion about the absence of such a spurious magnetic field.

Spin-orbit coupling

The spin orbit coupling is important for both optical pumping, spin relaxation and Mott scattering. While an electron moves with velocity $\boldsymbol{v}$ in the external electric field $\boldsymbol{E} = -\boldsymbol{\nabla} V$, it is subject in its own reference frame to the magnetic field $\boldsymbol{B} = \frac{1}{c^2}\boldsymbol{E} \times \boldsymbol{v}$, which causes the precession of the electron spin $\boldsymbol{S}$. The coupling energy between the spin and magnetic field is $-\boldsymbol{\mu} \cdot \boldsymbol{B}$. In the case of central field (i.e. atomic potential), the energy is given by [Cagnac1971]:

$$H_{\text{so}} = -\boldsymbol{\mu} \cdot \boldsymbol{B} = \frac{\hbar}{2m_0^2 c^2} \frac{1}{r} \frac{dV}{dr} \boldsymbol{L} \cdot \boldsymbol{S} \tag{3.21}$$

The electron angular momentum is given by $\boldsymbol{L} = \boldsymbol{r} \times \boldsymbol{p}$ with $\boldsymbol{r}$ being the radius vector. In eq. (3.21) the proportionality of the potential V to the atomic mass Z suggest the use of heavy atoms as scatterer for spin detection. A detailed derivation of spin-orbit Hamiltonian from the Dirac equation is given, for instance, in [Kessler1985].

We have $dV/dr > 0$, which implies $H_{\text{so}} \propto +\boldsymbol{L} \cdot \boldsymbol{S}$. The electrons are preferentially scattered in the direction (left or right) corresponding to $H_{\text{so}} < 0$ (attractive potential), that

is $\boldsymbol{L}$ and $\boldsymbol{S}$ pointing in opposite directions. Thus, the electrons with spin $|\uparrow\rangle$ are scattered by the spin-orbit interaction to the detector B. Spin $|\uparrow\rangle$-polarized electron beam induces a negative asymmetry ($\mathcal{A} = (A-B)/(A+B) < 0$) in the number of electrons captured by the detectors.

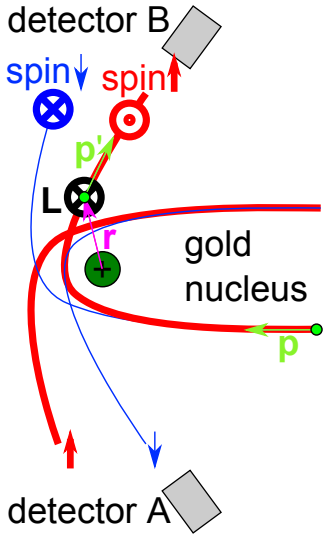


Figure 3.12: Mott scattering conventions. The scattering rate in a given direction is different for spin $|\uparrow\rangle$ and $|\downarrow\rangle$ electrons which leads to the left-right asymmetry when scattering a spin-polarized electron beam. $\boldsymbol{p}$ and $\boldsymbol{p}'$, the momentum vectors of the incident and scattered electron beams, define the scattering plane.

Effective spin scattering asymmetry calibration

The number of electrons captured by left and right counters[1] respectively is

$$\begin{cases} A = N_0(1 + S_{\text{eff}}\boldsymbol{P}\cdot\boldsymbol{n}_A) \\ B = N_0(1 + S_{\text{eff}}\boldsymbol{P}\cdot\boldsymbol{n}_B) \end{cases}$$

where S_{eff}, the so-called Sherman function, quantifies the spin selectivity, $\boldsymbol{p}$ and $\boldsymbol{p}'$ are the momentum vectors of incident and scattered electron beams respectively, and the normal to the scattering plane is given by (fig. 3.12)

$$\boldsymbol{n}_{A,B} = \frac{\boldsymbol{p}\times\boldsymbol{p}'_{A,B}}{|\boldsymbol{p}\times\boldsymbol{p}'_{A,B}|} \tag{3.22}$$

In this way

$$\begin{cases} A \propto 1 + S_{\text{eff}}P_z \\ B \propto 1 - S_{\text{eff}}P_z \end{cases}$$

[1]Commonly used notations are N_L and N_R. Here we denote these quantities by A and B for the sake of easier super- and subscript manipulation.

where A and B are numbers of electrons scattered to the left and right respectively.

The asymmetry resulting from the spin-orbit effect in the gold foil is defined as

$$\mathcal{A} = \frac{A - B}{A + B} \tag{3.23}$$

$\mathcal{A}$ is related to the z-component of spin polarization by

$$P_z = \mathcal{A}/S_{\text{eff}} \tag{3.24}$$

For the sake of compactness, the index z will be omitted in the description of experimental results.

According to the conventions given in the previous section, a positive value of P_z produces a negative asymmetry and thus:

$$S_{\text{eff}} < 0 \tag{3.25}$$

in agreement with [Lin1963; Gay1992]. One should note the error in the sign of S_{eff} given in [Campbell1985].

The theoretical (for $V_b \to 0$) and effective (measured for finite bias V_b) values of the Sherman function are given in table 3.3.

A linear regression of the theoretical Sherman function from for 120° scattering is given by (calculated in [Holzwarth1964], the data for the interpolation are extracted from the figure 9 of [Campbell1985], and represented in fig. 3.13):

$$S_{\text{th}}(V_{\text{foil}}[\text{kV}]) = -\left(-5.387 \times 10^{-8} {V_{\text{foil}}}^2 + 4.173 \times 10^{-5} V_{\text{foil}} - 1.264 \times 10^{-4}\right)^{1/6} \tag{3.26}$$

It is interesting to note that the calibration performed by Roux results in stepper increase of $S_{\text{th}}(V_{\text{foil}})$ compared to the theoretical prediction (fig. 3.13). However, this fact may be at least partially due to the uncertainty of the calibration. In the present work we take the theoretical values of Holzwarth and Meister, and use the calibration data from [Roux2008] only to reproduce the dependence of Sherman function on V_b for each given V_{foil}.

The most of measurement on the bulk sample [Roux2008] are performed at $V_{\text{foil}} = 30\,\text{kV} and V_b = 300\,\text{V}$, for which we estimate

$$S_{\text{eff}}(V_{\text{foil}} = 30\,\text{kV}, V_b = 300\,\text{V}) = 0.2707 \tag{3.27}$$

The most of measurements on SOI [5 µm] and SOI [2 µm] are carried out at $V_{\text{foil}} = 60\,\text{kV}$ and $V_b = 600\,\text{V}$, for which we take

$$S_{\text{eff}}(V_{\text{foil}} = 60\,\text{kV}, V_b = 600\,\text{V}) = 0.3109 \tag{3.28}$$

V_b	V_{foil}	
	30 kV	60 kV
0 V	$S_{\text{th}} = -0.32$	$S_{\text{th}} = -0.36$
300 V	$S_{\text{eff}} = -0.271$	$S_{\text{eff}} = -0.336$

Table 3.3: Values of the Sherman function for different V_{foil} and V_b

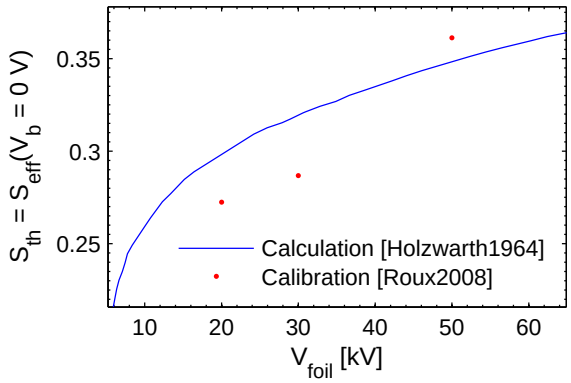


Figure 3.13: Comparison of calculated Sherman function with that calibrated on 1 µm gold foil using GaAs photocathode illuminated at $h\nu = 1.95\,\text{eV}$ at room temperature, considering $P_{el} = -25\,\%$ at σ^+-circularly polarized light.

The polarization data presented in chapter 4 are calculated using the above values of Sherman function.

An important quantity for the Mott detector is the figure of merit F^2. Let us fix the acquisition time t_a and incoming electron flux R_0. The total number of incoming electrons is $N_0 = t_a R_0$ and the number of detected electrons is $N = \epsilon N_0$, where ϵ is the scattering efficiency. The error in the polarization P is proportional to

$$\delta P \propto \frac{\delta \mathcal{A}}{|S_{\text{eff}}|} \propto \frac{1}{\sqrt{N}|S_{\text{eff}}|} \rightarrow min \tag{3.29}$$

where δA is the error in asymmetry. The minimization of SP is equivalent to the maximization of $NS_{\text{eff}}^2 = N_0 \epsilon S_{\text{eff}}^2$. The number of data events required increases quadratically as S_{eff} decreases. The defined figure of merit

$$F = S_{\text{eff}}^2 \epsilon \tag{3.30}$$

For a current of $10\,\text{pA} = 10^7$ electrons/s measured as EDC, we collect 10^2 scattered electrons per second in the detector. In order to attain the asymmetry statistical error of 10^{-3}, one have to accumulate 10^6 electrons/s, which corresponds to the counting time of $10^4\,\text{s} = 3\,\text{h}$.

The measurement of ϵ for the Mott detector used in the present work was performed in [Campbell1985], and resulted in two orders of magnitude lower efficiency compared to more recent Mott detectors [Ghiringhelli1999; Petrov2003]. Figure 3.14 shows F as a function of the retarding potential V_b for the setup used in the present study. It shows the optimum values of V_b dependent on V_{foil}. It follows from the fig. 3.14, that the optimum value of $V_b \propto V_{\text{foil}}$ (table 3.4). All the measurements in the present work are performed on 1 µm gold foil, the absolute majority of which with the potentials $V_{\text{foil}} = 60\,\text{kV}$ and $V_b = 300\,\text{V}$, which corresponds to $F \approx 2 \times 10^{-7}$.

[2] F is the usual notation, but in [Campbell1985] it is denoted by M.

V_{foil}	20 kV	30 kV	50 kV
$\arg\max_{V_b} F(V_{\text{foil}}, V_b)$	390 V	450 V	790 V

Table 3.4: Optimal retarding potential V_b for different high voltages V_{foil}

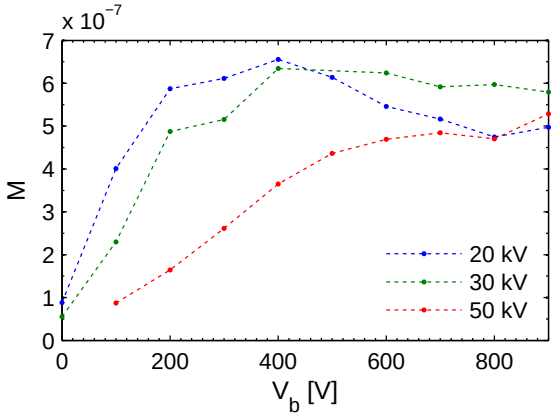


Figure 3.14: Figure of merit as function of retarding potential V_b for different values of V_{foil}

3.2.4 Coil calibration

The relationship between the coil current I and the magnetic field in the center B_0 was measured by a Hall effect sensor, placed inside the coil, which was for this purpose temporary dismounted from the Mott detector. The measured dependence is well described by the linear relationship:

$$B_0[\text{T}] = 1.262 \times 10^{-3}\ I[\text{A}] - 3.224 \times 10^{-5} \tag{3.31}$$

In order to evaluate the magnetic field necessary to flip the spins, a calibration is performed: the electron polarization is measured while running different currents through the coil. The oscillations in fig. 3.15 correspond to the rotation of spin direction in the magnetic field provided by the coil. The polarization direction was reversed (in other words minimum of P_z was attained) for the absolute value of the current of 4.6 A, for which $B_0 = 5.7\,\text{mT}$.

3.3 Studied Silicon samples

As it was discussed earlier in section 2.3.1, the idea behind the study of thin Silicon films is to limit effective electron dwell time. Indeed, the residence time of electrons in a thin film is bounded by

$$\tau_{\text{escape}} \lesssim \frac{d^2}{D} \tag{3.32}$$

where d is the film thickness and D is the electron diffusion coefficient. Comparison of measurements performed on samples of different thickness should allow evaluating the influence of τ_s/τ_e on the polarization. We want $\tau_{\text{escape}} < T_1 \approx 10\,\text{ns}$, that is $d < \sqrt{DT_1}$ with $D \approx 30\,\text{cm}^2/\text{s}$ one gets $d \lesssim 5\,\mu\text{m}$. So we have chosen SOI samples of thickness 2 µm and 5 µm. On the other

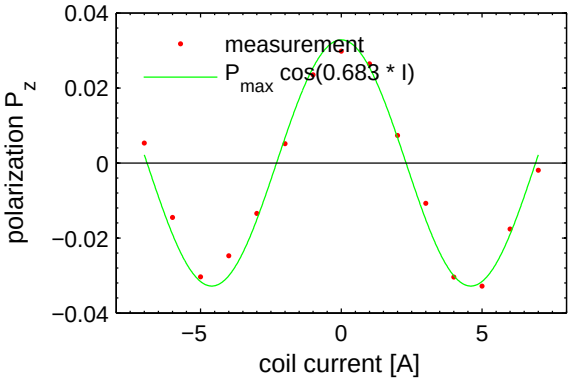


Figure 3.15: Coil calibration under excitation at $h\nu = 3.28\,\mathrm{eV}$. The peak positive polarization corresponds to 0 A, the peak negative polarization to $\pm 4.8\,\mathrm{A}$

hand we have studied (1 0 0) and (1 1 1) oriented samples in order to account for eventual orientation dependence of the polarization.

Table 3.5 summarizes the parameters of the samples studied in this work. The second and third samples are SOI structures, i.e., consisting of three layers: a thin Silicon layer (active layer), followed by SiO_2 layer, and the Silicon substrate. These samples were fabricated by wafer bonding technology, providing a high-quality monocrystalline composition of Silicon layers. Some of the measurements on bulk Silicon performed by [Roux2008] are reproduced for comparison with the results obtained in the present study of 5 µm-thick and 2 µm-thick samples. The ratio of absorption depth fig. 3.16 to the sample thickness determines the critical excitation energy, which separates the regimes of weak and strong injection.

The choice of doping level is guided by the following considerations

Sample name	bulk	SOI [5 µm][a]	SOI [2 µm] [a]
Study	[Roux2008]	present study	
Label in laboratory notebook	Si-A76	SOI-2	SOI-5
Active layer thickness	500 µm	5 µm	2 µm
Buried oxide layer		2 µm	
Handle wafer		300 µm	
Surface orientation	(1 0 0)	(1 1 1)	(1 0 0)
Equivalent direction in the BZ	$\Gamma - X$	$\Gamma - L$	$\Gamma - X$
Active layer resistivity	$0.01 - 0.02\,\Omega\,\mathrm{cm}$	$0.005 - 0.02\,\Omega\,\mathrm{cm}$	$0.02 - 0.05\,\Omega\,\mathrm{cm}$
Corresponding concentration	$3 - 8 \times 10^{18}\,\mathrm{cm}^{-3}$	$0.3 - 2 \times 10^{19}\,\mathrm{cm}^{-3}$	$1 - 3 \times 10^{18}\,\mathrm{cm}^{-3}$
Dopant	Boron		

Table 3.5: Sample parameters

[a] In square brackets, the thickness of the active layer is given

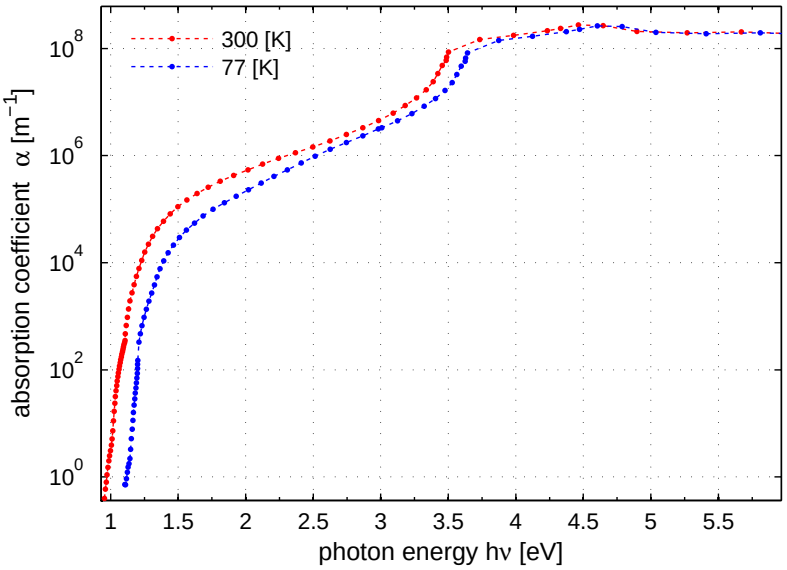


Figure 3.16: Absorption coefficient of Silicon [Macfarlane1959; Sze2006]

- Relatively high doping level allows to decrease the electron lifetime τ_e (fig. 3.17) faster than τ_s (fig. 6.8, which will be discussed in details in section 6.8.1) and thus to make the ratio τ_s/τ_e more favorable.
- For insufficiently doped samples the band bending region width close to their surface would be large and the photo-emission yield is low.

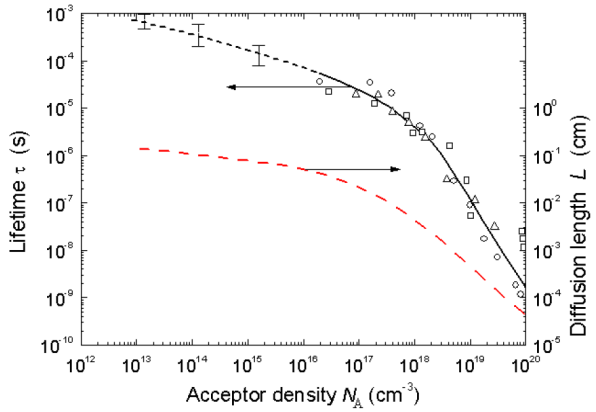


Figure 3.17: The variation of the lifetime and diffusion length of minority carriers in the p-type silicon at room temperature. The data is collected from different sources by [Tyagi1983]. The diffusion length is calculated from the time of life: $L = \sqrt{D\tau_e}$, where D is the diffusion coefficient.

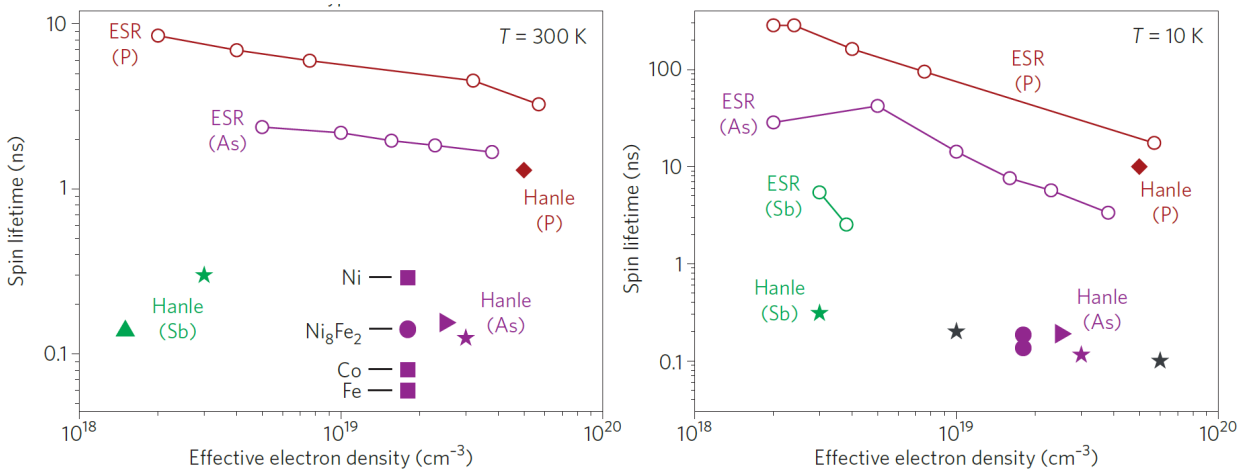


Figure 3.18: Spin lifetime in n-type Silicon extracted from Hanle measurements, combined together with ESR data on bulk Si. Silicon with different dopants (Sb, As and P) and dopant density were used, as indicated. [Jansen2012]

3.3.1 Sample holder

Figure 3.19 shows the flange used for sample preparation. The sample is held on an alumina ring by two molybdenum contacts. The use of alumina for the sample holder has the advantage of high thermal conductivity at low temperatures, and much lower thermal conductivity at high temperatures (which allows to avoid unnecessary outgassing of the holder during the sample annealing). Moreover the two molybdenum contacts which hold sample are electrically isolated which allows current heating of the sample. The Cesium dispenser is used for surface preparation.

The cryostat, shown on fig. 3.19, allows to perform measurements at low temperature. A copper braid, which is connected to cryostat, cools down the sample holder, and thus the sample itself. The sample holder is equipped with Pt100 thermoresistance for temperature measurements. One can see that a temperature gradient is likely to appear on the distance of $\approx 2\,\mathrm{cm}$ between the thermoresistance and the active surface of the sample. In the present work, the sample temperature is taken as the value measured by the thermoresistance. Thus, when the system is cooled down to 100 K, the real temperature of the sample is probably somewhat ($\approx 10\,\mathrm{K}$) higher than the value given in the following sections.

The need for a long time accumulation of weak signals (about a week for the spin polarization spectrum) required the development of an automatic cryostat filling system, which should not perturb the measurement of weak currents and small counting rates and ensure sufficient temperature stability.

3.3.2 Cathode preparation

Activation of a p-type semiconductor to negative electron affinity

The deposition of a surface layer consisting of alkali and halogen atoms under some conditions form a dipole surface layer and lower the electron affinity χ of a semiconductor. In the case

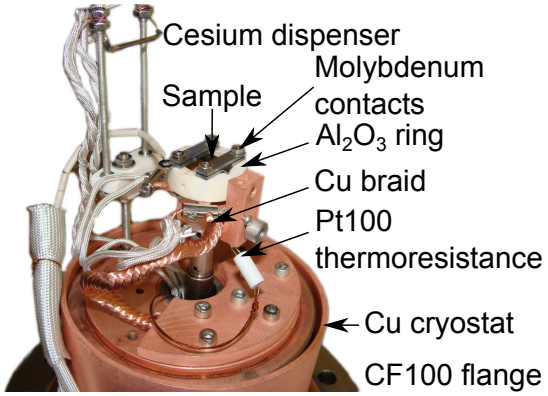


Figure 3.19: Interior of the sample holder flange

when χ is lower than the bottom of conduction band of the bulk material, the electrons can be photoemitted from the band bending region (BBR) (fig. 3.20). Such condition is called negative electron affinity (NEA). The deposition of only Cs results in negative electron affinity (NEA), for instance, for (1 0 0) diamond [Diederich1998], but requires to be completed by the deposition of an electronegative element (often Oxygen is used) in order to achieve the NEA for semiconductor with lower band gap, such as GaAs [Van Laar1965] or Si [Martinelli1970].

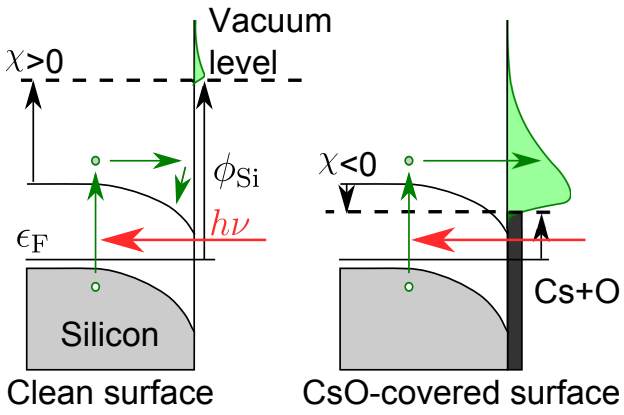


Figure 3.20: Principle of negative electron affinity in p-type semiconductor. By co-adsorption of Cesium and Oxygen, the vacuum level can be reduced below the conduction band in the solid. The work function of Silicon is denoted by ϕ_{Si}, the apparent electron affinity by χ and Fermi level by ϵ_F.

Allen and Gobeli measured affinity $\chi = 0.5\,\text{eV}$ (which corresponds to the work function of 1.6 eV) for Cs-covered (1 1 1) Silicon. The authors also reported that one-monolayer Cesium could absorb 0.5% of photons when illuminating the surface with light of 3 eV energy, and that the photoelectrically emitted electrons from the Cs monolayer represent about 10% of the emission from the bulk. Studies of Cesium adsorption on cleaved Silicon at room temperature using low-energy electron diffraction indicated that the Cesium atoms remain

in a disordered state at least during early stages of the deposition. The Oxygen deposition is not considered in [Allen1966].

In the case of GaAs, NEA is achieved by successive depositions of Cs and O. Howorth et al. shows that in the case of Silicon such the successive depositions do not improve the quantum yield under white light [Howorth1972].

The procedure of preparation of Silicon NEA photocathodes is quite different: NEA is achieved with a single shot deposition of Cs and subsequent exposure to Oxygen, as proposed in [Roux2008].

Silicon photomultipliers constitute the subject of an invention patent. However, no mention of used crystalline orientation of photocathode is provided [Howorth1978], and the achieved electron affinity is not specified neither.

Studied crystal orientations

In the present study two types of surfaces are considered:

(1 0 0)-oriented sample surface similar to that studied in [Roux2008]

Depending on cooling rate, an annealed (1 0 0) surface exhibits either $c(8 \times 8)$ reconstruction (fast cooling), or (4×4) reconstruction (slow cooling) [Arapkina2011]. The (4×4) is likely to be the modification of (2×2) reported by Levine due to the dimer buckling.

It was shown that the Cesium forms an ordered layer on (1 0 0)- (2×2) surface.

(1 1 1)-oriented sample surface Cleavage along the (1 1 1) surface at low-temperatures results in another (2×1) reconstruction, differing from the (1 0 0) surface by forming long pi-bonded chains in the first and second surface layers. However, when heated above 700 K this structure converts irreversibly to the more complicated (7×7) reconstruction [Binnig1983]. In addition, a disordered (1×1) structure is regained at temperatures above 1150 K, which can be converted back to the (7×7) reconstruction by slow cooling.

As it was shown by low-energy electron diffraction (LEED), Cesium is deposited on (1 1 1)-(2×1) in the ordered way, but its deposition on (1 1 1)-(7×7) is amorphous [Gobeli1966]. Based on this result, there was a wide-spread hypothesis in the scientific community that the NEA for (1 1 1)-(7×7) was unreachable by means of Cesium and Oxygen co-adsorption [Levine1973]. At the same time, no experimental works clearly demonstrated the impossibility of NEA on Si (1 1 1). In fact, Levine indicates that this fact was established only in an unpublished experiment of Martinelli.

Results obtained in the present work demonstrate the possibility of a negative affinity for the (1 1 1) surface. Since the method of surface preparation is similar to that used by Binnig et al., we can assume that for the given sample occurs (7×7) reconstruction. Probably the failure to obtain NEA in earlier experiments was associated with lack of the sufficiently clean surface.

It was shown that Cesium carriers partial positive charge and is bounded to (1 1 1) Silicon surface by Coulomb interaction, at least for (2×1) reconstruction [Tochihara1985]. The deposition of oxygen can modify the structure of Cesium layer, in particular induce the formation of structured dipole layer. According to [Tekker2001], the Cs - O surface layer itself possesses semiconductor properties, which more likely advocates towards a structured

rather than amorphous layer. However, there is no LEED study available on the structure of Cs - O surface layer. According to the exposure time and concentration used in the present study, the only conclusion which can be made is that the approximate thickness of Cs and O surface is on the order of magnitude of one monolayer.

The formation of ordered surface layer of Cs on (1 0 0) compared to amorphous deposition on (1 1 1) can be interpreted by lower lattice constant of the latter surface, which thus does not provide enough space to accommodate a relatively large Cesium atom.

The procedure of photocathode preparation is similar to that used by Roux, and consists of four steps indicated in table 3.6, a detailed description of which is given in the next paragraph:

It is well-known that a flash heating (a few minutes) of a Silicon crystal at 1400 K leaves on oxygen-free clean surface. Then, an annealing at lower temperature allows to obtain a well-ordered reconstructed surface. According to [Cricenti1995], the structures due to defects and/or high order reconstructions on (1 0 0) disappear at 750 K. An annealing temperature of 1100 K was chosen as a compromise between 750 K and 1400 K in order to provide a fast restoration of surface.

Experimental protocol

In our work we consider two cesiation protocols:

1. O_2 injection at the end of Cs deposition procedure (the left panel in fig. 3.21). This method is used, for instance, for bulk (1 0 0) Si in [Roux2008].
2. Deposition of Cs followed by injection of O_2 (the right panel in fig. 3.21).

We have found that contrary to the result of Roux, the second protocol provides more stable photocathodes and higher quantum yield for both (1 1 1) and (1 0 0) surfaces. Such a difference with [Roux2008] may reside in the use of different samples (for instance different heating conditions of SOI compared to bulk Silicon sample, etc.)

Figure 3.22 shows the Cesium current and photocurrent recorded during a cesiation of SOI [5 µm].

Similarly to the GaAs case [Tereshchenko2004], the surface preparation mechanism can be decomposed into following steps:

1. Cesium deposition with low surface coating θ lowers the work function.

Step	Duration	Purpose
Flash heating of the sample up to 1400 K	≈ 100 s	Clean the surface from the oxide layer
Annealing at 1100 K	$\approx 100 - 300$ s	Restore the surface reconstruction
Deposition of the Cs	$0.5 - 4$ h	Reduce the work function and
Exposure to Oxygen	$60 - 300$ s	eventually achieve NEA

Table 3.6: Steps of surface preparation procedure

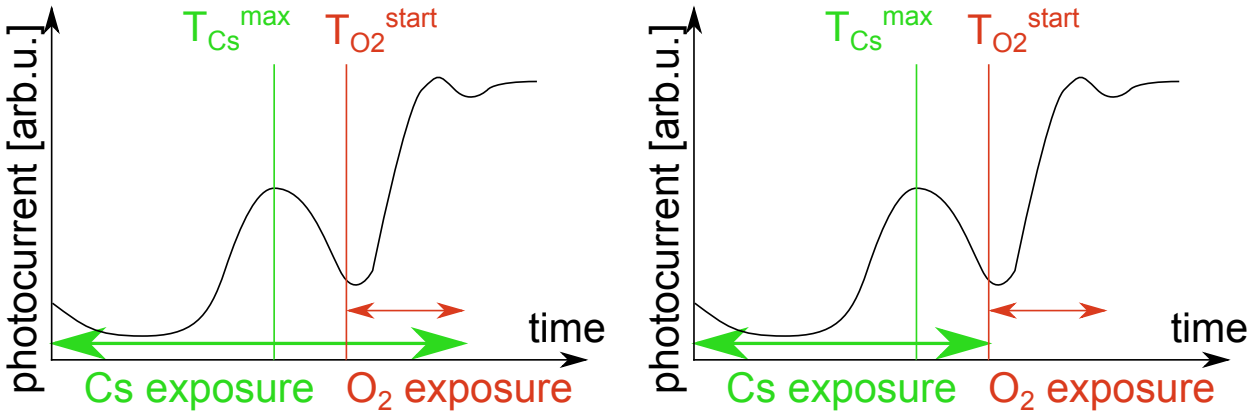


Figure 3.21: Surface preparation procedure, used by Roux (left) and used in the present work (right)

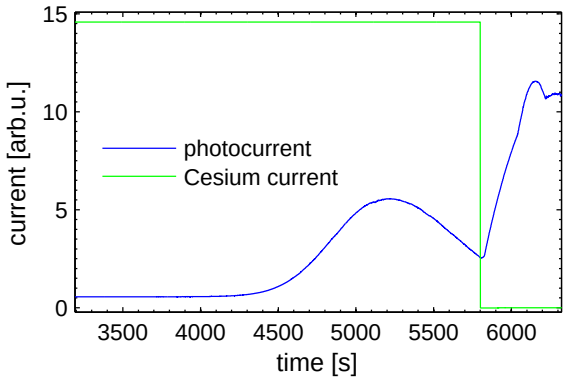


Figure 3.22: Example of surface preparation procedure, used in present work

2. For relatively high surface coating $\theta > 0.5$, repulsive interaction between Cesium atoms results in dipole perturbation and increase of the work function.
3. The deposition of Oxygen screens the Cesium atoms and stabilizes the dipoles, which results in decreasing the work function.
4. When all the dipoles are stabilized, the subsequent addition of oxygen atoms leads to an increase in the work function.

Compared to the Cesium on Silicon deposition process, which was addressed in several works, the Oxygen deposition process on cesiated Silicon remains less understood. In particular, it would be of interest to study the dependence on O_2 coverage of the photocurrent, as well as the reasons for photocurrent re-increase after the end of Oxygen exposure.

It is interesting to note that contrary to the preparation of NEA on GaAs surface, which usually consists in successive depositions of Cs and O layers, the preparation of NEA Silicon photocathode is possible only when one iteration of Cs and O deposition is performed.

In agreement with Roux, we found that excessive cesiation of the sample worsens the stability of the photocathode.

Oxygen exposure

As can be seen from the fig. 3.23, when using a fresh cesium dispenser, typical Oxygen exposure is of about 3 L (1 L = 1 Langmuir = 10^{-6} Torr s), which substantially exceeds, for example, the characteristic exposure used for preparation of GaAs photocathodes. In the case of nearly empty Cesium sputter the deposition of Cesium requires a longer time. Probably simultaneously with Cesium adsorption a contamination of the surface takes place, reducing the adhesion of Oxygen at a later stage, and thus requiring longer exposures (about 5 L for $T_{O_2}^{start} = 4$ h).

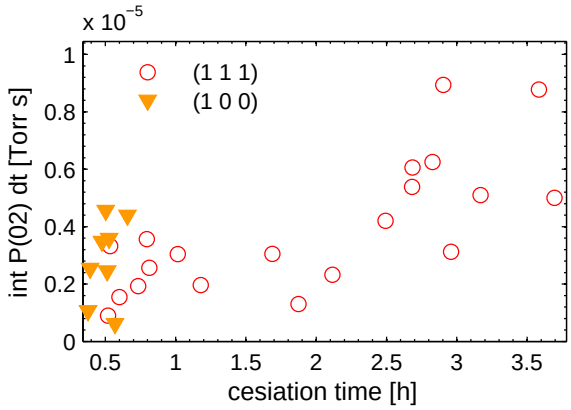


Figure 3.23: The dependence of O_2 exposure versus Cesium deposition time $T_{O_2}^{start}$

3.3.3 Stability of Silicon on insulator structure

Excitation with high optical density

High power irradiation causes local heating of the sample, which provokes an out-gazing of Cs - O layer. Depending on the power the evaporation time can vary from a few seconds to several days, the latter being comparable with the characteristic time of surface layer contamination due to the presence of residual molecules in vacuum.

Similarly to a mechanism found in GaAs [Toropetsky2008], if the excitation energy is large (typically in the UV range), an activation of Oxygen atoms and subsequent formation of covalent bonds with Silicon atoms can also take place. These bonds result in more uniform distribution of the partial negative charge between Oxygen and Silicon, and thus decrease the binding energy of the Oxygen - Cesium bond. As a consequence, Cesium atoms become more sensitive to thermal evaporation.

It is shown that both pulsed and continuous IR irradiation with optical powers up to 2 W does not produce apparent degradation of Cs - O layer. At the same time, prolonged (> 60 s) exposure to high power IR irradiation leads to heating by several degrees of the thermoresistance located on the sample holder at 5 cm from the sample (see fig. 3.19). With 2 W of optical power in near IR, the steady-state regime is attained within 5 min of irradiation and corresponds in an increase in the sample holder temperature by about 15 K. It should be

expected that the temperature of the illuminated point on the sample is much higher than that recorded by the thermoresistance. Since the irradiation of the sample is not accompanied by pressure increase, it can be concluded that the temperature at heating point does not exceed 10^3 K.

It is noted that about 0.7 W of picosecond visible radiation causes an instantaneous degradation of surface layer. In the femtosecond regime, fundamental or SHG radiation does not result in an instantaneous evaporation of the surface layer even at maximum output power.

However, even a small increase of degradation rate plays an important role for long measurements. Thus, with the exception of measurements related to the study of two-photon processes, we used the lowest power which provided sufficient signal level, and if possible, performed acquisitions under continuous irradiation.

The excitation with photon energy above 4 eV (i.e. using THG) causes fast degradation of Cs - O layer starting from average power of several mW. Indeed, the absorption layer thickness is inversely proportional to the photon energy (fig. 3.16). A shallow absorption volume implies a localized temperature increase and hence results in more intense evaporation of the surface layer. Thus, the evaporation rate is proportional to the photon energy.

As for the measurement of two-photon process, a low temperature measurement was considered in order to avoid unnecessary heating of the sample.

In addition to lower temperature away from the laser spot, the thermal conductivity K of Silicon is one order of magnitude higher at 115 K compared to room temperature [Glassbrenner1964]. This means that at room temperature low thermal conductivity leads to a more localized heating. In the framework of one-dimensional steady-state heat transfer model,

$$\begin{cases} K\dfrac{\partial^2 T}{\partial x^2} = 0 \text{ for } x \in [0, L] & \text{(3.33a)} \\ K\dfrac{\partial T}{\partial n}(0) = Q & \text{(3.33b)} \\ T(L) = T_L & \text{(3.33c)} \end{cases}$$

with $T(x)$ - temperature distribution in the sample and Q - heat flux originated from laser irradiation, one obtains

$$T(x) = T_L + \frac{Q}{K}(x - L)$$
$$T(x = 0) = T_L - \frac{QL}{K} \quad (3.34)$$

In other words, the increase in K by 10 may result in significant increase of temperature at the heating point $x = 0$.

Nevertheless, these advantages are counterbalanced by the following drawbacks:

- Cryogenic pumping at low temperatures, which accelerates the surface contamination
- The rectification of zones due to weaker recombination of carriers at low temperature. This effect is especially noticeable for high carrier concentration, which are typical for pulsed excitation. In particular, this effect complicates the measurements with $h\nu \approx \epsilon_{g,\Gamma}$, where a certain number of the photoelectrons are emitted from the BBR.

Successive annealings

Initially it was assumed that heating an SOI structure up to 1400 K could lead to delamination of the active Silicon layer and / or oxide layer. To exclude this possibility and to confirm that the polarization measurements were carried out in the active layer, SOI [5 µm] sample, extracted from the setup after the measurements (20 annealings), was analyzed by scanning electron microscopy. First, the outer face of the sample was considered. As illustrated in the right panel of fig. 3.24, no delamination of the surface layers was observed, only a few damaged regions are seen.

The sample was then cut into several pieces, and inner sections were studied. In particular, the cut which passes through the area of the laser irradiation was investigated. No significant damage was found, which proves that the measurements has been carried out on the thin active layer.

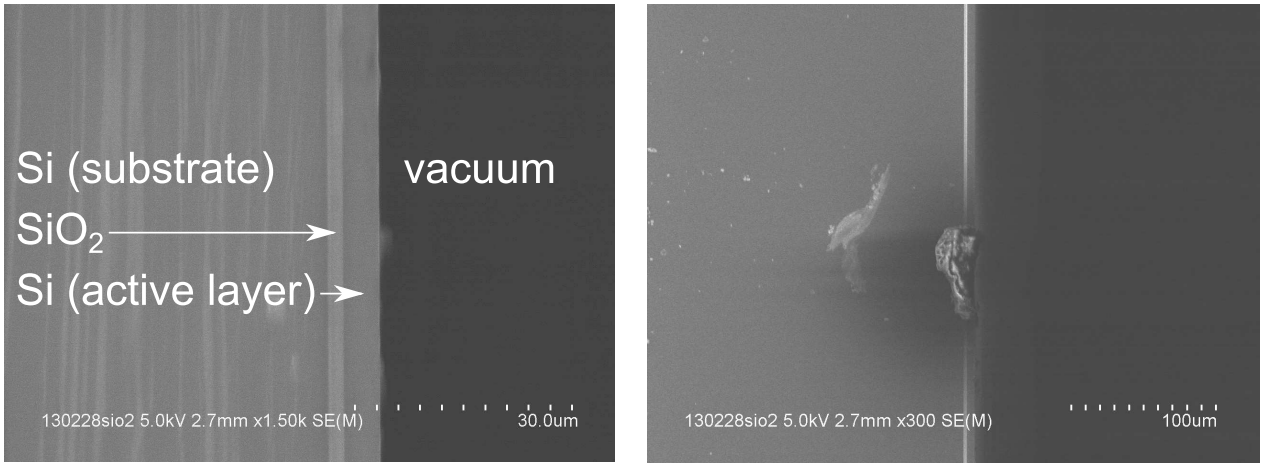


Figure 3.24: Scanning electron microscopy images of SOI [5 µm] active layer. Preserved active layer in the interior of the sample (left), active layer deterioration on the exterior edge (right).

3.3.4 Internal stress

The sample curvature $R \approx 10\,\mathrm{m}$ of SOI [5 µm] was measured by scanning electron microscopy. The corresponding stress is given by

$$\sigma = E\frac{2d}{R} \approx 80\,\mathrm{kPa} \tag{3.35}$$

where $E = 180\,\mathrm{GPa}$ is the Young modulus, $d = 2\,\mu\mathrm{m}$ is the sample thickness. The order of magnitude of the band structure deformation $10^{-10}\,\mathrm{eV/Pa}$ clearly indicates that such stress does not imply any significant distortions of Si band structure.

Another source of stress is the mismatch between Si and SiO_2 lattice parameters. [Jaccodine1966] measures the value of compressive stress in SiO_2 grown by thermal oxidation of Si, which is about 70 GPa.

According to the mechanical considerations, the normal to the sample surface strain is proportional to stiffness, i.e. to the thickness cubed. This implies that 2 µm-thick sample is

$\left(\frac{5}{2}\right)^3 = 6.25$ times more strained than 5 µm. The strain in the plan of the sample, which is more likely to take place in a thin film on a substrate with different crystal lattice, is linearly proportional to the thickness. In this case we obtain the difference by the factor of 2.5 between SOI [5 µm] and SOI [2 µm]. The build-in stress could explain at least partially the observed slight increase of IR polarization measured on the thinner sample via the modification of its band structure, namely increased splitting between heavy hole, light hole and split off valence bands.

As discussed in [Allain2013], the residual stress in SOI structures can attain 300 MPa, in which case the band structure deformations can be on the order of magnitude of spin-orbit coupling (30 meV). However, as will be discussed in chapter 4, no polarization enhancement in the thinnest sample, which should be associated with such high build-in stress, was observed experimentally, suggesting that in our case the stress is lower that 10^2 MPa.

3.3.5 Quantum yield-based estimation of escape probability and diffusion length

We define the quantum yield Y as

$$\Phi_e = Y\Phi_{ph} \tag{3.36}$$

where electron flux density is given by $\Phi_e = \dfrac{I}{eS}$ and the photon flux density is given by $\Phi_{ph} = \frac{W}{h\nu S}$. Here I is the photocurrent, S is the excited area, W is the incident optical power and $h\nu$ is the photon energy.

Following simple analytic model from [Martinelli1970], we reconstruct the yield dependence on energy for an EDC with negative affinity. In this way, we obtain the escape probability at the interface B and the diffusion length L_e. The quantities B and L_e are averaged over the distribution of kinetic energies of electrons.

The product BL_e is estimated as a proportionality factor between the yield and absorption coefficient:

$$Y = BL_e\alpha \tag{3.37}$$

This estimation is performed for the excitation energies where the two quantities are proportional, i.e. $h\nu < 1.75$ eV in fig. 3.25.

Here B is estimated considering the mean quantum yield for the interval $1.75 - 2.5$ eV. For this interval a flattening is observed both in [Martinelli1970] and our quantum yield data.

The dispersion in the quantum yield can be explained as follows:

- A lower quantum yield often indicates problems at the alignment of optics, which is possible due to long optical path and presence of components which could derive the laser beam (e.g. crystals for second harmonic generation).

Temperature T	115 K	300 K
Escape probability B	2×10^{-5}	1.2×10^{-4}
Diffusion length L_e	4.6 µm	1.3 µm

Table 3.7: Quantum yield-based estimation of escape probability and diffusion length

- Another possible source is the variation in the electron affinity, errors in the estimation of this quantity, or electron spectrometer saturation (see section 5.2.2).

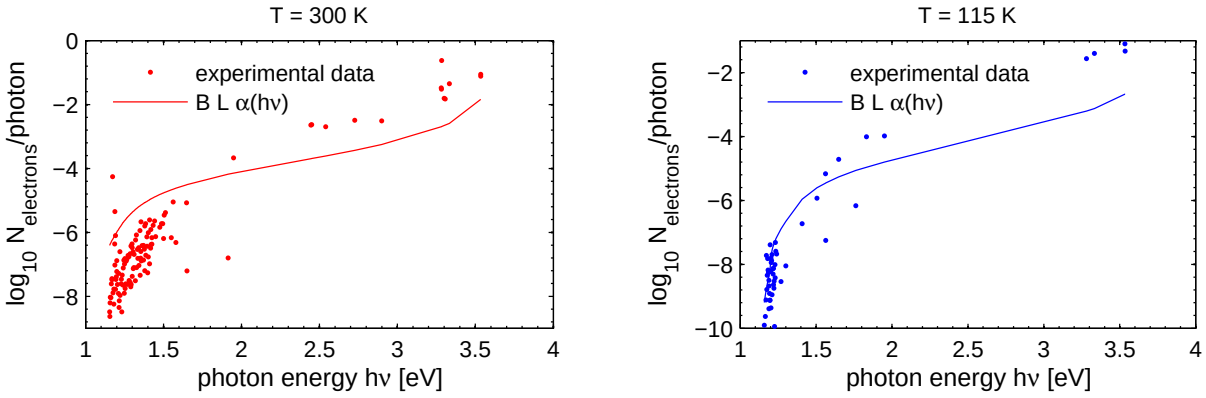


Figure 3.25: Quantum yield of Silicon photocathodes. Least-squares fit provides an estimation of B and L_e. The measurements performed on all the samples are shown. The observed quantum yield is very similar for all the three samples analyzed in the present work.

It is interesting to note that the proportionality between the quantum yield and the absorption coefficient holds on the whole interval of $h\nu$. The obtained values of the L_e are substantially lower than usually considered $L_e \approx 10^2$ µm, which can be explained by

- The fact that they were measured on a thin film rather than on bulk Silicon[3]
- The variation of electron affinity, which heavily influences the estimated quantities.
- A substantially lower (by the factor of 10^{-3}-10^{-4}) escape probability (i.e. quantum yield under UV excitation) compared to the work [Martinelli1970], which is likely to be explained by the differences in the experimental setups.

3.4 Electron distribution curves (EDCs) measurements

The setup allows for the measurement of the kinetic energy distributions curves (EDCs) of electrons emitted in vacuum. Each EDC is characterized by following parameters:

- Sample type (band structure, doping level)
- Cathode current I_{cath} (the total cathode current may influence the operation of the spectrometer and thus the measured EDC shape)
- Temperature
- Excitation
  - Energy $h\nu$
  - Output power
  - Pulsed or continuous mode

[3]There is not enough data to provide a reliable estimation of L_e considering only bulk sample.

3.4.1 Energy reference

The EDC is initially recorded as a function of V_{cath}, but the relevant quantity is the electron energy in the crystal ϵ. In the present work the zero energy is chosen to be the conduction band minimum.

Dependence of EDC(V_{cath}) on the settings of the electron optics

Suppose that the low-energy and high-energy thresholds of an EDC are identified by signal processing technique, and denoted by $V_{\text{cath}}^{\text{LE}}$ and $V_{\text{cath}}^{\text{HE}}$ respectively (fig. 3.26). Such information allows us to validate the linear dependence of electron energy ϵ on the cathode potential V_{cath}, given by eq. (3.15):

$$eV_{\text{cath}} = \epsilon + \epsilon_{g,X} - \phi_{\text{Au}} \approx \epsilon - 3.7\,\text{eV} \tag{3.38}$$

In fact, since both the Silicon band gap $\epsilon_{g,X}$ and the work function of Gold ϕ_{Au} are constants, $V_{\text{cath}}^{\text{HE}}$ should depend linearly on $h\nu$, at least when $h\nu < \epsilon_{g,\Gamma}$.

Deviations from this dependence can be explained by two factors:

1. Unaccounted in eq. (3.38) **dependence of EDC position on potentials of electrodes** located close to the sample (entrance rotator slit, etc.). Such a dependence may be explained, for instance, by the variation of ϕ_{Au} due to the cesiation of the surrounding gold electrodes.
2. **Inaccuracy of the systematic threshold determination** in EDC (analyzed further in section 3.4.2)

Considering the data presented in fig. 3.26 EDCs, obtained under continuous excitation (the more complicated issue of the effect of pulsed excitation is described in section 5.2), it can be seen that the position of the EDC on the axis V_{cath} varies for a given $h\nu$, which can be explained only by the first hypothesis.

The right panel of fig. 3.26 represents examples of such a shift. Different EDCs were recorded with different settings of the electron optics. The graph shows that both thresholds are often simultaneously shifted from one measurement to another. Thus, eq. (3.38) does not allow to link V_{cath} and ϵ for the series of measurements carried out using various settings of the electron optics.

On the observed linear dependence in fig. 3.27 a significant discrepancy of the values of $V_{\text{cath}}^{\text{HE}}$ is measured. Such behavior appears to be independent on whether $h\nu$ is smaller of larger than $\epsilon_{g,\Gamma}$, and is also observed for measurements recorded under pulsed excitation) as shown fig. 3.27.

Energy calibration

Photoelectrons excited from the maximum of the valence band have the energy $\epsilon_{\text{HE}} = h\nu - \epsilon_{g,X}$, referred to the conduction band minimum. At the same time,

$$\epsilon - \epsilon_{\text{HE}} = e(V_{\text{cath}} - V_{\text{cath}}^{\text{HE}})$$

$$\epsilon = e(V_{\text{cath}} - V_{\text{cath}}^{\text{HE}}) + h\nu - \epsilon_{g,X} \tag{3.39}$$

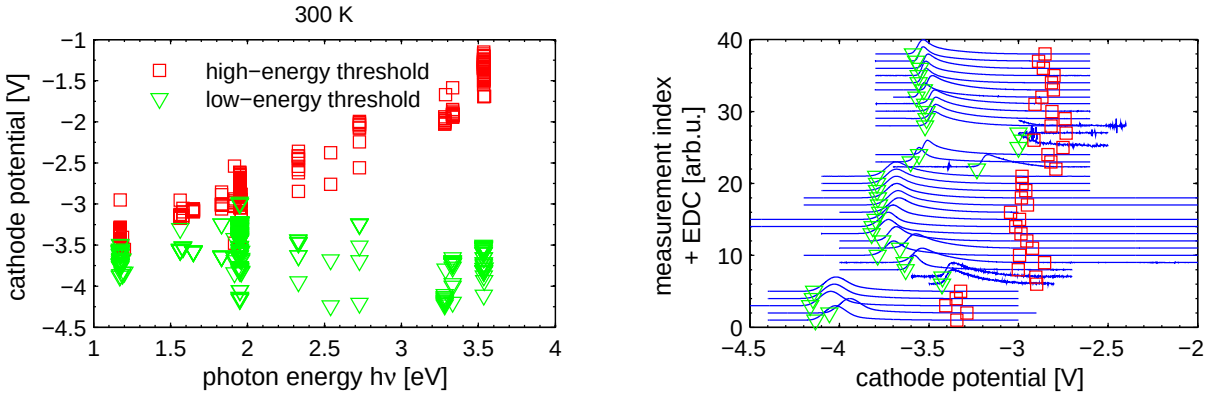


Figure 3.26: $V_{\text{cath}}^{\text{LE}}$ and $V_{\text{cath}}^{\text{HE}}$ for measurements under continuous excitation (left). Example of threshold shift for different measurements at $h\nu = 1.95\,\text{eV}$ (right). The data shown were measured on bulk Silicon at $T = 300\,\text{K}$.

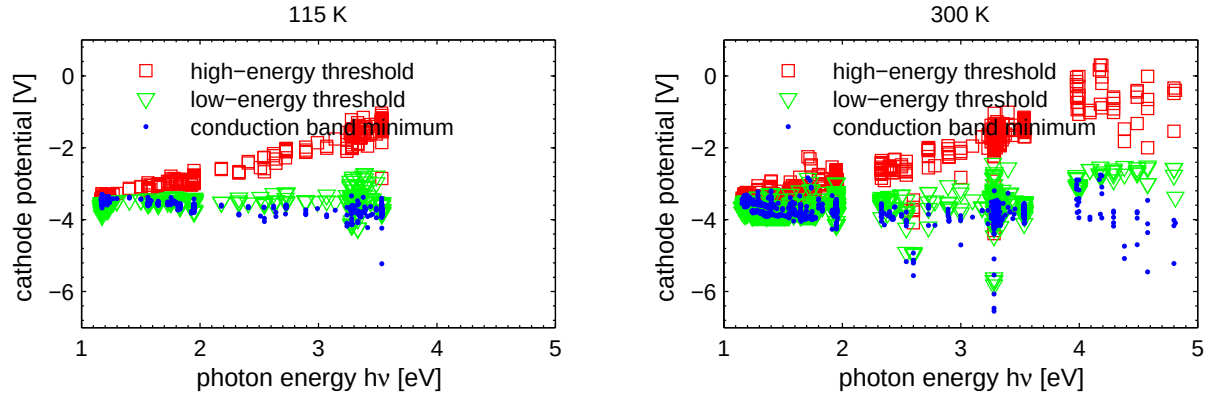


Figure 3.27: Position of thresholds versus excitation energy for all measurements on all the three samples

The energy of photoelectrons, located at the low-energy threshold, satisfies $\epsilon_{\text{LE}} = \chi$. On the other hand, $\epsilon_{\text{LE}} = e(V_{\text{cath}}^{\text{LE}} - V_{\text{cath}}^{\text{HE}}) + h\nu - \epsilon_{g,X}$. Thus, the electron affinity can be obtained as

$$\chi = e(V_{\text{cath}}^{\text{LE}} - V_{\text{cath}}^{\text{HE}}) + h\nu - \epsilon_{g,X} \tag{3.40}$$

Excluding the measurements at which the threshold is likely to be mistakenly identified (for example, measurements which are separated from the $< V_{\text{cath}}^{\text{CB}} >$ by more than $\sigma(V_{\text{cath}}^{\text{CB}})$), we can estimate the value

$$\phi_{\text{Au}} = (4.81 \pm 0.14)\,\text{eV} \tag{3.41}$$

in good agreement with previous works [Anderson1959; Fomenko1966].

Comparison of onsets of direct and indirect transitions

In the case of $h\nu > \epsilon_{g,\Gamma}$, the optical transitions of highest energy (i.e. starting at Γ) may be indirect, and therefore may contribute weakly to the EDC compared to direct transitions. In

this case, the high-energy threshold is essentially given by the highest of the allowed direct transitions which does not necessarily occur at the zone center. Hence we have:

$$\epsilon_{\mathrm{HE}} < h\nu - \epsilon_{g,X} \tag{3.42}$$

In particular, for the direct transitions towards Γ_8^- with excitation energy in the vicinity of the zone center:

$$\epsilon_{\mathrm{HE}} = (h\nu - \epsilon_{g,\Gamma})\frac{m^v_{\mathrm{eff}}}{m^c_{\mathrm{eff}} + m^v_{\mathrm{eff}}} + \epsilon_{g,\Gamma} - \epsilon_{g,X} \tag{3.43}$$

where m^c_{eff} and m^v_{eff} are effective masses in conduction and valence bands respectively. This effect does not influence the ϵ_{LE}.

3.4.2 Determination of thresholds

From the conclusion drawn in section 3.4.1, there is a need for an algorithm for the determination of the thresholds in EDC. The algorithm proposed here can be decomposed into 2 steps:

1. Individual analysis of each EDC
   (a) Determination of thresholds
   (b) Analysis of EDC quality (noise level, presence of the zero level below low-energy (LE) threshold and above high-energy (HE) threshold)
2. Alignment of HE thresholds for all the EDCs with the same excitation energy

Analysis of individual EDC

In an experiment which combines high voltage and low current detection several parasitic phenomena perturb the measurement. In particular we often observed the presence of spikes on EDCs. In order to clean the data, a spikes removal procedure was applied. Such selective treatment preserves the raw data from unnecessary modification.

The algorithm is based on the analysis of the second derivative of the signal. All the points where $\frac{\partial^2 I_{Faraday}}{\partial V^2}$, calculated with three-point stencil, is above its standard variation multiplied by adjustable constant are considered as potential spikes. Finally, the value of $I_{Faraday}$ in their proximity is analyzed in order to ensure that the determined points are real spikes, and these few noisy points are replaced by a local linear interpolation (fig. 3.28).

The signal to noise ratio is defined as

$$\mathrm{SNR} = \frac{\left\langle \widehat{N(f)}\mathbb{I}_{f>f_n} \right\rangle_f}{\max(N(V)) - \min(N(V))} \tag{3.44}$$

where $\widehat{N(f)}$ is Fourier transform of an EDC $N(\epsilon)$, and f is "frequency" in inverse volts. Given the sampling frequency F_s, the cutoff frequency defined as $f_n = \frac{F_s}{4}$ describes well the noise on our experimental data. At the same time, for typical value $\frac{1}{F_s} = 1\,\mathrm{mV}$, $\frac{1}{f_n} = 4\,\mathrm{mV}$, which is below the lowest accessible spectrometer resolution (20 meV).

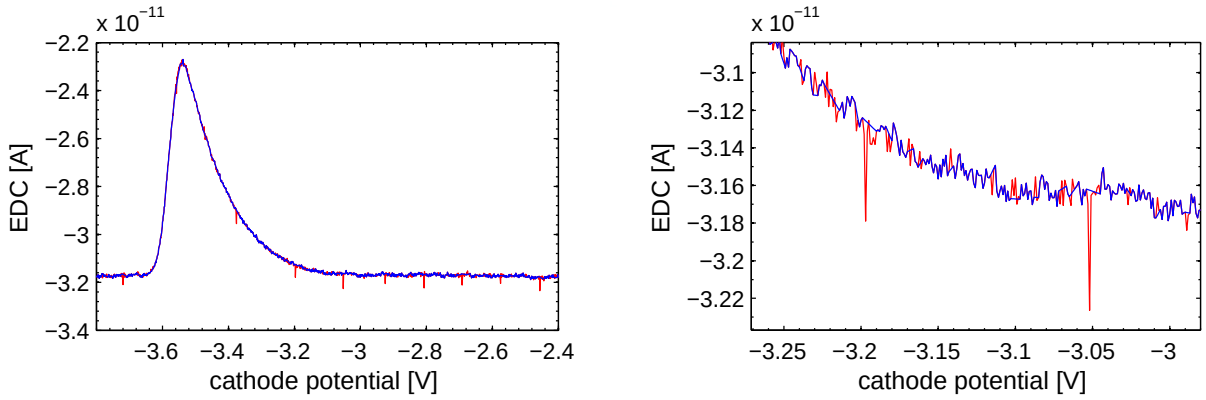


Figure 3.28: Illustration of spikes removal procedure on EDC (SOI [5 µm], $h\nu = 1.93\,\mathrm{eV}$, $T = 300\,\mathrm{K}$)

In order to determine the thresholds, we first normalize the EDC

$$y = r(N) = \frac{(N - \min(N))}{\max((N - \min(N)))} \tag{3.45}$$

The low-energy threshold is defined as the intersection of a linear interpolation with the background level (fig. 3.29). A Savitsky-Golay filter with adaptive parameters is employed to obtain a noise-resistant estimation of the EDC slope.

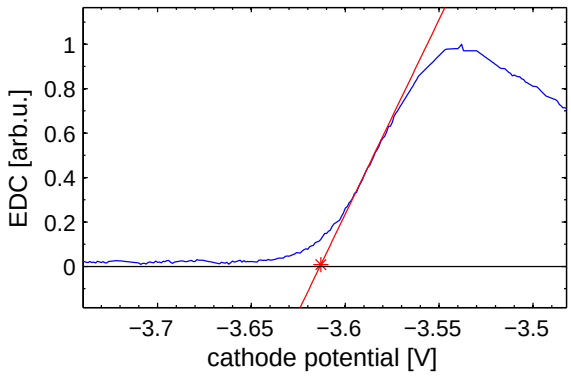


Figure 3.29: Low energy threshold determination (SOI [5 µm], $h\nu = 1.93\,\mathrm{eV}$, $T = 300\,\mathrm{K}$)

The crucial step is the determination of the high-energy threshold on the EDC. As the part of EDC for $V_{\mathrm{cath}} > \arg\max N(V_{\mathrm{cath}})$ is not necessarily monotonous (see, for instance, section 3.4.5), the method shown in fig. 3.29 cannot be applied to HE threshold. In order to make the procedure robust with respect to the typical noise, an algorithm consisting of several steps is proposed.

First, we construct a histogram of descendant EDC slope. Let us note $x(i)$ the bins and $n(i)$ corresponding number of points in each bin i. First, we obtain a background signal

position (green point in fig. 3.30) defined as $x_{bg} = x(i_{bg}) = x(\arg\max_i n(i))$. The onset level of non-zero signal (red point in fig. 3.30) is defined as

$$x(j) \text{ such that } j \text{ is the first solution of } n(i) - \delta \langle n(i) \rangle_i = 0 \text{ for } j > i_{bg} \tag{3.46}$$

with an adjustable parameter δ. Under the hypothesis of Gaussian noise for $V_{\text{cath}} > V_{\text{cath}}^{\text{HE}}$ and given that there is enough data to obtain a reliable estimation of probability density function of this noise, such procedure allows to build a noise robust onset level estimate. In fact, if signal is characterized by larger amount of noise, the Gaussian curve in the right panel of fig. 3.30 would be enlarged and $x(j)$ would be greater.

We define the signal onset potential as V_1 a first zero of $y(V) - x(j)$.

A similar histogram $(x_2(i), n_2(i))$ is constructed for $V_{\text{cath}} > V_1$ in order to determine a point V_2 which close enough to the high-energy threshold and at the same time at which no signal appears. V_2 is defined as the first solution of $V_{\text{cath}} - x_2(\arg\max_i n_2(i)) = 0$.

The exact location of the signal onset between V_1 and V_2 is found under the approximation of linear absorption onset. Given i_1 and i_2 the indexes of V_1 and V_2 (that is $V_j = V_{\text{cath}}(i_j)$) and the index i_{HE} and the slope s_{HE} of high-energy threshold, we define a piece-wise linear function (fig. 3.31)

$$y_{onset}(i, i_{HE}, s_{HE}) = L\left(V(i_1 : i_{HE}),\ y(i_1),\ s_{HE}\langle y(i_{HE} : i_2)\rangle\right)\ \mathbb{I}_{i \le i_{HE}} + s_{HE}\langle y(i_{HE} : i_2)\rangle\, \mathbb{I}_{i > i_{HE}} \tag{3.47}$$

with linear function

$$L(x, y_1, y_2) = \frac{y_2 - y_1}{x(1) - x(end)}(x(1 : end) - x(1)) + y_1$$

The position of high-energy threshold is estimated as $V_{\text{cath}}(j_{HE})$ where

$$j_{HE} = \arg\min_{i_{HE}} \min_{s_{HE}} \|y_{onset}(i_1 : i_2, i_{HE}, s_{HE}) - y(i_1 : i_2)\|_2 \tag{3.48}$$

where $\|\cdot\|_2$ is the Euclidean norm.

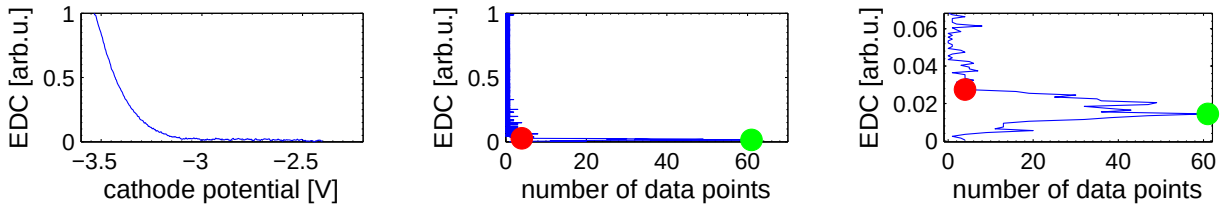


Figure 3.30: Decreasing part of an EDC (left), constructed histogram $(x(i), n(i))$ (center) and its zoom (right) (SOI [5 µm], $h\nu = 1.93\,\text{eV}$, $T = 300\,\text{K}$)

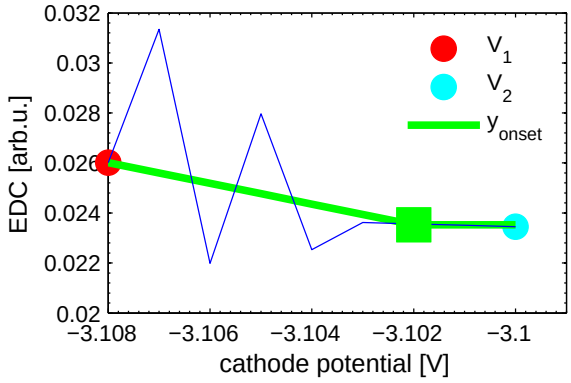


Figure 3.31: Piecewise linear interpolation for the determination of high-energy threshold (SOI [5 µm], $h\nu = 1.93\,\mathrm{eV}$, $T = 300\,\mathrm{K}$). The determined HE threshold is marked with the square.

Alignment of EDCs with the same energy

Thresholds determined on each individual EDC may contain some numerical inaccuracies. Thus, for the same photon energy a scattering in ϵ_{HE} may appear, while in an ideal case, the condition

$$\epsilon_{\mathrm{HE}} = h\nu - \epsilon_{g,X} \tag{3.49}$$

should be fulfilled. The purpose of the algorithm described in this section is to superimpose the high-energy thresholds of EDCs for the same photon energy and temperature fig. 3.32.

Given $i_{max} = \arg\max_i y(V_{\mathrm{cath}}(i))$ we construct a function with a sharp maximum at $V_{\mathrm{cath}} = V_{\mathrm{cath}}^{\mathrm{HE}}$ as

$$y_{HE} = \tan\left(\frac{\pi}{2} r\left[L(i_{max} : end, y(i_{max}), y(end)) - y(i_{max} : end)\right] - \gamma\right) \tag{3.50}$$

with an adjustable parameter γ. The shift between two EDC is determined as the maximum of convolution of corresponding y_{HE}. The position of high-energy threshold is determined as $\left\langle V_{\mathrm{cath}}^{\mathrm{HE}} \right\rangle$ over high-quality EDCs. Low quality EDCs are just shifted to match this quantity, but are not taken into account in the mean value.

Precision of high-energy threshold determination

Figure 3.33 represents the comparison between the thresholds determined on the EDCs (denoted by $\epsilon_{\mathrm{HE}N}$) with the last acquired point on the corresponding PEDC (denoted by $\epsilon(end)_P$). The latter point is determined by hand for each polarization measurement and is usually quite close to the HE threshold. Since the acquisition program performs measurement only if a non-zero number of counts was captured at the first cycle, the inequality

$$\epsilon_{\mathrm{HE}N} < \epsilon(end)_P \tag{3.51}$$

should be satisfied.

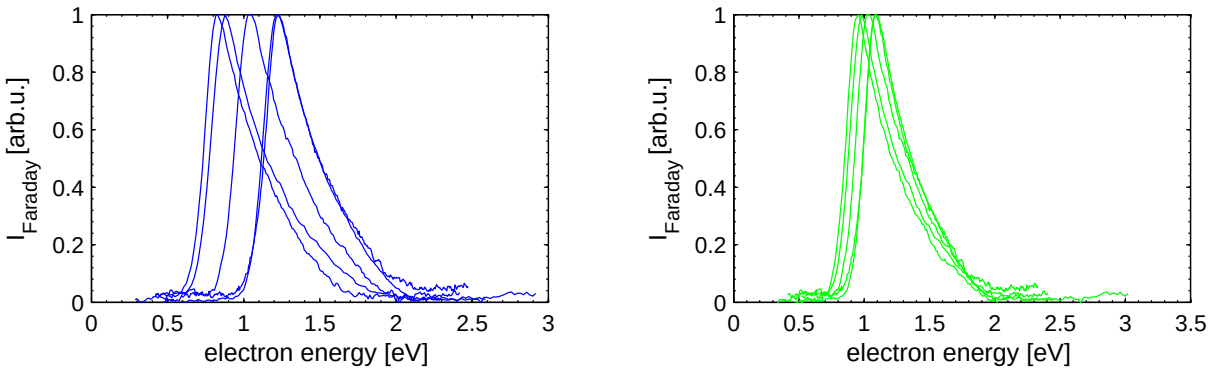


Figure 3.32: EDCs before (left panel) and after alignment (right panel) of HE threshold for the same $h\nu$ (all samples, $h\nu = 1.95\,\mathrm{eV}$, $T = 300\,\mathrm{K}$)

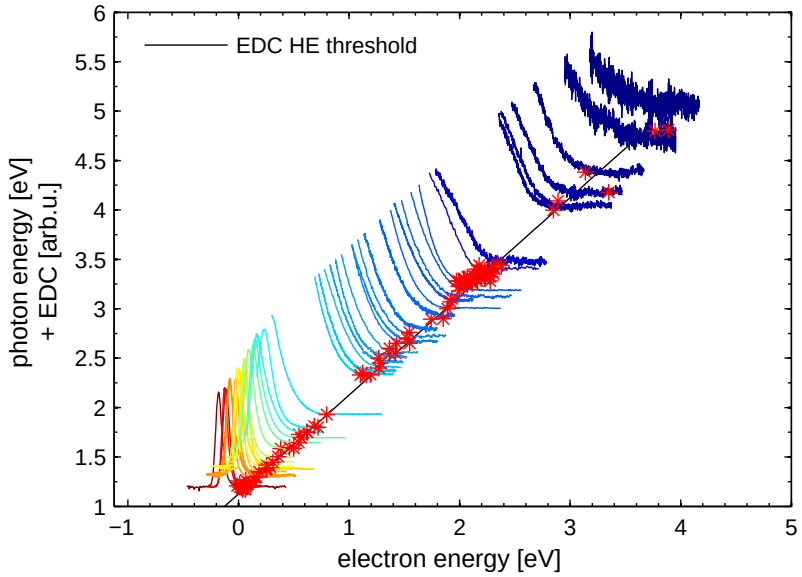


Figure 3.33: HE thresholds of EDCs for different excitation energies (some of the measurements on SOI samples, $T = 300\,\mathrm{K}$)

For measurements where the threshold $\epsilon_{\mathrm{HE}N}$ is overestimated by the automatic procedure, the previous inequality does not hold (for instance for some points near 3.3 eV). Large overestimations for $h\nu > 4\,\mathrm{eV}$ are due to EDCs "broadening" under intense pulsed irradiation, which modifies in particular the shape of the signal onset on the EDC. The physical reasons of such the broadening will be discussed further in section 5.2.4.

The quantity

$$\Delta_{\text{HE determination}} = \left(\sum_{h\nu} (\epsilon_{\mathrm{HE}N}(h\nu) - \epsilon(end)_P(h\nu))^2 \right)^{1/2} = 50\,\mathrm{meV} \tag{3.52}$$

gives the upper bound of the mean error committed by this procedure on the whole set of PEDC data, which is comparable with the normally used spectrometer resolution (40 meV) and more accurate than the result of manual determination procedure.

3.4.3 Temperature variations of thresholds

Figure 3.34 shows a series of measurements with the temperature ranging from 200 K to 300 K at $h\nu = 1.95\,\text{eV}$, performed with a fresh photocathode. The x-axis is given in

$$\epsilon V_{\text{cath}} = \epsilon + \epsilon_{g,X} - \phi_{\text{Au}}$$

where ϵ denotes the electron kinetic energy, $\epsilon_{g,X}$ is the fundamental band gap of Silicon and ϕ_{Au} is Gold work function. (see eq. (3.15) for the details). Among all the measurements performed with significant temperature variations, both the decrease and increase (such an increase is shown in fig. 3.34) of LE threshold with temperature are observed. Given that

$$\chi = eV_{\text{cath}}^{\text{LE}} + \phi_{\text{Au}} - \epsilon_{g,X} \tag{3.53}$$

and known that the value of indirect band gap $\epsilon_{g,X}(115\,\text{K}) - \epsilon_{g,X}(300\,\text{K}) = 1.16\,\text{eV} - 1.125\,\text{eV} = 0.037\,\text{eV}$, we deduce that the rise of electron affinity in fig. 3.34 is in fact 37 meV higher than observed on V_{cath} scale. Deriving eq. (3.53) with respect to temperature, we obtain

$$e\frac{\partial V_{\text{cath}}^{\text{LE}}}{\partial T} = \frac{\partial \chi}{\partial T} + \frac{\partial \epsilon_{g,X}}{\partial T} \tag{3.54}$$

where the variation of band gap $\frac{\partial \epsilon_{g,X}}{\partial T} < 0$. The variations of $e\frac{\partial V_{\text{cath}}^{\text{LE}}}{\partial T}$ can be due to the variations of electron affinity, induced by

- Cryopumping on the sample surface (during the cooling)
- Cryodesorption from the sample surface (during the heating)
- Deterioration of the surface with time.

For all the measurements an increase of $eV_{\text{cath}}^{\text{HE}}$ with increasing temperature was observed. The averaged variation of $eV_{\text{cath}}^{\text{HE}}$ over the measurements with $h\nu < 2\,\text{eV}$ is

$$\begin{cases} V_{\text{cath}}^{\text{HE}}(300\,\text{K}) - V_{\text{cath}}^{\text{HE}}(115\,\text{K}) \approx 0.1\,\text{eV for } h\nu < 2\,\text{eV} & \text{(3.55a)} \\ V_{\text{cath}}^{\text{HE}}(300\,\text{K}) - V_{\text{cath}}^{\text{HE}}(115\,\text{K}) \approx 0\,\text{eV for } h\nu > 2\,\text{eV} & \text{(3.55b)} \end{cases}$$

The increase of the high-energy threshold can be described by the following factors

- Decreasing dependence of $\epsilon_F(T)$ due to the increasing concentration of active impurity atoms
  - If we suppose that the Fermi level pinning at the surface is independent of temperature, such the decreasing dependence of $\epsilon_F(T)$ results in increasing band bending.
- Increasing contribution of the absorption of the phonon modes. At low temperature the dominating mechanism is the phonon emission, whereas at room temperature both absorption and emission can take place. In particular, this hypothesis is supported by the values given eq. (3.55) since the difference between the emission and absorption an optical phonon $2\epsilon_{TO} \approx 0.122\,\text{eV}$.

Increasing temperature variance of $V_{\mathrm{cath}}^{\mathrm{HE}}$ is associated with increasing level of noise on EDCs, and does not reflect any process in the sample itself.

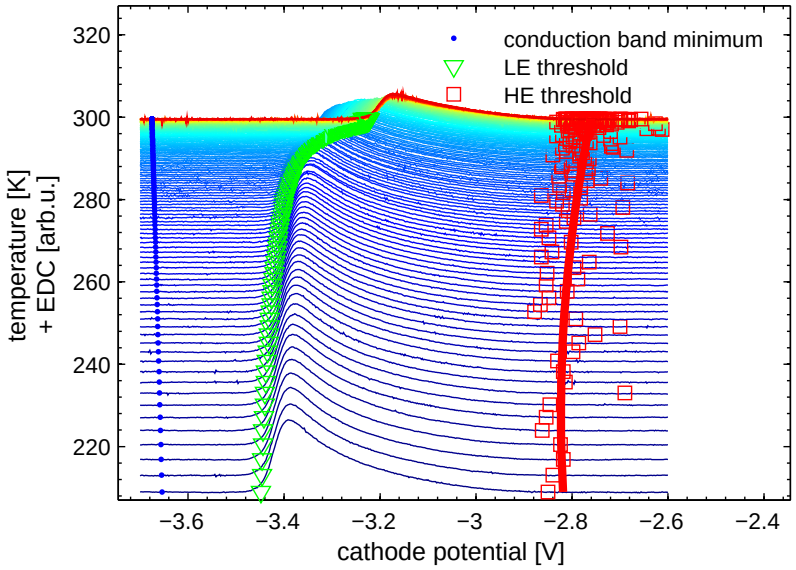


Figure 3.34: Series of EDCs versus temperature measured on bulk Silicon under $h\nu = 1.95\,\mathrm{eV}$. The observed increase is 0.23 eV and 0.1 eV for LE and HE thresholds respectively.

3.4.4 Slope of the low-energy onset

It is interesting to observe affinity-induced variation of the slope of low-energy part of EDCs. Let us denote the width of increasing part of EDC by $\arg\max_{\epsilon} N(\epsilon) - \epsilon_{\mathrm{LE}}$, and the spectrometer resolution V_{res}. Normally, if the smearing of EDC is due to finite spectrometer resolution,

$$\arg\max_{\epsilon} N(\epsilon) - \epsilon_{\mathrm{LE}} \approx V_{\mathrm{res}} \tag{3.56}$$

Figure 3.35 represents the quantity $\arg\max_{(\epsilon)} N(\epsilon) - \epsilon_{\mathrm{LE}}$ as function of electron affinity χ. One can see that the smearing due to finite spectrometer resolution increases with the increase of the latter. The fact that $\arg\max N - \epsilon_{\mathrm{LE}} > V_{\mathrm{res}}$ can be interpreted as due to non-homogeneous affinity level throughout the surface [Pakhnevich2004]. Within this hypothesis, it follows from fig. 3.35 that the non-homogeneity increases with the increase of χ due the surface deterioration.

The step observed in the measurements with the resolution 40 meV for $\chi \approx 0$ suggests the dependence on the slope on other parameters (incident optical power (discussed further in section 5.2), settings of the spectrometer potentials, sample type). For example the points concentrated at $\chi = 0 - 0.15\,\mathrm{eV}$ and width of $0.08 - 0.09\,\mathrm{eV}$ are acquired on (1 0 0)-oriented bulk sample, whereas the points at $\chi = -0.15 - 0\,\mathrm{eV}$ and width of $0.04 - 0.05\,\mathrm{eV}$ correspond to (1 1 1)-oriented SOI [5 µm].

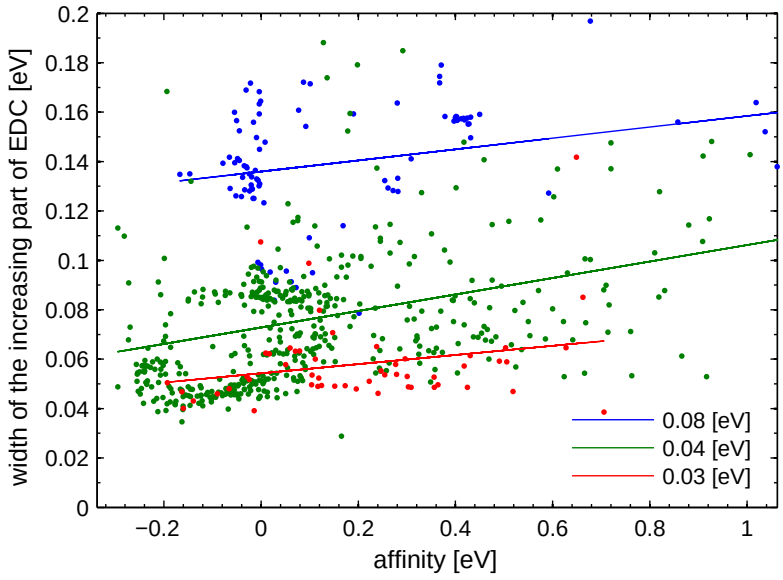


Figure 3.35: Dependence of EDC rising width on the electron affinity for the measurements made at different spectrometer resolutions (V_{res} is indicated in legend). Straight lines are the guide for eyes. The measurements for all the excitation energies are represented.

For $\epsilon_{g,X} = 1.12eV$ the lowest measured affinity for all measurements is $-0.3\,\text{eV}$, which gives upper limit of band bending energy δV_p. In the n-type Silicon the typical band bending is of $\delta V_n = 0.8\,\text{eV}$, in agreement with our measurements, because

$$\delta V_p = \epsilon_{g,X} - \delta V_n \approx 0.3\,\text{eV} \tag{3.57}$$

3.4.5 Features on EDCs: interpretation and detection

Let us note ϵ_{min} the energy of a given conduction band minimum. The accumulation of photoelectrons in this minimum results in a significant contribution to the photoemission spectrum (fig. 3.36). Thus, a local minimum of the band structure can be represented on the EDC as a fragment with a share of electrons above the expected for the area in the case of a monotone exponent-like decrease.

Obviously there is no a priori reason for every observed feature to be originated from an extremum of the band structure. For instance, as will be discussed in chapter 5, the features can be also induced by the operation of the electron spectrometer itself.

In order to attribute a feature to specific to the crystal optical transition, both its low-energy threshold (which is the energy of electrons originated from the extremum and thermalized in the BBR) and its high-energy threshold (which is the point of creation in the bulk material) should not depend on the excitation energy. Generally speaking, such crystal-specific transitions can be divided into two categories: the emission of photoelectrons accumulated in the extrema of the band structure, and some specific optical transitions (such as Auger effect). However, the latter is three-particle process and thus possesses much lower amplitude compared with the main photoemission signal.

Normally, the extrema of the band structure appear over the high-symmetry directions and are well-known, so the detected $h\nu$-independent features are supposed to be found near them. Furthermore, the kinetic energy of electrons corresponding to a given feature should ascend with the decreasing temperature due to the band gap increase. Normally, both the low energy and high energy thresholds are affected by this shift.

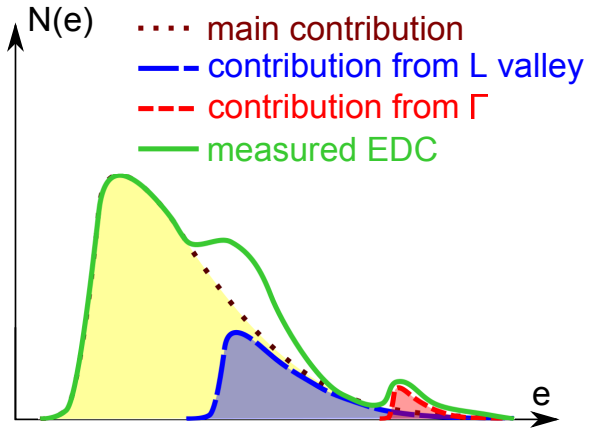


Figure 3.36: Typical decomposition of an EDC with $h\nu \gtrsim \epsilon_{g,\Gamma}$ into the contributions from L valley and the vicinity of zone center, which are superimposed on the main part of the photoemission spectrum.

The setup allows a measurement of analog derivatives of EDCs via lock-in modulation, in order to better resolve fine features which appear on EDCs.

An alternative algorithm for automatic determination of features was proposed. It is based on the following formal definition of structure: Let us denote the EDC by $N(\epsilon)$. The feature is defined as the interval of electron energies ϵ such that $N(\epsilon)'' < 0$ or $N(\epsilon)''' > 0$. It should be noted, that the high-order derivatives are only useful for the determination of potential features, but in order to minimize the likelihood of false positive detection case, the final conclusion about feature presence has to be performed on the basis of analysis of feature amplitude on original EDC.

Its main idea is the following: The signal and its three numerical derivatives are calculated using Savitsky-Golay filters [Savitzky1964] with window size adapted to typical resolution and signal-to-noise ratio. Potential features on signal y are determined as intervals separated by the zeros of y''. Among them, the intervals with negative curvature are selected. A similar treatment is applied to find the features on y' based on the zeros of y'''. Resulting features are obtained as a union of overlapping features on y and y' (the right panel in fig. 3.37).

One can note that the features can be also determined on the EDCs reconstructed as the sum of counts $(A + B)(h\nu)$, which are obtained during the polarization measurements. The advantage of this method is low noise level of $(A + B)(h\nu)$ due to the long acquisition time of a PEDC.

Although presented in the left panel of fig. 3.37 feature is visible without the use of a detection algorithm, the use of latter enables

- Identification of structures in other less obvious cases

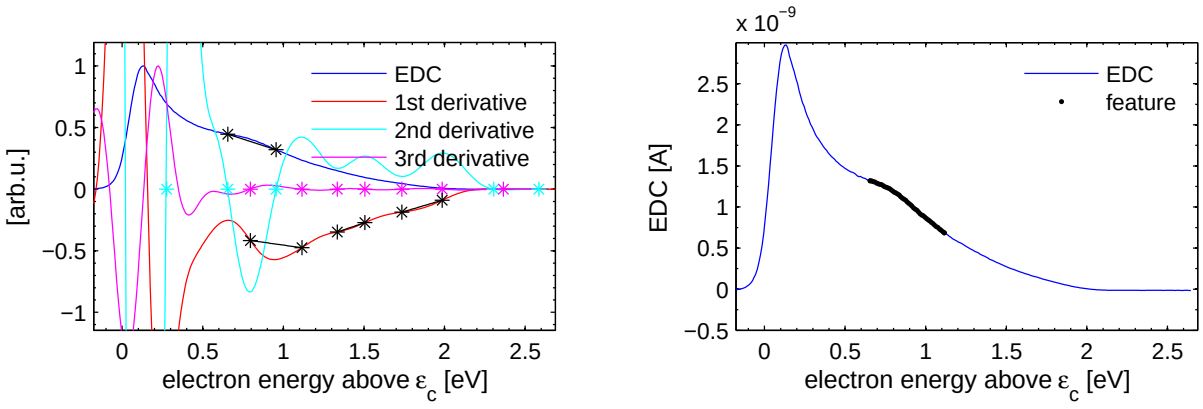


Figure 3.37: Determination of features on an EDC (left), the detected feature is located in the interval $0.6 - 1.1\,\mathrm{eV}$ (right) (SOI [5 µm], $h\nu = 3.28\,\mathrm{eV}$, $T = 300\,\mathrm{K}$)

- Standardization of criteria for the beginning and the end of features

Care must be taken while interpreting the features measured with pulsed laser, since such excitation may induce artificial features (discussed in section 5.2).

3.5 Polarized energy distribution curves (PEDCs) measurements

The experimental setup gives access to polarization spectra of photoemitted electrons, also called PEDC. The electronic polarization for a given photoemission energy is defined as

$$P = \frac{N^+ - N^-}{N^+ + N^-} \tag{3.58}$$

where N^+ and N^- represent number of electrons with spins $|\uparrow\rangle$ and $|\downarrow\rangle$ respectively.

3.5.1 Characteristic regimes observed on PEDC

A typical PEDC can be divided into several parts (fig. 3.38):

- The electrons near the high-energy threshold escape into vacuum ballistically, with no or small loss in energy and spin polarization. The corresponding part of PEDC usually exhibits the highest polarization.
- With decreasing electron energy, spin relaxation becomes more important. In addition, transitions away from the zone center add their contribution to the measured value of polarization.
- The low-energy threshold of an EDC is limited by the vacuum level. In the case of NEA the electrons accumulated in the BBR provide a significant contribution to the low-energy side of the spectrum. The corresponding polarization is usually low, but a non-zero value can be observed. In principle, for positive electron affinity the polarization at low-energy threshold should not be modified during electron escape

from crystal. The electrons from this part of the spectra are described by a thermal distribution of typical width kT_e where T_e is an electronic temperature larger than the lattice temperature.

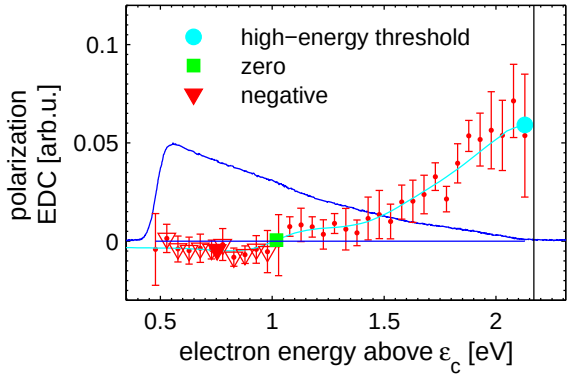


Figure 3.38: Characteristic EDC (blue curve) and PEDC (red errorbars) under UV excitation (SOI [5 µm], $h\nu = 3.33\,\mathrm{eV}$, $T = 114\,\mathrm{K}$)

3.5.2 Acquisition protocol

During the acquisition of a PEDC several parameters vary:

- Cathode potential V_{cath}
- Light polarization, subsequently set by the Babinet-Soleil compensator to four states:
  - Right circular polarization (denoted by σ^+)
  - Linear polarization (denoted by π)
  - Left circular polarization (denoted by σ^-)
  - Once again linear polarization
- The longitudinal magnetic field, which is modulated between zero and B_0 in order to flip the spin polarization of photoemitted electrons.

These parameters need to be changed at least once during the acquisition. However in practice it is preferred to perform several cycles over their different values in order to keep a possibility of detecting eventual drift in the measured values.

We define a cycle as a complete loop on the parameters

$$(V_{\mathrm{cath}}(i_{cath}), i, j) \text{ where } i_{cath} \in \{1, 2, ..N_{cath}\} \tag{3.59}$$

and $i \in \{\pi, \sigma^+, \sigma^+\}$ denotes the light polarization, $j \in \{H^{\mathrm{on}}, H^{\mathrm{off}}\}$ denotes the magnetic field, which allows to discriminate the polarization coming from the Silicon versus spurious instrumental asymmetries.

The raw data of a polarization measurement is described by two multidimensional arrays of counts on channels A and B (described in fig. 3.12), with the dimensions being given by eq. (3.59).

3.5.3 Correction of spurious instrumental asymmetries

To obtain the polarization from the arrays of counts, it is necessary to calculate and remove from the final result the instrumental asymmetry. The modulation of the magnetic field, as well as the use of linear polarization permits discrimination between the polarization originating from the Silicon and spurious asymmetry.

Let us fix the excitation energy $h\nu$ and the kinetic energy of electrons ϵ. Let $A_j^i, B_j^i, i \in \{\sigma^+, \sigma^-, \pi\}, j \in \{H^{\text{on}}, H^{\text{off}}\}$ counts measured on the left and right counters respectively, with and without transverse magnetic field j to flip the spins, under light with polarization i. In the ideal conditions (without instrumental asymmetry) the following holds

$$A_j^i(1 - S_{\text{eff}}P_j^i) = B_j^i(1 + S_{\text{eff}}P_j^i) \tag{3.60}$$

where P_j^i is the polarization of photo-emitted electrons, S_{eff} is the Sherman function.

$$S_{\text{eff}}P_j^i = \frac{A_j^i - B_j^i}{A_j^i + B_j^i} \tag{3.61}$$

$$\frac{A_j^i}{B_j^i} = \frac{1 + S_{\text{eff}}P_j^i}{1 - S_{\text{eff}}P_j^i} \tag{3.62}$$

In order to account for spurious instrumental asymmetry, we denote it by δ_j and redefine the polarization in eq. (3.62) as:

$$\frac{A_j^i}{B_j^i} = \frac{1 + S_{\text{eff}}P_j^i}{1 - S_{\text{eff}}P_j^i}\delta_j \tag{3.63}$$

where j index reflects the change in corresponding quantity under magnetic field, and $\delta_j = 1$ corresponds to the absence of instrumental asymmetry.

Let us consider special cases:

- In the case of right circularly polarized excitation (denoted by σ^+) the polarization equals $P_j^+ = |P_j|$
- In the case of left circularly polarized excitation (denoted by σ^-), $P_j^- = -|P_j|$,
- In the case of linearly polarized excitation (denoted by π), $P_j^\pi = 0$.

In particular, it follows from eq. (3.60) that

$$\begin{aligned}
\frac{A_j^+}{B_j^+} &= \frac{1 + S_{\text{eff}}|P_j|}{1 - S_{\text{eff}}|P_j|}\delta_j \\
\frac{A_j^-}{B_j^-} &= \frac{1 - S_{\text{eff}}|P_j|}{1 + S_{\text{eff}}|P_j|}\delta_j \\
\frac{A_j^\pi}{B_j^\pi} &= \delta_j
\end{aligned} \tag{3.64}$$

We obtain

$$\frac{A_j^- B_j^+}{A_j^+ B_j^-} = \left(\frac{1 - S_{\text{eff}}|P_j|}{1 + S_{\text{eff}}|P_j|}\right)^2$$

$$\pm\sqrt{\frac{A_j^- B_j^+}{A_j^+ B_j^-}} = \frac{1 - S_{\text{eff}}|P_j|}{1 + S_{\text{eff}}|P_j|}$$

Note that $\frac{1-S_{\text{eff}}|P_j|}{1+S_{\text{eff}}|P_j|} > 0$ since $0 \leq S_{\text{eff}}|P_j| \leq 1$. Thus only the positive sign has a meaning in the previous equality.

We note

$$x^+ = \sqrt{\frac{A_j^- B_j^+}{A_j^+ B_j^-}} = \frac{1 - S_{\text{eff}}|P_j|}{1 + S_{\text{eff}}|P_j|}$$

$$|P_j| = \frac{1}{S_{\text{eff}}} \frac{1 - x_j^+}{1 + x_j^+} \tag{3.65}$$

Or alternatively

$$x^- = \sqrt{\frac{A_j^+ B_j^-}{A_j^- B_j^+}} = \frac{1 + S_{\text{eff}}|P_j|}{1 - S_{\text{eff}}|P_j|}$$

$$|P_j| = -\frac{1}{S_{\text{eff}}} \frac{1 - x_j^-}{1 + x_j^-} \tag{3.66}$$

For $i \in \{\sigma^+, \sigma^-\}$ the eqs. (3.65) and (3.66) can be summarized as

$$P_j^i = \frac{1}{S_{\text{eff}}} \frac{1 - x_j^i}{1 + x_j^i}$$

Reconstructing the instrumental asymmetry from the data in circularly polarized light,

$$\delta_j^\sigma = \sqrt{\frac{A_j^+ A_j^-}{B_j^+ B_j^-}} \tag{3.67}$$

we can rewrite

$$P_j^i = \frac{1}{S_{\text{eff}}} \frac{A_j^i - \delta_j^\sigma B_j^i}{A_j^i + \delta_j^\sigma B_j^i}, \text{ with } P_j^+ = -P_j^-$$

Finally, we combine the instrumental asymmetry from eq. (3.67) with the values calculated from the counts calculated on linearly polarized light (3.64):

$$\delta_j = \frac{1}{2}\left(\delta_j^\sigma + \frac{A_j^\pi}{B_j^\pi}\right) \tag{3.68}$$

Using the value of δ_j above, we can redefine the expression for the polarization

$$P_j^i = \frac{1}{S_{\text{eff}}} \frac{A_j^i - \delta_j B_j^i}{A_j^i + \delta_j B_j^i} \tag{3.69}$$

With this new δ_j there is no more reason for P_j^+ and $-P_j^-$ to be equal.

So the final result can be calculated as

$$|P_j| = \frac{P_j^+ - P_j^-}{2} \tag{3.70}$$

In some cases, it is useful to exclude from consideration the Sherman function. To do this, instead of the polarization the asymmetry can be considered. It is defined by:

$$\mathcal{A} = S_{\text{eff}} P \tag{3.71}$$

For the calculation of the asymmetry one can use, for instance, eq. (3.69) without the factor $\frac{1}{S_{\text{eff}}}$.

As discussed in details in appendix A, it is preferable to use in eq. (3.61) the counts integrated (or numerically summed) over a long enough period of time, rather than to average the asymmetry calculated directly over short intervals of time. In fact, the first approach allows to avoid the division by zero in the asymmetry, which alters the total value of asymmetry.

3.5.4 Precision of the polarization measurements

Making the assumption that A_j^i, B_j^i are independent (which may be false in the case of systematic errors affecting all the measurements), the error of $|P_j|$ is given by

$$\Delta|P_j| = \sqrt{\sum_{x\in\{A_j^i, B_j^i\}} \left(\frac{\partial|P_j|}{\partial x}\Delta x\right)^2} \tag{3.72}$$

where Δx denotes the error on each of counters.

The argument above is valid for both measurements with and without magnetic field. Since these measurements are independent,

$$\Delta P_{\text{stat}} = \sqrt{\Delta P_{\text{on}}^2 + \Delta P_{\text{off}}^2} \tag{3.73}$$

Considering the simple expression for the polarization without instrumental correction eq. (3.23):

$$P = \frac{1}{S_{\text{eff}}}\frac{A-B}{A+B} \tag{3.74}$$

one can find a convenient estimation of the error on the polarization [Kessler1985]. Starting from the expression

$$\Delta P = \frac{1}{S_{\text{eff}}}\Delta\mathcal{A} \tag{3.75}$$

The error on the asymmetry $\mathcal{A}$ is given by

$$\Delta\mathcal{A} = \sqrt{\frac{\partial\mathcal{A}}{\partial A}(\Delta A)^2 + \frac{\partial\mathcal{A}}{\partial B}(\Delta B)^2} = \sqrt{\left(\frac{2B}{(A+B)^2}\right)^2 A + \left(\frac{-2A}{(A+B)^2}\right)^2 B} = \sqrt{\frac{4AB}{(A+B)^2}}$$

It follows from eq. (3.74) that

$$1 - P^2 S_{\text{eff}}^2 = \frac{4AB}{(A+B)^2} \tag{3.76}$$

One obtains

$$\Delta\mathcal{A} = \sqrt{\frac{1}{A+B}\left(1 - P^2 S_{\text{eff}}^2\right)} \tag{3.77}$$

and

$$\Delta P = \sqrt{\frac{1}{A+B}\left(\frac{1}{S_{\text{eff}}^2} - P^2\right)} \tag{3.78}$$

In practice $1/S_{\text{eff}}^2 \gg P^2$, thus

$$\Delta P \approx \frac{1}{S_{\text{eff}}\sqrt{A+B}} \tag{3.79}$$

The generalization of eq. (3.79) to the case with instrumental asymmetry correction results in

$$(\Delta P)' = \frac{1}{S_{\text{eff}}\left(\sum_{i,j}(A_j^i + B_j^i)\right)^{1/2}} \tag{3.80}$$

The comparison of error estimation for our experimental data provides

$$\frac{\Delta P_{\text{stat}}}{(\Delta P)'} \approx \text{from 0.05 to 2} \tag{3.81}$$

Another estimation can be performed as the standard deviation of the vector $(P_{\text{off}}^+, P_{\text{off}}^-, P_{\text{on}}^+, P_{\text{on}}^-)$. In ideal conditions, these four measurements (with and without transverse magnetic field, in σ^+ and σ^- light) should coincide in the absolute value. The estimation of $\underset{i,j}{\text{std}}\, P_j^i$ is usually one order of magnitude larger than the statistical error from the eq. (3.73).

It follows from correlation analysis that the quantity of the noise shown in the left panel of fig. 3.39 is inversely proportional to the spectrometer resolution. At the same time, such sharp features are not repeatable from one measurement to another, which does not allow to consider them as a meaningful signal, visible at fine spectrometer resolutions. The physical interpretation of this error remains an open issue.

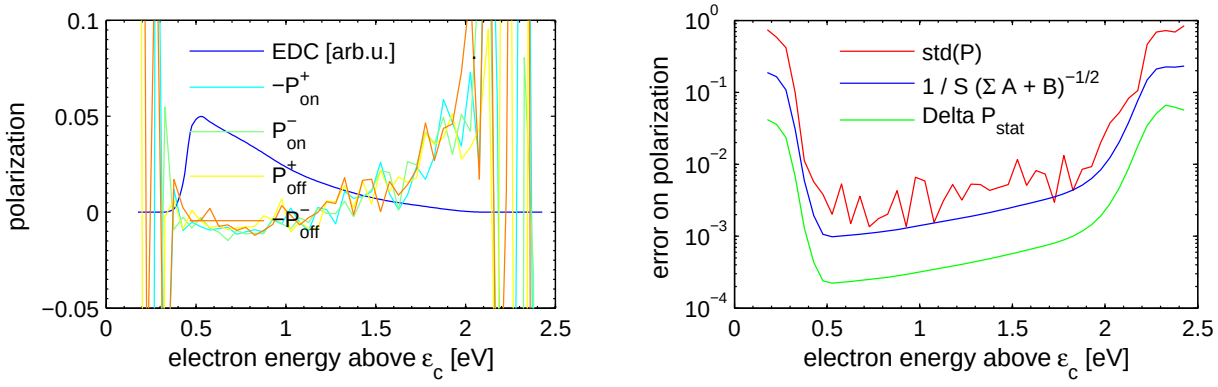


Figure 3.39: Estimation of error on the polarization (SOI [5 µm], $h\nu = 3.28\,\text{eV}$, $T = 300\,\text{K}$)

However, one needs to account for the statistical convergence while interpreting the results. Thus, the empirical estimations like

$$\Delta P_{total} = \alpha \operatorname*{std}_{i,j} P_j^i + (1-\alpha)\Delta P_{stat} \text{ where } \alpha \in (0,1) \tag{3.82}$$

may be of utility for error-based weighted regressions on polarization data, with typical weight being given in each point of photoemission spectrum ϵ:

$$W(\epsilon) = \frac{1}{\Delta P_{total}(\epsilon)} \tag{3.83}$$

α is usually chosen in order to balance both contributions.

3.5.5 Polarization at the high-energy threshold

Precise evaluation of the polarization on the high-energy threshold is a challenging task. Indeed, as can be seen from the right panel of fig. 3.39, this part of the PEDC is often characterized by insufficient statistical convergence due to vanishing signal. In the present work we consider three ways to assess the polarization:

1. Let us denote by $y^n_{\text{interp}}(\epsilon)$ a nth order polynomial $W(\epsilon)$-weighted interpolation. It is constructed by least-squares fit based on the data within the range

$$E_{\text{interp}} = [\epsilon_{\text{HE}} - \Delta^n_\epsilon; \epsilon_{\text{HE}}] \tag{3.84}$$

   such that $P(\epsilon) > 0$ for $\epsilon \in E_{\text{interp}}$, and where Δ^n_ϵ is a certain energy offset. The estimation of the polarization can be obtained as $y^n_{\text{interp}}(\epsilon_{\text{HE}})$. It is characteristic that high n lead to ill-conditioned system, and as consequence do not provide accurate assessment of the polarization on the high-energy threshold. In practice, two useful options are considered:

   (a) The average in the vicinity of ϵ_{HE} (i.e. $n = 0$, $\Delta^0_\epsilon = 0.2\,\text{eV}$)

   (b) Linear interpolation over a wider range (i.e. $n = 1$, $\Delta^1_\epsilon = 1\,\text{eV}$)
   As will be discussed later in section 3.5.1, depending on $h\nu$ the positive parts of the polarization spectra $P(E_{\text{interp}})$ can have zero or negative curvature. Thus, $P(E_{\text{interp}})$ is sometimes better described by the linear and sometimes by quadratic least-squares fit. However, it was found that the improvement in accuracy by increasing n from 1 to 2 is negligible compared with the interpolation error committed on noisy PEDCs.

2. Maximum of Gaussian-kernel smoothing regression $y_{\text{reg}}(\epsilon)$ [Cai2001], with weights also being given by $W(\epsilon)$. Compared with $y^n_{\text{interp}}(\epsilon)$, this interpolation do not have a predefined form and can account for the potentially non-linear dependence of $P(\epsilon)$. At the same time, the extrapolation to $y_{\text{reg}}(\epsilon_{\text{HE}})$ sometimes leads to a significant error due to lack of statistical convergence of the last points on the PEDC. Thus, the threshold polarization is estimated as:

$$P(\epsilon_{\text{HE}}) \approx y_{\text{reg}}(\epsilon(end)_P) \tag{3.85}$$

where $\epsilon(end)_P$ is the last energy point of the PEDC measurement.

Figure 3.40 shows the results of these three types of interpolation. For a PEDC with relatively low noise level all of them should give similar results. A combination of all the three estimations above is used for studying the behavior of the polarization on the high threshold (sections 4.2 and 4.3).

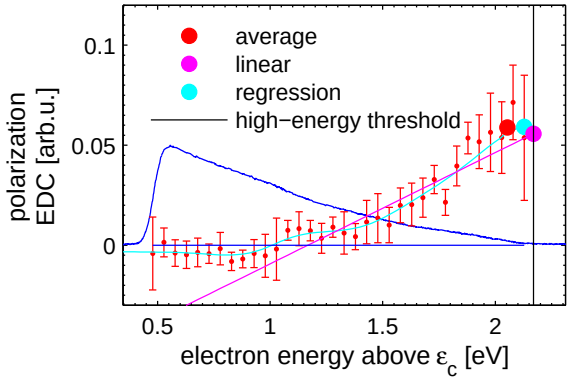


Figure 3.40: Estimation of the polarization near high-energy threshold (SOI [5 µm], $h\nu = 3.33\,\text{eV}$, $T = 114\,\text{K}$). A combined value of all the three estimation is used for the analysis of the polarization.

3.5.6 EDC-averaged polarization

A spin distribution curve can be defined as

$$S(h\nu,\epsilon) = P(h\nu,\epsilon)N(h\nu,\epsilon) = N^{+}(h\nu) - N^{-}(h\nu) \tag{3.86}$$

Based on the measured values of polarization, we can calculate the corresponding value of EDC-averaged polarization:

$$\langle P\rangle(h\nu) = C\int_{V_0}^{h\nu} S(h\nu,\epsilon)d\epsilon \tag{3.87}$$

where the normalization factor

$$C(h\nu) = \left(\int_{V_0}^{h\nu} N(h\nu,\epsilon)dV\right)^{-1} \tag{3.88}$$

This quantity allows analyzing the magnetic properties even at the basis of incomplete measurements. In fact, if the measurement is not completed, the statistical error is proportionally $N(h\nu,\epsilon)^{-1}$. Thus, the greatest contribution to the $\langle P\rangle$ is provided by polarization measured with the smallest statistical error.

3.5.7 Magnetic moment

Unlike the polarization, the magnetic moment is an extensive quantity. In other words, in order to construct a dimensional value of the magnetic moment it is necessary to multiply $\langle P \rangle$ by a timescale. Typically, the escape time can be used to model magnetic moment of sample:

$$m(h\nu) = \mu_B \frac{\tau_{\text{magn}}}{e} \; I_{cath}(h\nu) \; \langle P \rangle (h\nu) \; [\text{A m}^2] \tag{3.89}$$

The calculation of the magnetization requires the additional knowledge of the photoexcited volume V:

$$M(h\nu) = \frac{m(h\nu)}{V} [\text{A/m}] \tag{3.90}$$

One notes that the multiplicative factor between the $\langle P \rangle (h\nu)$ and both of the quantities from eqs. (3.89) and (3.90) depends on the excitation power, but vary much slower with the excitation energy. Thus, the form of the dependence $m(h\nu)$ and $M(h\nu)$ for a small interval of excitation energies (such as the vicinity of direct band gap $h\nu \in [\epsilon_{g,\Gamma} - 0.1\,\text{eV}, \epsilon_{g,\Gamma} + 0.1\,\text{eV}]$) is proportional to the dependence $\langle P \rangle (h\nu)$.

The characteristic time for the calculation of the sample magnetic moment can be obtained as follows:

$$\frac{1}{\tau_{\text{magn}}} = \frac{1}{\tau_{\text{escape}}} + \frac{1}{\tau_s} \tag{3.91}$$

where the spin relaxation time being defined by eq. (6.47).

3.6 Conclusion

In the first sections of this chapter we defined the conventions on σ^+ circular light polarization, which will be essential for the comparison with other theoretical and experimental work. The peculiarities of exploitation of electron spectrometer were analyzed, in order to exclude the possibility of an eventual systematic error during the polarization measurements.

The sample types were presented, with an accent on the procedure of cathode preparation, which revealed unexpected NEA state of (1 1 1) Silicon surface, which is presumed to be (7×7) reconstructed since it was prepared according to the protocol similar to that given in [Binnig1983]. The SOI structures, which are studied in the present work, are shown to be relatively stable while subjected to successive high-temperature annealing and laser irradiation with high optical density. No significant stress was found in this structure, which implied that the band structure is similar to that of bulk Silicon.

An algorithm of computer-aided determination of high-energy threshold on EDC is described. Due to the instability of the EDC position versus applied bias V_{cath}, such the analysis tool is necessary for accurate comparison of PEDC measured on different samples with different photon energies.

As it is detailed in appendix A, the calculation of asymmetry over sum of counts is the preferable method of analysis of a counting experiment. In fact the average of asymmetry, if calculated over too short periods of time, may induce a bias in the calculated asymmetry.

The analysis of low-energy threshold of EDC indicates the non-homogeneities in the deterioration of surface layer, in agreement with previous studies. The temperature dependence of EDC thresholds is determined by relative contributions of several competing parameters.

Chapter 4

Experimental results

4.1 Introduction

In this chapter we classify the obtained results by the increasing excitation energy: from near the fundamental gap excitation (1.12 eV) towards second direct gap and above up to 4.8 eV.

In each section, we separately analyze spectroscopic results, following by the polarization observed on HE threshold of electron energy distribution, which is attributed to the ballistic electrons, finishing by the polarization of hot electrons. A comparative analysis of the measurement provided from all the three samples are considered in each section. In the section dedicated to the first direct band gap, we analyze the angular and temperature dependence of observed features on EDCs.

As the use of pulsed laser radiation causes spectrometer saturation[1], both the EDC and PEDC measurements presented in this chapter are made using a continuous wave radiation of the Tsunami laser, with the exception of the third-harmonic radiation, which can only be produced in the pulsed regime.

4.2 Excitation near $\epsilon_{g,X}$ indirect gap ($\Gamma_5^+ \rightarrow \Gamma_4^-$)

4.2.1 Energy of the absorption onset

The indirect absorption edge equals $\epsilon_{g,X} + \epsilon_{\mathrm{ph}}$ in the case of phonon absorption, and $\epsilon_{g,X} - \epsilon_{\mathrm{ph}}$ in case of phonon emission. Eventually some excitation from acceptor level is also possible. Because of selection rules, the indirect optical transitions are mainly assisted by optical phonons, even if the acoustical phonons are not completely excluded neither.

At low temperature the emission of phonons is more probable rather than absorption. So, for instance, at low temperature the creation of electrons with the kinetic energy below $\epsilon_{g,X} + \epsilon_{\mathrm{ph}}{}^{optical}$ (i.e. below the main part of an EDC), can be explained by:

- Excitation from acceptor level
- Phonon absorption
- Transitions implying acoustical phonons

[1] Which will be described and analyzed in the chapter 5

4.2.2 Light interference in SOI structure

During the measurements of SOI structure under IR excitation, the oscillations of photocurrent versus excitation energy are observed (fig. 4.1) for both low and room temperatures. As will be shown below, these oscillations coincide with the calculated variation of absorption coefficient in the SOI sample due to the laser light interference between the multiple reflections in the layers of the sample. Such successful description by the proposed model provides strong evidence that the observed oscillations are indeed due to the light interference in the sample, from which two important conclusions follow

- Circular polarization of the laser light is preserved upon the reflections[2], which implies:
  - The degree of circular polarization does not vary with excitation energy. Clearly the latter would not hold if the circular polarization would be altered by such interference.
  - The long counting experiment should be performed at the maximums of photocurrent in order to increase the counting rate.
- The thin active layer of the SOI structure was not lift off during the annealings, which preceded the interference measurement.

Experiment

In a structure composed of multiple layers the incident light undergoes multiple reflections from the interfaces. The SOI structure used in the present work is composed of the following interfaces:

1. Vacuum - Si (front surface of the sample)
2. Si - SiO_2
3. SiO_2 - Si(bulk)
4. Si(bulk) - vacuum (rear surface of the sample)

It is observed that the resulting multiple reflection interference does not affect the shape of the EDCs. Only the total emitted current intensity is affected.

Model

We consider a stratified structure, with N layers $j \in \{1, .., N\}$, the layer j being defined as the interval $z \in]d_j, d_{j+1}[$. Under the assumption that each layer is linear, homogeneous and isotropic, the optical response can be easily calculated with Maxwell equations, decomposing the electric field in the basis $o \in \{s, p\}$ of two orthogonal directions which would describe s and p polarization if the sample was illuminated with an off-normal incidence.

The propagation of descending (along z, the corresponding electric field is denote by $E_j^{o\downarrow}(z)$) and ascending (along $-z$, the corresponding electric field is denote by $E_j^{o\uparrow}(z)$) waves in each layer j is described by the matrix

$$\begin{pmatrix} E_j^{o\downarrow}(z) \\ E_j^{o\uparrow}(z) \end{pmatrix} = D_j(z) \begin{pmatrix} E_j^{o\downarrow}(d_j) \\ E_j^{o\uparrow}(d_j) \end{pmatrix} = \begin{pmatrix} e^{ik_j z} & 0 \\ 0 & e^{-ik_j z} \end{pmatrix} \begin{pmatrix} E_j^{o\downarrow}(d_j) \\ E_j^{o\uparrow}(d_j) \end{pmatrix} \tag{4.1}$$

[2]The sense of rotation of electric field changes, but the propagation direction changes too.

On the interfaces we choose the base of conserving components

$$\begin{pmatrix} E_j^y \\ cB_j^x \end{pmatrix} = A_j^s \begin{pmatrix} E_j^{s\downarrow} \\ E_j^{s\uparrow} \end{pmatrix} = \begin{pmatrix} 1 & 1 \\ -\frac{k_j}{k_0} & \frac{k_j}{k_0} \end{pmatrix} \begin{pmatrix} E_j^{s\downarrow} \\ E_j^{s\uparrow} \end{pmatrix} \tag{4.2}$$

and

$$\begin{pmatrix} cB_j^y \\ E_j^x \end{pmatrix} = A_j^p \begin{pmatrix} E_j^{p\downarrow} \\ E_j^{p\uparrow} \end{pmatrix} = n_j \begin{pmatrix} 1 & 1 \\ \frac{k_j}{\epsilon_{dj} k_0} & -\frac{k_j}{\epsilon_{dj} k_0} \end{pmatrix} \begin{pmatrix} E_j^{s\downarrow} \\ E_j^{s\uparrow} \end{pmatrix} \tag{4.3}$$

where n_j is the refractive index of j medium.

The optical response of the system is obtained by solving, separately for two polarizations, the equation

$$\begin{pmatrix} E_N^{o\downarrow} \\ E_N^{o\uparrow} \end{pmatrix} = M_{N1} \begin{pmatrix} E_1^{o\downarrow} \\ E_1^{o\uparrow} \end{pmatrix} = (A_N^o)^{-1} \prod_{j=N-1}^{2} \left(A_j^o D_j A_j^{o-1} \right) A_1^o \begin{pmatrix} E_1^{o\downarrow} \\ E_1^{o\uparrow} \end{pmatrix} \tag{4.4}$$

Here $E_1^{o\downarrow}$ is the incident wave, $E_1^{o\uparrow}$ is the reflected wave, $E_N^{o\downarrow}$ is the transmitted wave, and $E_N^{o\uparrow} = 0$. The total electric field at the point $z \in]d_j, d_{j+1}[$ is given by

$$E^o(z) = E_j^{o\downarrow}(z) + E_j^{o\uparrow}(z) \tag{4.5}$$

The difference of electric field amplitudes of two polarizations is given by

$$\Delta E(z) = E^s(z) - E^p(z) = e^{ik_j z}(E^{s\downarrow}(d_j) - E^{p\downarrow}(d_j)) - e^{-ik_j z}(E^{s\uparrow}(d_j) - E^{p\uparrow}(d_j)) \tag{4.6}$$

If $E^{s\downarrow}(d_j) - E^{p\downarrow}(d_j) = 0$ and $E^{s\uparrow}(d_j) - E^{p\uparrow}(d_j) = 0$, the initial polarization state is the conserved throughout the layer j.

Comparison

Note that $\epsilon_{d2,4}$ influences greatly the result of the calculation. Figure 4.3 shows calculated absorption in the active layer of SOI structure for different datasets of the complex dielectric constant. In the calculations shown on figs. 4.1 and 4.2 we used the absorption spectra from [Macfarlane1959] and the refractive index from [Sze2006].

The following features are correctly described by the model (figs. 4.1 and 4.2):

- Period and beat period dependence on sample thickness.
- Oscillations have larger amplitude at temperature. It follows that the change in amplitude is explained by temperature dependence of the dielectric function of Silicon $\epsilon_{d2,4}$, the latter being the only temperature dependent parameter in the model.

If the phase difference between low and room temperature is effectively due to temperature change, this brings evidence that the interferences are built in the sample, and not in another point of optical path. Note that the period stays the same for different measurement.

Since there was no a priori evidence that the interference took place in the sample itself, the choice was to avoid any unnecessary modification of the optical path during the interference measurements. That is why the output optical power was maintained constant by the adjustment of the pump power (which is not generally recommended since results in

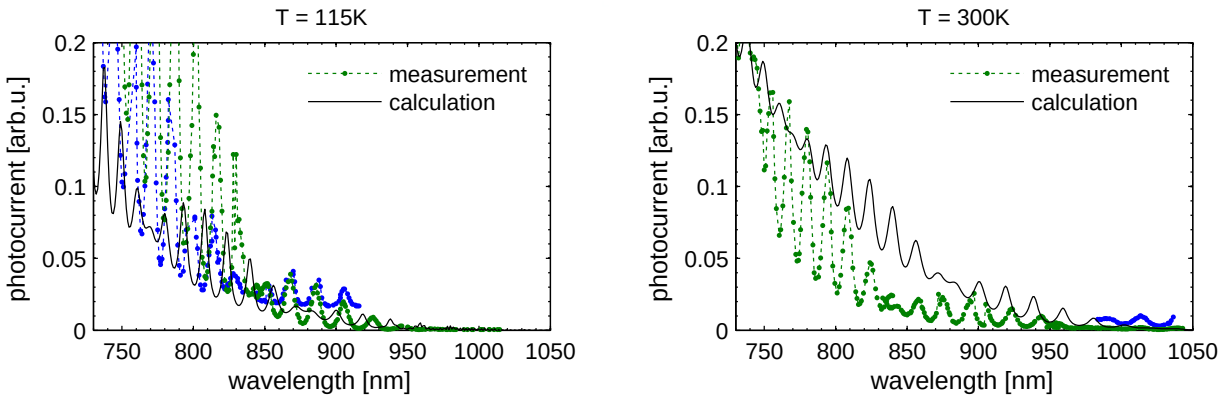


Figure 4.1: Light interference in SOI [5 µm]

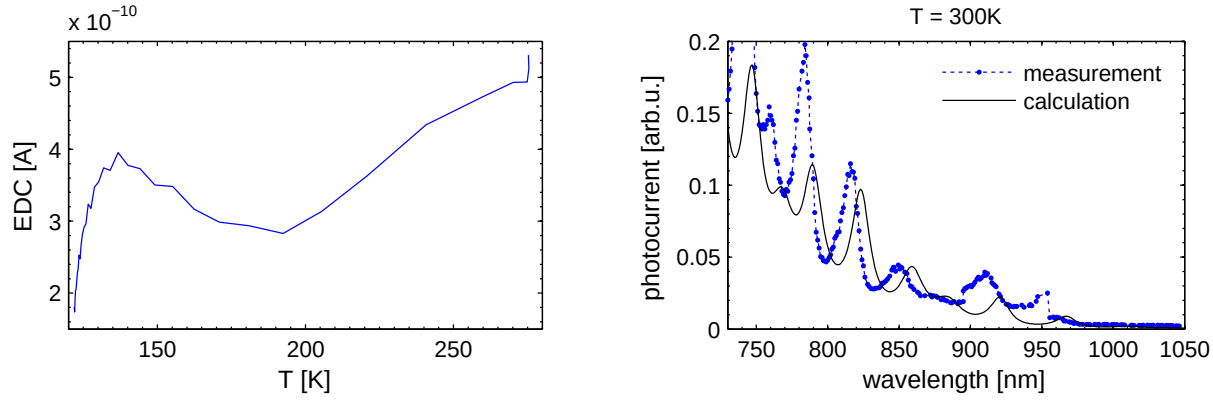


Figure 4.2: Maximum of an EDC at $h\nu = 1.7\,\mathrm{eV}$ as a function of temperature (left), light interference in SOI [2 µm] (right)

fluctuations of the output power, but here was exceptionally used in order to preserve the optical path to the maximum extent possible).

The SHG does not provide a sufficiently fine control of both output power[3] and excitation energy, and thus does not allow to easily measure the interference for $h\nu > 2.3\,\mathrm{eV}$. However, from the general considerations it follows that the interference only appears for $\frac{d}{\alpha} \lesssim 1$, since the amplitude of the reflected electromagnetic field has to be comparable, and not exponentially lower than that of the incident field.

4.2.3 Polarization of ballistic electrons

As shown in fig. 4.4, both for 300 K and 115 K a close to zero polarization is observed in the photon energy range $1.2 - 1.75\,\mathrm{eV}$.

[3]Without the modification of optical path, i.e. only by the means of pump power.

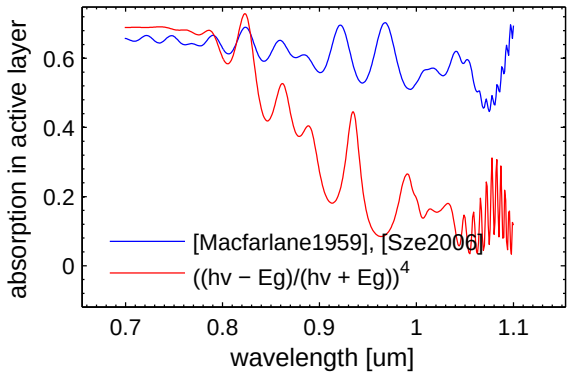


Figure 4.3: Comparison of calculated light interference in SOI [5 µm], $T = 115\,\mathrm{K}$, based on different datasets of Silicon absorption coefficient

For both room and low temperatures, the observed polarization is low even for

$$h\nu \in [\epsilon_{g,X}, \epsilon_{g,X} + \Delta_{SO}] = \begin{cases} 1.12 - 1.164\,\mathrm{eV} & T = 300\,\mathrm{K} \\ 1.16 - 1.204\,\mathrm{eV} & T = 115\,\mathrm{K} \end{cases} \tag{4.7}$$

At 115 K, a non-zero value of polarization could be also expected for energies

$$h\nu \in [\epsilon_{g,X} + \epsilon_{\mathrm{ph}}, \epsilon_{g,X} + \epsilon_{\mathrm{ph}} + \Delta_{\mathrm{SO}}] \tag{4.8}$$

since the phonon creation is dominant at low temperatures. For instance, considering the transverse optical phonons, which provide the main contribution to the band-edge absorption spectrum, and are known to give rise to negatively polarized photoelectrons under σ^+ light excitation [Li2010], one can consider ${\epsilon_{\mathrm{ph}}}^{TO} \approx 60\,\mathrm{meV}$. However, no significant polarization in this interval was experimentally observed.

At the same time, the due to the lack of experimental points in eq. (4.8) with $\epsilon_{\mathrm{ph}} = {\epsilon_{\mathrm{ph}}}^{acoustic} \approx 15\,\mathrm{meV}$ [4], no conclusion can be made on the basis of the experimental data about the band-edge polarization transmitted by the acoustic phonons.

4.2.4 EDC-averaged polarization

Let us recall the definitions. The spin distribution curve (initially defined in eq. (3.86)) is given by:

$$S(h\nu, \epsilon) = P(h\nu, \epsilon)N(h\nu, \epsilon) = N^+(h\nu) - N^-(h\nu) \tag{4.9}$$

Based on S, we can calculate the EDC-averaged polarization (initially defined in eq. (3.87)), which is in fact proportional to the magnetic moment:

$$\langle P \rangle (h\nu) = C \int_{V_0}^{h\nu} S(h\nu, \epsilon) d\epsilon \tag{4.10}$$

[4] We failed to acquire these points due to insufficient signal level at excitation energies very close to the band edge.

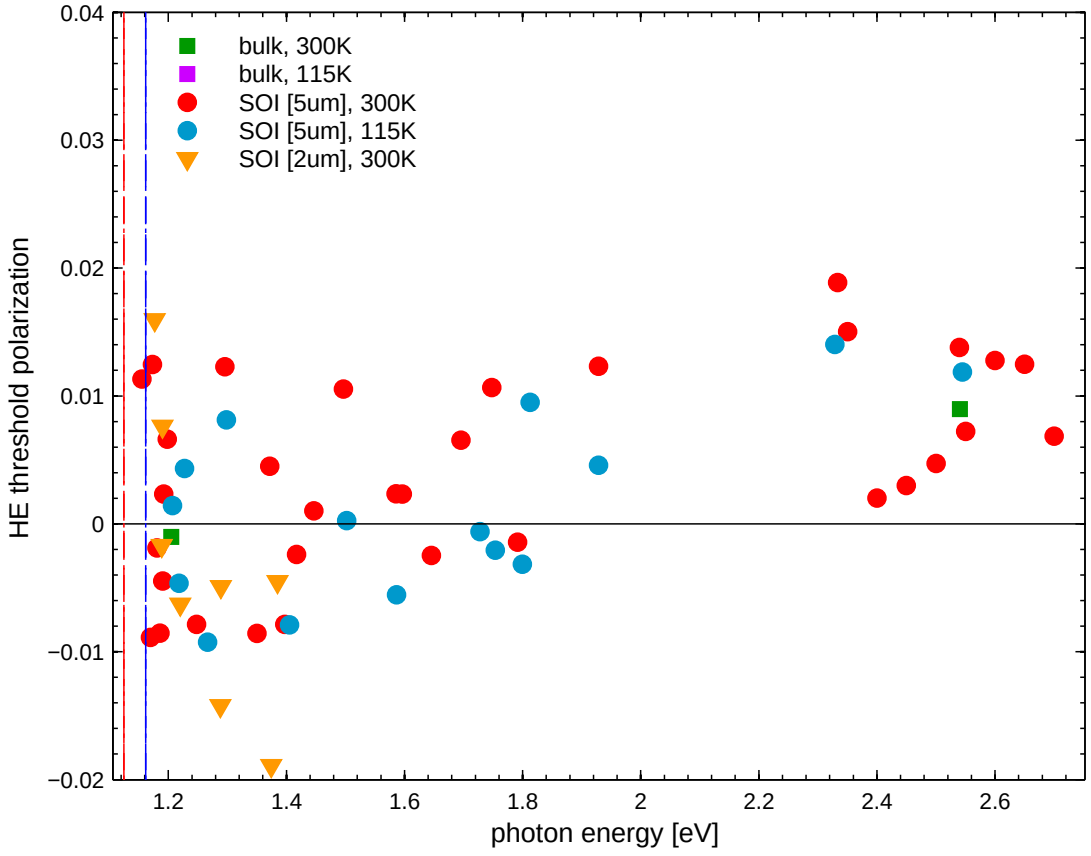


Figure 4.4: Polarization at high-energy threshold versus photon energy starting close to the indirect band gap $\epsilon_{g,X}$. $\epsilon_{g,X}(300\,\mathrm{K}) = 1.125\,\mathrm{eV}$ and $\epsilon_{g,X}(115\,\mathrm{K}) = 1.16\,\mathrm{eV}$ are shown with red and blue lines respectively.

where the normalization factor

$$C(h\nu) = \left(\int_{V_0}^{h\nu} N(h\nu, \epsilon) dV \right)^{-1} \tag{4.11}$$

Unlike the polarization of ballistic electrons, the EDC-averaged polarization does not vanish when $h\nu$ tends to the fundamental gap fig. 4.6. In order to compare our result with [Lampel1968a], we need to integrate the polarization over electron energy and excitation energy. Integrating the product of EDC-averaged polarization and absorption coefficient from $\epsilon_{g,X}$ to -1.4 eV, we obtain following results summarized in table 4.1. The results for SOI [5 µm] are in good agreement with $-0.4\,\%$, measured by nuclear magnetic resonance [Lampel1968a]. The negative sign is also in agreement with theoretical results on indirect optical pumping [Cheng2011a], [Li2010].

In is interesting to compare the presented in table 4.1 polarization with low polarization of hot luminescence in Silicon ($P_{lum} = 0.1$), observed for the excitation energies

Sample	300 K	115 K
bulk	-7.2×10^{-4}	
SOI [5 µm]	-3.8×10^{-3}	-3.8×10^{-3}
SOI [2 µm]	-2.4×10^{-3}	

Table 4.1: EDC- and $h\nu$- averaged polarization near the fundamental gap

$h\nu \in [1.23\,\text{eV}, 1.32\,\text{eV}]$ and doping levels $10^{15} - 10^{18}\,\text{cm}^{-3}$ (fig. 4.5, [Roux2008]). Such polarization is observed only at low temperature (77 K), probably due to the mixing contributions of phonon emission/absorption at 300 K. When the doping level is decreased from $10^{18}\,\text{cm}^{-3}$ to $10^{15}\,\text{cm}^{-3}$, the observed polarization decreases from 10 % down to 8 %, which is likely to be explained by the increasing ratio τ_s/τ_e.

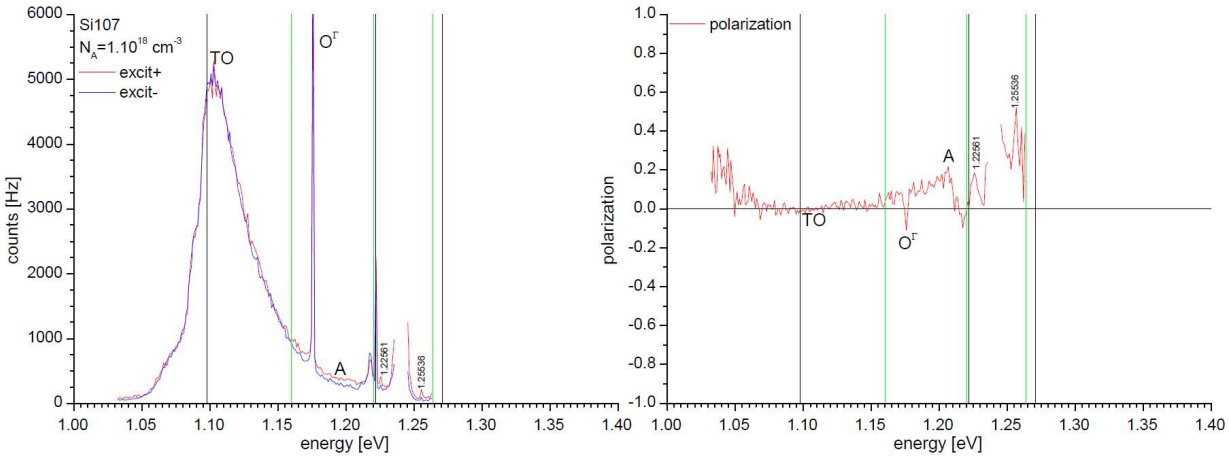


Figure 4.5: Spectra of σ^- (blue image) and σ^+ (red image) components of photoluminescence under σ^+-circularly polarized excitation (left). The peak polarization of hot photoluminescence is denoted with A (right). The inelastic scattering of the incident photons on an optical phonon at Γ of energy 64 meV is denoted with O_Γ. The negative contribution at the energy of 1.24 eV is also likely to be attributed to Raman scattering. ($h\nu = 1.24\,\text{eV}$, $T = 77\,\text{K}$, bulk Silicon) [Roux2008]

The measured photoluminescence polarization

$$P_{\text{PL}}^{hot} = {P_i}^2 \frac{{\tau_s}^{hot}}{{\tau_e}^{hot}} \approx 0.1$$

implies

$$P_i \frac{{\tau_s}^{hot}}{{\tau_e}^{hot}} \approx 0.3 \tag{4.12}$$

on the same order of magnitude as the theoretical predictions [Li2010].

The remaining open issue in the photoluminescence results of Roux is the inability to observe Hanle effect with use of the transverse magnetic field up to 0.3 T, implying that the

spin lifetime of hot photoelectrons ${\tau_s}^{hot}$ is lower than 50 ps. The latter could be effectively the case since the lifetime is given by

$$\frac{1}{{\tau_s}^{hot}} = \frac{1}{{\tau_e}^{hot}} + \frac{1}{{T_1}^{hot}} \tag{4.13}$$

where the momentum relaxation time ${\tau_e}^{hot}$ of hot electrons could be extremely short, whereas the spin relaxation time ${T_1}^{hot}(\epsilon)$ increases with the kinetic energy of electrons ϵ [Cheng2010]. Thus,

$${\tau_s}^{hot} \approx {\tau_e}^{hot} \tag{4.14}$$

is a probable situation. Indeed, similar effect takes place in GaAs, where ${\tau_s}^{hot} \approx 1\,\text{ps}$, and requires high magnetic fields of several Teslas for the observation of Hanle effect.

The theoretical considerations relative to the polarization of hot luminescence in Silicon are discussed in [Efanov1983].

It should be noted that the degree of circular polarization of hot luminescence can significantly exceed the analytically calculated P_i, which is in fact angle-averaged. So, in GaAs the predicted polarization of hot photoluminescence exceed the theoretically predicted 0.25 due to the anisotropic distribution of the spins at the moment of their creation [Dymnikov1976]. Experimentally, the polarization up to $P_{lum} = 0.45$ is observed in the energy interval $h\nu_{lum} \in [\epsilon_{g,X} - 0.1\,\text{eV}, \epsilon_{g,X}]$ [Zemskii1976; Zakharchenya1977].

As shown in fig. 4.6, no significant enhancement is observed while decreasing the sample thickness from bulk to SOI [5 µm], neither from SOI [5 µm] to SOI [2 µm]. Indeed, the only available IR measurement on bulk sample ($h\nu = 1.2\,\text{eV}$) yields $\langle P \rangle$ similar to that measured on SOI. If, based on this result, we suppose that $\langle P \rangle_{\text{bulk}} \approx \langle P \rangle_{\text{SOI}}$ over the whole range of excitation energies, a higher polarization could be also be expected for bulk sample at $1.3 - 1.4\,\text{eV}$, given that

$$|\langle P \rangle_{\text{SOI}}(1.3 - 1.4\,\text{eV})| > |\langle P \rangle_{\text{SOI}}(1.2\,\text{eV})| \tag{4.15}$$

It is interesting to observe the change in sign of $\langle P \rangle$ (or equivalently of the magnetization, defined in section 3.5.7) for $h\nu = 1.45\,\text{eV}$. A slightly higher band-edge polarization at low temperature probably implies that

$$\frac{\tau_s(115\,\text{K})}{\tau_e(115\,\text{K})} > \frac{\tau_s(300\,\text{K})}{\tau_e(300\,\text{K})} \tag{4.16}$$

4.2.5 Possible reasons for the low observed polarization

Contrary to our expectations, the measurements performed on thin active layers of SOI structures, does not result in the enhancement of the measured polarization under the near fundamental gap excitation. In this section we discuss the reasons for such the unexpected result.

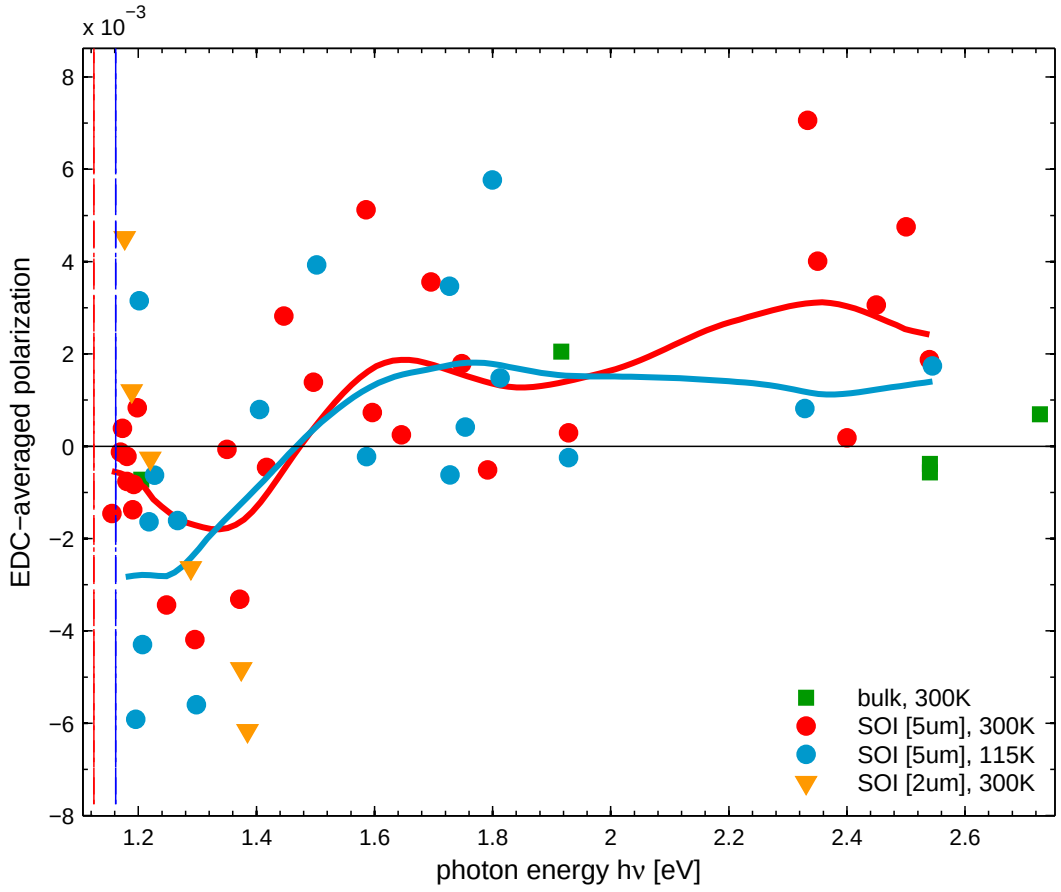


Figure 4.6: EDC-averaged polarization in IR region. Only the results with statistical error less than 2×10^{-3} are shown. The cumulative error on each individual point, which can be estimated from the scattering, is about 4×10^{-3}. The solid lines are the running average interpolations, which account for the relative error of each measurement. $\epsilon_{g,X}(300\,\mathrm{K}) = 1.125\,\mathrm{eV}$ and $\epsilon_{g,X}(115\,\mathrm{K}) = 1.16\,\mathrm{eV}$ are shown with red and blue lines respectively.

Non-uniform angular sensitivity of the photoemission setup

It is possible that the low polarization can be explained by the opposite contributions of the longitudinal and transverse (with respect to the light excitation direction) valleys. Indeed, Cheng et al. calculate positive polarization for longitudinal valleys and negative polarization for the transverse valleys [Cheng2011a] (fig. 4.7). The formula for the resulting polarization is similar to the described within the theoretical model of the optical pumping [5], i.e. implies averaging with uniform angular distribution over all the 6 conduction valleys.

However, a photoemission setup is possibly more sensitive to the contribution from the longitudinal valleys, since the electrons in this valley have higher longitudinal component of the wave vector $k_\perp$. Thus, a positive contribution to the measured polarization is higher than in the case of uniform averaging, and hence the resultant polarization could negative but be

[5] Specifically, the eq. (6.44) of the chapter 6

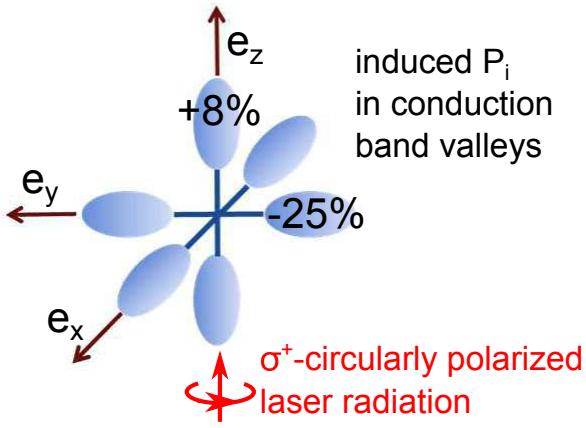


Figure 4.7: Calculated initial polarization under near indirect gap excitation along $\boldsymbol{e}_z$ [Cheng2011a]. The electrons photoexcited to the longitudinal (located on $\boldsymbol{e}_z$ axis) condition valleys are +10 %-spin polarized, whereas the electrons photoexcited to the transverse with respect to $\boldsymbol{e}_z$ valleys are −25 %-spin polarized. The predicted angular-averaged polarization is around −10 %.

closer to zero than is presented in [Cheng2011a].

However, in the case of a (1 1 1)-oriented sample a uniform contribution of the longitudinal and transverse valleys can be assumed. But no significant difference in the measured polarization between the 'valley-sensitive' (1 0 0) sample and 'valley-insensitive' (1 1 1) sample was observed. This can be explained by:

- Insufficient sensitivity of the experimental setup to the initial polarization.
- Independence of P_i on sample orientation.

In both cases, it would be of interest to calculate the polarization for the [1 1 1]-oriented irradiation.

Insufficient sensitivity to the ballistic electrons

According to the uni-dimensional spin diffusion model, which will be detailed in section 6.8.2, it is expected that the diffusion of thermalized electrons reduces their initial polarization in SOI [2 µm] by at most 2 times.

Thus, among explanations to the low measured polarization in IR one can cite the insufficient sensitivity of the setup to the ballistic electrons. Indeed, if the proportion of ballistic electrons in the measured PEDC is close to zero, the polarization would be mainly determined by electrons thermalized in the BBR, whose polarization can be significantly lower, due to efficient spin relaxation in the BBR.

In the case of SOI [2 µm] it can be argued that the photoelectrons experienced the diffusion in the crystal at the length of at maximum 2 µm. On the basis of the experimental results it can be concluded that such electrons do not exhibit any significant polarization. However, one should not exclude that electrons may also experience several reflections at the Silicon-vacuum and Silicon-oxide interfaces, which would result in an increase of the effective electron escape

depth (this would be the case if interface recombination velocity is weak). As a consequence, reducing the SOI active layer thickness would not allow improving the ratio τ_s/τ_e

Depolarization in the BBR and CsO - covered surface

Traversing the BBR, in which Dyakonov-Perel relaxation mechanism takes place due to the build-in electric field, and Cs - O surface may a priori cause additional spin relaxation. Two cases should be considered:

- The ballistic electrons are in principle less affected by such relaxation, since their transit of the shallow BBR and Cs - O layers is very fast.
- Thermalized electrons explore the surface layers much more intensively: in fact, they may experience multiple reflections from the surface layers before their escape into vacuum. That is why the relaxation induced by the surface layers can be much more important for $h\nu \approx \epsilon_{g,X}$, where the share of the thermalized electrons is extremely high.

In the case of GaAs (i.e. high initial polarization) and negative electron affinity the low polarization at low-energy threshold (which corresponds in this case to the minimum of valence band in the BBR) can be explained by the presence of strongly relaxed electrons [Drouhin1985]. In addition, stronger relaxation in this region is explained by the presence of the electric field, intrinsic for the BBR. The same reasoning is a priori applicable for optical transitions in Si near its fundamental gap.

Figure 4.8 combines all the polarization measurements performed under NEA conditions. Since the figure is a compilation of measurements for different excitation energies, the different signs of different curves are expected. The idea of the following analysis is to verify if all of them vanish to zero for $\epsilon < 0$.

Based on the comparison of polarization (the left panel of fig. 4.8) in the BBR ($\epsilon < 0$) and in the bulk ($\epsilon > 0$), we can see that the average polarization over the BBR is indeed slightly lower than the average throughout the PEDC. However, the quantitative analysis of polarization relaxation in this region is complicated by the lack of statistical convergence for most of measurements explained by the short duration of NEA state of the photocathode, combined with the low quantum yield of near-fundamental gap transitions.

In the ultraviolet range (the right panel of fig. 4.8), the transitions away from the Brillouin zone center can contribute significantly to the polarization of the low-energy electrons, and hence the resulting polarization does not necessarily vanish. The observed non-zero polarization can also be at least partially explained by inaccuracy in the positioning of the EDC (which is about 50 meV, see section 3.4.2).

The following arguments contrast the spin relaxation in surface BBR and Cs - O layers as the main reason for the low observed polarization in Si:

- Non-zero polarization of thermalized electrons is measured under UV excitation (the right panel of fig. 4.8).
- High measured polarization (near 25 %) of thermalized electrons from GaAs, in which the NEA is also achieved by means of Cesium and Oxygen deposition [Drouhin1985]. In fact, according to the results of Drouhin, Hermann, and Lampel, the ratio of the

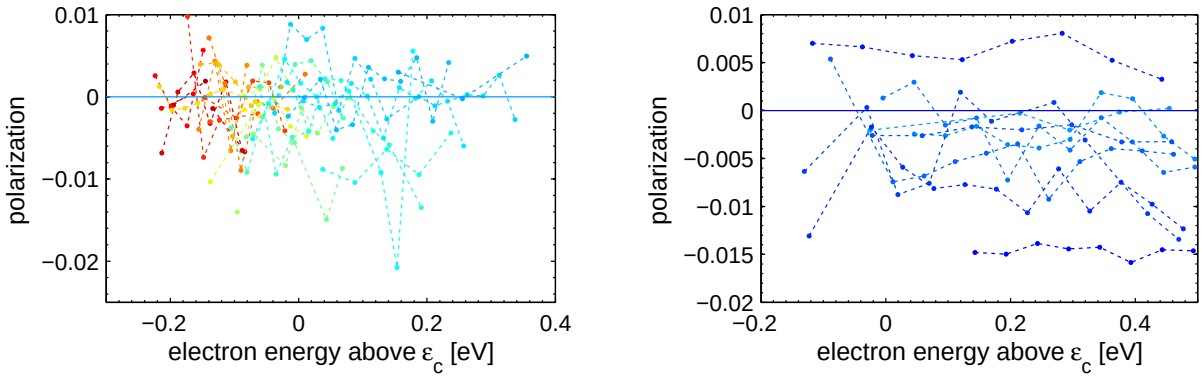


Figure 4.8: Polarization in BBR under IR excitation (left) and UV excitation (right). The measurements for the temperatures and samples are shown.

polarizations on low and high energy thresholds[6] constitute about 2/3 for $h\nu = 1.65\,\mathrm{eV}$ in GaAs, which can be explained by the presence of strongly relaxed electrons from the heavy hole band.

  - The comparison of temperature dependence of the polarization acquired under positive and negative electron affinity conditions indicates that the polarization is independent from Cesium coverage [Allenspach1984].
  - Measurement of nearly 80% polarization on constrained GaAs at NEA (achieved by deposition of Cs and NF_3): the total amount of relaxation in bulk and on the surface is less than $100\% - P_{measured} = 20\%$ [Maruyama1992].

- Comparison of the polarization of photoelectrons emitted from clean and Cesium-covered Cobalt also suggests a negligible impact of Cesium layer (without considering Oxygen) on the resulting polarization [Busch1972].

4.2.6 Conclusion

In the present section we discussed the main reasons for the low measured spin polarization of conduction electrons in vicinity of the fundamental band gap of Silicon. The numerical results [Cheng2011a] suggest that the measured polarization can be low due to the non-homogeneous angular sensitivity of photoemission setup. Furthermore, it is likely that experimental setup is mainly sensitive to the thermalized electrons, which are affected by higher degree of spin relaxation due to

- Long dwell time in the crystal
- Sensitivity to the additional spin relaxation mechanisms, which occur in BBR and on Cs - O- covered surface.

[6] In the case of $h\nu \approx \epsilon_{g,X}$, the low-energy threshold corresponds to the minimum of the conduction band in the BBR, whereas high-energy threshold is close to the minimum of the conduction band in the bulk material.

None of these reasons can be solely responsible for the very low observed polarization, but their combination can easily describe the decrease in the polarization by at least one order of magnitude compared to the theoretically predicted values [Cheng2011a].

4.3 Excitation near $\epsilon_{g,\Gamma}$ first direct gap ($\Gamma_5^+ \rightarrow \Gamma_4^-$)

The polarization of emitted photoelectrons is studied using excitation energy varying from 2.9 eV to 4.5 eV.

4.3.1 Analysis of features in EDCs

Figure 4.9 represents the derivatives of EDCs acquired at low temperature for excitation energies varying from 2.9 eV to 3.5 eV, with the same parameters of lock-in amplifier. For $h\nu < \epsilon_{g,L}^{\text{direct}}$ only indirect transitions occur. For $h\nu > 3.2$ eV the EDCs reveal a feature located at $\epsilon = 1.15$ eV independently of the excitation energy. The position of this feature is close the position of L valley above the conduction band minimum $\epsilon_{g,L} - \epsilon_{g,X} = 1.08$ eV, and thus can be interpreted as the photoemission of electrons from L valley The observed accumulation of electrons in this valley can be due to several processes (fig. 4.10):

- The excitation from L valley of Γ_5^+ to the L valley of Γ_4^-
- The relaxation of electrons, which were photoexcited with higher energy.

When the excitation energy approaches $\epsilon_{g,L}^{\text{direct}}$, the contribution of direct transitions becomes more important, and the structure becomes more visible. For even higher excitation energies $h\nu > \epsilon_{g,L}^{\text{direct}}$, other transitions take place, and the observed features smear (fig. 4.11).

According to the analysis made of EDCs obtained with the use of continuous-wave radiation, it can be concluded that for the (1 0 0) orientation the position and amplitude of the features on EDCs do not exhibit an apparent temperature dependence (the left panel in fig. 4.12). Furthermore, it can be concluded that a small raise of the electron affinity does not affect the electrons emitted from the L valley (represented by dot-dashed line in the left panel of fig. 4.12). At the same time, for the (1 1 1) sample orientation and $h\nu > \epsilon_{g,\Gamma}$, the features are more diffused at ambient temperature (right EDCs in fig. 4.12).

In fig. 4.13 one can see that the feature corresponding to the indirect transitions to the L valley appears for $h\nu \geq 1.95$ eV. Presumably at high excitation energy, when the electrons are created in the shallow surface layer of the sample, an EDC reflects the distribution of electrons at the moment of their creation, rather than the thermalized distribution.

Structure diagrams

Figure 4.14 presents the variation of the high-energy threshold of the observed features. Three main contributions appear, which HE threshold ϵ_{HE}^f is situated respectively at $\epsilon = 1.2$ eV, $\epsilon = 1.65$ eV and $\epsilon = 2.2$ eV. One can notice that the ϵ_{HE}^f of the feature at $\epsilon = 2.2$ eV depends linearly on the excitation energy, which is likely to be explained by its proximity to the high-energy threshold of the EDCs themselves. The features at $\epsilon = 1.2$ eV and $\epsilon = 2.2$ eV are also visible on the derivatives presented in previous section (fig. 4.9). The high-energy threshold of feature at $\epsilon = 1.65$ eV takes slightly higher values at low temperature.

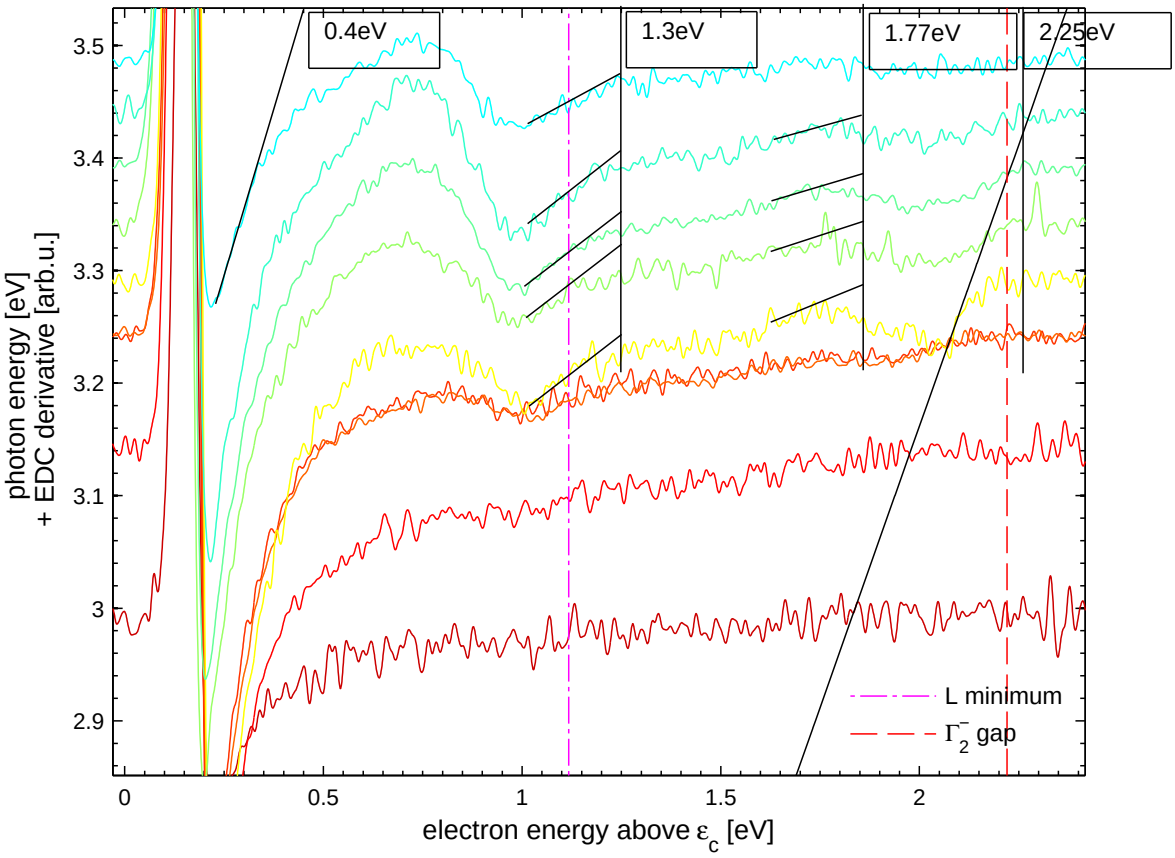


Figure 4.9: First derivative of the EDCs (denoted by $N'(\epsilon)$) for $h\nu \approx \epsilon_{g,\Gamma}$, (1 1 1) (SOI [2 µm]) and 115 K. High energy threshold is represented with black line. Dot-dashed line locates the L valley emission (situated at $\epsilon = 1.12\,\text{eV}$), dashed line locates the emission from the first direct gap (situated at $\epsilon = 2.22\,\text{eV}$).

Shown in the left panel transitions to Γ_2^- band are not clearly visible due to the spectrometer saturation effects produced by pulsed laser. These effects will be discussed in chapter 5.

In general, the position of features is similar for different crystal orientations (figs. 4.14 and 4.15). It is visible both in the derivative spectra (fig. 4.9), and in the EDC itself (fig. 4.13).

The independence of LE threshold energy ϵ_{LE}^f versus the excitation energy $h\nu$ (fig. 4.15) provides an indication that the observed features represent the effect which takes place in the sample itself. In this way, the feature at 1.2 eV is attributed to the electrons photoemitted from L valley, and yields an estimation of

$$\epsilon_{g,L} = 1.2\,\text{eV} + 1.12\,\text{eV} \approx 2.3\,\text{eV} \tag{4.17}$$

in good agreement with $\epsilon_{g,L} = 2.25\,\text{eV}$, calculated with the 30 bands k.p model (table 2.2). In the same manner, the feature at 2.2 eV corresponds to the photoelectrons emitted from the Γ point, with the direct gap estimation of $\epsilon_{g,\Gamma} = 3.3\,\text{eV}$.

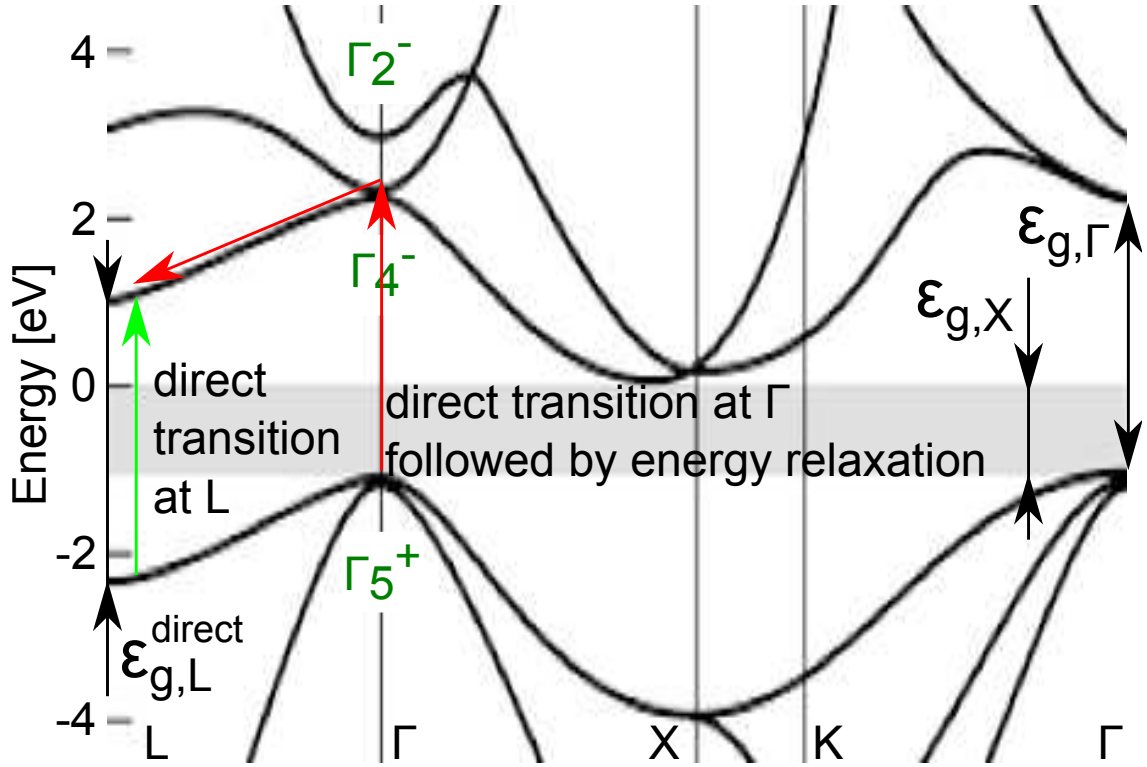


Figure 4.10: Two processes leading to the accumulation of electrons in L valley of Γ_4^- conduction band.

The origin of the feature at 1.65 eV remains unclear. It could be explained by the photoemission from

- An accumulation point away from the high symmetry directions
- Surface states

In fig. 4.16 one can clearly distinguish 3 main features discussed above.

We observe that both LE and HE thresholds of features slightly ascend (by about 0.05 eV for bulk and 0.1 eV for SOI [5 µm]) with decreasing temperature. To the observed in fig. 4.16 value, one should add the shift of the indirect band gap $\epsilon_{g,X}(115\,\mathrm{K}) - \epsilon_{g,X}(300\,\mathrm{K}) = 40\,\mathrm{meV}$, which is already accounted for in the kinetic energy of photoelectrons. The finally obtained values of 0.9 eV measured on bulk Silicon are in good agreement with previous experimental works (table 2.3 of chapter 2). The higher value of 0.14 eV measured on SOI [5 µm] could be explained by the following:

- Temperature-induced strain in SOI [5 µm]
- High incertitude of the results from fig. 4.16, in particular due to the discussed in section 3.4.1 difficulty of calibration of EDCs with $h\nu > \epsilon_{g,\Gamma}$.
- Differences in the temperature variation of different points of the band structure.

Let us recall that the HE threshold of a feature corresponds to the accumulation energy in the bulk material, whereas LE threshold represents its position after relaxation in the BBR. Therefore, the width of features corresponds to the energy of the band bending region. The width of all the observed features is near 0.3 eV in agreement with the band bending energy

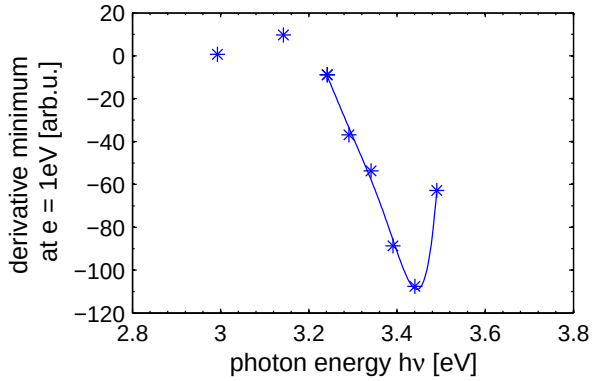


Figure 4.11: The amplitude of the first derivative minimum ($N'(1\,\mathrm{eV})$) from fig. 4.9 for different excitation energies. The minimum of the derivative allows to estimate $3.2\,\mathrm{eV} \lesssim \epsilon_{g,L}^{\mathrm{direct}} \lesssim 3.44\,\mathrm{eV}$.

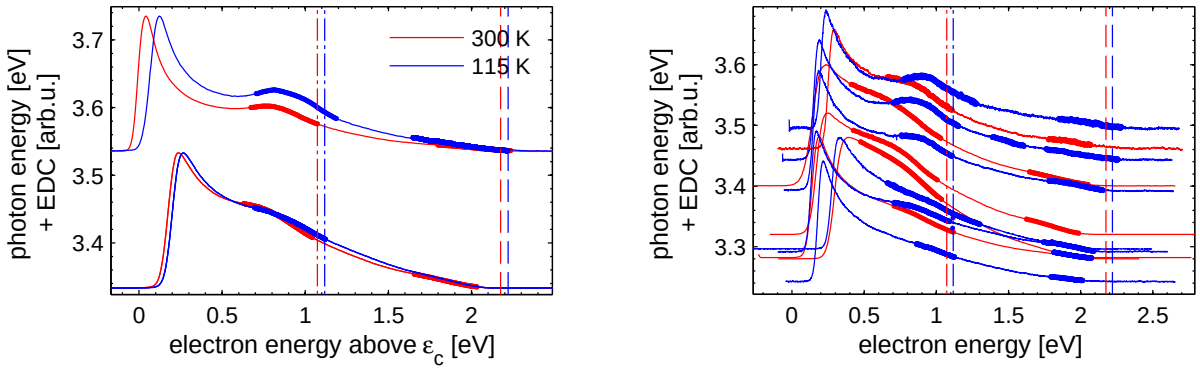


Figure 4.12: Temperature dependence of features: (1 0 0)-oriented bulk Si (left) and (1 1 1)-oriented SOI [2 µm] (right). Multiples EDCs are shown in order to illustrate the uncertainty in the feature thresholds. Features are represented with bold lines. Dot-dashed lines locate the L valley emission (1.07 eV and 1.12 eV at room and low temperatures respectively), dashed lines locate the emission from the first direct gap (2.175 eV and 2.2 eV).

of p-type Silicon at moderate doping levels.

4.3.2 Electron momentum relaxation in Cs surface layer

In order to interpret the spectroscopy results obtained on a sample, covered with Cs - O surface layer, it is important to estimate the degree of momentum relaxation which it induces.

Gobeli, Allen, and Kane demonstrate that the cesiated surface causes complete relaxation of wave vector direction. The experiment consist in illuminating Si (1 1 1) and (1 1 0) surfaces with linearly polarized light and measuring the ratio of directional photoemitted currents in two perpendicular crystal directions.

The excitation is of 5.8 eV, whereas the photo-threshold for clean Si is about 5.1 eV. The

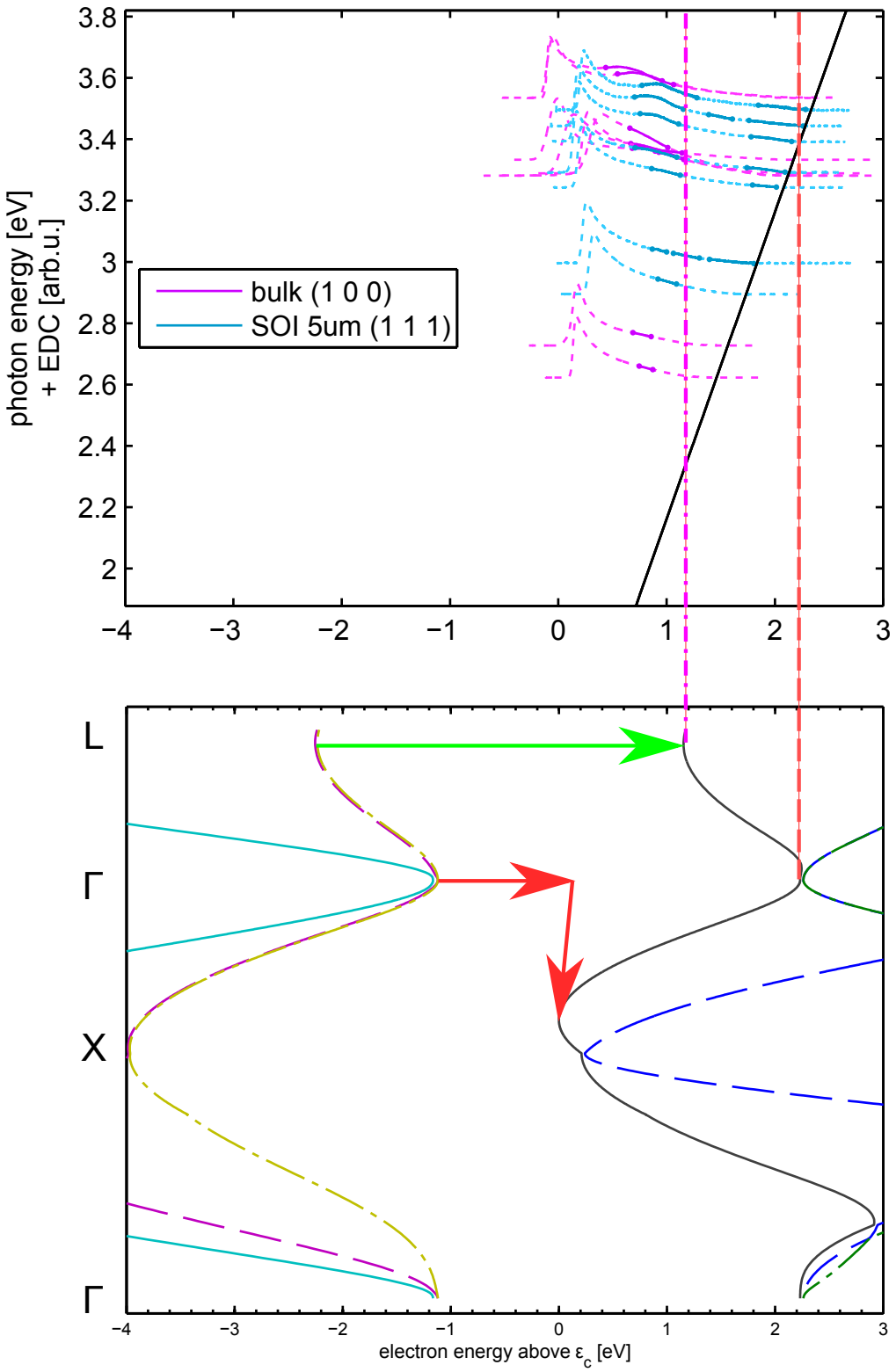


Figure 4.13: Comparison of features at 115 K for different samples). The structures are found for excitation energies $h\nu = 1.95 - 3.53\,\mathrm{eV}$. The indirect (i.e. phonon-assisted) transition to the minimum of the conduction band and a direct transition to L valley are shown. Black line on the top panel represents the high-energy threshold dependence on excitation energy $\epsilon_{\mathrm{HE}} = h\nu - \epsilon_{g,X}$

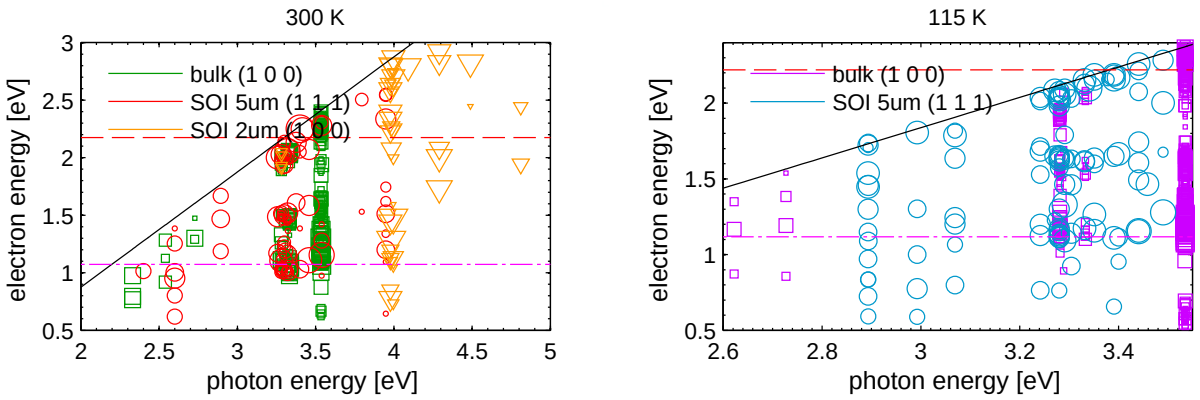


Figure 4.14: High-energy threshold (HE) of the features detected in EDCs. The size of each marker is proportional to the amplitude of the detected feature.

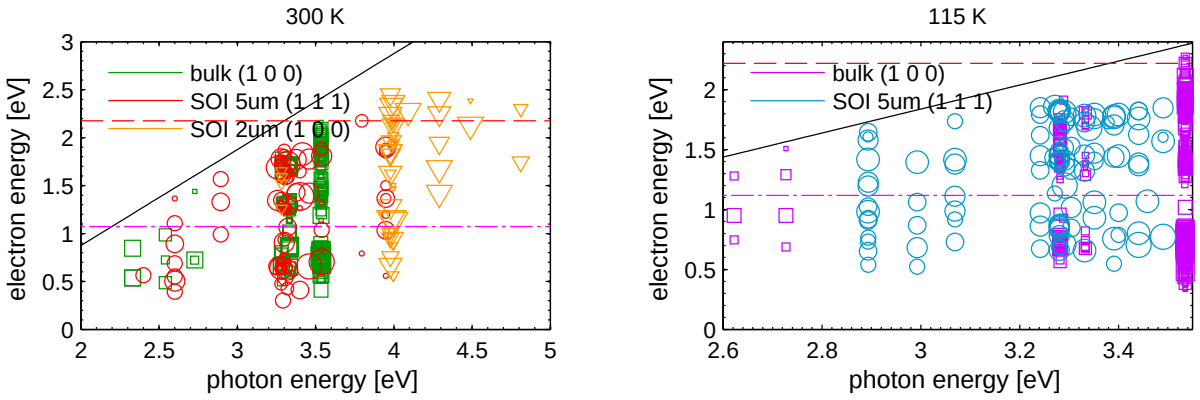


Figure 4.15: Low-energy threshold of the features detected in EDCs. The size of each marker is proportional to the amplitude of the detected feature.

photo-threshold for cesiated Silicon is not mentioned, but is probably lower than for clean sample. The measured directional photocurrent is averaged in this energy window, which implies that the momentum relaxation takes place for all the considered energies. Indeed, if for some electron energy the momentum were not relaxed, the corresponding light polarization would vary with the direction of incident light, contributing to some variation of scattered light polarization, which was not observed.

The fact that the experiment in [Gobeli1964] is performed using quite high excitation energy in principle does not influence the conclusion, as corresponding absorption depth is still much larger than the thickness of the Cs surface layer.

In context of our study, this result implies that the structures measured for samples with surfaces oriented normal to the different crystallographic directions, should be similar. On the other hand, the Oxygen deposition, which was not considered by Gobeli, Allen, and Kane, may a priori add supplementary momentum relaxation.

For each surface orientation, the surface structure of Cs - O layer may be different, which may in particular result in different intensity of k relaxation.

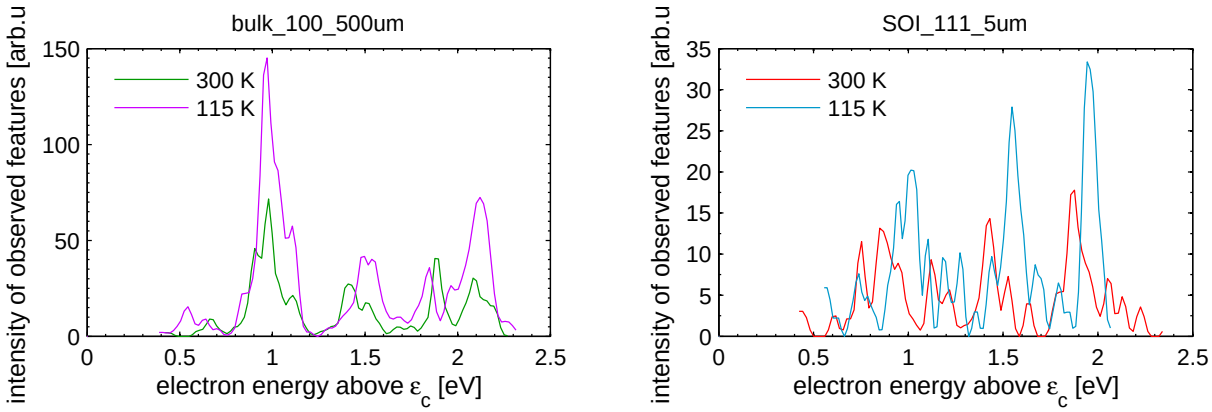


Figure 4.16: Histograms of feature $(\epsilon^f_{HE} + \epsilon^f_{LE})/2$ from figs. 4.14 and 4.15

The fact that L feature is observed on (1 0 0) implies that there is an important momentum relaxation at least for (1 0 0) surface, in agreement with the result of Gobeli, Allen, and Kane.

The observation of this feature on (1 1 1) provides no evidence on the momentum relaxation intensity for this type of surface. In fact (1 1 1) corresponds to $\Gamma - L$ direction in the BZ, and therefore a significant number of electrons from L minimum are emitted from a (1 1 1) photocathode independently on the surface momentum relaxation rate.

4.3.3 Difference between the contributions of the direct and indirect optical transitions

Normally the intensity of direct transition should be more important compared to indirect ones. However, because of the continuity of joint density of states as the function of excitation energy, and the insignificance of the contribution of electrons with energies $\epsilon \approx \epsilon_{\mathrm{HE}}$ in the EDC, there appears no noticeable difference in the EDCs at $h\nu \approx \epsilon_{g,\Gamma}$ depending on the sign $h\nu - \epsilon_{g,\Gamma}$. The absence of influence of direct transitions on the high-energy threshold was shown in section 3.4.1.

One should note that if the sample thickness satisfies $d \gg \alpha^{-1}$, the total number of photo-electrons created in the sample volume is essentially the same as for direct transitions, independently of the magnitude of α. In particular, at least for bulk material, the photocurrent is essentially the same in the regimes of direct and indirect transitions.

4.3.4 PEDCs

The characteristic regimes observed on PEDC were discussed in details in section 3.5.1. Let us recall that if the value of excitation energy is situated in the vicinity of a direct gap, the ballistic electrons are generated in the point of Brillouin zone where the gap is located, Γ in the case of $\Gamma_5^+ \to \Gamma_4^-$ transition in Silicon.

The right panel of fig. 4.17 shows that the positive part of the PEDCs with excitation energy $h\nu < 3.325\,\mathrm{eV}$ have negative curvature (i.e. $P''(\epsilon) > 0$), while starting from $h\nu = 3.325\,\mathrm{eV}$ the increasing part of the PEDCs becomes linear (i.e. $P''(\epsilon) \approx 0$).

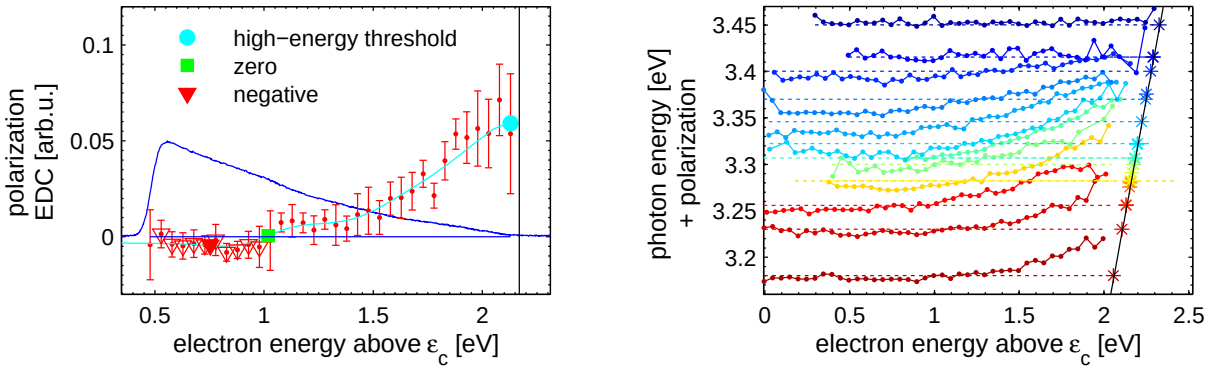


Figure 4.17: Typical EDC (blue curve) and PEDC (red errorbars) under UV excitation (SOI [5 µm], $h\nu = 3.33\,\mathrm{eV}$, $T = 114\,\mathrm{K}$) (left). PEDCs with $h\nu \approx \epsilon_{g,\Gamma}$ (right).

4.3.5 Polarization of ballistic electrons

The maximum polarization, observed at $h\nu = 3.3\,\mathrm{eV}$ at room temperature, and $h\nu = 3.32\,\mathrm{eV}$ at 115 K indicates that the direct gap is situated in the proximity of this energy, in excellent agreement with previous experimental results (table 2.3). The increase of gap with decreasing temperature[7]

$$\epsilon_{g,\Gamma}(115\,\mathrm{K}) - \epsilon_{g,\Gamma}(300\,\mathrm{K}) = 3.32\,\mathrm{eV} - 3.3\,\mathrm{eV} = +20\,\mathrm{meV} \tag{4.18}$$

is slightly lower than +50 meV observed by [Jellison1983], but the both values have the same sign in agreement with theoretical predictions.

As can be seen from the fig. 4.18, the polarization gradually decreases for the excitation energies $h\nu$ away from the $\epsilon_{g,\Gamma}$. One should note that both for bulk and SOI samples a slightly higher polarization is measured at low temperature, which is explained by longer low-temperature spin relaxation time T_1 in eq. (2.14).

In fig. 4.18 one observes, that the $P_{HE}(\epsilon_{g,\Gamma})$ takes lower values on SOI samples compared to bulk. The interpretation of this fact remains unclear, but it may be at least partially explained by the error in the calibration of the Sherman function for different potentials V_{foil} and V_b. In fact, considering the precision on the Sherman function, the absolute values on the polarization axis are subject to the error of 1/10 of its value (i.e. ±1 % in the case of $P = 10\,\%$), which affects all the data points acquired at the same (V_{foil}, V_b) simultaneously. In occurrence, the settings of (V_{foil}, V_b) used for measurements of bulk Si differ from those used for SOI [5 µm] and SOI [2 µm].

The observed effect is opposite to the increase in polarization, which would be expected if the SOI samples would possess a significant build-in strain, and therefore is probably unrelated to the latter.

It should be noted, that if the process of photoemission is mediated by an excitonic state, the exciton energy should be added to the estimated gap value. However, the relatively high doping level ($\gg 10^{16}\,\mathrm{cm}^{-3}$) of the considered samples leads to insignificance of exciton con-

[7]The value of the direct band gap is estimated as the excitation energy at which the maximum of interpolated polarization curve (solid line at fig. 4.19) is attained.

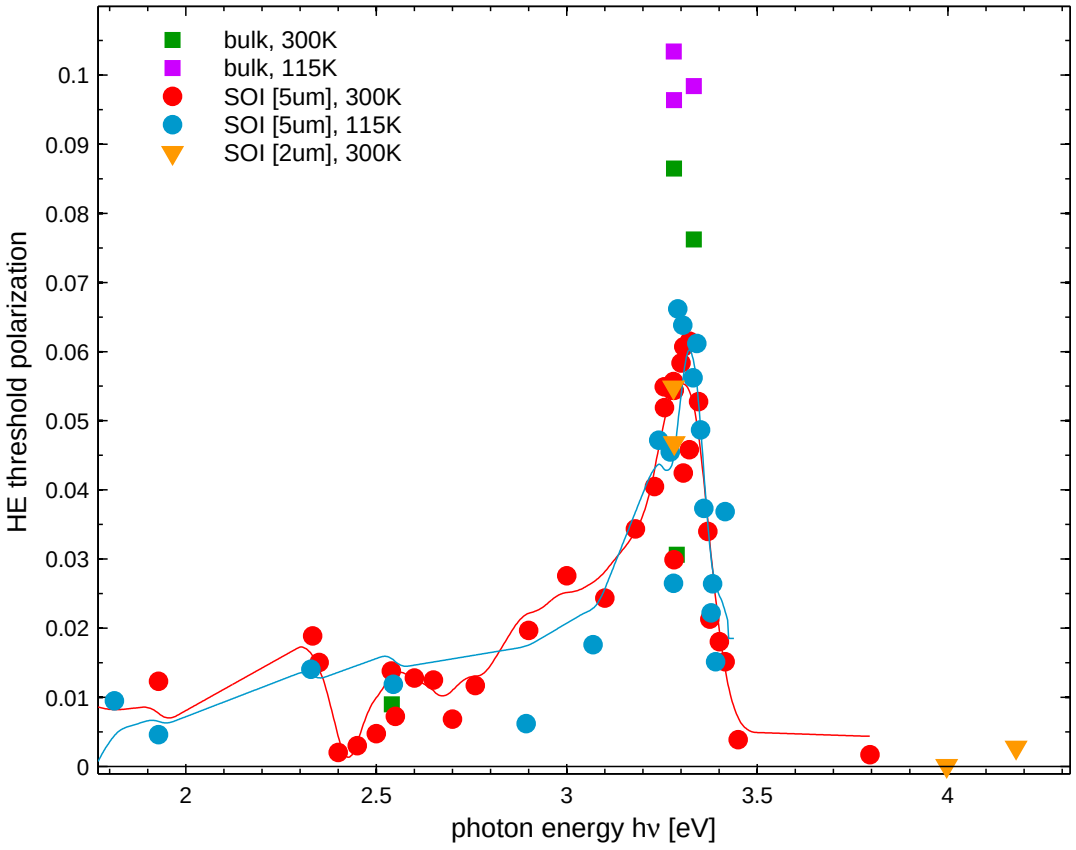


Figure 4.18: Polarization at the EDC's high-energy threshold versus photon energy in visible and near UV range. The solid lines are the running average interpolations, which account for the relative error of each measurement.

tribution. At the same time, the employed doping level is not high enough for the excitation to take place from the acceptor level in the band gap.

Let us consider the regime of indirect transition: $\epsilon < \epsilon_{g,\Gamma}$. Then ϵ approaches $\epsilon_{g,\Gamma}$, the contribution of the direct transition near the zone center becomes more important. The polarization at the high-energy threshold is the most sensitive quantity (compared to integral parameters such as magnetization or susceptibility) to the proximity of conduction bands. According to the symmetry of crystal wave functions at the zone center (detailed further in section 6.3) the corresponding polarization at direct transition onset is of $+1/6$. So the increasing part of $P_{HE}(h\nu)$ can be attributed to indirect optical transitions.

As shown by the k.p OP model [Nastos2007] (which will be further discussed in section 6.4.2), the polarization reaches its maximum in the vicinity of direct gap, in agreement with natural expectation based on symmetry considerations.

Once $\epsilon > \epsilon_{g,\Gamma}$ (regime of direct transitions), the transitions with k_{final} away from zone center start contributing to the polarization. If the corresponding contribution to the polar-

ization is lower than the polarization of Γ, the resulting $P(\epsilon_{\mathrm{HE}})$ decreases, like it is observed experimentally in fig. 4.18.

Assuming that the observed maximum of P_{HE} corresponds to the interval $[\epsilon_{g,\Gamma}, \epsilon_{g,\Gamma}+\Delta^c_{\mathrm{SO}}]$, we can estimate $\Delta^c_{\mathrm{SO}} = 40\,\mathrm{meV} \pm 10\,\mathrm{meV}$ slightly higher than the generally accepted calculation of $\Delta^c_{\mathrm{SO}} = 30\,\mathrm{meV}$ [Wepfer1971]. The decrease in the polarization at low temperature within $50\,\mathrm{meV} \pm 20\,\mathrm{meV}$ (fig. 4.19) provides an estimation to the spin-orbit splitting Δ_{SO} in agreement with previously measured value of $\Delta_{\mathrm{SO}} = 44\,\mathrm{meV}$ [Nishino1974]. However, a detailed modeling of $P_{HE}(h\nu)$ behavior is required in order to validate this estimation. .

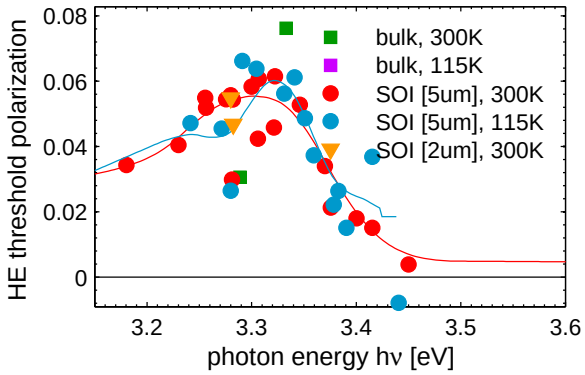


Figure 4.19: Polarization at the EDC's high-energy threshold in the vicinity of the first direct band gap. The solid lines are the running average interpolations, which account for the relative error of each measurement.

4.3.6 Negative contribution to the HE threshold polarization

According to the analytical model, the contributions from direct transitions $\Gamma_8^+ \to \Gamma_6^-$ and $\Gamma_8^+ \to \Gamma_8^-$, which have different sign, are separated by only $\Delta^c_{\mathrm{SO}} \approx 30\,\mathrm{meV}$. Let us recall the eq. (2.8):

$$\begin{cases} P_i(\Gamma_8^+ \to \Gamma_6^-) = \dfrac{1(-\frac{\hbar}{6}) + 3(\frac{\hbar}{6})}{(\hbar/2)(1+3)} = \dfrac{1}{6} & \text{(4.19a)} \\ P_i(\Gamma_8^+ \to \Gamma_8^-) = \dfrac{2(-\frac{3\hbar}{6}) + 2(\frac{\hbar}{6})}{(\hbar/2)(2+2)} = -\dfrac{1}{3} & \text{(4.19b)} \\ P_i(\Gamma_7^+ \to \Gamma_8^-) = \dfrac{1(-\frac{3\hbar}{6}) + 3(-\frac{\hbar}{6})}{(\hbar/2)(1+3)} = -\dfrac{1}{2} & \text{(4.19c)} \end{cases}$$

If the HE threshold of a PEDC with $h\nu \gtrsim \epsilon_{g,\Gamma}$ would correspond only to ballistic electrons, photoexcited via direct transitions, the negative polarization corresponding to eqs. (4.19b) and (4.19c) should be measured.

In a real experiment, in order to minimize the mixing of electrons with negative and positive polarization in the PEDC, the attempt to measure electrons with negative polarization was performed on fine spectrometer resolution (30 meV), which has been chosen as

balance between sensitivity to the different transitions in eq. (4.19) and sufficient signal level to attain a reasonable statistical convergence. Some of the measurements revealed the expected negative polarization (fig. 4.20), but the reproducibility of the results remained poor. The inability to clearly measure negative polarization at HE threshold can be explained by following:

- Lack of statistical convergence of PEDC measurements
- Low joint density of states associated with the transitions $\Gamma_8^+ \to \Gamma_6^-$ and $\Gamma_8^+ \to \Gamma_8^-$
- Limitation of analytical model that does not take into account the smearing of PEDC due to
  - Optical transitions in the neighborhood of Γ. Given the form of Γ_6^- band at Γ (represented in fig. 2.6 of section 2.2.2), both the indirect and direct transitions can result in the smearing of PEDC.
  - Insufficient resolution of the electron spectrometer. In order to correctly resolve the transitions $\Gamma_8^+ \to \Gamma_6^-$ and $\Gamma_8^+ \to \Gamma_8^-$, the spectrometer resolution and the distance between adjacent points on the PEDC should be significantly lower than Δ_{SO}^c, which is not easily achievable taking into account the statistical requirements.

    In particular, such smearing may explain the observed in the left panel of fig. 4.20 negative polarization for $h\nu = 3.28\,\mathrm{eV} < \epsilon_{g,\Gamma} + \epsilon_{\mathrm{ph}}$.
- Inaccuracy in determining the wavelength
  - Insufficient precision of optical spectrometer
  - Fluctuations in the wavelength of laser radiation during the measurements

    Both of the factors above result in errors of about 1 nm, which is close to 0.01 eV at $h\nu \approx 3.3\,\mathrm{eV}$.

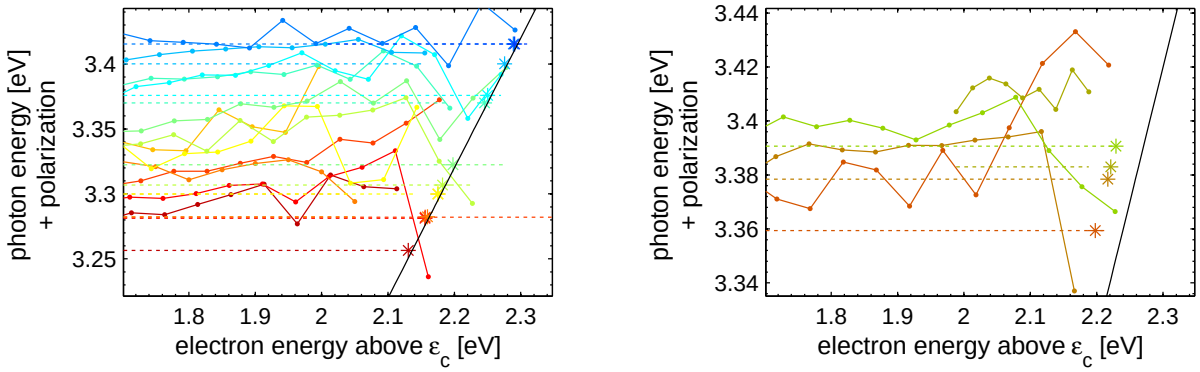


Figure 4.20: PEDC measurements where the negative contribution on HE threshold was observed for 300 K (left) and 115 K (right). Measurements on all the three samples are shown.

4.3.7 Average polarization of hot electrons

For the PEDC obtained using the excitation energy close to $\epsilon_{g,\Gamma}$, a characteristic feature is the negative polarization of the electrons in the low-energy part of the spectrum (fig. 4.17). Note that the high positive polarization of the most energetic electrons can only decrease in absolute value with energy relaxation. Thus, the observed negative polarization can only be explained by optical transitions leading to the excitation of conduction electrons with negative polarization.

For each excitation energy where a negative polarization is observed, the electron kinetic energy corresponding to a change of sign of the polarization can be estimated (marked with square at $\epsilon = 1\,\mathrm{eV}$ in the left panel of fig. 4.17). It gives a lower estimate of the maximum kinetic energy of the negatively spin-polarized photoelectrons. In fact, on the onset of optical transitions with negative polarization their contribution is low, and the overall polarization is obtained from eq. (3.58) with the number of electrons of each spin being defined by

$$N^i(\epsilon) = N^i_{\mathrm{created}}(\epsilon) + N^i_{\mathrm{relaxated}}(\epsilon) \tag{4.20}$$

When reducing the energy of the electrons, the optical transitions with negative polarization gain more weight.

Figure 4.21 represents the energy of such the sign change as a function of $h\nu$.

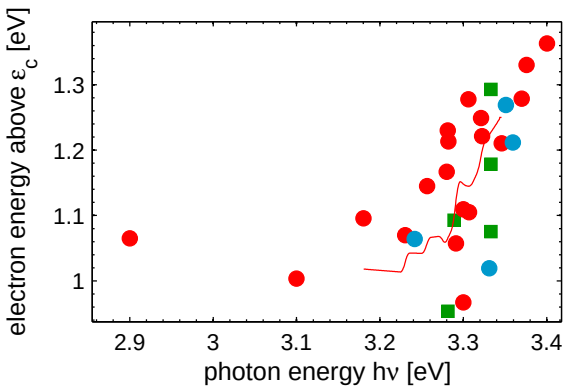


Figure 4.21: Energy, corresponding to a change of sign on PEDC. Electron kinetic energy values giving change in sing of the polarization in PEDCs. The solid line is the running average interpolation, which accounts for the relative error of each measurement.

In fig. 4.22 and fig. 4.23 the average polarization of electrons with kinetic energy in the range $0.5 - 1\,\mathrm{eV}$ is given. For instance for PEDC shown in fig. 4.17, the values on which the average was calculated are highlighted with triangles.

In order to interpret the origin of negative polarization of low-energy electrons, it is important to consider the angular sensitivity of the experimental setup, which is composed of the angular sensitivity of the spectrometer itself and the intensity of the momentum relaxation at the Cs - O- covered surface. According to previously cited works of [Gobeli1964] and the similarity of structures on EDC measured for different crystallographic directions (section 4.3.2), we can conclude to a significant momentum relaxation at the surface.

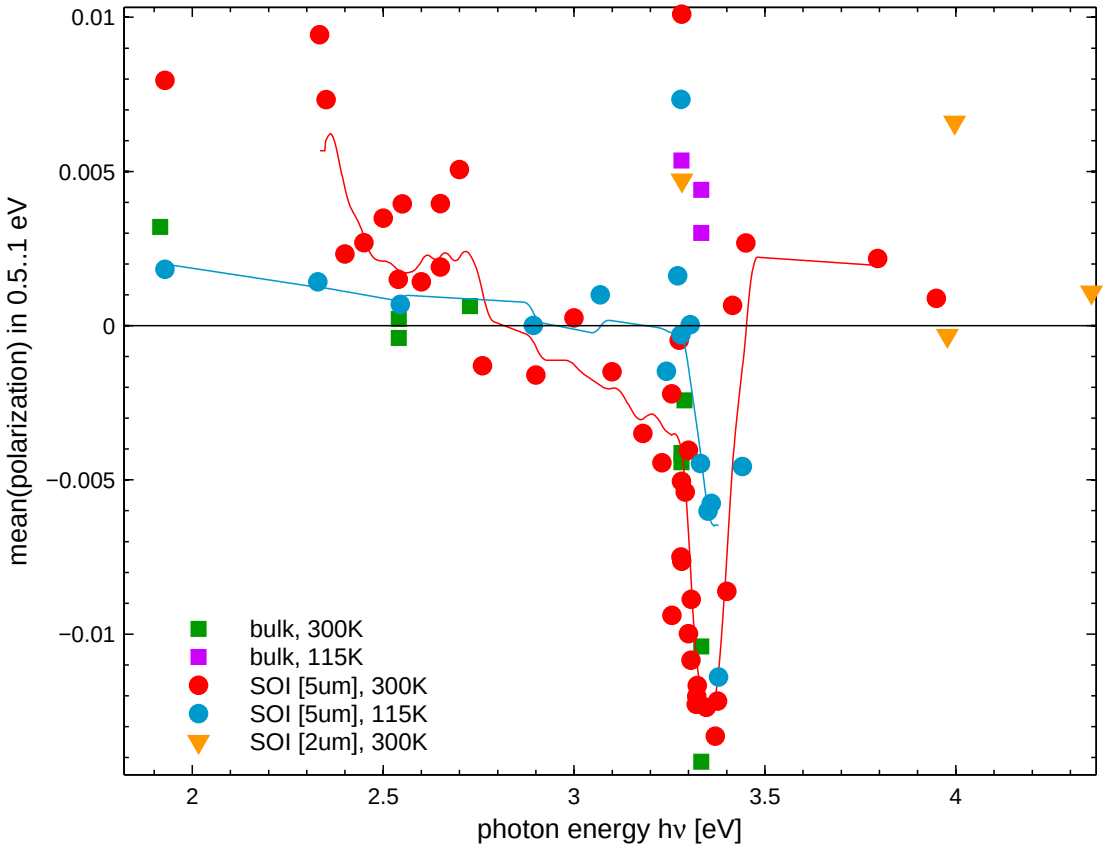


Figure 4.22: Mean polarization of hot electrons in the electron kinetic energy range $0.5 - 1\,\text{eV}$. The solid lines are the running average interpolations, which account for the relative error of each measurement. The bulk sample measurements are performed with Kr+ laser, whereas SOI samples are measured with Ti:Sapphire laser except some measurements at $h\nu = 3.282\,\text{eV}$, which are performed with UV diode laser.

Thus, the minimum polarization of the hot electrons gives an estimation of the mean value of direct gap in the part of the Brillouin zone where Γ_5^+ and Γ_4^- bands are parallel, in particular in the direction $[\Gamma, L]$. The reasoning is similar: while the transitions remain indirect, the absolute value of polarization increases, and then it vanishes because of interference of more and more different states. Following facts confirm that the negative polarization mainly corresponds to optical transitions in L valley

- One can note that the minimum of the negative polarization with respect to electron kinetic energy is attained at $\epsilon \in [0.8\,\text{eV}, 0.9\,\text{eV}]$, which corresponds to the L feature in EDCs.
- In the right panel of fig. 4.17 one can notice a slight decrease in the negative polarization of the electrons photoemitted with $\epsilon < 0.5\,\text{eV}$. Such the observation can be interpreted as the relaxation of polarization of electrons created in L valley and scattered to lower energies prior to their emission into vacuum.

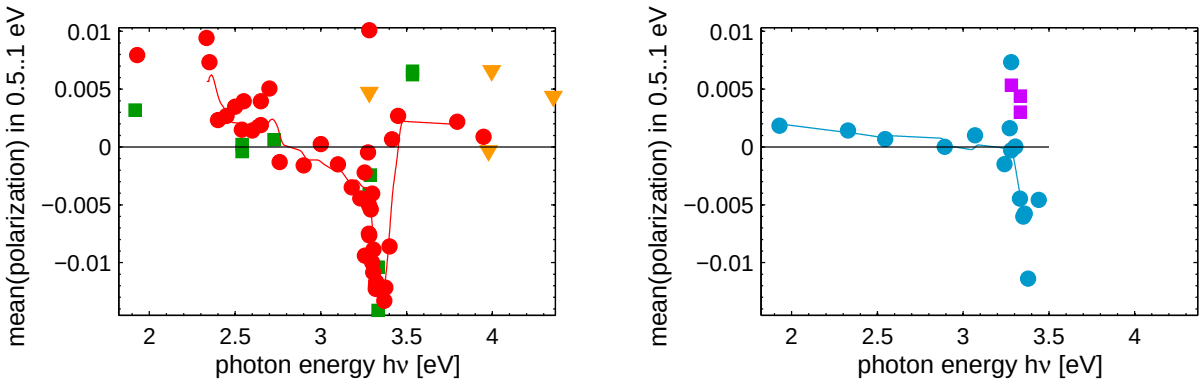


Figure 4.23: The sets of data points from fig. 4.22 plotted separately for ambient (left panel) and low (right panel) temperatures.

- The negative polarization appears starting from $h\nu \in [2.5\,\mathrm{eV}, 3\,\mathrm{eV}]$, at the same excitation energies as the L feature.

The comparison with theoretical calculations, which will be given in section 6.4.2, allows to extend the list of these arguments.

The minimum of polarization is achieved for the excitation energy $h\nu = 3.35\,\mathrm{eV}$ at 300 K, which provides an estimation of direct band gap $\epsilon_{g,L}^{\mathrm{direct}}$ in reasonable agreement with the value from table 2.2. The observed difference in the direct band gap $\epsilon_{g,L}^{\mathrm{direct}}$ between room and low temperature is about 40 meV, which is slightly lower than the comparison of experiments from table 2.2. In fact, supposing linear dependence, we obtain

$$\begin{aligned}(\epsilon_{g,L}^{\mathrm{direct}}(5\,\mathrm{K}, [\mathrm{Zucca1970}]) - \epsilon_{g,L}^{\mathrm{direct}}(300\,\mathrm{K}, [\mathrm{Grover1974}]))\frac{115\,\mathrm{K} - 300\,\mathrm{K}}{5\,\mathrm{K} - 300\,\mathrm{K}} = \\ = (3.45\,\mathrm{eV} - 3.36\,\mathrm{eV})\frac{115\,\mathrm{K} - 300\,\mathrm{K}}{5\,\mathrm{K} - 300\,\mathrm{K}} = 55\,\mathrm{meV}\end{aligned} \tag{4.21}$$

The use of Varshni dependence instead of linear interpolation would result in slightly higher variation of the band gap. Such underestimation of temperature variation of both $\epsilon_{g,\Gamma}$ and $\epsilon_{g,L}^{\mathrm{direct}}$ band gaps may be at least partially explained by higher temperature of the sample compared to 115 K measured by the thermoresistance (the latter effect was described in section 3.3.1).

Following the similar estimation at Γ, the decrease of the absolute value of polarization shown in fig. 4.22 between $h\nu = 3.37\,\mathrm{eV}$ and $h\nu = 3.47\,\mathrm{eV}$ allows to estimate

$$\Delta_{\mathrm{SO}L} + \Delta_{\mathrm{SO}L}^{c} = 0.1\,\mathrm{eV} \tag{4.22}$$

For room temperature, negative polarization is observed in the range $2.85 - 3.46\,\mathrm{eV}$. In this interval, it is interesting to consider the energy where the polarization sign changes (fig. 4.21). In fact, the choice of 1 eV as the upper limit for fig. 4.22 can be justified by the fact that for $h\nu < \epsilon_{g,\Gamma}$ the sign change occurs at a constant energy close to 1 eV.

4.3.8 EDC-averaged polarization - comparison with [Bona1985]

Bona and Meier measured the EDC-averaged polarization at room temperature for two different affinities using a synchrotron radiation source (fig. 4.24). Although it is not specified in the article, their measurements are apparently performed under σ^- light. In fig. 4.26 the polarization measured by Bona and Meier is multiplied by -1 in order to keep consistency with our measurements, represented for σ^+ excitation.

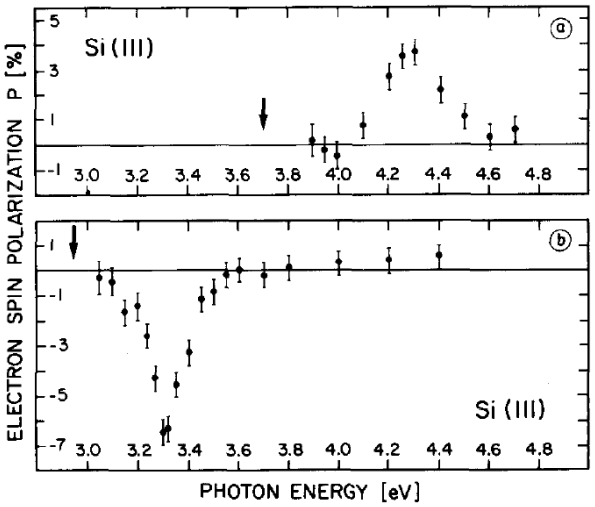


Figure 4.24: Energy- and angle-integrated spin polarization. The arrows indicate the photothresholds from which the polarization was energy-integrated [Bona1985].

It should be noted that the EDC-averaged polarization strongly depends on the electron affinity. So, if thermalized electrons have a negative polarization, the measurement with high electron affinity leads to an overestimation of the average polarization (fig. 4.25). Thus, fig. 4.26 shows EDC-averaged polarization, plotted for all the measurements with electron affinity lower than 0.6 eV. The above energy is a compromise between the exclusion of measurements with too high affinity and preservation of a representative number of points on the graph.

Once again, for low temperature the onset of negative $\langle P \rangle$ happens for energies of about 80 meV higher.

Figure 4.27 represents the EDC-averaged polarization in the interval of $0.5 - 1$ eV above the minimum of conduction band. The difference with fig. 4.22 resides in the fact that the L structure on EDC provides a supplementary contribution to the EDC-averaged polarization. In other words, fig. 4.27 represents the average polarization of electrons in L valley.

It is interesting to note that the minimum of the negative EDC-averaged polarization in L valley (which coincides with the minimum of corresponding contribution to the magnetization), observed around 3.4 eV at 115 K, corresponds to the highest intensity of direct transitions to this valley, detected on the derivatives of EDCs (fig. 4.9).

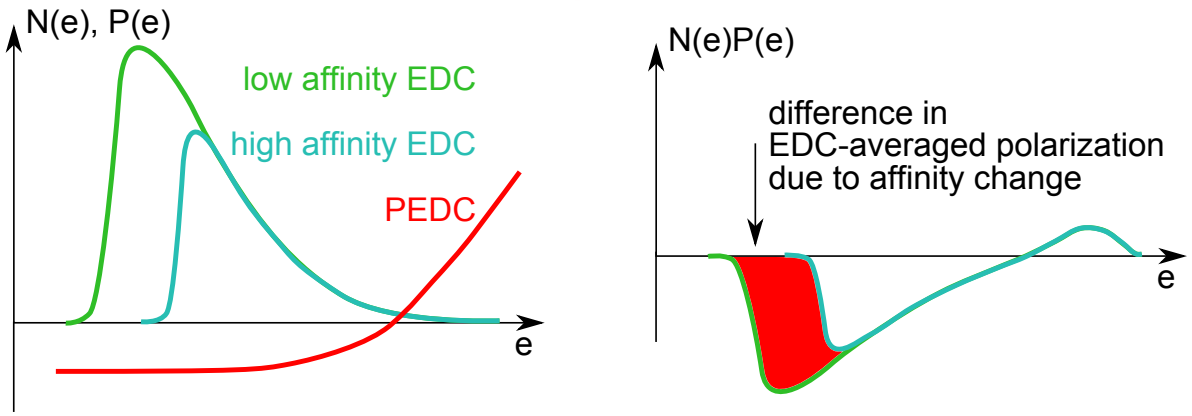


Figure 4.25: Dependence of the EDC-averaged polarization $\langle P \rangle$ on the electron affinity. The solid lines are the running average interpolations, which account for the relative error of each measurement.

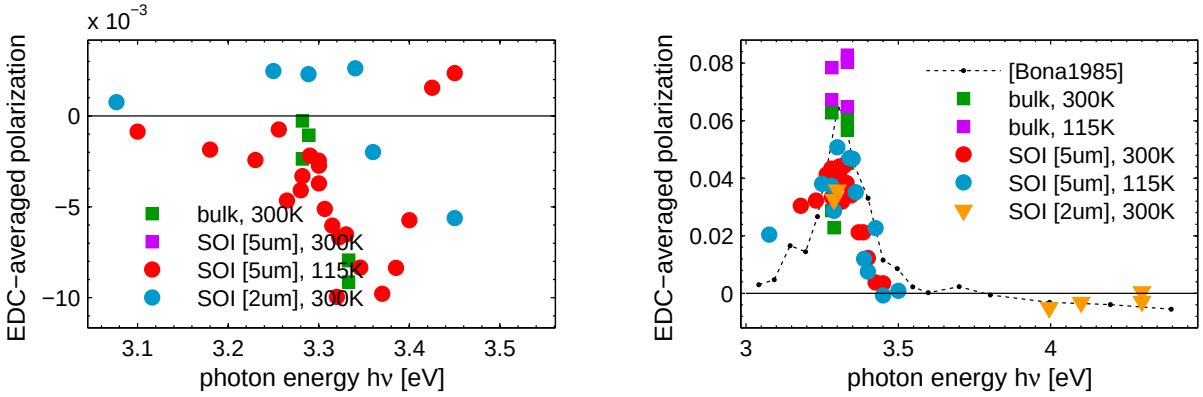


Figure 4.26: EDC-averaged polarization $\langle P \rangle(h\nu)$, integrated from: onset of absorption (left), from $\epsilon = 1.82\,\mathrm{eV}$ (right)

4.4 Excitation near $\epsilon^2_{g,\Gamma}$ second direct gap ($\Gamma^+_5 \to \Gamma^-_2$)

PEDCs measured with THG are characterized by a high noise level, which is at least partially explained by insufficient convergence on the number of counts. In fact, the use of third harmonic generation is only possible in pulsed regime, and pulsed light at these high photon energies causes rapid degradation of photocathodes. For the whole set of measurements with $h\nu > 4\,\mathrm{eV}$ the absolute value of observed polarization does not exceed 0.01.

4.4.1 Polarization of ballistic electrons

As can be seen in fig. 4.29, $h\nu$-averaged polarization of ballistic electrons in this range is about -0.01. Note that the negative sign of the polarization coincides with the result obtained by Bona and Meier for electrons with $\epsilon > 2.56\,\mathrm{eV}$.

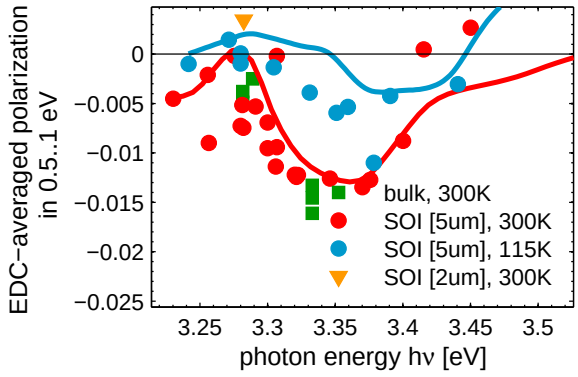


Figure 4.27: EDC-averaged polarization, energy-integrated in the limits where L feature on EDCs is observed.

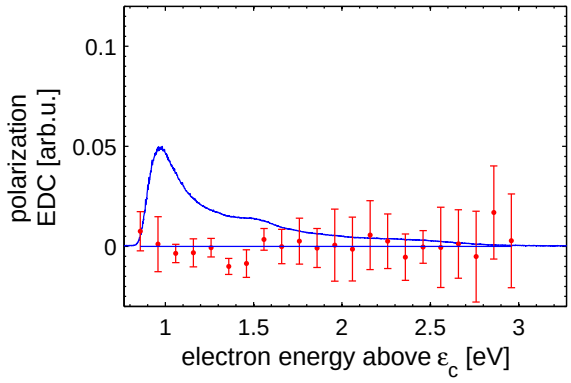


Figure 4.28: Typical EDC and PEDC acquired with THG (SOI [2 µm], $h\nu = 4.29\,\mathrm{eV}$, $T = 309\,\mathrm{K}$)

4.4.2 EDC-averaged polarization

In [Busch1972] it is indicated that the quantum yield of the surface layer of Cesium under ultra-violet irradiation is comparable with metallic substrate quantum yield (in occurrence Busch et al. used Cobalt substrate). Even if the photoemission quantum yield of a semiconductor is significantly higher than that of metals, taking into account the dependence of the absorption length in Silicon (fig. 3.16) one can suppose that $h\nu > 4\,\mathrm{eV}$ a substantial proportion of absorption may as well occur in the surface layer. Compared with [Bona1985], in the present work the surface layer is usually composed not only of Cesium, but also of Oxygen. In order to eliminate the possible effect due to the presence of Oxygen on the surface of the sample, a polarization measurement was performed after annealing and subsequent work function reduction by Cesium only, i.e. under conditions similar to those of [Bona1985]. It was shown that such modification of experimental protocol does not result in polarization enhancement.

The results shown in fig. 4.30 were obtained, similarly to the work of Bona and Meier, on

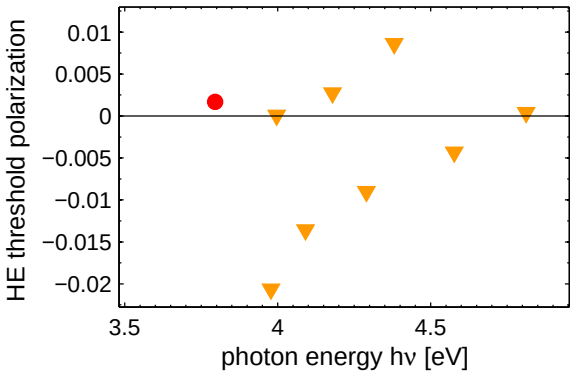


Figure 4.29: Polarization at high-energy threshold in far UV. A large ±0.15% scatter is explained by the incertitude at the HE threshold of PEDCs.

(1 1 1)-oriented sample.

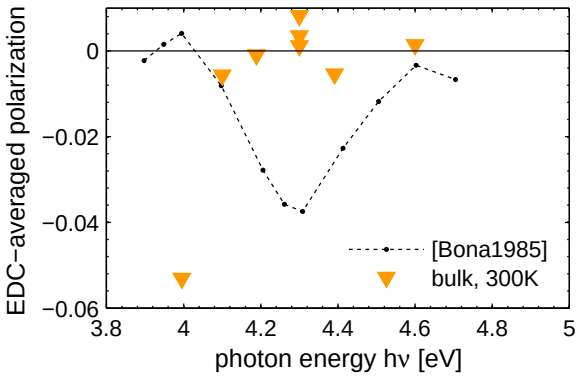


Figure 4.30: EDC-averaged polarization integrated from $\epsilon = 2.56\,\mathrm{eV}$

4.4.3 Polarization of Cs surface layer

While analyzing the polarization measured with $h\nu > 3.5\,\mathrm{eV}$, some attention must be paid to the Cs - O layer as a potential source of spurious highly polarized photoelectrons (fig. 4.31). In fact, the absorption depth of Silicon for such high excitation energy is very shallow and may constitute down to 4 nm at 4.5 eV (fig. 3.16). However, the electronic structure of Cesium monolayer, in addition covered with the monolayer of electronegative O_2 molecules, may be significantly different from the electronic structure of individual atoms in gaseous phase, which could explain the inability to measure the high polarization represented in fig. 4.31 in our experiment.

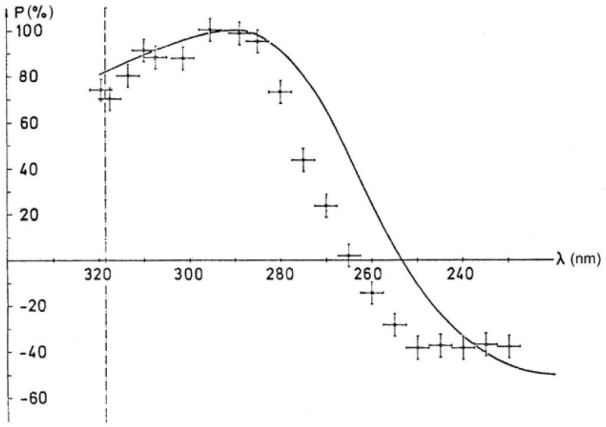


Figure 4.31: Spin polarization of electrons, photoemitted from gaseous Cesium under σ^+ circularly polarized light [Heinzmann2012]

4.5 Conclusion

The main conclusion of the chapter is that decreasing the thickness of Silicon sample down to 2 µm does not result in significant polarization enhancement with excitation near the indirect band gap. The main reasons are the non-homogeneous angular sensitivity of the photoemission setup, the low number of ballistic electron under near-indirect gap excitation, and the spin relaxation in surface layer. In particular, this result holds for

$$h\nu \in [\epsilon_{g,X}, \epsilon_{g,X} + \Delta_{\mathrm{SO}}] \tag{4.23}$$

which is likely to be explained by mixing of contribution of the different phonon modes, since the energy of dominant phonon mode (TO) ${\epsilon_{\mathrm{ph}}}^{\mathrm{TO}} \approx \Delta_{\mathrm{SO}}$.

We have seen that the direct optical transitions to the L valley of Γ_4^- conduction band have both spectroscopic (feature on EDCs) and polarimetric (negative polarization of PEDCs) signatures. In agreement with the theoretical model [Nastos2007], which will be detailed in chapter 6, this negative polarization rapidly vanishes as the excitation energy exceeds the direct band gap $\epsilon_{g,L}^{\mathrm{direct}} + \Delta_{\mathrm{SO}} + \Delta_{\mathrm{SO}}^{c}$.

Compared to the estimations of band gaps deduced from the position of features observed on EDCs, the use of excitation energy scale allows to reduce the incertitude due to the determination of EDCs position on the electron kinetic energy scale, and thus results in more reliable band gap estimations. The peak of the high-energy polarization spectrum in vicinity of first direct gap allows to assess $\epsilon_{g,\Gamma}(300\,\mathrm{K}) = 3.3\,\mathrm{eV}$, whereas the analysis of negative polarization of hot electrons provides $\epsilon_{g,L}^{\mathrm{direct}} \approx 3.35\,\mathrm{eV}$, which is in agreement with the k.p model ($\epsilon_{g,L}^{\mathrm{direct}} - \epsilon_{g,\Gamma} = 80\,\mathrm{meV}$, [Richard2004b]). Table 4.2 summarizes the main values obtained in the present work.

Similar positions of EDC features and similar values of the polarization, measured on bulk, SOI [5 µm] and SOI [2 µm] support the conclusion about relatively low build-in stress in the considered SOI samples.

In this chapter we have also shown that due to significant momentum relaxation in the surface Cs - O layer, the photoemission setup is essentially sensitive to the angle-averaged

Transition	Temperature	Band gap value	P_{HE}	$\langle P \rangle$
$\epsilon_{g,X}$	300 K, 115 K		$< 2\,\%$	$-0.4\,\%^{a}$
$\epsilon_{g,\Gamma}$	300 K	$3.3\,\mathrm{eV}^{b}$	6 % (SOI), 8 % (bulk)	$-1.25\,\%$
	115 K	3.32 eV	6.5 % (SOI), 10 % (bulk)	$-0.6\,\%$
$\epsilon^{\mathrm{direct}}_{g,L}$	$300\,\mathrm{K}^{c}$	3.35 eV		
	115 K	3.39 eV, $3.44\,\mathrm{eV}^{d}$		
$\epsilon^{2}_{g,\Gamma}$	300 K		$< 1.5\,\%$	$< 1\,\%$

[a] $\langle P \rangle$ changes the sign at $h\nu = 1.45\,\mathrm{eV}$ and becomes $+0.4\,\%$ at $h\nu = 1.6\,\mathrm{eV}$ for both 115 K and 300 K

[b] The spin-orbit splitting is found to be $\Delta_{\mathrm{SO}} = 50\,\mathrm{meV} \pm 20\,\mathrm{meV}$ in valence band, and $\Delta^{c}_{\mathrm{SO}} = 40\,\mathrm{meV} \pm 10\,\mathrm{meV}$ in conduction band. Within the precision of our experiment no measurable temperature variations of above values were observed.

[c] The sum of spin-orbit splitting if found to be $\Delta_{\mathrm{SO}\,L} + \Delta^{c}_{\mathrm{SO}\,L} = 100\,\mathrm{meV}$ for 300 K.

[d] This value is estimated via the analysis of the EDCs, whereas all the other band gaps are estimated via the analysis of the PEDCs.

Table 4.2: Estimated in the present work parameters of Silicon band structure

quantities. In particular, the features observed on EDCs are similar for (1 0 0) and (1 1 1) orientations. The same conclusion follows from the comparison of measured polarization in IR with the calculations [Cheng2011a]. This observation confirms previous results on momentum relaxation of the electrons photoemitted through Cs - O surface layer [Gobeli1964].

Chapter 5

Two-photon optical pumping

5.1 Introduction

Since the Tsunami laser is designed for pulsed and not for continuous wave use, its operation in continuous and 'pseudo-pulsed' modes yield low optic powers, especially with SHG. That is why the measurements performed in previous chapter required particularly long integration times[1] due to the low photocurrent. Therefore, in this chapter we consider the use of pulsed radiation for spectroscopic and polarimetry measurements.

Furthermore, the use of high optical density irradiation gives access to interesting phenomena, such as two-photon optical pumping. In fact, in order to get a measurable probability of two-photon absorption, the photon flux must be extremely high.

Two-photon excitation requires the absorption of two photons of theoretically half of the energy usually required for one photon excitation. The interest of the two-photon OP follows from its greater sensitivity to the direct optical transitions. To illustrate this statement let us compare the intensity of the optical transitions at $h\nu_i = 2.9\,\mathrm{eV}$ (phonon-assisted transitions) and $h\nu_d = 3.3\,\mathrm{eV}$ (direct transitions are possible). In a single-color two-photon process optical absorption process, let us denote $h\nu_{1\mathrm{PA}}$ - the energy of each photon, and the total energy absorbed by the photoelectron:

$$h\nu_{2\mathrm{PA}} = 2h\nu_{1\mathrm{PA}} \tag{5.1}$$

Taking the values of the absorption coefficient α from [Macfarlane1959] and two-photon cross-section β from [Reitze1990; Bristow2007] for energy $h\nu_{1\mathrm{PA}} = \frac{1}{2}h\nu_{2\mathrm{PA}}$, we deduce

$$\frac{\alpha(\epsilon_i)}{\alpha(\epsilon_d)} = \frac{3.5 \times 10^6\,\mathrm{m}^{-1}}{1.2 \times 10^7\,\mathrm{m}^{-1}} = 0.29 \tag{5.2}$$

and

$$\frac{\beta(\epsilon_i)}{\beta(\epsilon_d)} = \frac{1.5\,\mathrm{cm/GW}}{40\,\mathrm{cm/GW}} = 0.037 \tag{5.3}$$

Thus, for the above energies two-photon optical pumping is almost one order of magnitude more sensitive to the direct optical transitions.

[1] For instance, compared to these done with continuous wave laser in [Roux2008].

As shown in [Bensoussan1983], the direct gap $\epsilon_{g,\Gamma}$ also corresponds to a peak in the quantum yield dependence on excitation energy for the energy of each photon in two-photon process $h\nu_{1\mathrm{PA}} \approx \epsilon_{g,\Gamma}$. In fact, for $h\nu_{1\mathrm{PA}} = \epsilon_{g,\Gamma}$ the probability of two-photon transition is higher due to the accessibility of the intermediate state which are situated in the vicinity of the first conduction band (Γ_5^-) in the center of BZ.

Finally, the investigation of two-photon absorption could in principle allow to explore with the same light source higher conduction bands compared to these available with one-photon absorption. The advantages and challenges of high-energy two-photon absorption (2PA) will be discussed.

However, the presentation of the experimental results on two-photon absorption has to be preceded by the analysis of the electron spectrometer operation at high electron fluxes, which reveal some experimental challenges.

Unless otherwise specified, the measurements are performed on SOI [2 µm], and the pulsed radiation used for the measurements presented in this chapter has typical pulse duration of 100 fs and repetition rate of 80 MHz.

5.2 Operation of the electron optics in the regime of high electron flux

5.2.1 Description

When using a high power radiation (both pulsed and continuous), one should take into consideration that for powers below the threshold of instant evaporation of Cs - O surface layer and modification of surface reconstruction of Silicon itself due to increased temperature [Ulrych1995], the distortion of the photoemission spectra takes place (see for example the figs. 5.3 and 5.15 below). Specifically, the distortion consists in the following features:

- Broadening of EDCs
  - In pulsed mode operation, a stretching of EDCs by a factor of 6 for IR excitation and a factor of 4 for UV excitation is observed.
  - In continuous mode operation, a loss of resolution is observed.
    Further examined influence on the polarization (described in section 5.2.2) implies that a loss of resolution is proportional to the time-averaged, not to the peak photocurrent. The broadening of EDCs under continuous excitation is observed for different spectrometer resolutions (80 meV and 40 meV), and apparently depends on total rather on transmitted through spectrometer photocurrent. The observed stretching of spectra in continuous regime can reach the factor of 1.5 under IR excitation (fig. 5.5), and is almost negligible under UV excitation.
    For both regimes the broadening of the EDC results in a reduction in the apparent electron affinity, as well as in the blurring of features.
- Linear dependence $I_{\mathrm{cath}}(V_{\mathrm{cath}})$

The observed distortion of EDC is similar in picosecond and femtosecond modes. In the section on two-photon absorption study, we present mainly results for femtosecond mode,

because it corresponds to higher peak power and thus is a priori more favorable to the two-photon process.

Pulsed excitation implies that the electrons are generated by packets. The concentration of electrons in each packet exceeds by up to 10^5 times the typical concentration attained with a continuous laser of same power. Each packet is composed of electrons with different speeds. In fact, their speed varies from about 10^5 m/s for electrons with energy in vacuum compared to the finest spectrometer resolution (20 meV) to 10^6 m/s for electrons with 1 eV. The difference in their speed, especially significant for broad EDC (i.e. under UV excitation), leads to dissipation and even overlapping of consecutively generated electron packages, but in itself does not affect the process of selection in energies. The corresponding transit times of proportional electron optics are about $10 - 100$ ns.

5.2.2 Influence of the excitation mode on polarization

Continuous excitation

In order to analyze the operation of the spectrometer saturation under continuous high-power radiation, a series of measurements of EDC and PEDC at fixed $h\nu = 3.31$ eV and identical potentials of the electrodes was performed. The measurements with 300 nA in fig. 5.1 was conducted prior to a deposition of fresh surface layer, i.e. with a high electron affinity and consequently at a sufficiently low photocurrent. The measured polarization of ballistic electrons was of 0.07. After deposition of fresh Cs - O surface layer the experiment was repeated, this time varying the radiation power. As it can be seen in fig. 5.1, Cs - O layer reduced the work function (given by the low-energy threshold for EDC) to ϵ_{CB}. The figure shows that the use of 4 µA photocurrent led to the described above saturation effects, namely the increase in EDC width and decrease in polarization of ballistic electrons of 0.07 down to 0.04.

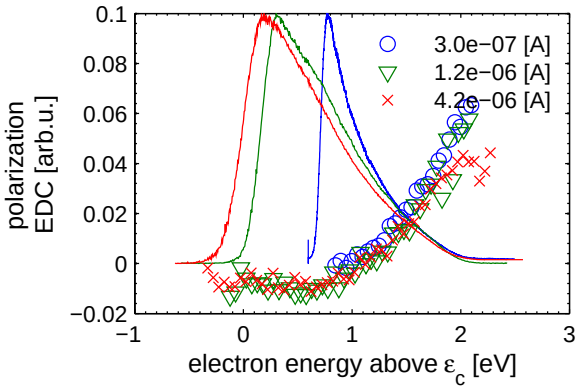


Figure 5.1: Broadening of EDCs and decrease in the polarization due to saturation of electron optics by high photoemitted currents under continuous excitation (SOI [5 µm], $h\nu = 3.31$ eV, $T = 300$ K)

Pulsed excitation

To estimate the variation of the polarization under pulsed radiation, the polarization is measured for photon energy, for which the results in continuous regime are already well established. As can be seen in fig. 5.2, up to a linear transform $V_{\text{final}} = 0.14V - 1.86$ of the horizontal axis, the shapes of the spectra of polarization in pulsed and continuous modes coincide. The coincidence of the maximum values of the polarization means that the electrons preserve their polarization despite an incorrect analysis of their energy. Moreover, the value of the electron affinity estimated by pulsed EDC in the right panel of fig. 5.2, coincides with the value of the affinity expected for that given experiment (around 1.5 eV, whereas the affinity of represented in the right panel continuous PEDCs was close to 0 eV). This result, as well as the work [Bona1985] (picosecond excitation) confirms that the use of pulsed radiation has no significant effect on the measured polarization of the photoelectrons.

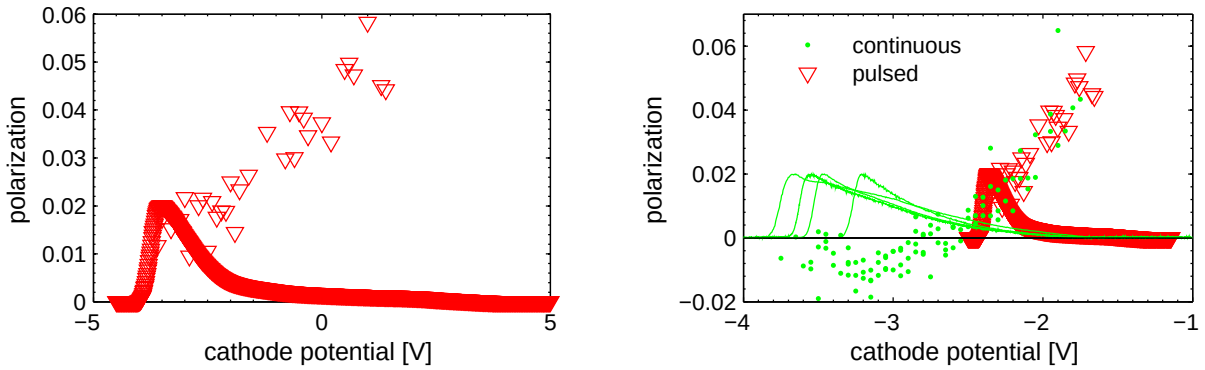


Figure 5.2: EDC and the corresponding PEDC for pulsed measurement at $h\nu = 3.29\,\text{eV}$, $T = 300\,\text{K}$, SOI [2 µm] (left), same data with rescaled x-axis superposed onto continuous measurements with similar photon energy, temperature and sample (right).

The average photocurrent corresponding to the measurement in fig. 5.2 was about 1.1 µA at the beginning of measurement, and gradually decreased down to 0.3 µA.

5.2.3 Methods of distortion minimization under pulsed irradiation

If possible, for a given wavelength, the simplest way for minimizing the EDC distortion is to work in pseudo-continuous mode, in other words with much longer pulses. Of course, reasonable pulse energy must be used and attention of the beam is most often necessary. Different settings of the laser allow to control the peak power in pulsed mode:

1. A reduced aperture of the entrance diaphragm of SHG decreases the total power.
2. In principle the power can be attenuated by deregulating the angle of the non-linear crystal. In the case of THG, both the crystals for second and third harmonics can be used. However, the intensity variation is often too sharp to be used as a convenient attenuation control.

3. Deregulate the acousto-optical modulator, in order to increase the pulse duration.

4. Work with excessively low or high pump powers so that to degrade the conversion efficiency and increase the pulse duration.

In practice the two last methods result in EDCs quite similar to those acquired in continuous mode. The drawback of using such 'pseudo-continuous' modes is a lower cathode current compared to continuous excitation, which results in longer acquisition time. Such low efficiency may be partially explained by Boersch effect, i.e. by spurious transverse velocity components due to the electron-electron interaction in a high-density beam [Rose1983].

5.2.4 Interpretation

The distortion of the EDCs has two possible reasons.

1. First, high electron concentrations can induce periodic charge accumulation:
   (a) On the electrodes. Such periodic charges may distort the potentials of electron optics and thus result in incorrect analysis of electron energy. It appears that the RC constants of electrodes are smaller than $(80\,\mathrm{MHz})^{-1}$, and thus the distortion of EDC is determined by the average, not the maximum photocurrent.
   (b) In the sample itself. Trapped charges or modification of surface states may explain the variation of effective electron affinity.
   Such charge accumulation is determined by the total current at the inlet of selector (i.e. $\propto I_{\mathrm{cath}}$), rather than by the current, transmitted by the selector.
2. The interaction between the electrons creates transverse velocity components and in consequence alters the longitudinal velocity component. This process, called **Boersch effect**, is proportional to the electron concentration and inversely proportional to their speed [Rose1983]. It has the greatest impact near cathode, where the packages have not enough time to dissipate. In addition to the distortion of the longitudinal speed, the acquired transverse speed leads to the deviation of electrons from the beam path. Deviated electrons do not reach the selector, thus reducing the overall spectrometer efficiency $\frac{I_{\mathrm{Faraday}}}{I_{\mathrm{cath}}}$. This effect is characterized by the power-of-law dependence of the EDC width versus power with exponent of 2/3.

Both mechanisms can be classified as spectrometer saturation due to large current densities. Given that electron optics cannot analyze correctly the continuous electrons fluxes greater than 2 µA (section 5.2.2), it is natural to suppose that similar phenomena are applicable on larger scale for measurements with pulsed excitation, where peak currents are much higher ($\approx 10^{-1}\,\mathrm{A}$). The large number of conduction electrons is likely to produce similar effects in the crystal, such as ambipolar diffusion and high rate of spin relaxation.

The variation in photon energy due to broadening of optical spectra in pulsed regime is about 0.05 eV (full width at half maximum value) for excitation at $h\nu = 1.4\,\mathrm{eV}$ (fig. 5.4), and cannot explain such effect.

5.2.5 Conclusion

From the combination of the results presented in this section, we can conclude that the electron spectrometer is in principle capable of working with pulsed radiation, albeit with the restrictions mentioned above. The main features are still reproduced correctly under pulsed radiation:

- General structure of an EDC (with main peak corresponding to thermalized electrons, and decrease for higher energies) is usually preserved
- The electronic spin polarization (section 5.2.2) is either preserved (in the case of pulsed excitation), either decreased (for the continuous excitation the observed decrease was of 30 % for 4 mA photocurrent).
  Pulsed: preserved
  Continuous: decreased by

5.3 Fundamental (infra-red) range

5.3.1 Number of particles per pulse

For 1 W of optical power, the typical energy per 100 fs pulse at 80 MHz modulation frequency is 1.25 nJ. For $h\nu = 1.5\,\mathrm{eV}$ we obtain 5×10^{10} photons per pulse, which corresponds to peak value of 5×10^{23} photons per second. The average current of 2 µA corresponds to peak current of 0.25 A, which represents is 1.5×10^5 photoelectrons per pulse, or the peak value of 1.5×10^{18} electrons per second.

5.3.2 Analysis of peaks on pulsed EDCs

In this section we compare the EDCs acquired using continuous and pulsed radiation of different optical power. In parallel with the acquisition of EDCs, represented in fig. 5.3, the measurements of the optical spectrum of the laser radiation were performed (fig. 5.4). The latter allows to determine the length of pulses (wider spectra correspond to shorter pulses), and reveal the presence of eventual continuous component (represented as a narrow line on optical spectra).

In the right panel of fig. 5.3 one can see that with the increasing power the EDC becomes more symmetric, indicating a high-energy broadening and a loss in energy resolution.

The width of EDCs acquired with pulsed and continuous radiation is shown in fig. 5.5. Regardless of the use of radiation energy, this relationship is characterized by a horizontal asymptote at infinity, and cannot be well described by the $W^\alpha, \alpha > 1$. Thus, the observed expansion of the EDCs cannot be explained solely by Boersch effect, as the latter is usually $\propto W^{2/3}$.

The following arguments support the hypothesis that the peak at −3.5 eV on pulsed EDCs is due to the electrons excited by the continuous component of the laser radiation

- The similarity of this peak with the EDC recorded with low-power continuous excitation (right panel of fig. 5.3) with respect to the following characteristics:

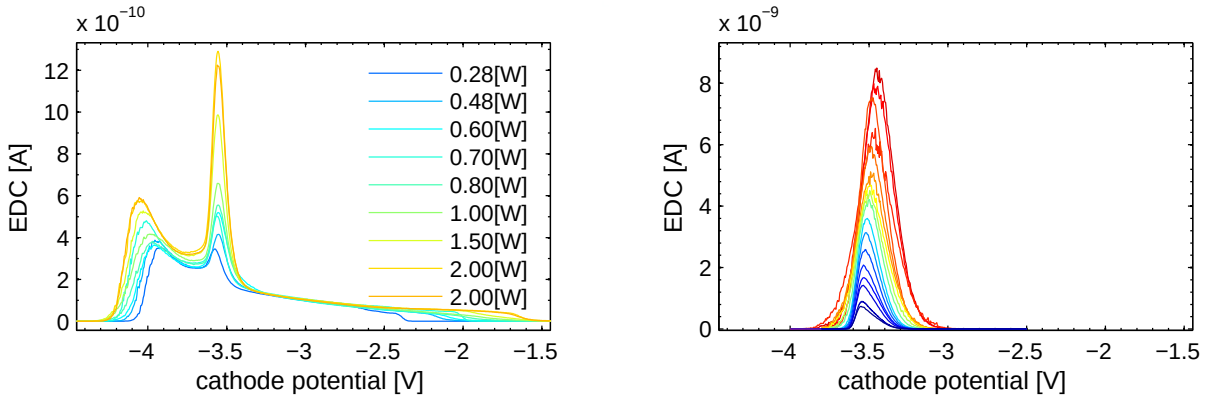


Figure 5.3: Pulsed (left) and continuous (right) EDCs at $h\nu = 1.4\,\mathrm{eV}$ and spectrometer resolution 40 meV. The power in the right panel vary from 50 mW (blue curve) to 2.2 W (red curve) (SOI [2 µm], $T = 300\,\mathrm{K}$). The typical peak photon fluxes at 1 W of optical power are 1.6×10^{31} photons/m^2/s and 1.3×10^{26} photons/m^2/s for pulsed and continuous modes respectively.

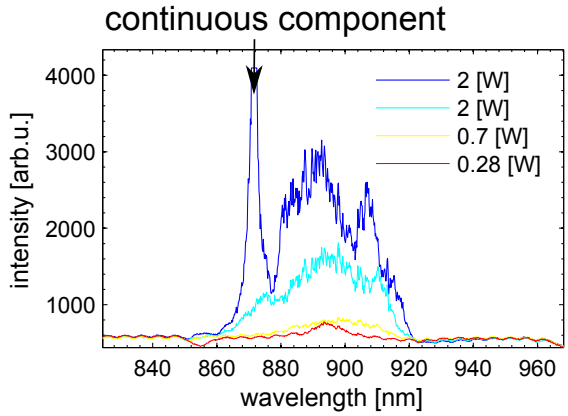


Figure 5.4: Optical spectra of femtosecond laser radiation at wavelength $\lambda = 885.6\,\mathrm{nm}$ (i.e. photon energy of $h\nu = 1.4\,\mathrm{eV}$) emitted at different optical powers

  - Amplitude and its linear dependence on the applied power (the right panel of fig. 5.6)
  - Position
  - Shape
- Some of corresponding optical spectra from fig. 5.4 exhibit a clearly visible continuous component. The inability to observe the continuous component for some spectra (whereas the corresponding peak on EDC is systematically present) indicates that a continuous component, which gives rise to the peak in EDC, is in fact unobservable by the optical spectrometer. Such phenomenon can probably be explained by the redistribution of continuous component in the plan transverse to the beam propagation direction during laser alignment.

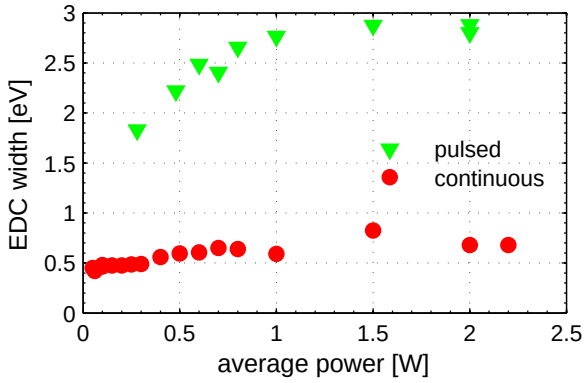


Figure 5.5: Energy width of EDCs deduced from fig. 5.3

- The absence of a similar peak under excitation with SHG, which acts as a transmitting filter for the pulsed component. Indeed, the two-photon conversion efficiency depend quadratically on laser power, and so it is several orders of magnitude higher for pulses rather than for continuous background radiation.

As shown in the left panel of fig. 5.6, the total photocurrent also depends linearly on excitation power, which is a signature of single-photon process. The proportionality coefficient provides information about the one-photon yield. For pulsed excitation $Y = 2.5 \times 10^{-6} \frac{N_{\text{electrons}}}{\text{photon}}$, in agreement with typical values given in section 3.3.5. For continuous excitation the quantum yield decreases by a factor of 4 in the high power limit.

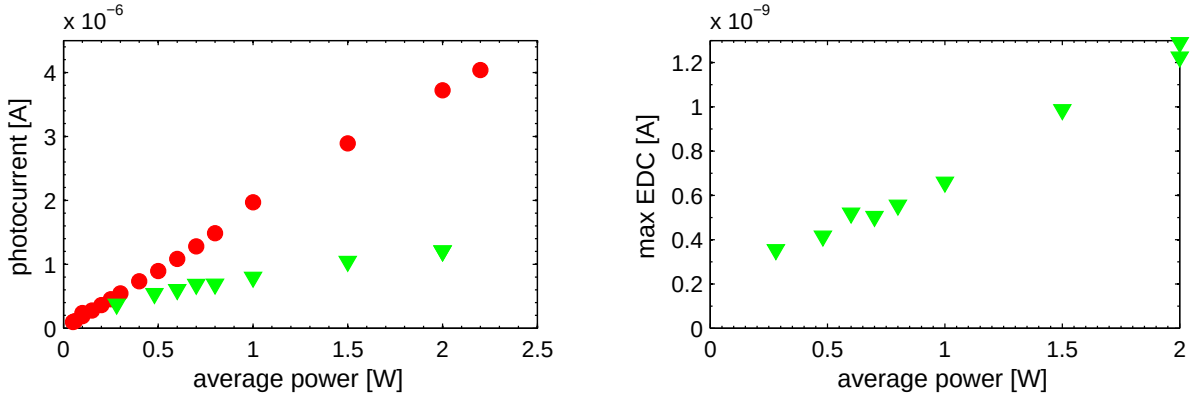


Figure 5.6: Cathode current and the maximum of EDC at $V_{\text{cath}} = -3.5\,\text{V}$ versus optical power

One can see in fig. 5.7, the spectrometer transmission decreases with the applied optical power in both pulsed and continuous modes, and is significantly lower in the pulsed mode.

We can conclude that the EDC measured with the use of pulsed radiation consists of two parts:

1. Electrons whose energy is measured without significant distortion. These electrons may originate from either continuous background radiation or from the electron packet,

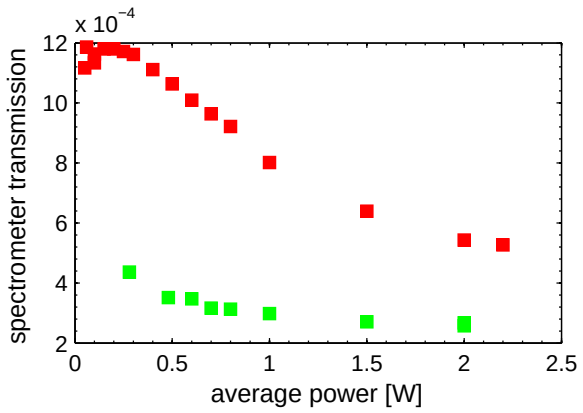


Figure 5.7: Spectrometer transmission $\int N(\epsilon)d\epsilon/I_{\text{cath}}$ at $h\nu = 1.4\,\text{eV}$

generated by laser pulse.

2. Electrons whose energy is measured incorrectly.

In fact, in order to attribute a feature on EDC to two-photon absorption process, several conditions should be fulfilled:

- The kinetic energy of electrons contributing to the feature should be close to $2h\nu - \epsilon_{g,X}$
- The position of the feature should not depend on applied optical power
- The amplitude of the feature should be proportional to the square of optical power

The signatures described above are fulfilled, for instance, by a small feature, which appears on the pulsed EDCs with the excitation energy $2h\nu > \epsilon_{g,\Gamma}$. Indeed, the point of $2h\nu$ in fig. 5.8 is situated at approximately $V_{\text{cath}} = -1.2\,\text{V}$, and thus coincides with high-energy threshold of the considered feature. Another structure at $V_{\text{cath}} \approx -2.3\,\text{eV}$ can be associated with electrons excited with a 2-photon process in the L minimum.

Due to limitations in optical power density we could not verify the quadratic dependence of feature amplitude versus optical power. However, the ratio of the amplitude of the 2-photon feature to the peak corresponding to the single-photon absorption:

$$\frac{I_{2\text{PA}}}{I_{1\text{PA}}} = \frac{10^{-11}\,\text{A}}{2 \times 10^{-9}\,\text{A}} = 5 \times 10^{-3} \tag{5.4}$$

is in good agreement with the value of $\frac{\beta I_0}{\alpha}$, estimated for this $h\nu$ in section 5.6.

While interpreting the experimental data on two-photon absorption, care must be taken in order to

1. Distinguish between 2PA and background signal (i.e. electrons collected from pressure gauge, signal from ambient light). To eliminate this effect it is required to systematically vary the optical power during two-photon measurement.
2. Distinguish between two-photon generation in the sample and in optical components. The symmetry of both Silicon and quartz lattices implies the impossibility of two-photon generation in perfect crystals. However, the presence of defects (including interfaces) as well a significant space charge region results in disruption of symmetry and thus enables the two-photon process.

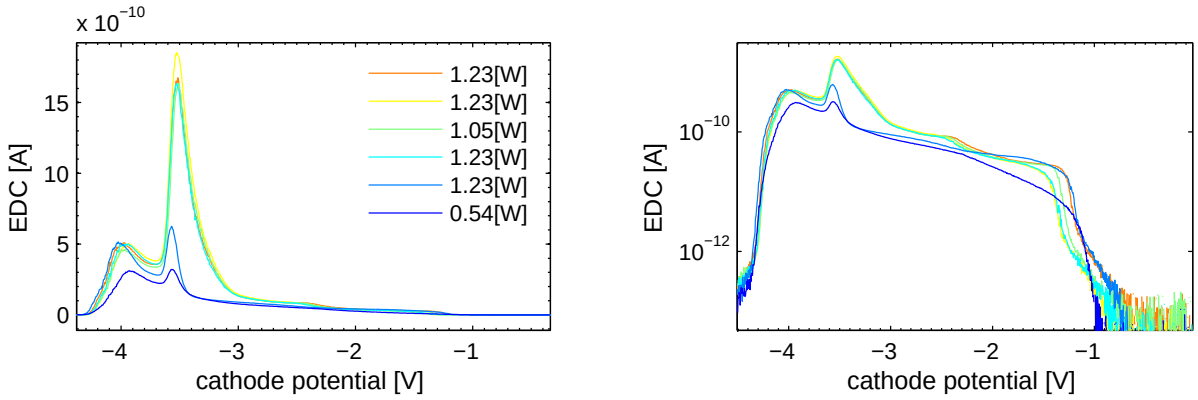


Figure 5.8: Linear (left) and logarithmic (right) EDCs for $h\nu = 1.67\,\mathrm{eV}$ (SOI [2 µm], $T = 300\,\mathrm{K}$, 100 fs-pulsed radiation). The HE threshold of PEDCs presumably corresponds to excitation at Γ, whereas the feature at $V_{\mathrm{cath}} \approx -2.3\,\mathrm{V}$ can be associated with L valley.

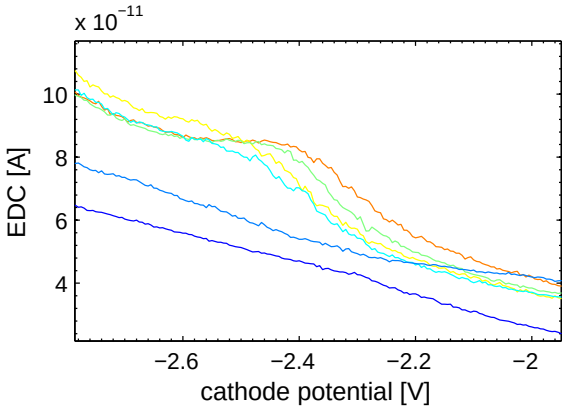


Figure 5.9: Zoomed-in feature, corresponding to electrons transported or directly excited by a two-photon absorption process in L valley (zoom of the left panel of fig. 5.8)

Therefore, to exclude this possibility, a measurement of the optical spectra at $2h\nu$ after quartz components (before beam enters the vacuum chamber) using pulsed radiation was performed. Presented in fig. 5.10 spectra show no second harmonic up to the spectrometer sensitivity. Moreover, if the use of silica would result in a substantial generation of the second harmonic there would be a noticeable difference between the EDC, measured under irradiation transmitted through glass lens and UHV viewport compared to quartz lens and UHV viewport (the latter was installed at the same time as SOI [2 µm]). On the available experimental data no such difference was observed.

5.3.3 Photocathode $I_{\mathrm{cath}}(V_{\mathrm{cath}})$ curve

For low photoemitted currents (conditions fulfilled in the measurements presented in chapter 4) (fig. 3.5), the photocurrent I_{cath} does not influence electrode potentials and its value does not depend on the voltage applied to the cathode.

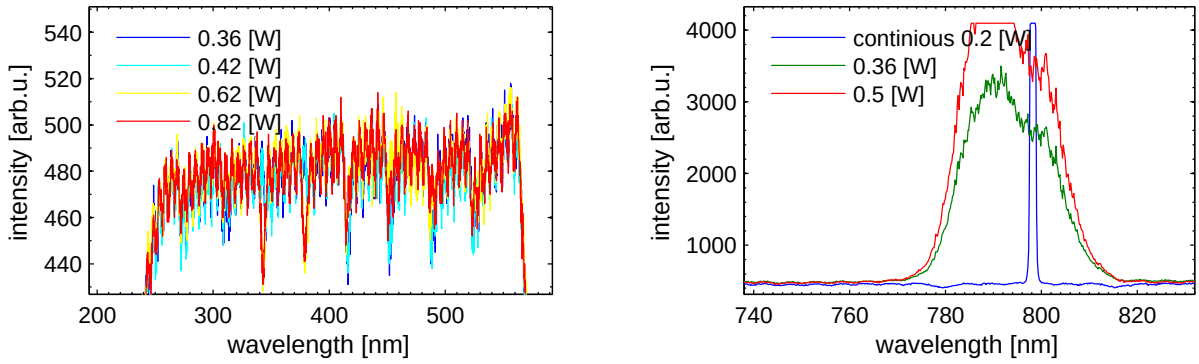


Figure 5.10: Optical spectra measured after quartz optical components in the IR pulsed regime (100 fs pulses at 80 MHz repetition rate)

Under high optical density irradiation condition the photocurrent varies while changing V_{cath} (fig. 5.11). This dependence takes place at different photon energies, and, for a given mean laser power, is more pronounced for pulsed radiation. Thus, we can conclude that the effect is essentially proportional to the density of photoelectrons.

Each curve in fig. 5.11 is obtained by several successive scans on V_{cath}, to exclude the effect of photocurrent reduction due to deterioration of the surface Cs - O layer. As a result, it is found that these successive cycles coincide almost perfectly, thus characterizing the effect of infrared radiation of the considered power on the surface layer as negligible.

We can conclude that when the number of electrons entering the rotator becomes higher than $1.5 - 2\,\mu\text{A}$ under continuous illumination mode, the geometrical aberration due to deviation from paraxial assumption and space charge due to electron - electron interaction occur. It is known that increasing the filling factor of electrostatic lenses above 50 % gives rise to a rapid increase in aberration.

However, as shown in fig. 5.11, the dependence of $I_{\text{cath}}(V_{\text{cath}})$ is linear, and there is no visible trace of the corresponding EDCs. Such result is explained by low spectrometer efficiency $\frac{EDC}{I_{\text{cath}}} \approx 10^{-4}$ (see for instance fig. 5.6). The observed dependence $I_{\text{cath}}(V_{\text{cath}})$ is likely to be explained by charge effects.

5.3.4 Polarization of two-photon absorption peak

A weak positive polarization can be associated with two photon absorption peak (fig. 5.12).

As the simplest approximation, the polarization of the electrons excited by the two-photon process follows the analytical model at Γ, i.e. be at the order of 1/6. However, the large width of optical spectra of pulsed irradiation probably implies an important mixing of positive and negative contributions, which may result in vanishing overall polarization. A complete numerical model would be required to get a more precise answer to this question.

Unfortunately, up to date no theoretical investigation of two-photon OP in Silicon exists for $h\nu > \epsilon_{g,X}$, the only calculation of two-photon optical orientation being provided in [Cheng2011c] for $h\nu < \epsilon_{g,X}$. This calculation predicts the polarization of two photon optical pumping, which is similar to that of one-photon process for $T = 300\,\text{K}$ and (1 0 0)-oriented

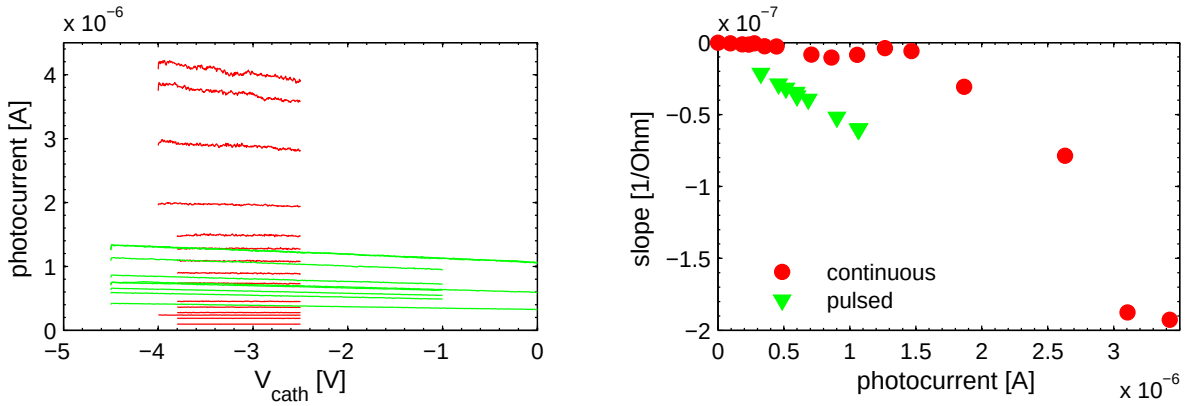


Figure 5.11: Photocathode $I_{\mathrm{cath}}(V_{\mathrm{cath}})$ curves (left) and corresponding slopes for different photocurrents (right) (SOI samples, $h\nu = 1.4\,\mathrm{eV}$)

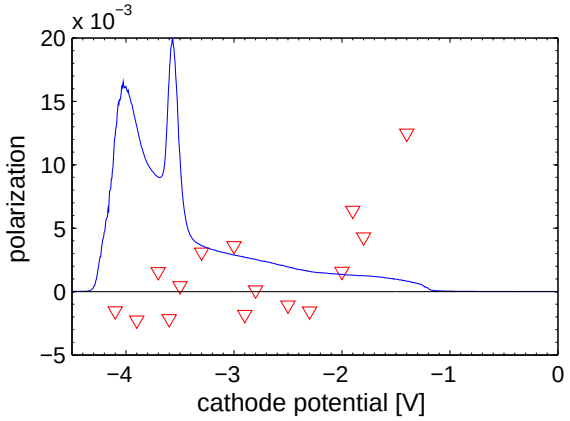


Figure 5.12: Polarization measurement of 2PA feature at $h\nu = 1.67\,\mathrm{eV}$ (SOI [2 µm], $T = 300\,\mathrm{K}$, 100 fs-pulsed radiation))

sample, but differs in sign for 4 K. It can be understood that in the case of indirect band-edge absorption the selection rules could be significantly different for these two processes[2], thus resulting in different polarization of photoelectrons. On the basis of comparison of [Cheng2011a; Cheng2011c], we can suppose that if the symmetry of states results in polarized one-photon optical transitions, the two-photon transitions would also probably exhibit certain spin polarization.

Extending this hypothesis, one can expect that a non-zero polarization of 2PA takes place at $h\nu \approx \epsilon_{g,\Gamma}/2$. Indeed, the situation with the direct two-photon optical transitions is simpler, since, contrary to the indirect absorption, the only difference between direct one- and two-photon transitions resides in the presence of the intermediate virtual state during the latter. Finally, our conclusion is supported by the fact that the measured polarization of two-photon OP in GaAs [Miah2009] coincides with that of one-photon process.

[2]Both of which are complex since involve photons and interference of a number of intermediate states

5.3.5 High affinity quadratic photocurrent dependence

The two-photon quantum yield is defined, following [Bensoussan1981], as a proportionality coefficient between electron flux density Φ_e and photon flux density Φ_{ph}^2

$$\Phi_e = Y_{2\mathrm{PA}}\Phi_{ph}^2 \tag{5.5}$$

The notations here are similar to those used for one-photon yield (eq. (3.36)).

For pure two-photon process this quantity is given by

$$Y_{2\mathrm{PA}} = \frac{I_{cath}Sh\nu^2}{eW^2} \tag{5.6}$$

In our case both one and two-photon processes are present, so in order to identify only two-photon contribution, the measurement represented in fig. 5.13 was performed with affinity about 1.5 eV above the indirect conduction band minimum. Furthermore, in order to eliminate from consideration eventual linear (i.e. due to one-photon absorption) component from curves from fig. 5.13, $Y_{2\mathrm{PA}}$ was calculated as coefficient before Φ_{ph}^2 in the second order least squares fit.

One should note that only the fundamental radiation of laser used in this work is powerful enough to achieve the effect presented above. When using the light generated by SHG or THG, a similar effect is not observed, probably due to insufficient power density.

Typical average photon flux for $h\nu = 1.5\,\mathrm{eV}$, $W = 1\,\mathrm{W}$ and $S = \pi\ 0.1\,\mathrm{mm}^2$ is

$$\Phi_{ph} = 1.3 \times 10^{26}\,\mathrm{m}^{-2}\ \mathrm{s}^{-1} \tag{5.7}$$

which is four orders of magnitude higher than same quantity from [Bensoussan1981]. At the same time the two-photon quantum yield of work above is much lower $Y_{2\mathrm{PA}}(h\nu = 2.53\,\mathrm{eV}) = 7 \times 10^{-41}\,\mathrm{m}^2\,\mathrm{s}$, which is likely to be explained by the difference in the work function: it was given by $\chi_{\mathrm{Si}} = 4.6\,\mathrm{eV}$, whereas for the measurement from fig. 5.13 $\chi \approx 1.65\,\mathrm{eV}$. Such difference in $Y_{2\mathrm{PA}}$ shows that, similarly to the single-photon process, $Y_{2\mathrm{PA}}$ is inversely proportional to χ.

$h\nu$	$Y_{2\mathrm{PA}}$ [m^2 s]
1.65 eV	1.6×10^{-34}
1.55 eV	2.1×10^{-34}
1.43 eV	3.3×10^{-35}

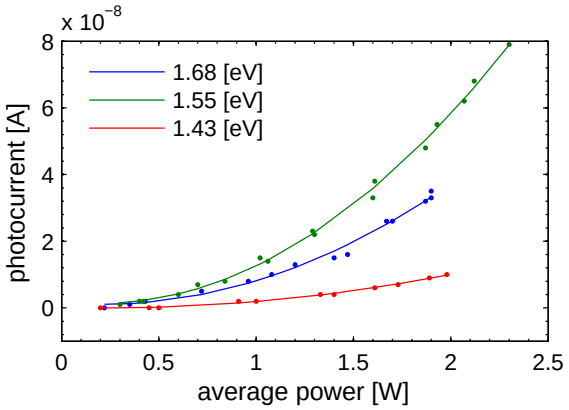


Figure 5.13: Parabolic dependence of cathode current under femtosecond pulsed excitation in two-photon regime (SOI [2 µm], $T = 300\,\mathrm{K}$)

Provided in fig. 5.13 data support the assumption of proportionality between the two-photon quantum yield and two-photon cross-section, similar to that observed in section 3.3.5 for one-photon absorption.

5.4 Second harmonic (visible-ultraviolet) range

The use of the radiation generated with SHG leads to EDCs having characteristics similar to those in IR region. Like in the infrared range, the photocurrent depends linearly on output power, and the use of high optical power causes widening of EDCs (fig. 5.14).

The use of ultraviolet radiation leads to more important EDCs distortion compared to infrared range. Indeed, the ratio of the maximum concentration of electrons in these two modes with characteristic $W_{\mathrm{IR}} = 2\,\mathrm{W}$ and $W_{\mathrm{UV}} = 200\,\mathrm{mW}$:

$$\frac{n_{\mathrm{IR}}}{n_{\mathrm{UV}}} \propto \frac{\alpha_{\mathrm{IR}}}{\alpha_{\mathrm{UV}}} \frac{Y_{\mathrm{IR}}}{Y_{\mathrm{UV}}} \frac{W_{\mathrm{IR}}}{W_{\mathrm{UV}}} = 10^{-2}10^{-3}10^{1} = 10^{-4} \tag{5.8}$$

The peak corresponding to the continuous component on infrared EDCs (fig. 5.3) is completely absent when using SHG (fig. 5.15). This means that the SHG acts like a filtering component for the continuous laser radiation.

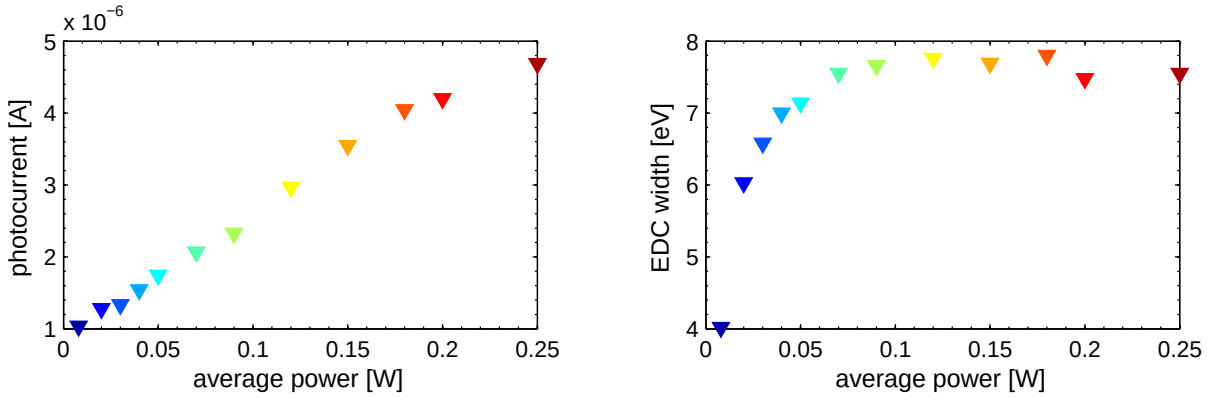


Figure 5.14: Photocurrent and EDC width versus average optical power (SOI [2 µm], $h\nu = 3.29\,\mathrm{eV}$, $T = 300\,\mathrm{K}$, 100 fs-pulsed radiation))

A distinctive feature of the EDCs acquired with the UV excitation is the presence of features (section 4.3.1). Figure 5.15 shows that the feature corresponding to the minimum of the conduction band L is visible only on the EDC measured at the minimal power. Thus, we can conclude that the use of higher power in pulsed regime leads to a blurring of the EDCs.

As seen from fig. 5.15, while reducing the power the EDCs measured in a pulsed mode approaches the EDCs obtained using a continuous radiation. However, in order for pulsed EDC to practically coincide with a continuous one, a pseudo-pulsed mode should be used (section 5.2.3). Because of the linear dependence of $I_{\mathrm{cath}}(W)$ both values (I_{cath} or W) can be used to access the degree of EDCs distortion.

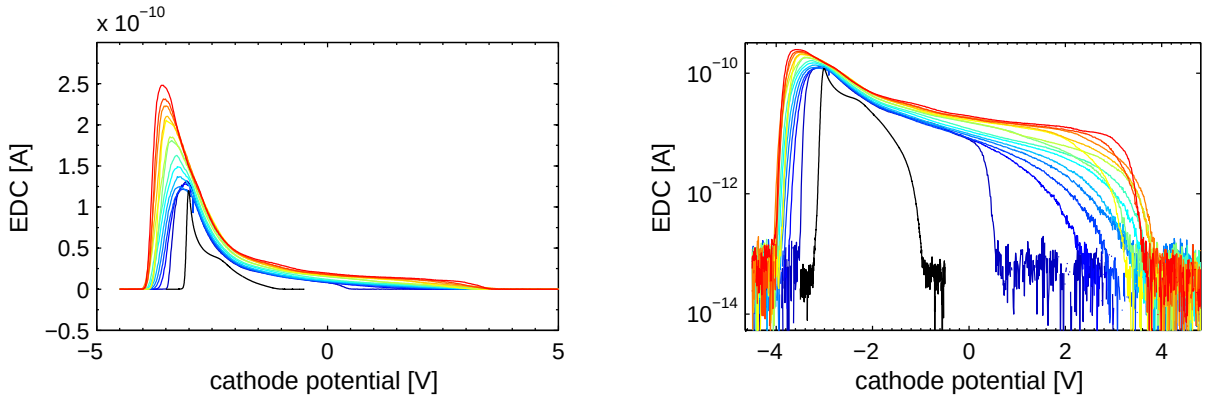


Figure 5.15: Pulsed EDCs (colored curves) with power $50 - 250\,\mathrm{mW}$ compared with continuous EDC of same $h\nu = 3.29\,\mathrm{eV}$ (black curve). (SOI [$2\,\mu\mathrm{m}$], $T = 300\,\mathrm{K}$)

5.5 Third harmonic (ultraviolet) range

Since THG is characterized by lower average power (the maximum available power does not exceed $10\,\mathrm{mW}$), the EDCs acquired using this mode are less distorted compared to fundamental and SHG regimes. Among the whole set of measurements with THG no distortions as strong as in fig. 5.15 were observed neither in picosecond nor in femtosecond modes.

By way of example, fig. 5.16 shows the effect of spectrometer saturation in picosecond mode, whereas all the previous results of this chapter were obtained in the femtosecond mode. The only observed difference between these two regimes is slightly lower saturation in the picosecond mode.

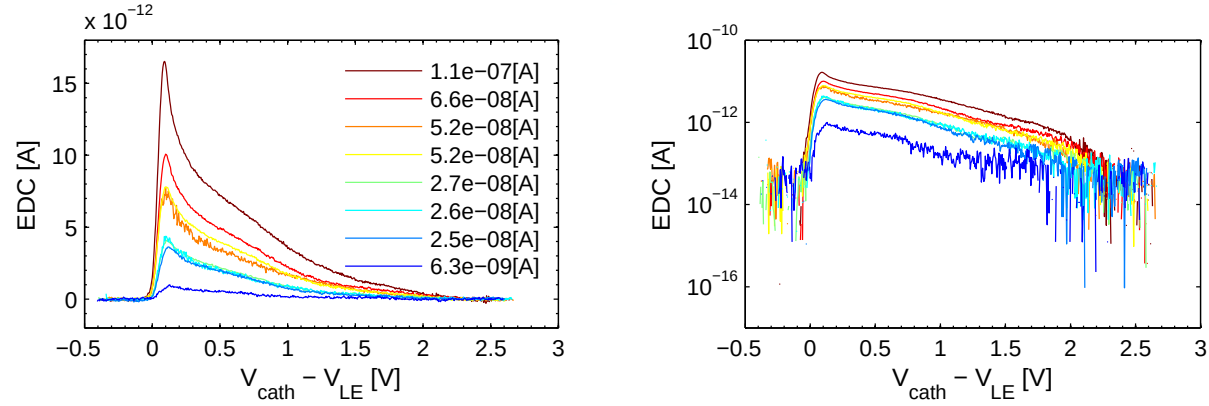


Figure 5.16: Spectrometer saturation in picosecond mode (THG, SOI [$2\,\mu\mathrm{m}$], $h\nu = 3.8\,\mathrm{eV}$, $T = 300\,\mathrm{K}$)

5.5.1 Possibility of second harmonic generation above ϕ_{Si}

Without Cs - O layer the work function of Silicon is estimated to $\phi_{\mathrm{Si}} = 4.76\,\mathrm{eV}$ [Allen1966]. As we can see from fig. 5.17, the relative intensity of two-photon absorption at $h\nu_{1\mathrm{PA}} = 2.4\,\mathrm{eV}$

is quite low. Furthermore, the available power with SHG does not exceed the power used for two-photon measurement in IR, and thus such measurement is not likely to provide any advantage in $\frac{N_{2PA}}{N_{1PA}}$ compared to IR two-photon measurement.

At the same time, the observation of photocurrent from clean Si photocathode for $h\nu < \phi_{Si}$ would unambiguously indicate that the measured effect corresponds to the multi-photon excitation process (and not to the saturation of electron spectrometer), since the electrons generated with one photon do not have enough energy to escape from the crystal. In this manner, the observed broadening of EDC measured on clean Silicon [Bensoussan1983] was interpreted as two photon absorption.

5.6 Relative intensities of one and two-photon processes

Let us denote I_0 incident optical power density, and $I(x)$ - optical power density in the material. Light absorption process involving one photon can be described by the exponential law

$$dI = -\alpha I(x)dx \tag{5.9}$$

with its solution

$$I_{1PA}(x) = I_0 \exp(-\alpha x) \tag{5.10}$$

In the case of pure two-photon process (i.e. if one-photon process is impossible), a similar equation can be written as

$$dI(x) = -\beta I(x)^2 dx \tag{5.11}$$

where β is two-photon cross-section. The corresponding solution is

$$I_{2PA}(x) = \frac{I_0}{1 + \beta I_0} \tag{5.12}$$

However, if both processes are possible (which is the case for Silicon and photon energy above indirect band gap), one have to solve

$$dI(x) = -(\alpha I(x) + \beta I(x)^2)dx \tag{5.13}$$

with the solution given by

$$I_{1,2PA}(x) = I_0 \frac{\exp(-\alpha x)}{1 + \frac{\beta I_0}{\alpha}(1 - \exp(-\alpha x))} \tag{5.14}$$

Note that

$$I_{1,2PA}(x)|_{\beta=0} = I_{1PA}(x) \tag{5.15}$$

and

$$\lim_{\alpha \to +0} I_{1,2PA}(x) = I_{2PA}(x) \tag{5.16}$$

Thus, the ratio of number of photons absorbed via one- and two- photon processes, denoted as N_{2PA} and N_{1PA} respectively, is given by

$$\frac{N_{2PA}}{N_{1PA}} = \frac{\beta I_0}{\alpha} \tag{5.17}$$

For a circular spot the peak power density is given by

$$I_0 = \frac{W}{\pi r^2} \frac{1}{T_{pulse} F} \tag{5.18}$$

where W is average laser power, F is pulse repetition frequency, T_{pulse} is pulse duration, and r is the radius of spot on the sample.

Our experimental conditions are typically characterized by $W = 1\,\mathrm{W}, F = 80\,\mathrm{MHz}, T_{pulse} = 100\,\mathrm{fs}$ and the laser focused to $r = 0.1\,\mathrm{mm}$, thus yielding the optical power density $I_0 = 0.5\,\mathrm{GW/cm^2}$. Given the dependence on excitation energy of the absorption coefficient $\alpha(h\nu)$ from fig. 3.16 and two-photon cross-section $\beta(h\nu)$ from fig. 5.18, the quantity from eq. (5.17) versus excitation energy is represented at fig. 5.17

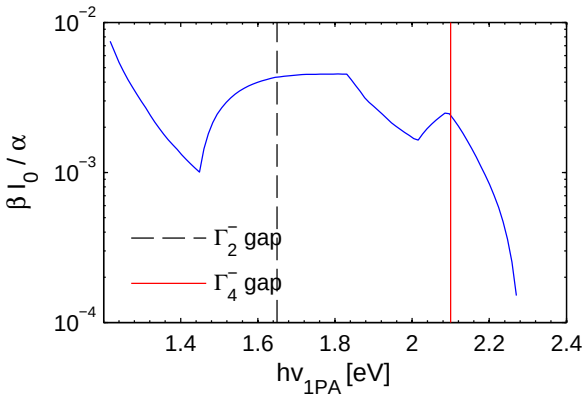


Figure 5.17: Theoretical ratio of the intensities of one- and two-photon absorption. The direct band gaps, represented by vertical lines, are indicated at half of their energy, since the energy of the photoelectron in a two-photon absorption is $h\nu_s 2PA = 2h\nu_{1\mathrm{PA}}$.

For a typical measurement at $h\nu = \frac{\epsilon_{g,\Gamma}}{2} = \frac{3.3\,\mathrm{eV}}{2} = 1.65\,\mathrm{eV}$ this ratio becomes $\frac{\beta I_0}{\alpha} = 3.8 \times 10^{-3}$.

5.7 Two-photon cross-section

[Bristow2007] measured $\beta = 2\,\mathrm{cm/GW}$ at $h\nu_{1\mathrm{PA}} = 1.55\,\mathrm{eV} = hc/800\,\mathrm{nm}$. The value at the fundamental gap is slightly lower, about $1.5\,\mathrm{cm/GW}$. On the upper side the value of $40\,\mathrm{cm/GW}$ was measured by [Reitze1990] at $h\nu_{1\mathrm{PA}} = 2\,\mathrm{eV} = hc/620\,\mathrm{nm}$. One should note the characteristic feature on β spectrum corresponding to Γ_2^- band gap.

The combination of data from these two works is represented in fig. 5.18. However, up to our knowledge, there is no available data on β for intermediate region $h\nu_{1\mathrm{PA}} = 1.55 - 2\,\mathrm{eV}$, that is in the vicinity of Γ_4^- direct band gap. One could suppose that the trend measured by Reitze et al. continue at lower energies, resulting in a peak on spectrum at $h\nu_{1\mathrm{PA}} = \epsilon_{g,\Gamma}/2$. If this reasoning is valid, one may expect $\beta(1.65\,\mathrm{eV}) \approx 10^2\,\mathrm{cm/GW}$.

In order to perform further analysis, we joined two datasets by a simple linear interpolation. If a peak at Γ_4^- is effectively present, such interpolation would cause about a 4

times underestimation of $\beta(1.65\,\mathrm{eV})$. The difference in β for data from [Bristow2007] and [Reitze1990] allows to estimate the intensity ratio of the direct and indirect two-photon processes. Considerable difference between $\beta(1.42\,\mathrm{eV}) = 2\,\mathrm{cm/GW}$ and $\beta(1.81\,\mathrm{eV}) = 38\,\mathrm{cm/GW}$ implies that the onset of direct transitions may result in a sharp feature on β spectrum.

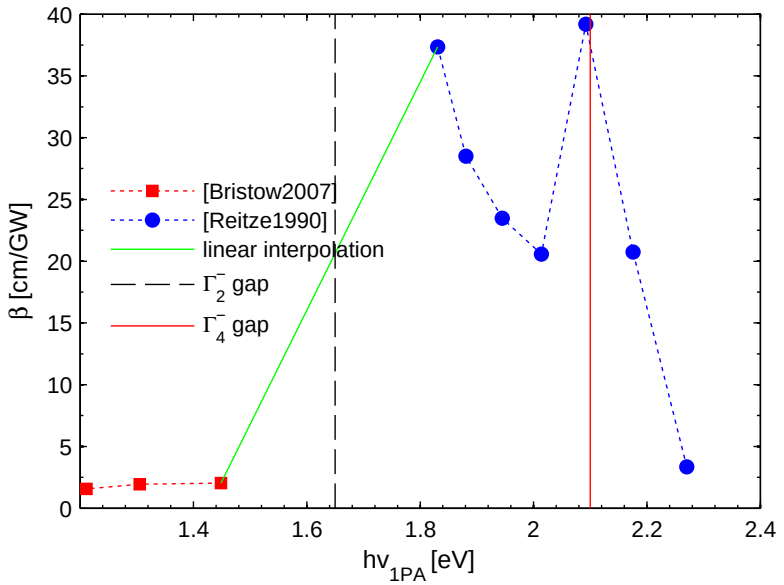


Figure 5.18: Theoretical data on the two-photon cross-section for Si

5.8 Conclusion

The higher relative sensitivity of two-photon optical pumping to the direct optical transitions constitutes the motivation of further study of the subject. A preliminary polarization measurement resulted in a weak positive contribution which was coincident with the position of two-photon part of the EDC.

However, the analysis of spectroscopic data on two-photon absorption is complicated by the problems of spectrometer operation under high optical density irradiation. A modification of power supply electronics can be considered in order to reduce the space charge effects induced by pulsed laser irradiation.

The measurements with high electron affinity remains very challenging due to low signal level, but at the same time represent the guarantee that the captured signal is due to the two-photon process, since the electrons excited with one photon do not possess a sufficiently high energy to escape the crystal.

Chapter 6

Theoretical and modeling aspects of the optical pumping and spin diffusion

6.1 Introduction

In this chapter we review the theoretical models of both of the initial polarization under OP conditions and of its decrease during the electron diffusion towards the sample surface. In particular, the comparative analysis of existing models with of our experimental data allows to draw interesting conclusions about the properties of optical pumping in Silicon. In section 6.8 we analyze the process of spin relaxation which occurs during the electron extraction from the sample.

6.2 Light absorption in semiconductor

The power absorbed by the crystal is proportional to the probability of electronic transition per unit volume multiplied by the energy of each photon absorbed:

$$dI = Th\nu \tag{6.1}$$

where dI is the decrease in the incident light power, T is the transition probability. This quantity can be linked to the dielectric constant by

$$dI = -\frac{dI}{dt} = \frac{c}{n}\alpha I = \frac{2\pi\Im(\epsilon_d)I}{n^2}$$

where c is the speed of light, n is the refractive index and $\Im(\epsilon_d)$ is the imaginary part of the dielectric function. Thus, the absorption spectrum of a semiconductor is determined by the electron transition probability.

6.2.1 Fermi's golden rule

Let us recall the principle of calculating such probability in the case of direct optical transitions. With the use of the vector potential $\boldsymbol{A}$, we write the Hamiltonian describing a system

of electrons:

$$H = \frac{(\boldsymbol{p} + e\boldsymbol{A}/c)^2}{2m_e} + V(r) \tag{6.2}$$

where $\boldsymbol{p} = -i\hbar\boldsymbol{\nabla}$ is the momentum operator of electron, e is the charge of electron, and $V(r)$ is the total potential acting on electron. This Hamiltonian can be decomposed into unperturbed Hamiltonian, describing the system before the application of electromagnetic field, and the perturbing contribution:

$$H = H_0 + \frac{e}{m_e c}\boldsymbol{A}\cdot\boldsymbol{p} \tag{6.3}$$

For simplicity let us consider only the direct optical transitions. Assuming that $\boldsymbol{A}$ is sufficiently small, the time-independent perturbation theory can be used. The Fermi golden rule assess the probability of transition of an electron in a valence state, denoted by $\langle v|$ to a conduction state, denoted by $\langle c|$

$$P = \frac{2\pi}{\hbar}\sum_{\boldsymbol{k}_v,\boldsymbol{k}_k}\left|\langle c|\,\frac{\epsilon}{m_e c}\boldsymbol{A}\cdot\boldsymbol{p}\,|v\rangle\right|^2 \delta(\epsilon_c(\boldsymbol{k}_c) - \epsilon_v(\boldsymbol{k}_v) - h\nu) \tag{6.4}$$

where $\boldsymbol{k}_v$, $\boldsymbol{k}_c$ are wave vectors of respectively valence and conduction states, and ϵ_v, ϵ_v are corresponding eigenenergies. Here the delta function $\delta(\epsilon_c(\boldsymbol{k}_c) - \epsilon_v(\boldsymbol{k}_v) - h\nu)$ imposes the energy conservation.

6.3 Analytical model

In this section we review the analytical calculation of the polarization induced by direct optical transitions at Γ. This calculation is based on the symmetry of wave functions at the center of BZ, which are obtained via group theory considerations.

The derivation of the presented results was initially performed in [Garwin1974] for GaAs (which is equivalent to the polarization given in section 6.3.5), and in [Lampel1968b; Weisbuch1974] for Si (sections 6.3.3 and 6.3.4). These results were later reviewed in [Verhulst2004; Roux2008].

6.3.1 Semiconductor wave functions at $k = 0$

The one-electron crystal Hamiltonian in the absence of spin-orbit coupling is given by

$$H = \frac{p^2}{2m_e} + V(\boldsymbol{r}) \tag{6.5}$$

where $p = -i\hbar\boldsymbol{\nabla}$ is the momentum operator, m_e is the electron mass, $V(\boldsymbol{r})$ is the periodic potential of nuclei. Using the group theory, one can show that the angular part of eigenfunctions of this Hamiltonian are given by spherical harmonics $\mathrm{Y}_{l,m}$ [Fishman2010].

We define the functions S, X, Y, Z as

$$\begin{cases} S = \mathrm{Y}_{0,0} & \text{(6.6a)} \\ X = \dfrac{\mathrm{Y}_{1,-1} - \mathrm{Y}_{1,1}}{\sqrt{2}} & \text{(6.6b)} \\ Y = i\dfrac{\mathrm{Y}_{1,-1} + \mathrm{Y}_{1,1}}{\sqrt{2}} & \text{(6.6c)} \\ Z = \mathrm{Y}_{1,0} & \text{(6.6d)} \end{cases}$$

The basis of $H + H_{so}$ (the spin-orbit coupling Hamiltonian H_{so} is defined in section 3.2.3) is given by

$$\{\langle X\uparrow|, \langle Y\uparrow|, \langle Z\uparrow|, \langle S\uparrow|, \langle X\downarrow|, \langle Y\downarrow|, \langle Z\downarrow|, \langle S\downarrow|\} \tag{6.7}$$

from which we form linear combinations that are the eigenfunctions of $H + H_{so}$. For an entire orbital moment (0 or 1 here) and a half-integer spin, the standard basis $|j; m_j\rangle$ is given by :

For $j = \frac{3}{2}$ (which is the Γ_8^+ valence band):

$$\begin{cases} \left|\frac{3}{2}; -\frac{3}{2}\right\rangle = |Y_{1,-1}; \downarrow\rangle = \left|\dfrac{X - iY}{\sqrt{2}}; \downarrow\right\rangle \\ \left|\frac{3}{2}; -\frac{1}{2}\right\rangle = \left|\frac{1}{\sqrt{3}} Y_{1,-1}; \uparrow\right\rangle + \left|\sqrt{\frac{2}{3}} Y_{1,0}; \downarrow\right\rangle = \left|\dfrac{X - iY}{\sqrt{6}}; \uparrow\right\rangle + \left|\sqrt{\frac{2}{3}} Z; \downarrow\right\rangle \\ \left|\frac{3}{2}; \frac{1}{2}\right\rangle = \left|\sqrt{\frac{2}{3}} Y_{1,0}; \uparrow\right\rangle + \left|\frac{1}{\sqrt{3}} Y_{1,1}; \downarrow\right\rangle = \left|\sqrt{\frac{2}{3}} Z; \uparrow\right\rangle + \left|\dfrac{X + iY}{-\sqrt{6}}; \downarrow\right\rangle \\ \left|\frac{3}{2}; \frac{3}{2}\right\rangle = |Y_{1,1}; \uparrow\rangle = \left|\dfrac{X + iY}{-\sqrt{2}}; \uparrow\right\rangle \end{cases} \tag{6.8}$$

For $j = \frac{1}{2}$ (which is the Γ_7^+ valence band):

$$\begin{cases} \left|\frac{1}{2}; -\frac{1}{2}\right\rangle = -\left|\sqrt{\frac{2}{3}} Y_{1,-1}; \uparrow\right\rangle + \left|\frac{1}{\sqrt{3}} Y_{1,0}; \downarrow\right\rangle = -\left|\dfrac{X - iY}{\sqrt{3}}; \uparrow\right\rangle + \left|\frac{1}{\sqrt{3}} Z; \downarrow\right\rangle \\ \left|\frac{1}{2}; \frac{1}{2}\right\rangle = -\left|\frac{1}{\sqrt{3}} Y_{1,0}; \uparrow\right\rangle + \left|\sqrt{\frac{2}{3}} Y_{1,1}; \downarrow\right\rangle = -\left|\frac{1}{\sqrt{3}} Z; \uparrow\right\rangle - \left|\dfrac{X + iY}{\sqrt{3}}; \downarrow\right\rangle \end{cases} \tag{6.9}$$

The conduction wave functions are obtained by formal replacement of X, Y, Z by X_c, Y_c, Z_c: in this way eq. (6.8) yields the states of Γ_8^- band (denoted by $\left|\frac{3}{2}; -\frac{3}{2}\right\rangle_c$, $\left|\frac{3}{2}; -\frac{1}{2}\right\rangle_c$, $\left|\frac{3}{2}; \frac{1}{2}\right\rangle_c$ and $\left|\frac{3}{2}; \frac{3}{2}\right\rangle_c$), and eq. (6.9) yields Γ_6^- band (denoted by $\left|\frac{1}{2}; -\frac{1}{2}\right\rangle_c$ and $\left|\frac{1}{2}; \frac{1}{2}\right\rangle_c$) [Fishman2010]. The employed notations of different bands are recalled in fig. 6.1.

Γ_7^- is composed of

$$\begin{cases} |S_C\uparrow\rangle = |Y_{0,0}\uparrow\rangle & \text{(6.10a)} \\ |S_C\downarrow\rangle = |Y_{0,0}\downarrow\rangle & \text{(6.10b)} \end{cases}$$

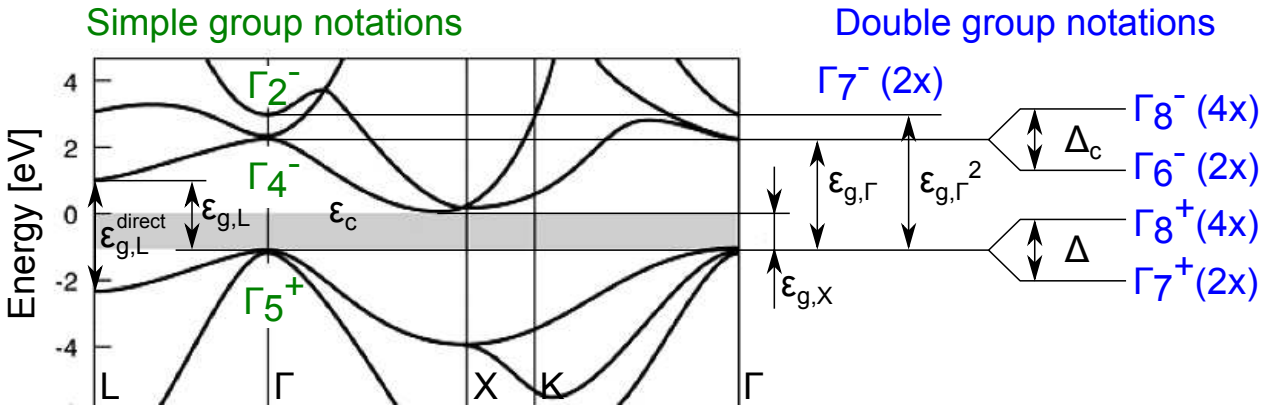


Figure 6.1: Silicon band structure along high symmetry directions calculated by non-local pseudopotential method [Chelikowsky1976]. Bands are labeled according to [Koster1963]. The numbers in parentheses indicate the degeneracy of bands.

6.3.2 Calculation principle

We recall the definition given previously in eq. (3.5):

$$\boldsymbol{e}_+ = \frac{\boldsymbol{e}_x + i\boldsymbol{e}_y}{\sqrt{2}},\ \boldsymbol{e}_- = \frac{\boldsymbol{e}_x - i\boldsymbol{e}_y}{\sqrt{2}} \tag{6.11}$$

Since the vectors above belong to a vector space over complex numbers, $\boldsymbol{e}_+, \boldsymbol{e}_- \in \mathbb{C}^3$, an appropriate scalar product needs to be introduced. For $\boldsymbol{a}, \boldsymbol{b} \in \mathbb{C}^N$ it is defined by

$$(\boldsymbol{a}, \boldsymbol{b})_{\mathbb{C}} = (\boldsymbol{a}, \boldsymbol{b}^*)_{\mathbb{R}} \tag{6.12}$$

where $(\cdot,\cdot)_{\mathbb{R}}$ is usual Euclidean scalar product of $\mathbb{R}^N$ and the asterisk denotes the complex conjugate. Obviously both scalar products coincide for real quantities. The vectors given in eq. (6.11) are orthonormal:

$$(\boldsymbol{e}_+, \boldsymbol{e}_+)_{\mathbb{C}} = (\boldsymbol{e}_+, \boldsymbol{e}_-)_{\mathbb{R}} = \frac{(\boldsymbol{e_x} + i\boldsymbol{e_y}, \boldsymbol{e_x} - i\boldsymbol{e_y})_{\mathbb{R}}}{2} = 1,$$

$$(\boldsymbol{e}_+, \boldsymbol{e}_-)_{\mathbb{C}} = (\boldsymbol{e}_+, \boldsymbol{e}_+)_{\mathbb{R}} = \frac{(\boldsymbol{e}_x + i\boldsymbol{e}_y, \boldsymbol{e}_x + i\boldsymbol{e}_y)_{\mathbb{R}}}{2} = 0.$$

In this section we consider a circularly polarized light propagating along the $\boldsymbol{e}_z$ axis, which is also chosen as the spin quantification axis. Under the electric dipole approximation, the Hamiltonian of the transition is proportional to the scalar product of the momentum operator $\boldsymbol{p}$ and the vector potential $\boldsymbol{A}$:

$$H_{\text{opt}} \propto (\boldsymbol{A}, \boldsymbol{p})_{\mathbb{C}} = (\boldsymbol{A}, \boldsymbol{p})_{\mathbb{R}} \tag{6.13}$$

The second equality holds since both $\boldsymbol{p}$ and $\boldsymbol{A}$ are real. The latter can be expanded in the basis of $\boldsymbol{e}_x$ and $\boldsymbol{e}_y$:

$$\boldsymbol{A} = A_x \boldsymbol{e}_x + A_y \boldsymbol{e}_y$$

Let us expand the same quantity in the basis to $\boldsymbol{e}_+$ and $\boldsymbol{e}_-$:

$$\boldsymbol{A} = A_+\boldsymbol{e}_+ + A_-\boldsymbol{e}_- = \frac{A_x - iA_y}{\sqrt{2}}\frac{\boldsymbol{e}_x + i\boldsymbol{e}_y}{\sqrt{2}} + \frac{A_x + iA_y}{\sqrt{2}}\frac{\boldsymbol{e}_x - i\boldsymbol{e}_y}{\sqrt{2}} = A_x\boldsymbol{e}_x + A_y\boldsymbol{e}_y \tag{6.14}$$

with

$$A_\pm = \frac{A_x \mp iA_y}{\sqrt{2}}$$

The momentum operators corresponding to optical transition is given by

$$\boldsymbol{p} = p_x\boldsymbol{e}_x + p_y\boldsymbol{e}_y = p_+\boldsymbol{e}_+ + p_-\boldsymbol{e}_- \tag{6.15}$$

where

$$p_\pm = \frac{p_x \mp ip_y}{\sqrt{2}} \tag{6.16}$$

are the momentum operators of optical transitions induced by circularly polarized light.

The Hamiltonian of direct optical transition can be decomposed to

$$H_{\text{opt}} \propto (A_+\boldsymbol{e}_+ + A_-\boldsymbol{e}_-, p_+\boldsymbol{e}_+ + p_-\boldsymbol{e}_-)_{\mathbb{C}} = A_+p_- + A_-p_+ = (A_+, p_+)_{\mathbb{C}} + (A_-, p_-)_{\mathbb{C}} \tag{6.17}$$

The term $(A_+, p_+)_{\mathbb{C}}$ corresponds to the absorption of σ^+, or equivalently to the emission of σ^- [Fishman1974].

In a crystal belonging to the O_h symmetry group, the matrix element of operator O between the states $\langle c|$, $|v\rangle$, which transforms like $x^\alpha y^\beta z^\gamma$, is given by [Fishman2010]:

$$\langle c \,|\, O \,|\, v\rangle \propto \left\langle x^\alpha y^\beta z^\gamma \right\rangle = \begin{cases} 0 & \text{if each of } \alpha, \beta \text{ and } \gamma \text{ is even} \\ \text{non-zero} & \text{otherwise} \end{cases} \tag{6.18}$$

The calculation of the initial electronic polarization involves the probabilities of transitions between the valence band and conduction band. In order to calculate the transition probabilities, the terms of the form $\langle c \,|\, p^+ \,|\, v\rangle$ between the valence state v and the conduction state c are to be calculated. Table 6.1 presents the symmetries of wave functions at $k = 0$. The momentum operators p_x and p_y are transformed as x and y respectively. According to eq. (6.18), the only non-zero elements are of the form:

$$\langle Y_C \,|\, p_x \,|\, Z\rangle = \langle Z_C \,|\, p_x \,|\, Y\rangle = \langle X_C \,|\, p_y \,|\, Z\rangle = \langle Z_C \,|\, p_y \,|\, X\rangle = \mathcal{P}_X \tag{6.19}$$

Band		Wave function	Symmetry
Simple group	Double group		
Γ_2^-	Γ_7^-	S_C	xyz
Γ_4^-	Γ_6^-, Γ_8^-	X_C, Y_C, Z_C	x, y, z
Γ_5^+	Γ_7^+, Γ_8^+	X, Y, Z	yz, zx, xy

Table 6.1: Wave functions symmetries at Γ for a crystal belonging to O_h point group [Fishman2010]

and

$$\langle S_C \,|\, p_x \,|\, X\rangle = \langle S_C \,|\, p_y \,|\, Y\rangle = \mathcal{P} \tag{6.20}$$

We aim to calculate the average initial polarization of the photoexcited electrons in the conduction band. The calculation of the average polarization is done using the density matrix formalism, which is written for σ^+ polarization, in a certain space of the conduction band functions:

$$\rho = \sum_v (p_+)^* \,|v\rangle \,\langle v|\, p_+ \tag{6.21}$$

Note that defined in eq. (6.16) p_+ is the complex conjugate of p^+ from (2-22) of [Roux2008], but this difference is accounted for in eq. (6.21) in order to preserve the correct sign of the polarization. The advantage of the presented here notation is the consistency between eq. (6.14) and eq. (6.15).

The operator S_z, which is the projection of the spin operator $\boldsymbol{S}$ on $\boldsymbol{e}_z$, is given in the same space of conduction wave functions:

$$S_z = \sum_c |c\rangle \,\langle c|\, \sigma_z \tag{6.22}$$

where the Pauli matrix $\sigma_z = \frac{\hbar}{2}\begin{pmatrix} 1 & 0 \\ 0 & -1 \end{pmatrix}$. The initially created electron polarization is defined by:

$$P_i = \frac{\mathrm{tr}[\rho S_z]}{\mathrm{tr}[S_z]} \tag{6.23}$$

where $\mathrm{tr}[S_z]$ is the mean value of S_z calculated on the basis of the conduction band. In the following calculations of analytical polarization, $\hbar/2$, which appears in both numerator and denominator of eq. (6.23), will be omitted for simplicity.

6.3.3 Polarization of virtual state for near-indirect gap excitation

The polarization of direct part of fundamental optical transition can be calculated via the described above method. We consider the basis composed of

$$\{\Gamma_6^-, \Gamma_8^-\} = \left\{ \left|\frac{1}{2}; -\frac{1}{2}\right\rangle_c, \left|\frac{1}{2}; \frac{1}{2}\right\rangle_c \right\}, \left|\frac{3}{2}; -\frac{3}{2}\right\rangle_c, \left|\frac{3}{2}; -\frac{1}{2}\right\rangle_c, \left|\frac{3}{2}; \frac{1}{2}\right\rangle_c, \left|\frac{3}{2}; \frac{3}{2}\right\rangle_c$$

as possible final states. For the transitions originating from the upper valence band, eq. (6.21) yields

$$\rho(\Gamma_8^+ \to \{\Gamma_6^-, \Gamma_8^-\}) = \frac{|\mathcal{P}_X|^2}{3} \begin{pmatrix} 2 & 0 & 0 & 0 & 0 & 0 \\ 0 & 0 & 0 & 0 & 0 & 0 \\ 0 & 0 & 2 & 0 & 0 & -\sqrt{2} \\ 0 & 0 & 0 & 0 & 0 & 0 \\ 0 & 0 & 0 & 0 & 3 & 0 \\ 0 & 0 & -\sqrt{2} & 0 & 0 & 1 \end{pmatrix}$$

and eq. (6.22) results in

$$S(\{\Gamma_6^-,\Gamma_8^-\}) = \frac{1}{3}\begin{pmatrix} -3 & 0 & 0 & 0 & 0 & 0 \\ 0 & -1 & 0 & 0 & -2\sqrt{2} & 0 \\ 0 & 0 & 1 & 0 & 0 & -2\sqrt{2} \\ 0 & 0 & 0 & 3 & 0 & 0 \\ 0 & -2\sqrt{2} & 0 & 0 & 1 & 0 \\ 0 & 0 & -2\sqrt{2} & 0 & 0 & -1 \end{pmatrix}$$

Thus, if the photon energy is in the range $h\nu \in [\epsilon_{g,X}, \epsilon_{g,X} + \Delta_{\mathrm{SO}}[$, the use of eq. (6.23) provides the expected polarization of the direct part of the optical transition from Γ:

$$P_i(\Gamma_8^+ \to \{\Gamma_6^-,\Gamma_8^-\}) = \frac{1}{4} \tag{6.24}$$

Contrary to [Verhulst2004], where $P_i(\Gamma_8^+ \to \{\Gamma_6^-,\Gamma_8^-\}) = -0.25$ for σ^+ circularly polarized light, we find $+0.25$ for σ^+, in agreement with [Nastos2007; Roux2008].

One should note that accounting for the contribution of Γ_7^- band results in lower polarization. Indeed

$$P_i(\Gamma_8^+ \to \{\Gamma_6^-,\Gamma_8^-,\Gamma_7^-\}) = \frac{-|P|^2 + |P_X|^2}{2|P|^2 + 4|P_X|^2} < \frac{1}{4} \tag{6.25}$$

Taking $\mathcal{P} = \sqrt{\frac{\hbar^2}{2m_0}19.96\,\mathrm{eV}}$ and $\mathcal{P}_X = \sqrt{\frac{\hbar^2}{2m_0}14.85\,\mathrm{eV}}$ [Richard2004b], we obtain negative polarization

$$P_i(\Gamma_8^+ \to \{\Gamma_6^-,\Gamma_8^-,\Gamma_7^-\}) = -0.051 \tag{6.26}$$

The introduction of energy denominators $\epsilon_{g,\Gamma}^2 - \epsilon_{g,X}$ and $\epsilon_{g,\Gamma} - \epsilon_{g,X}$, which describe the energy difference between the virtual and conduction states, results in

$$P_i(\Gamma_8^+ \to \{\Gamma_6^-,\Gamma_8^-,\Gamma_7^-\}) = \frac{\frac{-|\mathcal{P}|^2}{(\epsilon-\epsilon_{g,\Gamma}^2)^2} + \frac{|\mathcal{P}_X|^2}{(\epsilon-\epsilon_{g,\Gamma})^2}}{\frac{2|\mathcal{P}|^2}{(\epsilon-\epsilon_{g,\Gamma}^2)^2} + \frac{4|\mathcal{P}_X|^2}{(\epsilon-\epsilon_{g,\Gamma})^2}} = +0.06 \tag{6.27}$$

which is intermediate between the values of the polarization values given in eq. (6.24) and eq. (6.26).

Within the same framework it follows that for $h\nu \in [\epsilon_{g,X} + \Delta_{\mathrm{SO}}, \epsilon_{g,\Gamma}[$:

$$P_i(\{\Gamma_7^+,\Gamma_8^+\} \to \{\Gamma_6^-,\Gamma_8^-\}) = 0 \tag{6.28}$$

In fact, since in eq. (6.28) we do not consider the conduction band splitting induced by H_{so}, the same result can be obtained directly in the basis given eq. (6.7) and corresponding conduction states.

6.3.4 First direct gap

In the case of direct optical transitions, the final state consists of only one zone. For the first direct transition $\Gamma_8^+ \to \Gamma_6^-$ the density matrix is given by

$$\rho(\Gamma_8^+ \to \Gamma_6^-) = \frac{|\mathcal{P}_X|^2}{3}\begin{pmatrix} 3 & 0 \\ 0 & 1 \end{pmatrix}$$

and the spin projection

$$S_z(\Gamma_6^-) = \frac{1}{3}\begin{pmatrix} 1 & 0 \\ 0 & -1 \end{pmatrix}$$

Equation (6.22) yields

$$P_i(\Gamma_8^+ \to \Gamma_6^-) = \frac{1}{6}$$

This result coincides with the initial polarization P_i for $k = 0$ and $h\nu = \epsilon_{g,\Gamma}$. According to the symmetry considerations, P_i is a continuous function of k in Γ. If the excitation energy is slightly larger than $\epsilon_{g,\Gamma}$, the direct optical transition of maximum final state energy takes place in the neighborhood of Γ, and P_i stays close to $P_i(\Gamma_8^+ \to \Gamma_6^-)$. Another argument in favor of this assertion is the weak dependence $P_i(h\nu)$ for GaAs [Allenspach1984], as well as the dependence $P_i(h\nu)$, numerically integrated all over the BZ (fig. 2.3).

Thus, in a first approximation

$$P_i \approx \frac{1}{6} \text{ for } h\nu \in [\epsilon_{g,\Gamma}, \epsilon_{g,\Gamma} + \Delta_{\text{SO}}^c[\tag{6.29}$$

Strictly speaking, the polarization of direct transition at $h\nu = \epsilon_{g,\Gamma} + \Delta_{\text{SO}}^c$ is already given by $P_i(\Gamma_8^+ \to \Gamma_8^-)$ transition and not by $P_i(\Gamma_8^+ \to \Gamma_6^-)$, from which it follows the excluding square bracket [in eq. (6.29).

Similarly, for $\Gamma_8^+ \to \Gamma_8^-$ transition, the density matrix reads

$$\rho(\Gamma_8^+ \to \Gamma_8^-) = \frac{2|\mathcal{P}_X|^2}{3}\begin{pmatrix} 1 & 0 & 0 & 0 \\ 0 & 0 & 0 & 0 \\ 0 & 0 & 1 & 0 \\ 0 & 0 & 0 & 0 \end{pmatrix}$$

and the spin projection

$$S_z(\Gamma_8^-) = \frac{1}{3}\begin{pmatrix} -3 & 0 & 0 & 0 \\ 0 & -1 & 0 & 0 \\ 0 & 0 & 1 & 0 \\ 0 & 0 & 0 & 3 \end{pmatrix}$$

The mean value of spin projection

$$P_i(\Gamma_8^+ \to \Gamma_8^-) = -\frac{1}{3} \tag{6.30}$$

The bands Γ_7^+ and Γ_6^- are not coupled for $k = 0$, and so no optical transition takes place between these bands at Γ. Thus,

$$P_i \approx -\frac{1}{3} \text{ for } h\nu \in [\epsilon_{g,\Gamma} + \Delta_{\text{SO}}^c; \epsilon_{g,\Gamma} + \Delta_{\text{SO}} + \Delta_{\text{SO}}^c[$$

For the highest energy transition

$$P_i(\Gamma_7^+ \to \Gamma_8^-) = -\frac{1}{2}$$

which indicates the approximate polarization for $h\nu \gtrsim \epsilon_{g,\Gamma} + \Delta_{\text{SO}} + \Delta_{\text{SO}}^c$

6.3.5 Second direct gap

The symmetry of states involved in the optical transitions at the second direct gap of Silicon coincides with that of the fundamental gap of GaAs.

The Γ_7^- wave functions at $k = 0$ are given by $\{|S_C \uparrow\rangle, |S_C \downarrow\rangle\}$.

We obtain

$$\rho(\Gamma_8^+ \to \Gamma_7^-) = \frac{|\mathcal{P}|^2}{3} \begin{pmatrix} 1 & 0 \\ 0 & 3 \end{pmatrix}$$

and trivially

$$S_z(\Gamma_6^-) = \begin{pmatrix} 1 & 0 \\ 0 & -1 \end{pmatrix}$$

In this manner, the transition from Γ_5^+ band produces the spin polarization similar to that of the first direct gap of GaAs. In fact, the mean value of S_z operator is

$$P_i(\Gamma_8^+ \to \Gamma_7^-) = -\frac{1}{2}$$

and

$$P_i(\Gamma_7^+ \to \Gamma_7^-) = 1$$

The overall polarization is

$$P_i \approx -\frac{1}{2} \text{ for } h\nu \in [\epsilon_{g,\Gamma}^2; \epsilon_{g,\Gamma}^2 + \Delta_{\text{SO}}[\tag{6.31}$$

For $h\nu > \epsilon_{g,\Gamma}^2 + \Delta_{\text{SO}}$, a decrease of initial polarization probably takes place, similarly to that in GaAs (fig. 2.3).

6.4 Numerical models

In this section, a comparative analysis of existing models of optical pumping is carried out. Particular attention is paid to the remaining open issues in the modeling of OP in Silicon.

The term degree of spin polarization (DSP), used in numerical studies, is a synonym of the initial polarization of electrons along $\boldsymbol{e}_z$, denoted by P_i in the experimental part of the present work. In all of the following models the electron spin is quantified along $\boldsymbol{e}_z$ direction.

6.4.1 Indirect transitions

Li and Dery calculate the polarization of luminescence due to the recombination of 100 %-polarized $|\uparrow\rangle$ electrons in conduction band. Since the light propagates along $\boldsymbol{e}_z$, $\hat{x} + i\hat{y}$ corresponds to $E\boldsymbol{e}_+$, which results in σ^+ polarization. The light polarization is defined as ratio

$$P = \frac{I_{\sigma^+} - I_{\sigma^-}}{I_{\sigma^+} + I_{\sigma^-}}$$

The calculated polarization is of -0.23 for transverse acoustic (TA) phonons, and -0.14 for other phonon modes (the photoluminescence peak which is situated lower by 50 meV on the energy scale) [Li2010].

To date, the most accurate calculation of the polarization of indirect optical transitions in Silicon was made by Cheng et al. In particular, their work is the only one where a non-zero temperature is accounted for. An empirical pseudopotential model is used for electron states, and phonons are described by adiabatic bond charge model. Light propagates in $[\bar{1}\,0\,0]$ (i.e. $-\boldsymbol{e}_z$) direction, so the $E \propto (\hat{x} - i\hat{y})/\sqrt{2} \parallel \boldsymbol{e}_+$ corresponds to σ^+ in our notation [1]. According to symmetry of valence states at Γ, to the symmetry of conduction states at the minimum of Γ_4^-, and to the symmetry of phonons, the band edge polarization of -0.095 is obtained.

The key information from fig. 6.2 is the strong anisotropy of the band edge polarization: the electrons from Z valley (which is longitudinal to the light excitation direction) exhibit up to $+0.08$ of the polarization, whereas their counterparts from X valley (transverse) are up to -0.25 negatively polarized.

The band edge value of spin polarization, numerically integrated on a dense grid in the BZ, is -0.15 independently of temperature (fig. 6.2).

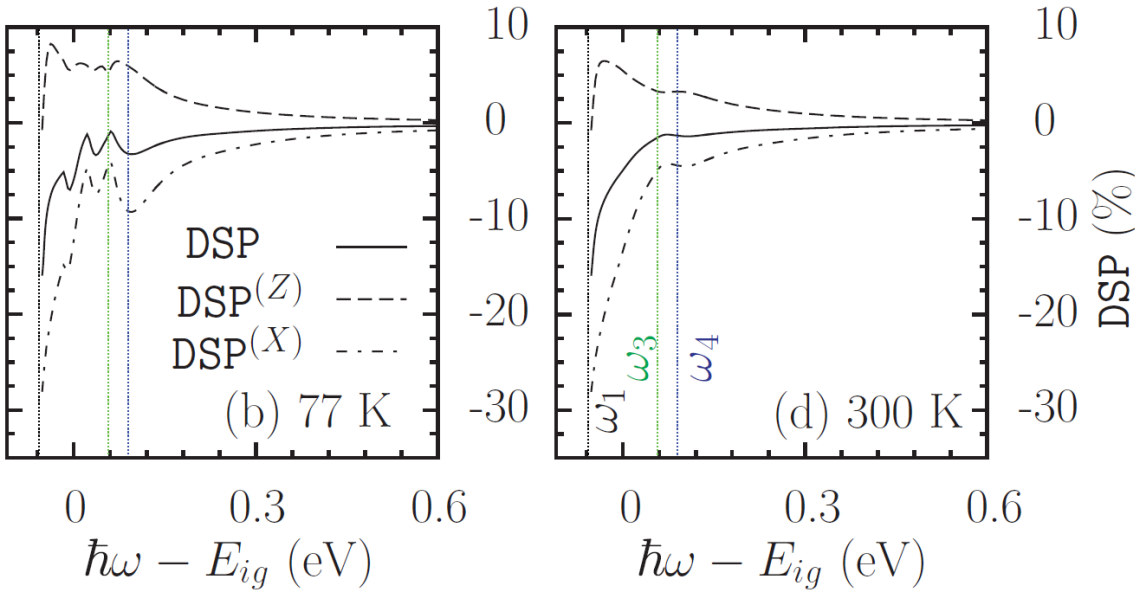


Figure 6.2: Calculated initial polarization of indirect transitions for 77 K (left) and 300 K (right) [Cheng2011a]

The analytical expression for the direct component of the optical transitions was initially proposed as an approximation for band-edge value of P_i by [Lampel1968b], and later reconsidered by Roux and Verhulst. As detailed in section 6.3.3, for the light propagating along $\boldsymbol{e}_z$ and $\boldsymbol{E} \parallel \boldsymbol{e}_x + i\boldsymbol{e}_y$, the predicted polarization is

$$P_i = \begin{cases} 0.25 & \text{for } h\nu < \epsilon_{g,X} + \epsilon_{SO} + \epsilon_{\text{ph}} \\ 0 & \text{otherwise} \end{cases} \tag{6.32}$$

Neglecting the phonon-assisted part of the transitions (eq. (6.24)), even if Γ_2^- band is accounted for (eq. (6.27)) results in the polarization of different sign compared to more

[1] The space $\mathbb{C}^3$ is isomorphic to $\mathbb{R}^6$. The notion of parallelism in $\mathbb{C}^3$ can thus be seen as parallelism of corresponding elements of $\mathbb{R}^6$.

accurate calculations. It is interesting to note that both [Li2010] and [Cheng2011a] predict band-edge polarization of the same sign and relatively similar in absolute value.

The comparison of the experimental data with [Cheng2011a] allows to conclude that the polarized photoemission setup is sensitive to the electrons both from longitudinal and transverse to light excitation direction valleys. In fact, if the setup would collect only the electrons from Z valley, this would result in positive measured polarization near the fundamental band gap.

The question of the polarization of photoelectrons emitted from (1 1 1)-oriented sample is still to be addressed in further numerical simulations. As it is shown for two-photon absorption [Cheng2011c], the polarization of two-photon indirect optical transitions vary between (1 0 0) and (1 1 1) due to the difference in the intensities of the optical transitions in different valleys of the conduction band. A similar effect may a priori take place for one-photon indirect optical transitions.

Another important open issue is the analysis of the influence of excitonic effects on the polarization. Indeed, the order of magnitude of binding energy of excitons in Silicon is 15 meV [Bludau1974], and thus may be comparable to the Δ_{SO} for some temperatures and doping levels, in which case the excitons may a priori influence the polarization.

6.4.2 Direct transitions

Nastos et al. calculate the polarization of direct optical transitions in GaAs and Silicon within LDA and k.p frameworks. For the ab initio calculation, the authors use local spin density approximation with Hartwigsen Goedecker Hutter (HGH) pseudopotential. A rigid shift of conduction bands is applied in order to rectify the underestimated within LDA band gap. For comparison, the authors review the analytical models for P_i in the case of Silicon and GaAs, with the polarization at Γ in agreement with that calculated in section 6.3.

The authors consider light propagating along $-\boldsymbol{e}_z$ and the electric field described by $E(\omega) = E_0(\hat{x} - i\hat{y})/\sqrt{2} \parallel \boldsymbol{e}_-$, which results in σ^+ light excitation according to the notations of the present work. However, all the obtained polarization values (both analytically and numerically calculated, for both GaAs and Si) correspond to σ^- excitation, which probably implies the presence of a supplementary detail not mentioned in the article and affecting the sign of the polarization.

It is important to emphasize, that the numerically calculated initial polarization is in fact energy-averaged over admissible direct transitions. For excitation energy $h\nu \gtrsim \epsilon_{g,\Gamma}$, this quantity stays close to P_i, since the direct transitions with such $h\nu$ appear for $k \approx 0$. As the excitation energy increases, the direct transitions may appear all over the BZ, and the calculated quantity reproduces distribution-averaged polarization $\langle P_i \rangle$ rather than the high-energy threshold polarization P_i.

Figure 6.3 presents the polarization calculated within k.p and LDA models. For k.p model (dashed line in the left panel of fig. 6.3), one can note a low polarization of the absorption onset $P(3.36\,\mathrm{eV}) = -0.05$ In fact, in the k.p calculation, where the direct gap is not located at the Γ point, it is the off-zone-center states that contribute near the onset of absorption. These states do not exhibit the high symmetry of Γ, which leads to $P(3.36\,\mathrm{eV}) < P(\epsilon_{g,\Gamma} = 3.4\,\mathrm{eV}) = -0.2$.

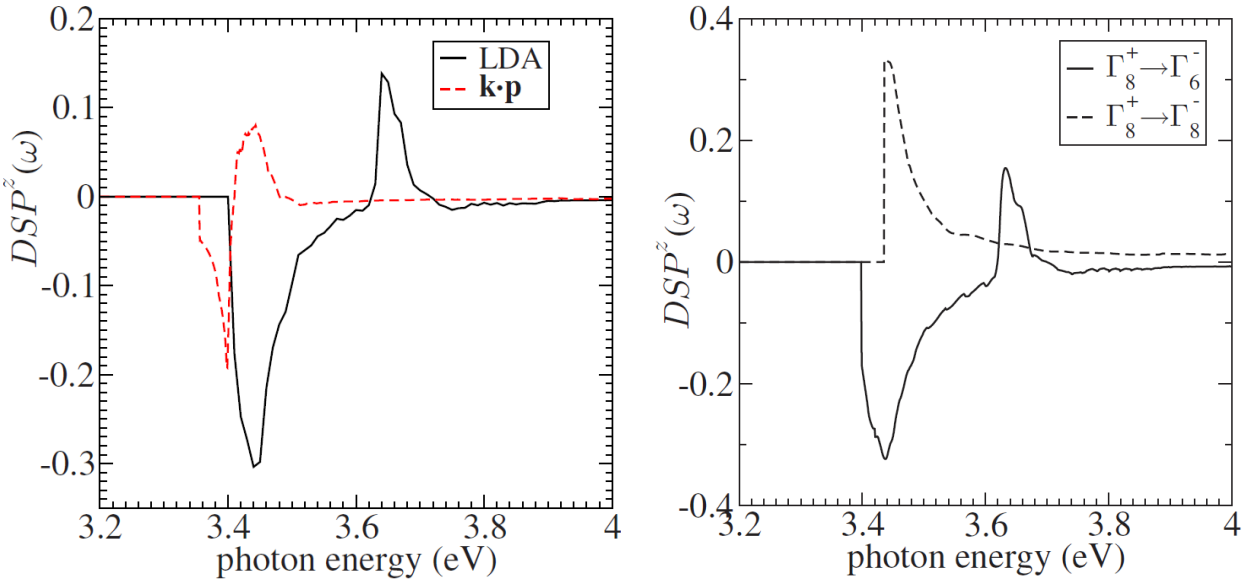


Figure 6.3: The initial polarization calculated with LDA and k.p methods (left). Initial polarization separated into contributions from different bands, calculated with LDA (right). The transitions from Γ_7^+ band make a small contribution to the total polarization, and are not shown.

The right panel of fig. 6.3 presents the band-resolved polarization. The transitions from the split-off band (Γ_7^+) are weakly coupled so they are excluded from the consideration. Shown in the right panel maximum of absolute value of polarization $\Gamma_8^+ \rightarrow \Gamma_8^-$ of 0.34 (under σ^- excitation) is in excellent agreement with analytically calculated value given by eq. (6.30).

The positive (under σ^- excitation) contribution of $\Gamma_8^+ \rightarrow \Gamma_8^-$ with maximum at $h\nu = 3.65\,\text{eV}$ closely corresponds to $\epsilon_{g,L}^{\text{direct}} = 3.62\,\text{eV}$ for HGH pseudopotential, and thus constitute a probable explanation of experimentally observed in our data negative (under σ^+ excitation) contribution to PEDC, attributed to the transitions away from the zone center (section 4.3.7). As shown in the right panel of fig. 6.4, even if such direct transitions at $h\nu \approx \epsilon_{g,L}^{\text{direct}}$ can occur for both $\Gamma - L$ and $\Gamma - X$ directions,

- The band is flatter in L direction, and thus the number of admissible transitions is higher in $\Gamma - L$ rather in $\Gamma - X$ direction
- The transitions to L valley occur farther from the center of the zone, which has a positive polarization. Since the variation of the polarization is expected to be gradual, the transitions to L valley are likely to have higher negative polarization than the transitions close to Γ in $\Gamma - X$ direction.

However, given that the negative polarization in PEDCs is observed for $h\nu$ starting from $2.5 - 3\,\text{eV}$, it cannot be explained only by the direct transitions. As shown in the left panel of fig. 6.4, the negative polarization for $\epsilon < \epsilon_{g,L} - \epsilon_{g,X} \approx 1.1\,\text{eV}$ can be interpreted as due to

- the indirect transitions in $\Gamma - X$ direction
- the interband relaxation of electrons created in L valley

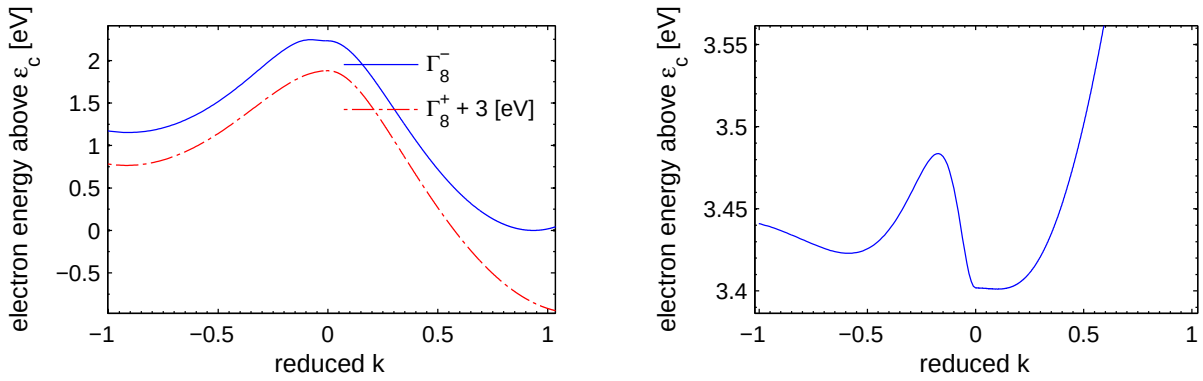


Figure 6.4: Comparison between the energy of Γ_6^-, shifted by 3 eV ($\epsilon_{\Gamma_6^-} + 3\,\mathrm{eV}$) and the energy of Γ_8^+ band ($\epsilon_{\Gamma_8^+}$) (left). Difference $\epsilon_{\Gamma_6^-} - \epsilon_{\Gamma_8^+}$ (right). $k < 0$ correspond to $\Gamma - L$ direction, $k > 0$ correspond to $\Gamma - X$ direction. The band structure is calculated by 30 band k.p method [Richard2004b].

The ratio of calculated polarizations (σ^-)

$$\frac{P_i(3.65\,\mathrm{eV})}{P_i(3.44\,\mathrm{eV})} = \frac{0.15}{-0.3} \tag{6.33}$$

is substantially greater than the ratio of experimentally measured polarizations (σ^+)

$$\frac{P_i(3.4\,\mathrm{eV})}{P_i(3.3\,\mathrm{eV})} = \frac{-0.01}{0.07} \tag{6.34}$$

Such difference is probably due to large contribution of unpolarized relaxed electrons, which participate in the photoemission from L valley. Since this negative component of PEDCs is well reproduced within the model accounting for direct transitions only, one can make the assumption of negligible influence of indirect transitions to the negative part of PEDCs.

The opened question is why the polarization raises from $P(\epsilon_{g,\Gamma}) = P(3.4\,\mathrm{eV}) = -0.167$ to $P(\epsilon_{g,\Gamma} + \Delta^c_{\mathrm{SO}}) = P(3.45\,\mathrm{eV}) = -0.3$, whereas the analytical model at Γ predicts $P(\epsilon_{g,\Gamma}) = -\frac{1}{6}$ and $P(\epsilon_{g,\Gamma} + \Delta^c_{\mathrm{SO}}) = \frac{1}{3}$ (in the case of σ^- excitation).

A priori, the transitions away from the zone center may create higher polarization than that in Γ. However, the fact that maximum polarization of k.p model is attained in $\epsilon_{g,\Gamma} = 3.4\,\mathrm{eV}$, as well as general symmetry considerations, are inconsistent with the hypothesis. The analysis of not presented in [Nastos2007] polarization spectrum (i.e. P_i versus energy of final states) may reveal important information in regards to this question.

Like for k.p model, such onset of the polarization could be at least partially explained by the fact that due to numerical issues the lowest energy transition does not exactly correspond to the transitions at Γ point. In this case, $P(3.45\,\mathrm{eV}) = P(\epsilon_{g,\Gamma}) = -0.3$ higher in absolute value than the analytical predictions, but at least consistent with it in sign.

The polarization for excitation energy $\epsilon^2_{g,\Gamma}$, which is located at 4.28 eV for HGH pseudopotential, is not calculated. It would also be of interest to confirm that considering only transitions at Γ the polarization corresponding to that analytically calculated in section 6.3 is obtained.

The PEDC measurement on GaAs with the excitation within $[\epsilon_g, \epsilon_g + \Delta_{\mathrm{SO}}]$ result in initial polarization of -0.45 [Drouhin1985], which is quite close to the theoretically predicted -0.5 (section 6.3.5). However, the difference between measured and theoretically predicted polarization of ballistic electrons under the excitation in vicinity of first direct band gap of Silicon constitutes

$$\frac{P_{\mathrm{measured}}}{P_{\mathrm{th}}} = \frac{0.06}{1/6} = 0.36 \tag{6.35}$$

The low measured polarization of ballistic electron may be interpreted as a mixture of positive contribution of $\Gamma_8^+ \to \Gamma_6^-$ direct transition and the negative contribution of $\Gamma_8^+ \to \Gamma_8^-$, and $\Gamma_7^+ \to \Gamma_8^-$ indirect transitions. The interpretation of eq. (6.35) would require a complete modeling of OP, which would account for both direct and indirect transitions for $h\nu \approx \epsilon_{g,\Gamma}$.

The similarity of the total polarization calculated by LDA (solid curve in the left panel of fig. 6.3) and the contribution the first transition $\Gamma_8^+ \to \Gamma_6^-$ clearly indicates the minority of the polarization attributed to other ($\Gamma_8^+ \to \Gamma_8^-$, $\Gamma_7^+ \to \Gamma_8^-$) transitions. Such disproportion provides an explanation to the absence of clear negative contribution in the polarization of ballistic electrons, discussed in section 4.3.6.

6.5 Calculation algorithm

We follow the algorithm proposed in [Cheng2011a] within the framework of ABINIT. In this section v denotes valence bands, n, c denote conduction bands, $\boldsymbol{k}_v$ and $\boldsymbol{k}_c$ are hole and electron wave vectors, $\epsilon_{v\boldsymbol{k}_v}$ and $\epsilon_{c\boldsymbol{k}_c}$ are the eigenenergies of valence and conduction bands respectively. $\hbar\Omega_{\boldsymbol{q}\lambda}$ is the phonon energy at wave vector $\boldsymbol{q}$ and mode λ, $N_{\boldsymbol{q}\lambda}$ is the equilibrium phonon number.

For an electric field $E(t) = E_\omega e^{-i\omega t}$ the carrier and spin injection rates can be written as

$$\begin{cases} \dfrac{d}{dt} n(T,\omega) &= \xi^{ab}(T,\omega) E^a_\omega (E^b_\omega)^* \quad (6.36a) \\ \dfrac{d}{dt} S^f(T,\omega) &= \zeta^{fab}(T,\omega) E^a_\omega (E^b_\omega)^* \quad (6.36b) \end{cases}$$

here $\xi^{ab}(T,\omega)$ and $\zeta^{fab}(T,\omega)$ are the injection coefficients for carriers and spins, respectively, at temperature T and excitation energy $\hbar\omega$. The superscript Roman characters denote Cartesian coordinates, and repeated superscripts are to be summed over.

The algorithm can be decomposed into following steps:

1. Calculate the matrix elements of electron-phonon interaction

$$M_{\bar{c}\boldsymbol{k}_c \bar{v}\boldsymbol{k}_v,\lambda} = \langle \bar{n}\boldsymbol{k}_c \,|\, H^{ep}_\lambda(\boldsymbol{k}_c - \boldsymbol{k}_v) \,|\, \bar{m}\boldsymbol{k}_v \rangle \tag{6.37}$$

where the unperturbed electron Hamiltonian is given by

$$H^{ep}_\lambda = \sum_{\boldsymbol{q}\lambda} H^{ep}_\lambda(\boldsymbol{q})(a_{\boldsymbol{q}\lambda} + a^\dagger_{\boldsymbol{q}\lambda}) \tag{6.38}$$

with $a_{\boldsymbol{q}\lambda}$ and $a^\dagger_{\boldsymbol{q}\lambda}$ being the phonon creation and annihilation operators respectively. During the calculation of matrix elements, it was found useful to add a non-zero smearing for the calculation of perturbations, in order to populate the conduction band.

2. Calculate the gradient of electron dispersion relation

$$v_{\bar{n}\bar{m}\boldsymbol{k}} = \left\langle \bar{n}\boldsymbol{k} \left| \frac{\partial H_e}{\partial \boldsymbol{p}} \right| \bar{m}\boldsymbol{k} \right\rangle \tag{6.39}$$

3. Calculate the transition matrix elements

$$T^a_{\bar{c}\boldsymbol{k}_c\bar{v}\boldsymbol{k}_v\lambda} = \frac{e}{\hbar\omega} \sum_{\bar{n}} \left(\frac{M_{\bar{c}\boldsymbol{k}_c\bar{n}\boldsymbol{k}_v,\lambda} \boldsymbol{v}^a_{\bar{n}\bar{v}\boldsymbol{k}_v}}{\omega - \omega_{nv\boldsymbol{k}_v}} + \frac{\boldsymbol{v}^a_{\bar{c}\bar{n}\boldsymbol{k}_c} M_{\bar{n}\boldsymbol{k}_c\bar{v}\boldsymbol{k}_v,\lambda}}{\omega_{cn\boldsymbol{k}_c} - \omega} \right) \tag{6.40}$$

where $\bar{v} = \{v, \sigma_v\}$ is the valence band index, $\bar{c} = \{c, \sigma_c\}$ is the valence band index, $\bar{n} = \{n, \sigma_n\}$ is the band index of virtual state. $\boldsymbol{k}_v$ and $\boldsymbol{k}_c$ are the valence and conduction wave vectors respectively.
The energy difference between bands n and m at wave vector $\boldsymbol{k}$ is defined by

$$\hbar\omega_{nm\boldsymbol{k}} = \epsilon_{n\boldsymbol{k}} - \epsilon_{m\boldsymbol{k}}$$

For the same initial state $\bar{v}$ in valence band and final state $\bar{c}$ in conduction band, two mechanisms are possible (fig. 6.5). One mechanism is a virtual direct optical transition from $\bar{v}$ to $\bar{n}$ followed by a phonon-assisted transition to final state $\bar{c}$. A second mechanism is a phonon-assisted transition to another intermediate state $\bar{n}'$, followed by a direct transition to $\bar{c}$. The second mechanism is weaker than first one due to large energy denominator

$$\omega_{cn\boldsymbol{k}_c} - \omega > \omega - \omega_{nv\boldsymbol{k}_v}$$

so the most important transition occurs in the conduction band. In the particular case of optical transitions originating from Γ, the phonon transition in the valence band involves all phonon modes, whereas the conduction band path does not imply LO phonons [Lax1961].

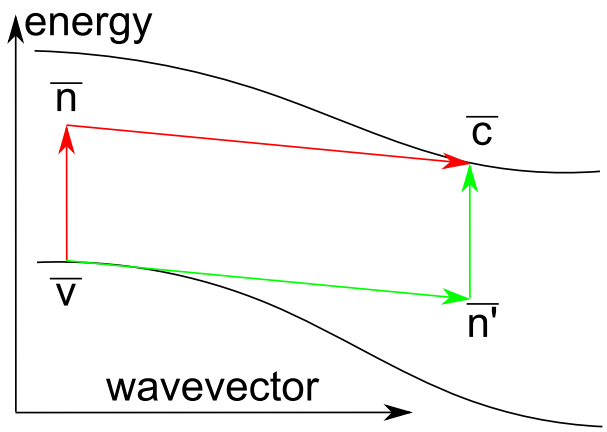


Figure 6.5: Two interfering paths of an indirect transition in the case of phonon emission

4. Calculate $\langle \bar{c}'\boldsymbol{k}_c \,|\, \mathcal{A} \,|\, \bar{c}\boldsymbol{k}_c \rangle$. In the case of spin injection $\mathcal{A}$ are the Pauli matrices.

5. Choose the admissible transitions, which respect the energy conservation

$$N_a = \{\{\bar{c}\boldsymbol{k}_c, \bar{v}\boldsymbol{k}_v, \lambda, \pm\} | \text{ such that } \epsilon_{c\boldsymbol{k}_c} - \epsilon_{v\boldsymbol{k}_v} \pm \hbar\Omega_{(\boldsymbol{k}_c - \boldsymbol{k}_v)\lambda} - \hbar\omega = 0\} \tag{6.41}$$

   where $\pm$ denotes the phonon emission $(+)$ or absorption $(-)$.

6. Using the Fermi golden rule, calculate the injection coefficients at given initial wave vector $\boldsymbol{k}_c$ and final wave vector $\boldsymbol{k}_v$.

$$A^{ab}_{\bar{c}\boldsymbol{k}_c\bar{v}\boldsymbol{k}_v\lambda\delta} = \sum_{\sigma'_c} \langle \bar{c}'\boldsymbol{k}_c \,|\, \mathcal{A} \,|\, \bar{c}\boldsymbol{k}_c \rangle \, T^a_{\bar{c}\boldsymbol{k}_c\bar{v}\boldsymbol{k}_v\lambda} (T^a_{\bar{c}\boldsymbol{k}_c\bar{v}\boldsymbol{k}_v\lambda})^* \tag{6.42}$$

   Here A can denote either the spin injection coefficient ζ, or the carrier injection coefficient ξ, introduced in eq. (6.36). These coefficients need to be calculated only for allowed transitions.

7. Perform the sum over wave vectors and phonon modes

$$A^{ab} = \frac{2\pi}{\hbar} \sum_{\{\bar{c}\boldsymbol{k}_c, \bar{v}\boldsymbol{k}_v, \lambda, \pm\} \in N_a} N_{(\boldsymbol{k}_c - \boldsymbol{k}_v)\lambda\pm} A^{ab}_{\bar{c}\boldsymbol{k}_c\bar{v}\boldsymbol{k}_v\lambda\delta} \tag{6.43}$$

   where $N_{\boldsymbol{q}\lambda\pm} = N_{\boldsymbol{q}\lambda} + \frac{1}{2} \pm \frac{1}{2}$.

8. The polarization is calculated as

$$P = \frac{\zeta^{xx}}{\hbar\xi xyz/2} \tag{6.44}$$

   In order to obtain the polarization for each valley, the integration in eq. (6.43) is performed only for $\boldsymbol{k}_c$ belonging to the chosen valley.

In order to properly model optical pumping, it is essential to include spin-orbit coupling term in the Hamiltonian of the system. The used version of ABINIT does not implement a spin-polarized GW formalism. So the computation is currently performed within LDA using Hartwigsen-Goedecker-Hutter pseudopotential [Hartwigsen1998], which accounts for the spin-orbit coupling term.

As for the calculation of the matrix elements a regular grid of $\boldsymbol{q}$-points in BZ is required, the calculation of the polarization for $\boldsymbol{k}_c$, $\boldsymbol{k}_v$ along to a certain direction does not provide any substantial simplification of the calculation.

6.5.1 Comparison of ab-initio and empirical pseudopotential models

It is expected that ab initio model may provide a more precise description of phonons. Because the resulting polarization in the neighborhood of $\epsilon_{g,X}$ is composed of two contributions of different signs (from different conduction valleys), it is possible that the use of ab initio phonon model may lead to a change of sign of the resulting polarization.

6.6 Calculation of band structure of strained Silicon

In fig. 6.6 one can see that the light hole and split-off band rapidly decrease in energy with the increasing stress. At non-zero stress the heavy and light hole bands are no more degenerate. It is interesting to note the anti-crossing of heavy and light hole bands at intermediate stresses (near 1.5 GPa).

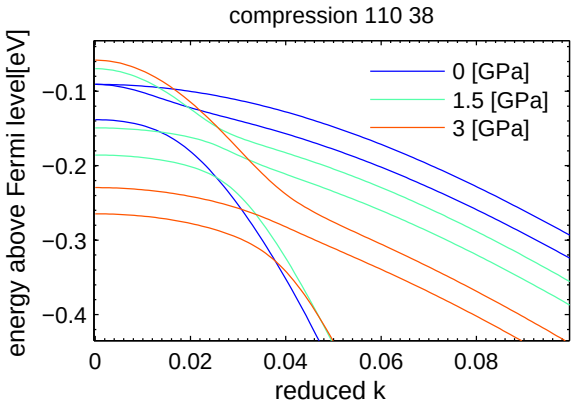


Figure 6.6: Calculated deformation of valence band under compressive stress in [1 1 1] direction

The left panel of fig. 6.7 represents the maximum of different valence bands under compressive stress with respect to the Fermi level calculated for $N_A = 3 \times 10^{17}\,\mathrm{cm}^{-3}$. One can note a significant increase of the splitting between heavy hole and split-off bands under compressive stress, which in fact occurs under the stresses applied in [1 0 0], [1 1 0] and [1 1 1] directions. The details of the calculation are given in [Milne2012].

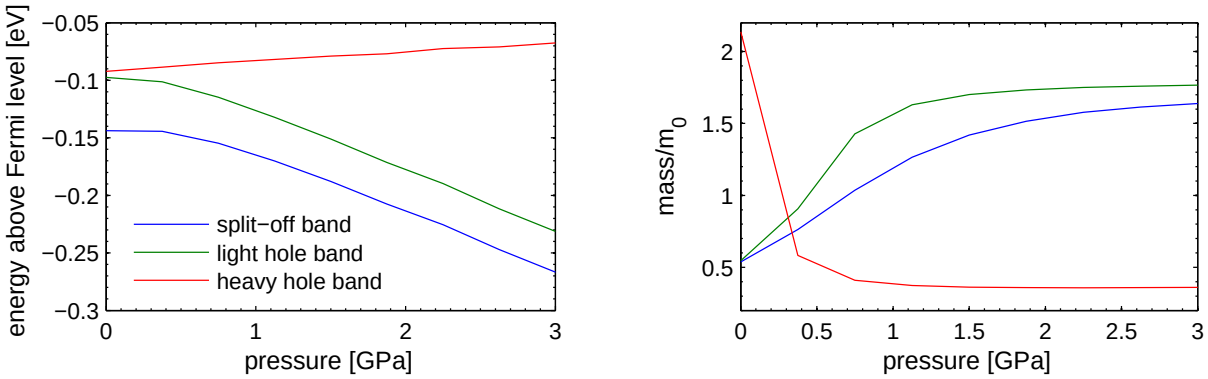


Figure 6.7: Calculated energies at Γ of valence bands (left) and corresponding longitudinal masses (right) under [1 1 1] compressive stress

In can thus be concluded that strained Silicon is an interesting material for further investigation of the optical pumping, since it's higher Δ_{SO} is expected to facilitate the discrimination

between the contributions to P_i from the different band-to-band optical transitions, which are known to produce the polarized electrons of opposite sign.

6.7 Perspectives

6.7.1 Carrier injection

Following properties of carrier injections are to be calculated:

- Absorption spectrum for $h\nu \in [\epsilon_{g,X}, \epsilon^2_{g,\Gamma}]$
- Considering only direct optical transitions, it is of interest to calculate the maximum injection energies (i.e. ϵ_{HE}) versus excitation energy for $h\nu > \epsilon_{g,\Gamma}$. This dependence can be compared with that observed experimentally in section 3.4.1.
- Comparison of carrier injection rate spectrum with the EDCs may allow to separate the contributions to $N(\epsilon)$
  - Due to the relaxation of electrons with higher energy
  - Due to excitation to the states with energy ϵ

6.7.2 Spin injection

The question about the angular sensitivity of the experimental setup to the electrons emitted from different valleys of Γ_4^- conduction band remains open.

Polarization of selected transitions

The polarization of transitions between high-symmetry points represents valuable test cases for a numerical OP model:

- Polarization obtained for the indirect transition from the BZ center to the minimum of conduction band $k = (0.85, 0, 0)$. The obtained transition rates validated with use of those theoretically predicted and given in table II of [Cheng2011a].
- Polarization obtained only for direct transition at Γ point for $\epsilon_{g,\Gamma}$ and $\epsilon^2_{g,\Gamma}$ gaps. Contrary to previous test, which requires numerical calculation of the electron-phonon matrix elements, the direct transitions at Γ provide a point of comparison with analytically obtained polarization.

Transition	P_i
$\Gamma_8^+ \to \Gamma_6^-$	$\frac{1}{6}$
$\Gamma_8^+ \to \Gamma_8^-$	$-\frac{1}{3}$
$\Gamma_7^+ \to \Gamma_6^-$	0
$\Gamma_7^+ \to \Gamma_8^-$	$-\frac{1}{2}$

Transition	P_i
$\Gamma_8^+ \to \Gamma_7^-$	$\frac{1}{2}$
$\Gamma_7^+ \to \Gamma_7^-$	-1

Table 6.2: Analytical model for the polarization of transitions in vicinity of the first direct gap $\epsilon_{g,\Gamma}$ (left) and second direct gap $\epsilon^2_{g,\Gamma}$ (right)

- Polarization of different transitions from $\{\Gamma_7^+, \Gamma_8^+\}$ to $\{\Gamma_6^-, \Gamma_8^-\}$ in the L valley of Γ_5^- conduction band. This calculation would allow to confirm the conclusion about negatively polarized electrons originating from this valley.

Spectrum versus excitation energy

The essential data to be calculated is the spectrum of the polarization at HE-threshold, as well as EDC-averaged polarization spectrum for different electron affinities. In order to correctly reproduce the high-energy polarization, both direct and indirect transitions need to be accounted for.

The calculated spectrum is of interest in the energy range from $\epsilon_{g,X}$ to $\epsilon_{g,\Gamma}^2$ in order to compare with the results of Bona and Meier. Like for the charge injection, the comparison of calculated polarization spectrum with an PEDC may allow to separate contributions due to $P(\epsilon)$

- Due to the spin of the electrons energy-relaxated from higher energies
- Due to optical pumping towards the states with final energy ϵ

Finally, strong valley anisotropy of optical injection near fundamental band edge [Cheng2010] suggests that the angular dependence of optical pumping process may take place. In other words, the result may vary for the samples oriented $(1\,0\,0)$ $(\Gamma - X)$ and $(1\,1\,1)$ $(\Gamma - L)$, given that the light is always normal to the surface, and the spin quantification axis is always parallel to the light wave vector. The inability to observe such a dependence in the presented experimental data is insufficient to make a conclusion about its absence, since the low measured polarization (and thus low signal to noise ratio) does not allow to resolve any fine effects on $P(\epsilon_{g,X})$.

6.7.3 Improvements in the model

Temperature dependence

From the theoretical point of view, the temperature dependence of asymmetry can be due to:

- Variation in electronic band structure:
  - Thermal dilatation of crystal
  - Re-normalization due to phonons [Boulanger2011]
- Variation in phonon occupation number. In particular, this number accounts for the probability of phonon creation / absorption.

The variation of phonon dispersion is presumed to be negligible.

New features

Once an ab initio model of initial polarization will be constructed, the following results of Cheng et al. can be reproduced, providing a point of comparison between ab initio and empirical pseudopotential models.

- Model of two-photon optical pumping near direct gap (following [Cheng2011b; Cheng2011c])
- Model of spin relaxation (following [Cheng2010])

6.8 Energy and spin relaxation

In this section, the difference in the polarization measured using samples of different thickness is evaluated.

6.8.1 Dynamics of the population of spin-polarized electrons

In following sections we review the measurements of times, which determine the dynamics of electrons and their spin polarization in Silicon.

Electron lifetime

The investigation of optical pumping by NMR provides important information on the lifetime of conduction electrons. So the electron relaxation time of $\tau_e = 3 \times 10^{-5}$ s was measured for Si at 77 K [Lampel1968a]. Bagraev, Vlasenko, and Zhitnikov show that deep impurities shorten the electron lifetime in Si [Bagraev1976a].

Spin relaxation mechanisms

During their lifetime in the conduction band electrons are subject to different processes which cause relaxation of the initially created electron spin polarization. Usually three spin relaxation mechanisms are distinguished [Dyakonov2008]:

- Elliot-Yafet mechanism. The relaxation happens during the collisions of electrons with lattice atoms and crystal defects, which act via spin-orbit interaction as an effective magnetic field in which the spin precesses [Elliott1954]. So if the electron wave vector is conserved (which is equivalent to the absence of collisions), the spin isn't affected neither. In other words, $\tau_s \propto \tau_e$.
- Bir-Aronov-Pikus mechanism. It is shown in [Bir1975] that electron-hole exchange scattering can lead to effective spin relaxation in heavily doped p-type semiconductors.
- Diakonov-Perel mechanism, which takes place in an electric field, and in particular for systems without inversion symmetry, such as zinc blende structure crystals [Dyakonov1971]. However, it may also appear in the band bending region of diamond structure semiconductors, under the condition that the direction of electron wave vector differs from that of the electric field. For this mechanism the relaxation appears between the collisions, and thus may also apply to the electrons which escape from crystal ballistically.

Since spin relaxation is an intraband property, in principle it is not affected by the direct or indirect type of the band structure of a given material.

In the case of the considered Si samples the following relaxation mechanisms take place

- Bulk crystal: Elliot-Yafet process
- In the BBR: Elliot-Yafet and Dyakonov-Perel processes (the latter takes place only for $k_\perp \neq 0$)
- The Cs - O surface layer can induce some supplementary depolarization of thermalized electrons (discussed in section 4.2.5).

Spin relaxation times

The presence of an external magnetic field causes the precession of electron spin. In this situation, one should distinguish between relaxation of the longitudinal to the magnetic field spin component, and dephasing of the perpendicular components. The corresponding relaxation times are usually called the spin-lattice relaxation time T_1 and the spin decoherence time T_2 respectively. It is obvious that the transport properties of the spin polarized electron population are essentially determined by the times above.

In general case, the spin decoherence time is on the same order of magnitude as T_1 [Fabian2007]. Usually $T_2 < T_1$ with the exception of anisotropic relaxation, taking place for instance in Si/SiGe quantum wells [Tyryshkin2005]. As it is detailed in [Dyakonov2008], in a solid without any external magnetic field, the spin makes a precession around the (random) direction of the effective magnetic field, which is originated from the spin-orbit interaction, with a typical frequency ω and during a typical time τ_c. After the time τ_c the direction and the absolute value of the field change randomly, and the spin starts its precession around the new direction of the field. After a certain number of such steps the initial spin direction is completely relaxed. Usually the typical precession angle

$$\omega\tau_c \ll 1 \tag{6.45}$$

In other words, the spin vector experiences a slow angular diffusion, with total angle being given by $\omega\tau_c\sqrt{t/\tau_c}$ after a time t, where t/τ_c is the number of experienced collisions. The spin relaxation time may be defined as time such that the corresponding angle is close to unity:

$$T_1 \approx T_2 \approx \omega^2\tau_c \tag{6.46}$$

As we can see, in the limit given in eq. (6.45), no distinction can be made between T_1 and T_2.

Let us recall the definition of spin lifetime

$$\frac{1}{\tau_s} = \frac{1}{T_1} + \frac{1}{\tau_e} \tag{6.47}$$

where T_1 is the spin-lattice relaxation time. Since in Silicon $\tau_e \gg T_1$, τ_s is essentially close to T_1 and T_2.

The spin relaxation measurement techniques can be divided into two categories:

- Measurements of spectral characteristics of magnetization depolarization. The widely used techniques of this type are the conduction-electron spin resonance and optical orientation combined with Hanle effect. These measurements are often conducted at high magnetic field, which significantly modify the spin relaxation times, but the values for zero magnetic field can be calculated. As one can see in fig. 6.8 the ESR measurements provide an upper bound of spin lifetime of conduction electrons.
- Measurements of time or space correlations of magnetization. The most important examples here are spin injection, time-resolved (pump-probe) photoluminescence and magneto-optical measurements.

A systematic ESR measurement yields $T_1 \approx 7.5\,\text{ns}$ for n-type Silicon at room temperature, the result being relatively doping-independent for concentrations up to $10^{17}\,\text{cm}^{-3}$ [Lepine1970]. This quantity is inversely proportional to the electron density. For 115 K, which is the temperature of interest in the present study, the spin-lattice relaxation time decreases from 90 ns for $10^{15}\,\text{cm}^{-3}$ down to 20 ns for $10^{17}\,\text{cm}^{-3}$. In high purity Silicon $\tau_s = 10^{-8}\,\text{s}$ is reported [Young1997]. For photoelectrons excited with near IR laser light, the spin relaxation time varying from $6 \times 10^{-8}\,\text{s}$ to $6 \times 10^{-9}\,\text{s}$ is measured at 77 K [Lampel1968a; Bagraev1976b]. Lampel combines an estimation of the ratio $T_1/\tau_e = 2 \times 10^{-3}$ with an independent measurement of $\tau_e = 3 \times 10^{-5}\,\text{s}$, which yields $T_1 = 6 \times 10^{-8}\,\text{s} \approx \tau_s$.

Figure 6.8 represents a compilation of the experimental data on the spin lifetime. The much lower values of spin lifetime measured via Hanle effect are explained by extrinsic factors affecting the spin lifetime, such as the interface spin relaxation due to reduced symmetry or the presence of the tunnel oxide [Jansen2012].

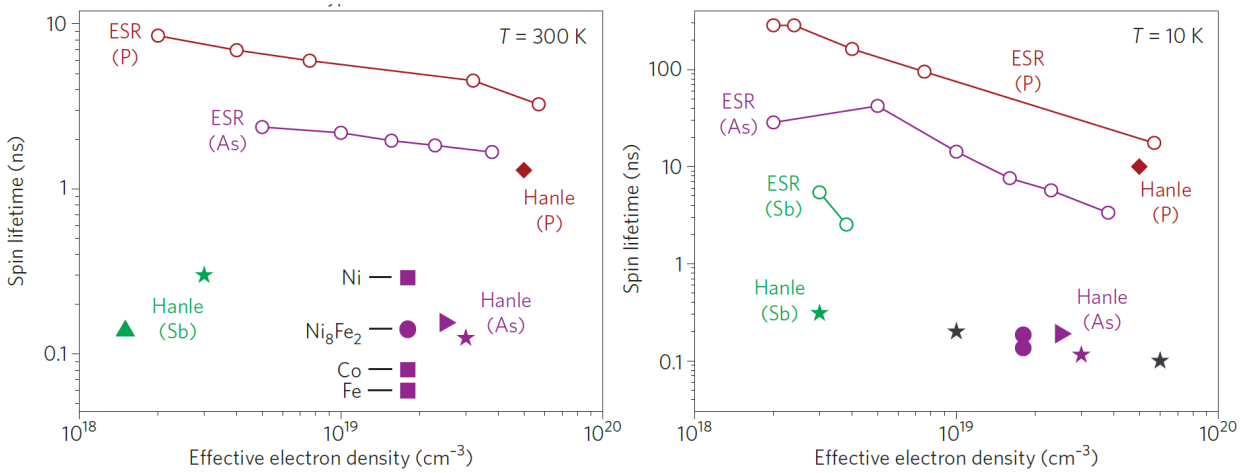


Figure 6.8: Spin lifetime in n-type Silicon extracted from Hanle measurements, combined together with ESR data on bulk Si. Silicon with different dopants (Sb, As and P) and dopant density were used, as indicated. [Jansen2012]

The right panel in fig. 6.9 shows that $T_1(115\,\text{K}) = 150 - 200\,\text{ns}$, $T_1(300\,\text{K}) = 10\,\text{ns}$. The numerical calculations predict the valley anisotropy of spin relaxation rates for hot electrons.

The spin relaxation time in Silicon exceeds by several orders of magnitude the similar times in direct gap semiconductors (for example $10^{-10}\,\text{s}$ for GaAs [Nishikawa1995]).

6.8.2 Diffusion equations

Following [Roux2008], we consider a semiconductor sample bounded by the planes $z = 0$ and $z = d$. It is illuminated along $\boldsymbol{e}_z$ by an incident photon flux ϕ of energy $h\nu$. We denote by V_r^0 and V_r^d the recombination rates at $z = 0$ and $z = d$ respectively, which are assumed to be spin-independent. Optical pumping in a semiconductor is characterized by the following processes:

- Generation of spin-polarized electrons. This process is proportional to the excitation power absorbed at a given point.

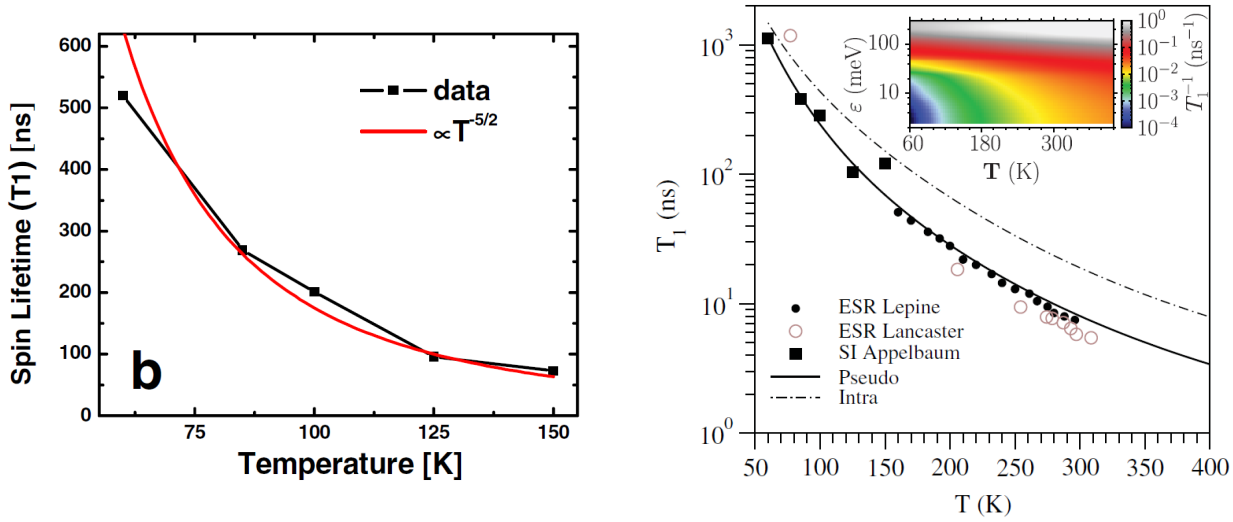


Figure 6.9: T_1 in undoped bulk Silicon estimated from transport properties [Huang2007]. The experimental ESR values are compared to Yafet's $T^{-5/2}$ power law for indirect gap semiconductors (left). Calculation of T_1 [Cheng2010]. The inset shows the contour plot of $1/T_1(T,\epsilon)$ of hot electrons, as a function of their kinetic energy ϵ and lattice temperature T (right).

- Relaxation of photoelectrons, characterized by spin-independent electron lifetime τ_e.
- Relaxation of spin, characterized by spin relaxation time T_1.

These processes can be described by a stationary spin diffusion equation, proposed in [Smith1978], and reviewed in [Roux2008; Favorskiy2010]

$$\begin{cases} \dfrac{\partial n^{|\uparrow\rangle}}{\partial t} = g^{|\uparrow\rangle}\alpha\phi(r)\exp(-\alpha z) - \dfrac{1}{\tau_e}n^{|\uparrow\rangle} - \dfrac{1}{2T_1}n^{|\uparrow\rangle} + \dfrac{1}{2T_1}n^{|\downarrow\rangle} + D\Delta n^{|\uparrow\rangle} = 0 & \text{(6.48a)} \\ \dfrac{\partial n^{|\downarrow\rangle}}{\partial t} = g^{|\downarrow\rangle}\alpha\phi(r)\exp(-\alpha z) - \dfrac{1}{\tau_e}n^{|\downarrow\rangle} - \dfrac{1}{2T_1}n^{|\downarrow\rangle} + \dfrac{1}{2T_1}n^{|\uparrow\rangle} + D\Delta n^{|\downarrow\rangle} = 0 & \text{(6.48b)} \end{cases}$$

where $\phi(r)\exp(-\alpha z)$ is the spatial distribution of light intensity in the sample, and α is the absorption coefficient. This equation accounts only to spin-lattice relaxation, neglecting Coulomb interaction between electrons and spin-spin interaction.

We denote electron diffusion length $L_e = \sqrt{D\tau_e}$ and spin diffusion length $L_s = \sqrt{D\tau_s}$. In the latter expression we neglect a small possible difference in charge in spin diffusion coefficients [Weber2005].

Taking the sum and the difference of eqs. (6.48a) and (6.48b), we obtain

$$\begin{cases} (g^{|\uparrow\rangle} + g^{|\downarrow\rangle})\alpha\tau_e\phi(r)\exp(-\alpha z) - n + {L_e}^2\Delta n = 0 & \text{(6.49a)} \\ (g^{|\uparrow\rangle} - g^{|\downarrow\rangle})\alpha\tau_s\phi(r)\exp(-\alpha z) - s + {L_s}^2\Delta s = 0 & \text{(6.49b)} \end{cases}$$

with

$$n = n^{|\uparrow\rangle} + n^{|\downarrow\rangle}$$

and

$$s = n^{|\uparrow\rangle} - n^{|\downarrow\rangle}$$

Let us consider the one-dimensional case (i.e. fix the position r in the transverse plane). In this case the general solution of eq. (6.49) is given by

$$\begin{cases} n(z) = A_n \exp\left(-\frac{z}{L_e}\right) + B_n \exp\left(-\frac{z}{L_e}\right) + \frac{(g^{|\uparrow\rangle} + g^{|\downarrow\rangle})\alpha\tau_e\phi(r)}{1-(\alpha L_e)^2}\exp(-\alpha z) & \text{(6.50a)} \\ s(z) = A_s \exp\left(-\frac{z}{L_s}\right) + B_s \exp\left(-\frac{z}{L_s}\right) + \frac{(g^{|\uparrow\rangle} - g^{|\downarrow\rangle})\alpha\tau_s\phi(r)}{1-(\alpha L_s)^2}\exp(-\alpha z) & \text{(6.50b)} \end{cases}$$

The boundary conditions for eq. (6.49) are given by

$$D\frac{\partial n^i}{\partial z} = V_r^z n^i(z) \text{ for } z \in \{0, d\} \tag{6.51}$$

where i denotes the spin polarizations $|\uparrow\rangle$ and $|\downarrow\rangle$.

Since the recombination rates are spin-independent, taking the sum and the difference of eq. (6.51) for $i = |\uparrow\rangle$ and $i = |\downarrow\rangle$ yields

$$\begin{cases} D\frac{\partial n}{\partial z} = V_r^z n(z) \text{ for } z \in \{0, d\} & \text{(6.52a)} \\ D\frac{\partial s}{\partial z} = V_r^z s(z) \text{ for } z \in \{0, d\} & \text{(6.52b)} \end{cases}$$

The constants can be obtained by substituting in eq. (6.50) the boundary conditions above:

$$\begin{cases} A_k = \frac{G_k}{C(1-(\alpha L_k)^2)} \cdots \\ \quad \left[\left(\alpha + \frac{V_r^0}{D}\right)\left(\frac{1}{L_k} + \frac{V_r^d}{D}\right)\exp\left(\frac{d}{L_k}\right) - \ldots \right. & \text{(6.53a)} \\ \quad \left.\left(\alpha - \frac{V_r^d}{D}\right)\left(\frac{1}{L_k} - \frac{V_r^0}{D}\right)\exp\left(-\alpha d\right)\right] \\ B_k = \frac{G_k}{C(1-(\alpha L_k)^2)} \cdots \\ \quad \left[\left(\alpha + \frac{V_r^0}{D}\right)\left(\frac{1}{L_k} - \frac{V_r^d}{D}\right)\exp\left(-\frac{d}{L_k}\right) - \ldots \right. & \text{(6.53b)} \\ \quad \left.\left(\alpha - \frac{V_r^d}{D}\right)\left(\frac{1}{L_k} + \frac{V_r^0}{D}\right)\exp\left(-\alpha d\right)\right] \end{cases}$$

with $k \in \{s, n\}$, the denominator given by

$$C = -\left(\frac{1}{L_k} + \frac{V_r^0}{D}\right)\left(\frac{1}{L_k} + \frac{V_r^d}{D}\right)\exp\left(\frac{d}{L_k}\right) - \left(\frac{1}{L_k} - \frac{V_r^0}{D}\right)\left(\frac{1}{L_k} - \frac{V_r^d}{D}\right)\exp\left(-\frac{d}{L_k}\right)$$

One should be aware of missing minus sign in $\exp\left(-\frac{d}{L_k}\right)$ in the counterpart of eq. (6.53b) given in [Roux2008]. The spin and charge creation rates are given by

$$\begin{cases} G_s = g^{|\uparrow\rangle} - g^{|\downarrow\rangle} & (6.54a) \\ G_n = g^{|\uparrow\rangle} + g^{|\downarrow\rangle} & (6.54b) \end{cases}$$

Accounting for the emission at the boundary

The total current density at the interface is governed by two contributions

$$i_{total} = i_{recombination} + i_{emission} \tag{6.55}$$

So at the interface $x = 0$ the recombination speed is decomposed as

$$S_{total}(E) = S_{recombination} + S_{emission}(E) \tag{6.56}$$

in this way modeling the faster escape of hot electrons compared to ballistic ones.

In order to choose numerical values for $S_{emission}(E)$, one have to find the emission probability given the energy and wave vector of an electron near surface.

Numerical results

Let's consider the general solution from eq. (6.50) for the samples of different thickness. We take spin lifetime $\tau_s = 1\,\text{ns}$, electron lifetime $\tau_e = 1\,\mu\text{s}$, which results in

$$\begin{cases} L_e = \sqrt{D\tau_e} = 55\,\mu\text{m} & (6.57a) \\ L_s = \sqrt{D\tau_s} = 1.7\,\mu\text{m} & (6.57b) \end{cases}$$

The photon flux is taken as

$$\phi = \frac{W}{\pi r^2 h\nu}[\text{photons/m}^2\text{/s}] \tag{6.58}$$

where the incident optical power of $W = 1\,\text{mW}$ is focused to the circular spot of $r = 100\,\mu\text{m}$. The diffusion coefficient is taken at relatively low value $D = 30\,\text{cm}^2\text{/s}$, which allows to provide a lower bound estimation to L_e, L_s, and thus to P_i. Thus, the real polarization in the sample must be greater than or equal to the calculated value, which allows to eliminate diffusion as the main reason for the low polarization in SOI [2 µm]. At the same time, since the diffusion coefficient is included in the model as $D^{1/2}$, the results presented in the graphs below are quite similar within $D = 30 - 300\,\text{cm}^2\text{/s}$.

No significant temperature dependence of the presented below results was observed. The curves presented below are calculated for $T = 300\,\text{K}$.

As it shown in fig. 6.10, there is an important change between 500 µm (bulk) and 5 µm (SOI) samples, but between 5 µm and 2 µm the polarization enhancement is expected to be low. For excitation energies in vicinity of direct gap, the polarization of both thermalized and ballistic electrons approaches corresponding initial polarization.

Figure 6.11 shows the calculated profiles of carrier and spin concentration for $h\nu \approx \epsilon_{g,X}$. One can see that close to the surface ($z < 10^{-6}\,\text{m}$) the ratio s/n is inversely proportional to sample thickness.

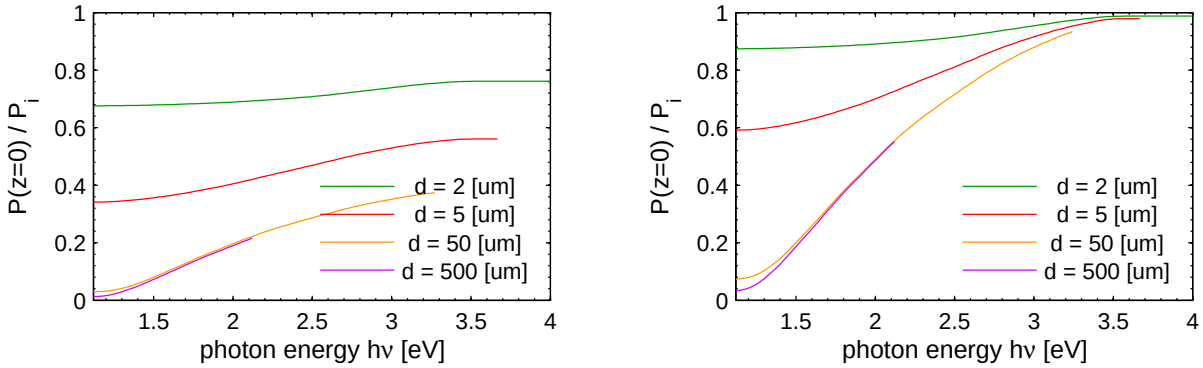


Figure 6.10: Dependence of initial polarization at $z = 0$ versus excitation energy for different sample thicknesses. The polarization of thermalized electrons is modeled with $V_r^0 = 10^3\,\mathrm{m/s}$ (left), whereas the polarization of ballistic electrons is modeled by higher recombination velocity $V_r^0 = 10^{10}\,\mathrm{m/s}$ (right).

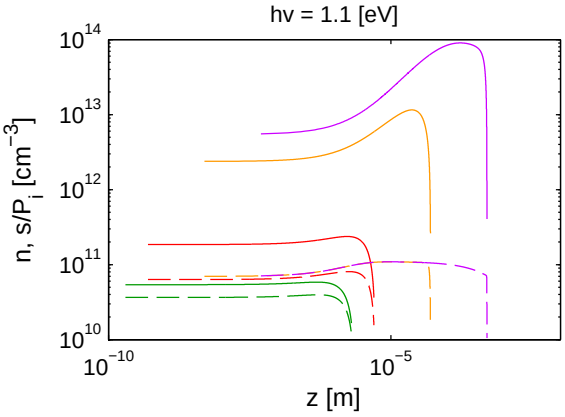


Figure 6.11: Profile of carrier concentration $n(z)$ (solid lines) and spin concentration $s(z)$ (dashed lines) for the absorption near the fundamental band edge. $V_r^0 = 10^3\,\mathrm{m/s}$, $V_r^d = 10^4\,\mathrm{m/s}$.

According to this model, the sample thickness of 2 µm should in principle be sufficient to measure a polarization on the same order of magnitude as P_i under the excitation near indirect band gap.

6.8.3 Modeling of conduction electrons energy distributions

Fokker-Plank approach

Let us denote $f(\epsilon, z, s)$ the probability density function (PDF) in phase space, which describes the electrons with kinetic energy ϵ, spatial coordinate x and spin coordinate s. The Fokker-Plank equation on probability density function can be written in the form of

$$u\frac{\partial f(\epsilon, z, s)}{\partial x} = \frac{\partial^2}{\partial \epsilon^2} D_E f(\epsilon, z, s) \tag{6.59}$$

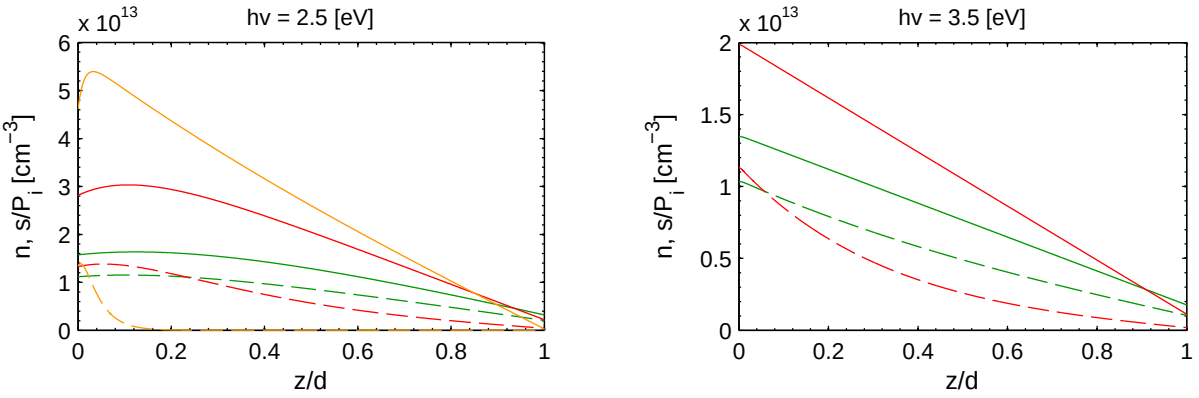


Figure 6.12: Profiles of carrier concentration $n(z/d)$ (solid lines) and spin concentration $s(z/d)$ (dashed lines) for different excitation energies. $V_r^0 = 10^3\,\mathrm{m/s}$, $V_r^d = 10^4\,\mathrm{m/s}$.

where $D_E \propto \frac{E^2}{\tau_e}$ is the diffusion coefficient and $u = \sqrt{\frac{2\epsilon}{m_e}}$ is the velocity of electrons.

The quantity of interest in such simulation would be the EDC, which is proportional to

$$N(\epsilon) \propto \sum_{s\in\{|\uparrow\rangle,|\downarrow\rangle\}} f(\epsilon, 0, s) \tag{6.60}$$

and PEDC, which is proportional to

$$P(\epsilon) \propto \frac{f(\epsilon, 0, |\uparrow\rangle) - f(\epsilon, 0, |\downarrow\rangle)}{f(\epsilon, 0, |\uparrow\rangle) + f(\epsilon, 0, |\downarrow\rangle)} \tag{6.61}$$

In fact, in a steady-state situation, the EDC is given by

$$N(\epsilon) = \mathrm{DOS}(\epsilon) n(\epsilon) \tag{6.62}$$

where $\mathrm{DOS}(\epsilon)$ is the density of states, and $n(\epsilon) = (\exp((\epsilon - \epsilon_\mathrm{F})/kT) + 1)^{-1}$ is the Fermi-Dirac function. However, under OP conditions this distribution is modified by the presence of generation term due to light excitation.

In order to evaluate D_E, one need to model the main thermalization mechanisms, which are intra- and inter-band electron-lattice relaxation, and Coulomb interaction between the electrons and crystal lattice.

Another essential question in such simulation is the choice of proper boundary conditions, which would probably need to account for the properties of BBR and eventually of Cs - O surface layer, as well as the energy-dependent probability of electron photoemission. For instance, [Brust1965] proposes a simple model for the escape probability $P(\epsilon, \boldsymbol{k})$ of an electron with energy ϵ and wave vector $\boldsymbol{k} = (k_t, \boldsymbol{k}_l)$ decomposed into transverse and longitudinal components with respect to the material surface. In fact, the classical escape condition

$$\epsilon(\boldsymbol{k}) > \frac{\hbar}{2m_0} k_t^2 + E_{vac} \tag{6.63}$$

is equivalent to

$$\frac{\hbar}{2m_0} k_t^2 + \frac{\hbar}{2m_0} k_l^2 > \frac{\hbar}{2m_0} k_t^2 + E_{vac}$$

$$\frac{\hbar}{2m_0}k_l^2 > E_{vac} \tag{6.64}$$

A Fokker-Plank description of electron transport was proposed in [Bringuier1999].

Langevin approach

However, in practice the PDF actually depends on wave vector $\boldsymbol{k}$ rather than directly on kinetic energy. Furthermore, even if initial conditions of the problem depend only on z coordinate, the resolution of three-dimension problem in terms of $\boldsymbol{r}$ is required in order to correctly describe the anisotropy of Silicon band structure

$$f = f(\boldsymbol{r}, \boldsymbol{k}, s) \tag{6.65}$$

Thus, the resolution of steady-state Fokker-Plank equation is to be performed in the space of 7 variables. In fact, since the calculation time of eq. (6.59) is exponentially proportional to the number of degrees of freedom, the reformulation of eq. (6.59) in terms of Langevin equations and its resolution by Monte-Carlo methods may represent significant advantages for the practical resolution. In fact, the latter yield a linearly growing computational cost and thus are well suited to solve PDF equations. For this reason the Monte Carlo methods have been traditionally used to solve the equations on PDF.

Fischetti and Laux propose a Monte-Carlo method for the calculation of transport properties in Silicon, which account for the band structure and the properties of BBR [Fischetti1988]. Brunetti et al. calculates the energy distribution curves of conduction electrons in Silicon under high electric fields [Brunetti1989], taking into consideration 4 lowest conduction bands.

In [Ma2012] a system of Langevin equations describing spin-lattice-electron dynamics of a magnetic material is presented. A particular case of system of three coupled heat diffusion equations, which describe the temperatures of the lattice, conduction electrons and spins is considered. The Hamiltonian of such a coupled system is given by

$$H = H_l + H_e + H_s \tag{6.66}$$

The lattice part of this Hamiltonian describes the collection of interacting atoms

$$H_l = \sum_i \frac{\boldsymbol{p}_i^2}{2m} + U(\boldsymbol{R}) \tag{6.67}$$

where $\boldsymbol{p}_i$ is the momentum of atom i and $U(\boldsymbol{R})$ is the interatomic potential of $\boldsymbol{R} = (\boldsymbol{R}_1, .., \boldsymbol{R}_N)$

The Hamiltonian of spin subsystem is described via coordinate-dependent exchange coupling function $J_{ij}(\boldsymbol{R})$:

$$H_s = -\frac{1}{2}\sum_{i,j}(\boldsymbol{R})\boldsymbol{S}_i \cdot \boldsymbol{S}_j \tag{6.68}$$

The system of Langevin equations is given by

$$\begin{cases} \dfrac{d\boldsymbol{r}_k}{dt} = \dfrac{\boldsymbol{p}_k}{m} & \text{(6.69a)} \\ \dfrac{d\boldsymbol{p}_k}{dt} = -\dfrac{\partial U}{\partial \boldsymbol{r}_k} + \dfrac{1}{2}\sum\limits_{i,j} \dfrac{\partial J_{ij}}{\partial \boldsymbol{r}_k}\boldsymbol{S}_i \cdot \boldsymbol{S}_j - \dfrac{\gamma_{el}}{m}\boldsymbol{p}_k + \boldsymbol{f}_k & \text{(6.69b)} \\ \dfrac{d\boldsymbol{S}_k}{dt} = \dfrac{1}{\hbar}(\boldsymbol{S}_k \times (\boldsymbol{H}_k + \boldsymbol{h}_k) - \gamma_{es}\boldsymbol{S}_k \times (\boldsymbol{S}_k \times \boldsymbol{H}_k)) & \text{(6.69c)} \end{cases}$$

where k is spin index of an electron with spatial coordinate $\boldsymbol{r}_k$, momentum $\boldsymbol{p}_k$ and spin $\boldsymbol{S}_k$, γ_{el} and γ_{es} are electron-lattice and electron-spin damping parameters, $H_k = \sum\limits_i \boldsymbol{J}_{ik}\boldsymbol{S}_i$ is the effective exchange field acting on spin k, $\boldsymbol{f}_k$ is δ-correlated fluctuating force and $\boldsymbol{h}_k$ is δ-correlated fluctuating exchange field.

In order to describe the energy and spin distributions of photoemitted electrons, a model which would combine eq. (6.69) with the description of Silicon band structure and phonon scattering needs to be proposed.

It is likely that the dependence $T_1(\epsilon)$, which can be either directly extracted from data given in [Cheng2010], or numerically calculated following the proposed in this article model, will be useful for the energy-dependent description of spin relaxation process.

6.9 Conclusion

The negative sign of the measured polarization with excitation in vicinity of indirect band gap is in agreement with the numerical calculations [Li2010; Cheng2011a], and also supports the hypothesis of slightly higher sensitivity of the photoemission setup to the electrons emitted from longitudinal with respect to the light excitation direction valleys (positive polarization) rather than to transverse valleys (negative polarization).

The comparison of theoretically predicted polarization under excitation in the vicinity of direct band gap indicates that our experimental measurements have similar sensitivity to both indirect and direct transitions. It follows from the comparison with theoretical calculation [Nastos2007] that the experimentally observed negative spin polarization can be due to both direct transitions in L valley and indirect transitions away from zone center in $\Gamma - X$ direction, with a predominance of the first of the above mechanisms. Finally, the perspectives of further development of theoretical description of OP in Silicon are summarized.

Considering the unipolar spin diffusion equations, initially proposed in [Smith1978], and later revisited by Roux, we show that the polarization of thermalized electrons excited with $h\nu \approx \epsilon_{g,X}$ in SOI [2 µm] is decreased by less than one order of magnitude due to the effects of diffusion. An important perspective of the development of this model is the description of the electron energy distribution curves and their spin polarization, which can be designed, for example, based on the provided review of existing studies.

Chapter 7

Conclusions and future work

7.1 Conclusions

We have shown the possibility of achieving NEA on (1 1 1)-oriented Silicon surfaces, as well as good stability of SOI structures under high temperature annealing and intense laser irradiation in both IR and UV parts of the spectra.

Using these thin Silicon films of different thicknesses, we performed a study of the optical pumping by means of spin- and energy- resolved high-resolution (30 meV) photoemission spectroscopy. The energy distributions of electrons photoemitted for the excitation energy varying from 1.15 eV to 4.8 eV at temperatures of 300 K and 115 K, as well as the spectrum of their spin polarization were measured. The use of a tunable laser source allowed fine adjustment of the excitation energy, especially relevant for resolving the transitions from the bands split by low spin-orbit coupling of Silicon.

The usage of the developed in the present work automated software/hardware tools for the control of the measurement progress and the data processing has played a key role in the success of a large number of complex long-term experiments. Several times on the basis of regular remote control over the course of the experiment the need for a prompt intervention in the setup operation was identified.

The initial distribution of photoelectrons is created in the layer which thickness is determined by the absorption depth. For the excitation near the fundamental band gap, the long absorption depth implies that the electrons, which are created throughout the sample volume, undergo significant momentum and spin relaxation before their extraction into vacuum.

It was shown that the a the use of circularly polarized excitation with photon energy close to the fundamental gap, as well as the use of thin 5 µm and 2 µm Silicon films, does not result in enhancement of the measured spin polarization of conduction electrons. In fact, a negative polarization of $-0.4\,\%$ was measured under such conditions, in particular with no noticeable effect at excitation energies $h\nu \in [\epsilon_{g,X}, \epsilon_{g,X} + \Delta^{\epsilon}_{\mathrm{SO}}]$. This result invalidates the hypothesis of long absorption length as the main cause of low band edge polarization in Silicon. Instead, we explain the low observed polarization by the mixing of opposite sign contributions of optical transitions, originated from different valleys of conduction bands ($-25\,\%$ for transverse and $+8\,\%$ for longitudinal valleys [Cheng2011a]), along with the insufficient sensitivity of electron spectrometer to the ballistic electrons under IR excitation.

The high-energy threshold polarization reveals the maximum of $6\,\%$ for $h\nu \approx \epsilon_{g,\Gamma}$. The

excitation energy, which corresponds to the maximum of ballistic electrons polarization, allows to estimate $\epsilon_{g,\Gamma}(300\,\mathrm{K}) = 3.3\,\mathrm{eV}$. The sign of low-energy threshold polarization depends on the temperature and on the excitation energy, which together with theoretical results [Nastos2007] constitute an indication of high negative spin polarization of the photoelectrons produced by the direct optical transitions to the L valley of Γ_5^- conduction band. The negative polarization of indirect optical transitions in $\Gamma - X$ direction probably plays a minor role, but cannot be completely excluded. The estimation $\epsilon_{g,L}^{\mathrm{direct}}(300\,\mathrm{K}) = 3.35\,\mathrm{eV}$ was obtained on the basis of minimum of energy-averaged polarization of hot electrons. The measured increase of $\epsilon_{g,\Gamma}$ and $\epsilon_{g,L}^{\mathrm{direct}}$ band gap with decreasing temperature is in reasonable agreement with the previous experimental data. The estimated in the present work band structure parameters are summarized in table 4.2.

The conventions on circular polarization were given for the present experimental setup, and compared to that used in the main theoretical works on the OP in Silicon [Lampel1968a; Weisbuch1974; Nastos2007; Li2010; Cheng2011a].

7.2 Future work

The present work can be continued in several directions. Using a rare in-class experimental setup, one may schedule a study of a number of samples that will allow a more detailed understanding of the band structure and OP in Silicon. More generally, the study of other materials in which a high electron polarization is detected, although not directly connected to Si, can also bring interesting results to the field of optical pumping physics.

Several improvements in the setup can be envisaged in order to extend its functionality. In the following sections they are classified by their feasibility: from already planned modifications, such as the installation of sample introduction chamber, to hypothetical considerations such as the addition of angular resolution.

Finally, the magnetic and surface properties of Silicon can be approached by other experimental techniques, notably by a magneto-optical measurement.

7.2.1 New sample types

In order to simplify the introduction of new samples, an important step to be undertaken is the finalization of sample introduction chamber (section 7.2.2).

Selective optical pumping

The initial polarization in the case OP on bulk Silicon consists of contributions of different sign, which often mutually vanish. In particular P_i can be decomposed into such contributions according to one of following schemes:

- Different band-to-band optical transitions
- Indirect transitions assisted by different phonon modes
- Indirect transitions to the different conduction valleys

In order to enhance P_i, a strategy of privileging a given contribution can be adopted.

Polarization of strained Silicon Both the ab initio calculations of strained Silicon band structure [Milne2012] and recent results on strained Germanium [Bottegoni2011] confirm that strained Si should be an interesting candidate for further spin polarization studies.

Valley selective OP According to [Kaplyanskii1976], at low temperature it is possible to selectively excite certain conduction valleys. The excitation with circularly polarized light may thus result in the increased polarization.

Photoemission from ultra-thin Silicon films

Although the considered in section 6.8.3 model showed insignificant influence on the polarization of the diffusion in the SOI [2 µm], the use of thinner films would experimentally confirm this fact. However, there are two major difficulties in this approach:

- In the regime of weak excitation the photocathode current is proportional to the active layer volume. So taking a film 10 times thinner would put the setup at the limit of acquisition feasibility.
- The thermal cleaning procedure, which is required for NEA, may cause the lift-off of the active layer.

For instance, previously an experiment with GaAs-coated Si substrate was performed in the same apparatus. The sample was unusable after 3-4 annealings, even if the required temperature for GaAs is 500 °C, two times lower than for Si.

On the other hand, GaAs film on Si substrate leads to important constraints, much higher than Si film deposed on amorphous SiO_2. Thus the photocathodes with ultra-thin Silicon films may represent an interesting perspective.

Spin-polarized surface states on Si

During the deposition of heavy elements with large spin-orbit splitting (Gold, Bismuth) on Silicon, the formation of spin-polarized surface states is known to take place. [Allen1962] provides an estimation of surface states on (1 1 1) Si $8 \times 10^{14}\,\mathrm{cm}^{-2}$. These states are located in two groups: one normally empty just below the center of the gap and another normally filled just above the valence-band edge.

Other materials

Other potentially interesting sample types may include:

- Following the work [Rikken2011], a measurement of electron distributions from chiral DNA molecules on Silicon substrate can be envisaged.
- Germanium. For instance, a polarization of 25 % was measured under $h\nu = 3\,\mathrm{eV}$ excitation (p.303 of [Meier1984]).
- Semiconductors of wurtzite crystal structure. According to [Nastos2007], the relatively low symmetry of this lattice type can result in up to 100 % band edge spin-polarization for CdTe.

- Nitrogen vacancy centers in diamond.

7.2.2 Improvements of the experimental setup

Sample introduction chamber

The studies of different samples can be greatly facilitated by the installation of a sample introduction chamber. Indeed, in the presently used setup, one must first load the sample into the calibration chamber for studying the process of surface preparation. Then, the sample must be removed from the calibration chamber, and placed in the main setup. Such procedure implies double achievement of UHV (one month or work), during which several components may be damaged, thus leading to the resumption of the procedure from zero:

- Sample itself (during the long outgassing at $200 - 250\,^{\circ}\mathrm{C}$). For instance, it took us 4 attempts before a functional SOI [2 µm] sample was introduced in the main setup.
- Electronic spectrometer, the electrodes of which are sometimes accidentally disconnected during the outgassing.
- Mott detector: thin self-supporting sheets of Gold may burst if the inlet or outlet of air is not performed slowly enough.

An airlock for sample introduction into Mott chamber was designed and tested separately from the Mott detector. The current version of the mounted airlock is shown in fig. 7.1. An important modification of main UHV chamber was also designed in order to interconnect the airlock chamber and to perform *in-situ* temperature measurement during the sample annealing. This improvement will significantly expand the functionality of the photoemission facility due reduction in load and calibration time of new samples. Moreover, use of such the airlock will improve the quality of the vacuum and hence the stability of the photocathodes.

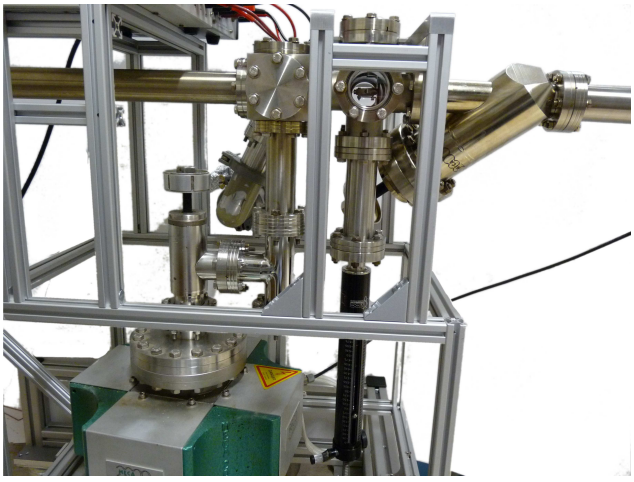


Figure 7.1: Sample introduction chamber

Further investigation of two-photon optical pumping

The spin polarization of 49.5 % was measured in bulk unstrained GaAs by two photon pump-probe technique at 4 K [Miah2009]. A difference between one and two photon optical

pumping for excitation in the proximity of indirect gap follows from theoretical calculation [Cheng2011c]. The main advantage of two-photon optical pumping is its higher sensitivity to the optical direct transitions, which often exhibit higher P_i compared to phonon-assisted transitions.

In order to reliably measure the polarization of the two-photon process it is important to solve the problem of EDC distortion under pulsed irradiation. One possible solution might be to install an additional grid near the sample, raised to a certain potential in order to filter the low-energy electrons and in this way avoid the spectrometer saturation.

Compared to performed in the present study electron filtering via high electron affinity, i.e. retaining electrons in the sample, such grid would allow to avoid possible accumulation of the surface charge in the sample, and hence probably would result in lower EDC distortion.

The measurement of two-photon OP could be also performed, following [Bensoussan1983], on clean Silicon surface, on the condition that the employed peak optical power would generate sufficient signal for a PEDC measurement.

In situ calibration of the energy scale of the spectrometer

Direct measurement of $\epsilon(V_{\text{cath}})$ dependence can be performed with a sample consisting of Gold and the investigated material (e.g. Silicon), the Fermi levels of which are equal due to electrical contact. This would allow to calibrate the dependence of $\epsilon(V_{\text{cath}})$ by the photoemission from the gold surface, and then to measure photoemission from the material of interest.

Such direct calibration can enable study of effects requiring precise knowledge of thresholds, such as

- Study of surface states below ϵ_{F}, similarly to the measurement of such states on GaN [Pakhnevich2004].
- Comparison of relative intensities of direct and indirect transitions (section 3.4.1).

It is possible to use such calibration method only after the installation of a lateral translation on sample holder flange.

Angular resolution of the spectrometer

An interesting problem, which arises in contexts of both charge and spin polarization spectra, is the separation of the contributions due to transitions away from the zone center and relaxation of ballistic electrons. Experimentally, these contributions can be separated by angle-resolved spectroscopy. Numerically, an energy-dependent description of EDC (PEDC) (discussed in section 6.8.3) together with the spectrum of charge (spin) injection rate is required to resolve these contributions.

In principle, angular resolution can be achieved by tilting the sample. However, such tilting implies several fundamental difficulties which hinder the implementation of its functionality:

- The extraction of electrons would be non-homogeneous throughout the sample surface due to the differences in distance from sample surface to the entrance slit. In particular, if electrons are not extracted normal to the surface, under some conditions the surface spin selectivity may appear [Kirschner1981].

- In order to interpret the experimental results, this tilt should be accounted for in the model of OP and electron extraction from sample.

7.2.3 Use of other experimental techniques

Magneto-optical measurement

As it was shown in section 4.3, the use of tunable UV excitation in vicinity of direct gap can be used to induce a non-zero magnetization in the sample (as discussed in section 3.5.7, the magnetization is in fact proportional to $\langle P \rangle$, represented in fig. 4.25). The energy-averaged magnetization can be measured by magneto-optical techniques. At the same time, the advantage of latter is the possibility to access the dynamical properties: the use of magnetic field in order to measure spin relaxation time or imaging techniques can be considered.

Investigation of Cs-O deposition on (1 1 1) surface

Gobeli, Lander, and Morrison demonstrated the ordered deposition of Cesium on (1 1 1)-(2×1) bulk Silicon and disordered deposition on (1 1 1)-(7×7). Since NEA usually takes place on the ordered surfaces [Levine1973], it would be interesting to study the electron diffraction the (1 1 1)-oriented SOI covered with:

- With Cs layer
- With Cs and O layer

The second experiment could allow verifying if the deposition of Oxygen on (presumably disordered) cesiated Silicon (1 1 1) surface result in a ordering of the surface layer.

Appendix A

Averaging in a counting experiment

Assume that the measurement of PEDC took K cycles. For simplicity, we consider the counts, measured for a fixed set of parameters eq. (3.59). We denote them by $A^k, B^k, k \in \{1, ..K\}$.

There are two ways of calculating the asymmetry (the instrumental asymmetry correction is omitted for the sake of simplicity):

$$\mathcal{A} = \left\langle \frac{A-B}{A+B} \right\rangle \tag{A.1}$$

where $\langle X \rangle = \frac{1}{K} \sum_{k=1}^{K} X^k$, or alternatively

$$\mathcal{A} = \frac{\langle A \rangle - \langle B \rangle}{\langle A \rangle + \langle B \rangle} \tag{A.2}$$

If for given cycle the acquisition time is insufficient, eq. (A.1) may imply division by zero, which means that the corresponding data will be ignored numerically and will not contribute to the final value of polarization, averaged over all performed cycles.

In this section, the comparative analysis of the eq. (A.1) and eq. (A.2) is performed.

A.1 Bernoulli variables

Let us model the measured counts by means of two independent Bernoulli variables A and B, with the probability p_A of measuring one count on channel A, and p_B on channel B respectively.

The asymmetry of expectation values is $\dfrac{p_A - p_B}{p_A + p_B}$. The conditional expectation value of asymmetry is

$$P(A+B>0)E\left(\frac{A-B}{A+B}\middle| A+B>0\right) = \frac{1-0}{1+0}p_A(1-p_B)+\frac{0-1}{0+1}(1-p_A)p_B+\frac{1-1}{1+1}p_Ap_B = p_A-p_B$$

obviously different from the asymmetry of expectation values.

At the same time, if we consider an electron with its spin S as a Bernoulli random variable,

$$S = \begin{cases} 1 & \text{with probability } p \\ -1 & \text{with probability } (1-p) \end{cases}$$

In this simple case, the mathematical expectation of asymmetry equals the asymmetry of expectations.

A.2 Independent Poisson variables

$$\left\langle \frac{A-B}{A+B} \right\rangle = \sum_{k_1=0}^{\infty} \frac{e^{-\lambda_1}}{k_1!}\lambda_1^{k_1} \sum_{k_2=0}^{\infty} \frac{e^{-\lambda_2}}{k_2!}\lambda_2^{k_2} \frac{k_1-k_2}{k_1+k_2} \tag{A.3}$$

The function $f(k_1,k_2) = \dfrac{k_1-k_2}{k_1+k_2}$ diverges at $(0,0)$. Furthermore, its limit takes different values dependent on direction in which this limit is taken. To make the result independent from $f(0,0)$, we are going to exclude $k_1 = 0,\ k_2 = 0$ from the consideration by taking the conditional expectation

$$P(A+B>0)\left\langle \frac{A-B}{A+B}\middle| A+B>0 \right\rangle = \sum_{k_1=1}^{\infty} \frac{e^{-\lambda_1}}{k_1!}\lambda_1^{k_1} \sum_{k_2=0}^{\infty} \frac{e^{-\lambda_2}}{k_2!}\lambda_2^{k_2} \frac{k_1-k_2}{k_1+k_2} + \frac{e^{-\lambda_1}}{0!}\lambda_1^0 \sum_{k_2=1}^{\infty} \frac{e^{-\lambda_2}}{k_2!}\lambda_2^{k_2}(-1) =$$

$$= \sum_{k_1=1}^{\infty} \frac{e^{-\lambda_1}}{k_1!}\lambda_1^{k_1} \sum_{k_2=0}^{\infty} \frac{e^{-\lambda_2}}{k_2!}\lambda_2^{k_2} \int_0^{\infty} (k_1-k_2)\ e^{-xk_1-xk_2}dx - e^{-\lambda_1}(1-e^{-\lambda_2})$$

Let $q = e^{-x}$, $dq = -e^{-x}dx = -qdx$, $dx = -\dfrac{dq}{q}$

$$= e^{-\lambda_1-\lambda_2} \int_0^1 \frac{dq}{q} \sum_{k_1=1}^{\infty} \frac{(\lambda_1 q)^{k_1}}{k_1!} \sum_{k_2=0}^{\infty} \frac{(\lambda_2 q)^{k_2}}{k_2!}(k_1-k_2) - e^{-\lambda_1}(1-e^{-\lambda_2}) =$$

$$= e^{-\lambda_1-\lambda_2} \int_0^1 \frac{dq}{q} \left(\sum_{k_1=1}^{\infty} k_1 \frac{(\lambda_1 q)^{k_1}}{k_1!} \sum_{k_2=0}^{\infty} \frac{(\lambda_2 q)^{k_2}}{k_2!} - \sum_{k_1=1}^{\infty} \frac{(\lambda_1 q)^{k_1}}{k_1!} \sum_{k_2=0}^{\infty} k_2 \frac{(\lambda_2 q)^{k_2}}{k_2!} \right) - e^{-\lambda_1}(1-e^{-\lambda_2}) =$$

$$= e^{-\lambda_1-\lambda_2} \int_0^1 \frac{dq}{q} \left(\lambda_1 q e^{\lambda_1 q} e^{\lambda_2 q} - (e^{\lambda_1 q}-1)\lambda_2 q e^{\lambda_2 q} \right) - e^{-\lambda_1}(1-e^{-\lambda_2}) =$$

$$= e^{-\lambda_1-\lambda_2} \left(\int_0^1 dq \left(\lambda_1 e^{\lambda_1 q} e^{\lambda_2 q} - e^{\lambda_1 q}\lambda_2 e^{\lambda_2 q} \right) + \int_0^1 dq \lambda_2 e^{\lambda_2 q} \right) - e^{-\lambda_1}(1-e^{-\lambda_2}) =$$

$$= e^{-\lambda_1-\lambda_2} \left((\lambda_1-\lambda_2) \int_0^1 dq\ e^{\lambda_1 q+\lambda_2 q} + \int_0^1 dq \lambda_2 e^{\lambda_2 q} \right) - e^{-\lambda_1}(1-e^{-\lambda_2})$$

$$= e^{-\lambda_1-\lambda_2} \left((\lambda_1-\lambda_2)\frac{e^{\lambda_1+\lambda_2}-1}{\lambda_1+\lambda_2} + e^{\lambda_2} - 1 \right) - e^{-\lambda_1}(1-e^{-\lambda_2})$$

$$= \frac{\lambda_1 - \lambda_2}{\lambda_1 + \lambda_2} - \frac{\lambda_1 - \lambda_2}{\lambda_1 + \lambda_2} e^{-\lambda_1 - \lambda_2} + e^{-\lambda_1} - e^{-\lambda_1 - \lambda_2} - e^{-\lambda_1} + e^{-\lambda_1 - \lambda_2}$$

$$= \frac{\lambda_1 - \lambda_2}{\lambda_1 + \lambda_2}(1 - e^{-(\lambda_1 + \lambda_2)}))$$

If $\lambda_1 + \lambda_2 \gg 1$, $P(A + B > 0)$

$$\left\langle \frac{A - B}{A + B} \middle| A + B > 0 \right\rangle \approx \frac{\lambda_1 - \lambda_2}{\lambda_1 + \lambda_2} \tag{A.4}$$

A.3 Normalized asymmetry

$$\left\langle \frac{A - \mu B}{A + \mu B} \right\rangle = \sum_{k_1=0}^{\infty} \frac{e^{-\lambda_1}}{k_1!} \lambda_1^{k_1} \sum_{k_2=0}^{\infty} \frac{e^{-\lambda_2}}{k_2!} \lambda_2^{k_2} \frac{k_1 - \mu k_2}{k_1 + \mu k_2} \tag{A.5}$$

The function $f(k_1, k_2, \mu) = \dfrac{k_1 - \mu k_2}{k_1 + \mu k_2}$ diverges at $(0, 0, 1)$. Since the μ is supposed take its values around 1, we are going to exclude $k_1 = 0,\ k_2 = 0$ from the consideration similarly to the previous section.

$$P(A + \mu B > 0) \left\langle \frac{A - \mu B}{A + \mu B} \middle| A + \mu B > 0 \right\rangle =$$

$$= \sum_{k_1=1}^{\infty} \frac{e^{-\lambda_1}}{k_1!} \lambda_1^{k_1} \sum_{k_2=0}^{\infty} \frac{e^{-\lambda_2}}{k_2!} \lambda_2^{k_2} \frac{k_1 - \mu k_2}{k_1 + \mu k_2} + \frac{e^{-\lambda_1}}{0!} \lambda_1^0 \sum_{k_2=1}^{\infty} \frac{e^{-\lambda_2}}{k_2!} \lambda_2^{k_2} (-1) =$$

$$= \sum_{k_1=1}^{\infty} \frac{e^{-\lambda_1}}{k_1!} \lambda_1^{k_1} \sum_{k_2=0}^{\infty} \frac{e^{-\lambda_2}}{k_2!} \lambda_2^{k_2} \int_0^{\infty} (k_1 - \mu k_2)\ e^{-x k_1 - x \mu k_2} dx - e^{-\lambda_1}(1 - e^{-\lambda_2})$$

Let $q = e^{-x}$, $dq = -e^{-x} dx = -q dx$, $dx = -\dfrac{dq}{q}$

$$= e^{-\lambda_1 - \lambda_2} \int_0^1 \sum_{k_1=1}^{\infty} \frac{(\lambda_1 q)^{k_1}}{k_1!} \sum_{k_2=0}^{\infty} \frac{(\lambda_2 q^{\mu})^{k_2}}{k_2!} (k_1 - \mu k_2) \frac{dq}{q} - e^{-\lambda_1}(1 - e^{-\lambda_2}) =$$

$$= e^{-\lambda_1 - \lambda_2} \int_0^1 \left(\sum_{k_1=1}^{\infty} k_1 \frac{(\lambda_1 q)^{k_1}}{k_1!} \sum_{k_2=0}^{\infty} \frac{(\lambda_2 q^{\mu})^{k_2}}{k_2!} - \sum_{k_1=1}^{\infty} \frac{(\lambda_1 q)^{k_1}}{k_1!} \sum_{k_2=0}^{\infty} \mu k_2 \frac{(\lambda_2 q^{\mu})^{k_2}}{k_2!} \right) \frac{dq}{q} - e^{-\lambda_1}(1 - e^{-\lambda_2}) =$$

$$= e^{-\lambda_1 - \lambda_2} \int_0^1 \left(\lambda_1 q e^{\lambda_1 q} e^{\lambda_2 q^{\mu}} - (e^{\lambda_1 q} - 1) \mu \lambda_2 q^{\mu} e^{\lambda_2 q^{\mu}} \right) \frac{dq}{q} - e^{-\lambda_1}(1 - e^{-\lambda_2}) =$$

$$= e^{-\lambda_1 - \lambda_2} \left(\lambda_1 \int_0^1 e^{\lambda_1 q} e^{\lambda_2 q^{\mu}} dq - \mu \lambda_2 \int_0^1 q^{\mu - 1} e^{\lambda_1 q} e^{\lambda_2 q^{\mu}} dq + \mu \lambda_2 \int_0^1 q^{\mu - 1} e^{\lambda_2 q^{\mu}} dq \right) - e^{-\lambda_1}(1 - e^{-\lambda_2})$$

A.4 Conclusion

As we have seen, in the limit of vanishing $P(A + B = 0)$, taking the asymmetry on mean values, or mean values of asymmetries is equivalent.

The only reason to perform several cycles is to discriminate and subsequently remove eventual drift phenomena. Since a drift-resistant acquisition protocol should not alter the result which would be obtained in the case without drift, one should avoid calculating asymmetry on cycles with few counts, since the cycles where $A = 0$ or $B = 0$ result in division by zero and are removed from the consideration in the mean value of asymmetry.

Appendix B

Density functional theory

The DFT is widely used framework for the numerical simulation of the electronic structure. It consists in a series of approximations, as well as set of extensions which provide more precise results at higher computational cost. These methods are reviewed in [Payne1992; Gross1995; Martin2004; Verstraete2005].

B.1 Kohn-Sham scheme

B.1.1 Hohenberg-Kohn theorem

This fundamental for the DFT theorem establishes the correspondence between the potential and the electron density of the quantum system.

Consider a system consisting of N electrons, and denote the position and spin state of i-electrons by $\boldsymbol{r}_i$ and s_i respectively. Given the potential in which the electrons are located, once can solve the Schrodinger equation for the wave function $\Psi(\boldsymbol{r}_1, s_1, ...\boldsymbol{r}_N, s_N)$, and then find the electron density.

The density $n(\boldsymbol{r})$ is called V-representable, if it is the ground state of the electron Hamiltonian with some external potential.

A sufficient condition of V-representability requires that the density be integrable to some integer number of electrons, and be sufficiently regular. This condition is usually assured by deriving $n(\boldsymbol{r})$ from a set of wave functions.

The Hohenberg-Kohn theorem (the proof is given in the original article [Hohenberg1964]) states that

- Suppose the ground state electron density $n(\boldsymbol{r})$ of the system to be V-representable. Then for any system of interacting particles in an external potential $V_{\text{ext}}(\boldsymbol{r})$, this potential is determined up to a constant by $n(\boldsymbol{r})$.
  Since the Hamiltonian is thus fully determined, it follows that $\Psi(\boldsymbol{r}_1, s_1, ...\boldsymbol{r}_N, s_N)$ is also determined, both for ground and excited states. Therefore all properties of the system are completely determined given only the ground state density $n(\boldsymbol{r})$.
- A universal functional for the energy $E[n]$ in terms of the density $n(\boldsymbol{r})$ can be defined, valid for any external potential $V_{\text{ext}}(\boldsymbol{r})$. For any particular potential, the exact ground state energy of the system is the global minimum value of this functional, and the density $n(\boldsymbol{r})$ that minimizes the functional is the exact ground state energy.

This implies that $E[n]$ alone is sufficient to determine the exact ground state energy and density.

This theorem enables a transition from the Schrodinger equation for the wave function to the equation on electron density $n(\boldsymbol{r})$, that is, to reduce the problem with $2N$ unknowns to a problem with one unknown.

According to the theorem presented in theappendix B.1.1, the total energy can be rewritten as a functional of the orthonormal set of auxiliary one-particle wave functions ψ_i:

$$E[n] = -\sum_i \langle\psi_i|\,\boldsymbol{\nabla}^2\,|\psi_i\rangle - \sum_l \frac{Z_l n(\boldsymbol{r})}{|\boldsymbol{r}-\boldsymbol{R}_l|} + \int d\boldsymbol{r}d\boldsymbol{r}'\frac{n(\boldsymbol{r})n(\boldsymbol{r}')}{|\boldsymbol{r}-\boldsymbol{r}'|} + E_{xc}[n]$$

where the electron density

$$n(\boldsymbol{r}) = \sum_i \langle\psi_i(\boldsymbol{r})\,|\,\psi_i(\boldsymbol{r})\rangle \tag{B.1}$$

The index l runs over the atomic nuclei in the system (placed at $\boldsymbol{R}_l$ and having a charge Z_l) and i runs over the occupied electronic states (i.e. bands and k-points in the BZ). $E_{xc}[n]$ is called the exchange-correlation energy, because it reflects the exchange interaction of electrons of same spin, and the correlation of the individual electrons, due to Pauli repulsion in particular. Minimizing $E[n]$ yields a Schrodinger-like equation for the ψ_i:

$$\left[-\frac{1}{2}\boldsymbol{\nabla}^2 + V_H[n] + V_{xc}[n]\right]\psi_i = \epsilon_i\psi_i \tag{B.2}$$

where Hartree potential is given by

$$V_H[n] = -\sum_l \frac{Z_l}{|\boldsymbol{r}_i-\boldsymbol{R}_l|} + \int d\boldsymbol{r}'\frac{n(\boldsymbol{r}')}{|\boldsymbol{r}-\boldsymbol{r}'|} \tag{B.3}$$

and exchange-correlation potential

$$V_{xc}[n] = \frac{dE_{xc}}{dn}[n] \tag{B.4}$$

Usually, these equations are resolved by a fixed point algorithm, consisting of the following steps

1. A trial set of wave functions ψ_i is taken.
2. The density is evaluated using eq. (B.1), and the potential is calculated according to one of the approximation detailed in following sections.
3. Solving the eq. (B.2) provides new wave functions.

B.1.2 Local density approximation

The LDA is a frequently used approximation to the DFT. It is obtained in the limit of slowly varying density by approximating the total energy functional by the means of a mean-field expression

$$E_{xc}^{\mathrm{LDA}}[n] = \int d\boldsymbol{r} \epsilon_{xc}^{\mathrm{HEG}}[n(\boldsymbol{r})] n(\boldsymbol{r})$$

where $\epsilon_{xc}^{\mathrm{HEG}}[n]$ is the exchange-correlation energy density for the homogeneous electron gas.

The success of LDA is due to a priori unexpected respecting of sum rules and spherical averaging of the interaction with all the other electrons. $\epsilon_{xc}^{\mathrm{HEG}}$ can be found either from analytical expression in simple cases, or by fitting the coefficients of a certain function (called parameterization) from the quantum Monte Carlo (QMC) calculations data.

B.1.3 Gradient-corrected approximations

In order to improve the precision of previous method, one can account for the gradients of the density. This approach still results in a local expression for ϵ_{xc}, and gives various gradient-corrected functionals. The latter approach is called generalized gradient approximation (GGA).

In order to include higher derivatives of the exchange-correlation energy, it is necessary to respect the sum rules (relationships between energy and the sum of the transition strengths). Among the methods with higher precision (and higher computational cost) the most common ones are

- Meta-GGA: adding additional constraints to the functionals of n, $\boldsymbol{\nabla} n$, Δn [Filatov1998; Tao2003]
- Hybrid approaches: mixing the Hartree-Fock exchange term with correlation functional from DFT [Lee1988; Becke1993]
- Exact exchange or optimized effective potential: implicit calculation of E_{xc} through an integral equation [Talman1976; Krieger1992]

B.2 Pseudopotentials

The idea of pseudopotential method is to replace the generic Coulomb potential $-Z/|\boldsymbol{r} - \boldsymbol{R}|$ by an operator that accounts not only for the potential of the nucleus, but also of core electrons. In this way, only the positions of electrons on exterior shells are calculated. This allows to work with a smoother potential, and thus smaller plane wave basis.

A reference all-electron calculation is carried out, and an analytical pseudopotential is fitted in order to reproduce the same spectrum and wave functions.

Following categories of pseudopotentials should be distinguished:

- Norm-conserving pseudopotentials. The charge contained inside a certain cut-off radius for the pseudo wave function must coincide with the charge of all-electron wave function.
  - Local. The simplest pseudopotential is a local multiplicative function. Far from the nucleus the potential must behave like

    $$V_{\mathrm{ps}}^{\mathrm{local}} \propto (Z - n_{\mathrm{core}})/|\boldsymbol{r}|$$

    n_{core} is the number of included into pseudopotential core electrons. However, such pseudopotential possesses few of degrees of freedom, which is often insufficient for a good description of valence states.

  - Non-local. This type of pseudopotentials consists in adding projectors in order to make the valence states orthogonal to the core states [Phillips1959]:

$$V_{\text{ps}} = V_{\text{ps}}^{\text{local}} + \sum_c \alpha_c \left|\psi_c\right\rangle \left\langle\psi_c\right|$$

    where the index c designates the core states. The ψ_c and α_c constitute the additional degrees of freedom for fitting.
  - With non-linear core corrections. The fitted core charge is added to the valence charge to give a better estimation of the electron density.
- Relaxing the norm-conservation condition can be used to construct a smoother pseudopotential, and thus obtain sufficient convergence with smaller plane-wave basis. Two commonly used techniques are distinguished:
  - Ultra-soft pseudopotentials [Vanderbilt1990]
  - Projector-augmented wave (PAW) pseudopotentials [Blöchl1994]

B.3 Calculated quantities

From the total energy and density obtained as a result of self-consistent calculation, the following quantities can be derived:

- Band structure. Koopmans' theorem states that up to the 0th order the one-particle eigenvalues are the eigenvalues of an additional particle added to the system [Koopmans1934]. The approximation is inexact, since no relaxation of the other electrons due to the perturbation is accounted for. Maximally localized Wannier functionss (MLWFs) can be used for the efficient interpolation of the band structure calculate on a coarse uniform grid towards a finer one [Marzari1997].
- Phonon dispersion curves. They can be obtained by variation derivation of the total energy with respect to atomic positions.

B.4 Approximations based on many-body perturbation theory

To obtain a more accurate description of the material properties (in particular to avoid the typical for LDA problem of band gap underestimation [Perdew1985]), is possible to use more general theories. GW is a commonly used approach [Hedin1965; Onida2002] to account for electron-electron interaction via Green's function method.

The numerical index i denotes the vector of position, time, and spin $(\boldsymbol{r}_i, t_i, s_i)$.

The set of coupled integral equations introduced in [Hedin1965]:

Dyson equation on the Green function G

$$G(1,2) = G_0(1,2) + \int d34 G_0(1,3)\Sigma(3,4)G(4,2) \tag{B.5a}$$

Irreducible vertex function

$$\tilde{\Gamma}(1,2;3) = \delta(1,2)\delta(1,3) + \int d4567 \frac{\delta\Sigma(1,2)}{\delta\Sigma(4,5)} G(4,6)G(7,5)\widetilde{\Gamma}(6,7;3) \tag{B.5b}$$

Irreducible polarizability

$$\tilde{\chi}(1,2) = -i \int d34 G(2,3)G(4,2)\tilde{\Gamma}(3,4;1) \tag{B.5c}$$

Screened Coulomb interaction

$$W(1,2) = v(1,2) + \int d34 v(1,3)\tilde{\chi}(3,4)W(4,2) \tag{B.5d}$$

Self-energy (i.e. the energy of an electron as a part of the interacting electron system)

$$\Sigma(1,2) = i \int d34 G(1,4)W(3,1^+)\tilde{\Gamma}(4,2;3) \tag{B.5e}$$

As illustrated in fig. B.1, this system is resolved iteratively, starting from some initial guess on G and Σ.

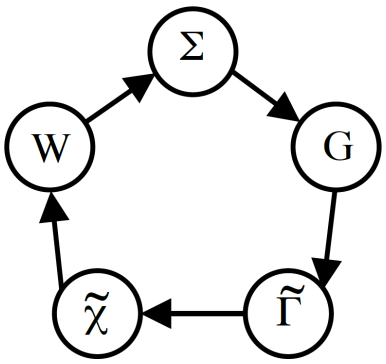


Figure B.1: Symbolical representation of the practical solution of the Hedin's system of equations

There are several options:

- The approximate solution at the end of first iteration is called GW approximation. In this case, the initialization consists in setting $\Sigma = 0$ in vertex function (B.5b):

  $$\tilde{\Gamma}(1,2;3) = \delta(1,2)\delta(1,3)$$

  It follows from eq. (B.5c) that

  $$\tilde{\chi}(1,2) = -iG(1,2)G(2,1)$$

  which is the definition of the independent particle polarizability. Equation (B.5e) yields the resulting self-energy

  $$\Sigma(1,2) = iG(1,2)W(2,1^+)$$

- Performing several iteration is called self-consistent GW method
  Dyson equation (B.5a) can be written in the operator form as

$$G = G_0 + G_0 \Sigma G$$

  with G the Green's function, G_0 is non-interacting Green function (i.e. corresponding to $\Sigma = 0$) G can be expressed as

$$(1 - G_0\Sigma)G = G_0$$

$$G = (1 - G_0\Sigma)^{-1} \cdot G_0$$

  with three possibilities for calculation
  - Resolution of full Dyson equation
    - in the basis of Kohn-Sham states

$$G = (1 - G_0\Sigma)^{-1} \cdot G_0|_{\text{KS states}}$$

    - in the basis of g states. Self-consistency is obtained by the calculation of χ^1, $\Sigma^{(1)} = iG^{(1)}W^{(1)}$, and injection of the wave functions and quasi-particle energies in the expression for G on the next iteration.
  - Self-consistency on quasi-particles. Here $\Phi = \Phi_{KS}$ are taken, but $\epsilon_i^{(N)} \to \chi$ in the sense

$$G^{(QP)} = \sum_i \frac{\phi_i^{(KS)K}(r')\phi_i^{KS)K}(r)}{\epsilon - \epsilon_i^{(QP)}}$$

    In practice this approach works better for calculation of energies than previous one, but the supplementary satellites in the complex plane $(\epsilon, \Im(G))$ are not taken into consideration.
    - Plasmon-pole model consists in adding a function in the plan $(\epsilon, \Im(G))$, and yield good results for `sp` electrons.
    - Numerical integration is better suited for `d` electrons.
  - Partial self-consistency

$$\Sigma = G^{(N)}W^0$$

B.5 Quantum chemistry packages

Today a number of packages for first-principles calculations are available. Open-source packages often implement a larger set of new numerical methods compared to the commercial software. Among them, the two actively developed are Abinit [Gonze2009] and QuantumEspresso [Giannozzi2009], both of which are based on pseudopotentials and plane-wave basis. An all-electron [ElkSoftware] and the Gaussian basis-based [Dovesi2005] software are also available. The proprietary software packages [Kresse1996] provide more restricted functionality but higher robustness and computational speed.

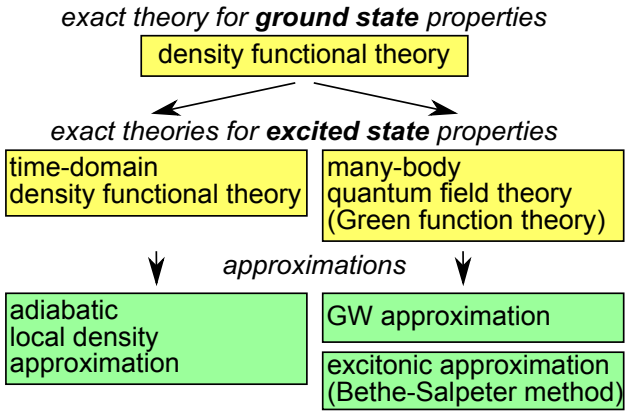


Figure B.2: Commonly used approaches for the calculation of properties of many-electron systems

Appendix C

Comparative convergence study of different pseudopotentials

C.1 Combination of scGW and $\mathrm{DFT_{SO}}$ eigenenergies

Current version of ABINIT does not implement GW formalism with spin-orbit coupling. Since the modeling of optical pumping require both precise description of bands, provided by quasiparticle calculation, and spin-orbit splitting, a method for combination of self-consistent GW eigenenergies $\epsilon_{scGW}(i)$ without spin-orbit splitting and LDA eigenenergies with spin-orbit splitting $\epsilon^{SO}_{DFT}(i)$ needs to be proposed.

The usual technique consists in calculating GW correction on a coarse k-point grid and then interpolating on the k-points of interest. [Heinz2010] shows that for Silicon the GW corrections to the band structure are weakly dependent on the k-point, thus justifying the simplest (scissor-shift) approach, which consist in a rigid shift of bands according to GW correction for a single k-point.

Here we use a more precise approach: the use of MLWF for the interpolation of GW eigenenergies from a coarse calculation grid to a fine interpolation grid.

For each pseudopotential i from table C.1, the band structures according to several approaches are calculated:

- $\epsilon_{DFT}(i)$ directly or using MLWF interpolation of values on uniform grid.
- $\epsilon^{SO}_{DFT}(i)$ with spin-orbit coupling, directly or using MLWF interpolation.
- $\epsilon_{scGW}(i)$ using self-consistent GW approximation, and MLWF interpolation to construct the band structure.
- $\epsilon_{scGW,\Gamma}(i)$ the same as previous but also using vertex correction.

Not all of methods above are available for all the considered pseudopotentials, so it is necessary to combine together eigenenergies calculated with different pseudopotentials.

For a self-consistent field method (SCF) run, it is sufficient to take the default number of bands, i.e. all the valence bands and one conduction band.

The parameters of MLWF interpolations are identical for all runs.

Pseudopotential	Exchange term	GGA	SO	MLWF	GW	GWGamma
14si.4.hgh	1		yes	yes		yes
14-Si.nlcc.fhi	7			yes	yes	yes
14-Si.nlcc.UPF	Perdew-Wang LDA			yes	yes	yes
14Si_pade-q4	1			yes		yes
14si.pspgth	1			yes	yes	yes
14si.pspnc	1			yes	yes	yes
14si.psp	1			yes	yes	yes
14si_WC.fhi	23	yes		yes	yes	yes
Si.GGA_X_PBE_SOL +GGA_C_PBE_SOL-paw.abinit	-116133	yes	yes		yes	
Si-LDA.paw	7		yes	yes	yes	
si_ps.736.lda	2		yes	yes	yes	
si_ps.736.pbe	11	yes	yes	yes	yes	

Table C.1: Pseudopotentials from ABINIT distribution which were considered in the present convergence study.

As is shown in fig. C.1, the difference appears, as expected, only for eigenvalues out of frozen energy window.

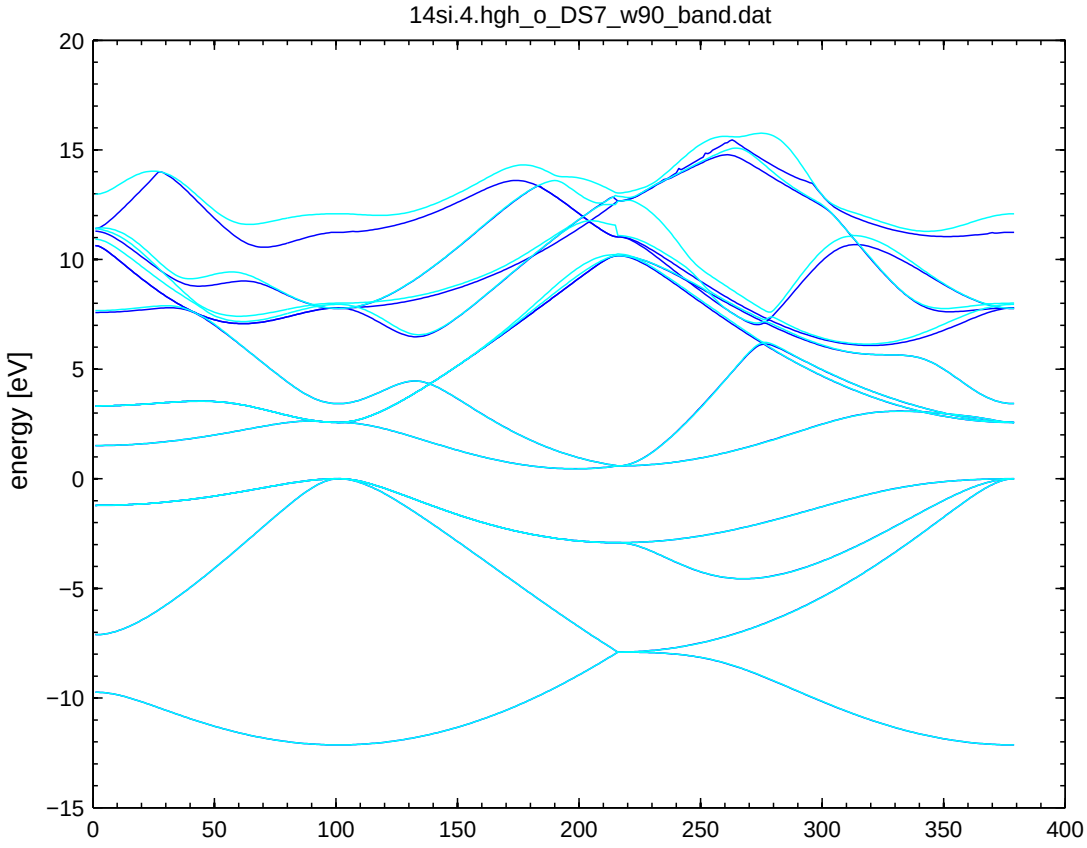


Figure C.1: Comparison of band structure, calculated directly by DFT or interpolated with MLWF (HGH pseudopotential)

The matching procedure is the following: for each pseudopotential i_{scGW} where scGW is available, we choose the closest pseudopotential j_{SO} among those with SO correction:

$$i_{SO} = \arg\min_{j_{SO}} \|\epsilon_{DFT}(i_{scGW}) - \epsilon_{scGW}(j_{SO})\|$$

Then the final band structure can be obtained as

$$\epsilon^{SO}_{scGW}(i_{scGW}, i_{SO}) = \epsilon_{DFT}(i_{scGW}) + (\epsilon_{scGW}(i_{scGW}) - \epsilon_{DFT}(i_{scGW})) + (\epsilon^{SO}_{DFT}(i_{SO}) - \epsilon_{DFT}(i_{SO}))$$

or equivalently as

$$\epsilon^{SO}_{scGW}(i_{scGW}, i_{SO}) = \epsilon_{DFT}(i_{SO}) + (\epsilon_{scGW}(i_{scGW}) - \epsilon_{DFT}(i_{scGW})) + (\epsilon^{SO}_{DFT}(i_{SO}) - \epsilon_{DFT}(i_{SO}))$$

The previous minimization is aimed to put these two results, both legitimate, as close as possible. The band structures for self-consistent GW with vertex correction are constructed in the same way.

In following figures ϵ_{scGW} is plotted with red lines, $\epsilon_{scGW,\Gamma}$ with blue lines. The improvement of the band gap value thanks to the vertex correction is less important than reported

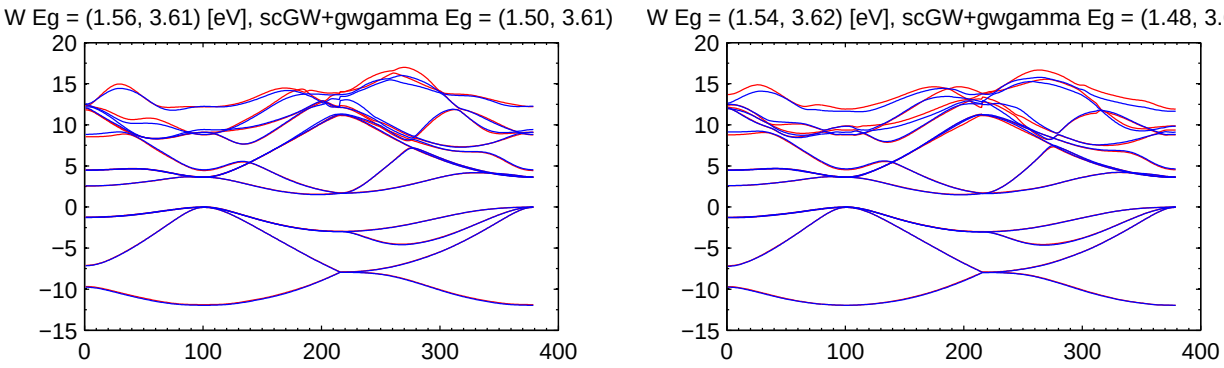


Figure C.2: Combination of GW pseudopotential and a pseudopotential accounting for SO coupling: 14-Si.nlcc.fhi and Si-LDA.paw (left), 14si.pspgth and 14si.4.hgh (right)

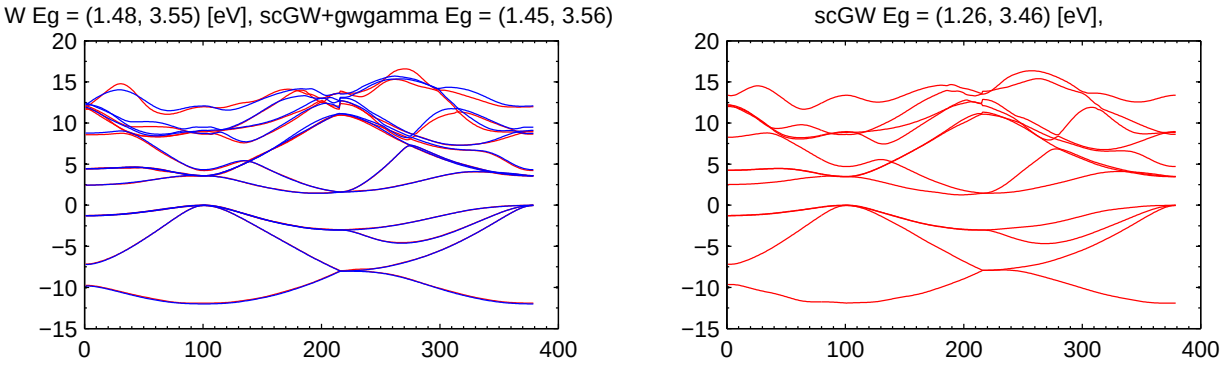


Figure C.3: Combination of GW pseudopotential and a pseudopotential accounting for SO coupling: 14si.pspnc and si.ps.736.lda (left), Si-LDA.paw and Si-LDA.paw (right)

by [Shishkin2007]. In order to calculate a more precise band gap, one may consider the numerical integration method instead of plasmon-pole model.

The band gap for pseudopotential `Si-LDA.paw` is very close to experimental data because of interpolation problem of scGW result with MLWF. The interpolation parameters being quasi-optimal for other pseudopotentials, it is difficult to improve the result for this one without worsening others. At the same time it would be less natural to combine eigenvalues interpolated with different parameters.

C.2 SCF convergence for different pseudopotentials

C.2.1 Convergence on `ecut` and `ngkpt`

Let the convergence criterion for SCF procedure `toldfe` $= 10 \times 10^{-6}$ Ha (1 Ha = 27.211 eV). First we choose `ecut` such that the difference between total energies for two consecutive values of `ecut` be lower than a given criterion. We set its value at 10×10^{-4} Ha.

It is interesting to see the influence of `pawecutdg` on the results for PAW pseudopotentials. The difference between `pawecutdg` = 30 Ha (upper curves) and `pawecutdg` = 3`ecut` (lower curves) becomes visible from `ecut` = 20 Ha.

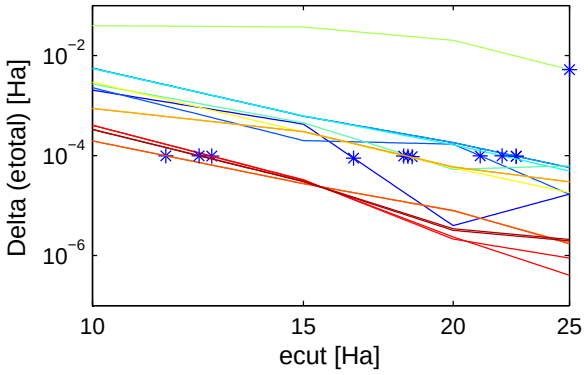


Figure C.4: Convergence in cutoff used for planewave basis (`ecut`)

The converged values of `ecut` being fixed, we proceed to the choice of `ngkpt`. This time we choose a more strict convergence criterion, for instance 1×10^{-6} Ha.

As we can see, for `ngkpt = 8 8 8` the desired precision is reached for all the preudopotentials except `14si.psp`. The parameters above were used to perform the cell relaxation.

For further use of MLWF plugin, a k-point grid should be non-shifted, which implies the necessity of another convergence study in regards to `ngkpt`. Here, to keep the calculation manageable we choose `ngkpt = 12 12 12` for all pseudopotentials.

Pseudopotential	`ecut` [Ha]
Norm-conversing:	
`14si.4.hgh`	22.6
`14-Si.nlcc.fhi`	16.5
`14-Si.nlcc.UPF`	21.1
`14Si_pade-q4`	22.6
`14si.pspgth`	22.0
`14si.pspnc`	18.5
`14si.psp`	25.0
`14si_WC.fhi`	18.2
PAW:	
`Si.GGA_X_PBE_SOL+GGA_C_PBE_SOL-paw.abinit`	18.3
`Si-LDA.paw`	11.5
`si_ps.736.lda`	12.6
`si_ps.736.pbe`	12.3

Table C.2: Converged values of `ecut`

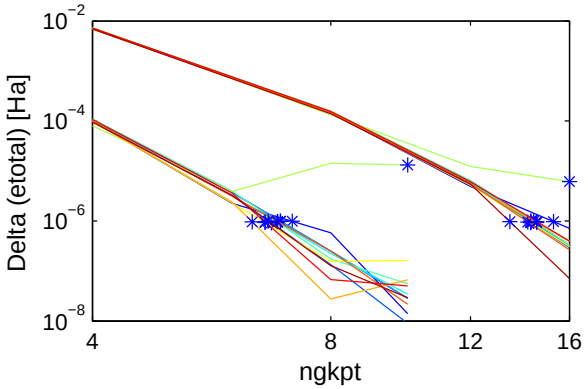


Figure C.5: Comparison of convergence with respect to number of k-points in BZ for shifted (`nshiftk 4`, curves on the left) and non-shifted (`nshiftk 1`, curves on the right) Monkhorst-Pack grids

C.3 Convergence on GW model parameters

We set the number of plane waves as following:

- The ground-state parameters `ecut`, `ngkpt` (and, if required, `pawecutdg`) on its converged value
- `ecuteps = ecut`
- `ecutsigx = min(4 ecut, pawecutdg)`
- `ecutwfn3 = ecutwfn4 = ecut` (default convention)

The convergence criteria is the residual between two successive sets of GW eigenvalues for `kptgw = 0 0 0`, which should be less than $Res = 10^{-4}[eV]$ for all studied bands (in this case $nband = 12$), that is $\frac{Res}{nband}$ per band. This quantity is used for plotting purposes.

The GW eigenvalues are given, for example in the output file of `GW` run. The precision of printed eigenvalues is increased by modification of the output procedure (`70_gw/m_sigma_results.F90, line 513`).

Such quite strict criterion is used in order to account for possible change in the convergence speed for different k-points. For the convergence study, we perform only one iteration of scGW with `optdriver = 28`.

In order to improve the convergence with respect to `nband`, we used `gwcomp = 1`. This formalism was described and illustrated by SiC example in [Bruneval2008].

Attention: with `kssform2 = 3` option (contrary to default `kssform2 = 1`), the number of bands used for GW calculation is limited by `nband2`. Still `kssform2 = 3` was used to keep the convergence study conditions the closest possible to a production run.

In the ABINIT tutorial it is stated that converged value of `ecutwfn3` could be smaller than `ecutwfn4`. Actually, the validity of this assertion depends on pseudopotential.

Pseudopotential	ecutwfn3 [Ha]	ecuteps3 [Ha]	nband3
14-Si.nlcc.fhi	14.9	17.0	156
14-Si.nlcc.UPF	12.7	17.4	158
14si.pspgth	17.1	17.4	160
14si.pspnc	15.7	17.0	200
14si.psp	17.7	17.4	176
14si_WC.fhi	15.9	17.0	200
Si.GGA_X_PBE_SOL+GGA_C_PBE_SOL-paw.abinit	16.1	17.0	200
Si-LDA.paw	6.8	11.3	200
si_ps.736.lda	7.2	11.2	200
si_ps.736.pbe	7.4	11.3	200

Table C.3: Converged parameters of screening part of GW calculation

The value of ecutsigx4 should be greater than ecut and lower than 4 ecut or pawcutdg. Numerically, the value of ecutsigx sometimes needs to be greater than these limits in order to obtain desired convergence.

C.3.1 Number of scGW cycles

Here the criterion of $10^{-4}[eV]$ was not reached due to the high computational time requirements. Nevertheless the figure provides an estimation of the convergence error for 4 scGW cycles. When using vertex correction, the convergence on eigenvalues is slightly faster for all the pseudopotentials.

Pseudopotential	ecutwfn4 [Ha]	ecutsigx4 [Ha]	nband4
14-Si.nlcc.fhi	11.3	9.2	128
14-Si.nlcc.UPF	11.5	9.6	126
14si.pspgth	15.7	10.9	128
14si.pspnc	13.1	10.5	126
14si.psp	16.9	21.2	126
14si_WC.fhi	15.7	10.9	179
Si.GGA_X_PBE_SOL+GGA_C_PBE_SOL-paw.abinit	16.7	45.2	139
Si-LDA.paw	7.4	46.5	151
si_ps.736.lda	7.4	16.9	200
si_ps.736.pbe	7.4	16.7	200

Table C.4: Converged parameters of quasiparticle part of GW calculation

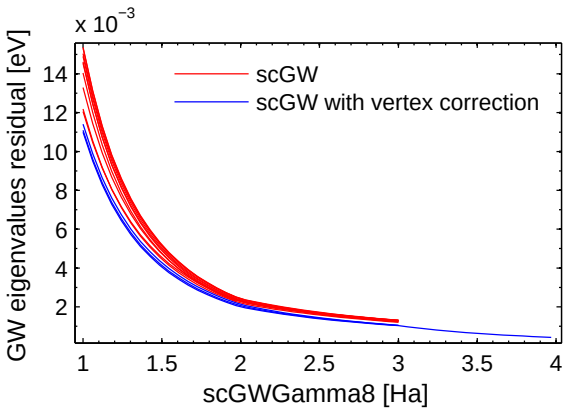


Figure C.6: Convergence as function of number of self-consistent GW cycles

C.3.2 MLWF interpolation parameters

With default values from the tutorial, the convergence of MLWF remains poor, about 10^{-1} eV. The convergence acceleration methods like use of guiding spheres of fixed step optimization make no significant difference in our case. Concerning initial guess, `s` or `p` orbitals usually give unsatisfactory results. Final method includes `sp`^{3} hybrid orbitals placed on central Silicon and on surrounding atoms, and Gaussian `s` orbitals placed at random positions in the unit cell. The initialization of random orbitals doesn't vary the same from one run to another.

To obtain good disentanglement results, the only parameter to set is `dis_froz_max`. It should be set in order to put at most `num_wann` bands for each k point. It is convenient to verify the latter condition using the output provided in `.eig` file.

List of Figures

2.1 Zinc blende crystal lattice (left), band structure of GaAs [Rohlfing1993] (right) 20
2.2 Left: Direct optical transition at the center of Brillouin zone of GaAs. Valence bands are denoted as: HH (heavy hole band), LH (light hole band), SO (split-off band). Right: Transition probabilities in an atomic-like model under σ^+-circularly polarized light excitation. The fractions denote the projection of total orbital angular momentum m_j of states at $k = 0$, the circled numbers are the transition intensities [Dyakonov2008]. 21
2.3 Numerically calculated dependence of the initial polarization (denoted as DSP in theoretical articles) on the excitation energy in GaAs, for σ^- excitation [Rioux2012] (left). Same dependence, measured by two-photon spin-polarized spectroscopy [Miah2009] (right). 22

2.4 Silicon crystal lattice in real (left) and reciprocal (right) spaces 23

2.5 Silicon band structure along high symmetry directions calculated by non-local pseudopotential method [Chelikowsky1976]. Bands are labeled according to [Koster1963]. The numbers in parentheses indicate the degeneracy of bands. The energy reference is taken at the minimum of the conduction band which is located at $k_0(0.83, 0, 0)$ 24

2.6 Zoom near Γ point: Γ_5^+ valence band (left), Γ_4^- conduction band (right). Negative values of k correspond to Λ direction, positive values to Δ direction. The bands are calculated by 30 band k.p method [Richard2004b]. 25

2.7 Real (top panel) and imaginary (bottom panel) parts of dielectric function of Si for different temperatures measured by ellipsometry [Jellison1983] (left). Temperature variation of peaks on $\Im(\epsilon_d)$. The experimental data is fitted with the empirical relation of Varshni (right). 26

2.8 A direct optical transition at the center of Brillouin zone of Si. The spin-orbit interaction-induced splittings of valence and conduction band are denoted as Δ_{SO} and $\Delta_{\mathrm{SO}}^{\mathrm{c}}$ respectively (left). Calculation of corresponding initial polarization under σ^+-circularly polarized light excitation. The fractions denote m_j orbital moment of states at $k = 0$, the circled numbers are the transition intensities (right). 29

2.9 Electron mean free path dependence on kinetic energy [Briggs1983] (left), the same curve for Silicon [Pi2000] (right) 30

2.10 Dispersion of phonons in Silicon. $100\,\mathrm{cm}^{-1} = 12.7\,\mathrm{meV}$ [Giannozzi1991]. Experimental data are taken from [Nilsson1972] 34

2.11 Absorption spectrum at 1.8 K with contributions of different phonon modes [Nishino1974]. The dots represent the neutron spectroscopy data from [Nilsson1972] 35

3.1 Setup operation principle (left), schematic view of UHV chamber (right) 38

3.2 Example of Babinet-Soleil calibration for $h\nu = 3.32\,\mathrm{eV}$ 40

3.3 Results of the Babinet-Soleil calibration for all measurements: period of intensity variation from fig. 3.2 (left), 0 order position (right) 41

3.4 The location of axis of the Babinet-Soleil compensator, and the direction of the mobile wedge displacement, which leads to σ^+ if shifted by the value given in eq. (3.11). Incident laser radiation is linearly polarized along $\boldsymbol{e}_x$. The orientation of fast axis was double-checked with help of a calibrated quarter-wave plate. 42

3.5 Schematic view of the electron optics. The sample faces the entrance slit of the rotator which is coupled to the selector by a decelerating electron optics. The selected electrons are either detected on a Faraday cup for EDC's measurements, or accelerated in a transport optics and projected into the Mott polarimeter. The P_z component of spin polarization is measured (left). Operation of the electron spectrometer: The bias voltage V_{cath} is applied to the cathode. The electrons which have a zero kinetic energy in the zero potential of the grounded gold electrode are selected. The electron optics potentials remain constant at the positive bias V_a. The conduction band minimum, the Fermi level and the valence band maximum are denoted as ϵ_{CB}, ϵ_F, ϵ_{VB} respectively (right). δE is the band pass energy of the spectrometer which can be chosen in the range $20 - 80\,\mathrm{meV}$ 44

3.6 Top view of the Mott detector chamber. Electrons are accelerated by V_{foil}, and those which scatter at $\pm 120°$, pass through cone-shaped apertures and enter in the retarding fields V_b. $\boldsymbol{p}$ and $\boldsymbol{p}'$, the momentum vectors of the incident and scattered electron beams, define the scattering plane (left). Selection of the ballistic electrons in the Mott detector. Only the electrons that have suffered small inelastic energy losses on scattering are detected (right). 46

3.7 Spot size dependence on accelerating voltage (20 kV, 40 kV, 60 kV, 80 kV and 100 kV). The round inlet aperture of Mott detector can be seen in e and f images. It is artificially colored in f image 47

3.8 Superimposed images of the electron spot with (red vertical line) and without (blue horizontal line) magnetic field. On the left HT=60 kV, $h\nu = 2.38$ eV, resolution 40 meV, on the right HT=60 kV, $h\nu = 3.425$ eV, resolution 30 meV. The size of spots depends mostly on the potentials on electrodes. The magnetic field is perpendicular to the image. 47

3.9 Planned (green line) and other possible (red dashed lines) electron trajectories in the selector. The electrons are polarized along $\boldsymbol{e}_z$ 48

3.10 The calculated electron trajectories with (red points) and without (blue lines) the coil magnetic field. Electrons propagate along $\boldsymbol{e}_x$ (i.e. south-north) direction, and the presence of electric and magnetic fields leads to weak deviations in (y, z) plane. Left and right panels correspond to initial velocity distribution $(v_x, 0, 0)$ and $(v_x, v_y, 0)$ respectively. The projections are represented further in fig. 3.11 49

3.11 Longitudinal and transverse components of electron speed and magnetic field of the coil (left), spot rotation angle (right). The discontinuities of v_x correspond to the positions of accelerating electrodes. 50

3.12 Mott scattering conventions. The scattering rate in a given direction is different for spin $|\uparrow\rangle$ and $|\downarrow\rangle$ electrons which leads to the left-right asymmetry when scattering a spin-polarized electron beam. $\boldsymbol{p}$ and $\boldsymbol{p}'$, the momentum vectors of the incident and scattered electron beams, define the scattering plane. 52

3.13 Comparison of calculated Sherman function with that calibrated on 1 µm gold foil using GaAs photocathode illuminated at $h\nu = 1.95$ eV at room temperature, considering $P_{el} = -25\,\%$ at σ^+-circularly polarized light. 54

3.14 Figure of merit as function of retarding potential V_b for different values of V_{foil} 55

3.15 Coil calibration under excitation at $h\nu = 3.28$ eV. The peak positive polarization corresponds to 0 A, the peak negative polarization to ± 4.8 A 56

3.16 Absorption coefficient of Silicon [Macfarlane1959; Sze2006] 57

3.17 The variation of the lifetime and diffusion length of minority carriers in the p-type silicon at room temperature. The data is collected from different sources by [Tyagi1983]. The diffusion length is calculated from the time of life: $L = \sqrt{D\tau_e}$, where D is the diffusion coefficient. 57

3.18 Spin lifetime in n-type Silicon extracted from Hanle measurements, combined together with ESR data on bulk Si. Silicon with different dopants (Sb, As and P) and dopant density were used, as indicated. [Jansen2012] 58

3.19 Interior of the sample holder flange 59

3.20 Principle of negative electron affinity in p-type semiconductor. By co-adsorption of Cesium and Oxygen, the vacuum level can be reduced below the conduction band in the solid. The work function of Silicon is denoted by ϕ_{Si}, the apparent electron affinity by χ and Fermi level by ϵ_{F}. 59
3.21 Surface preparation procedure, used by Roux (left) and used in the present work (right) 62
3.22 Example of surface preparation procedure, used in present work 62
3.23 The dependence of O_2 exposure versus Cesium deposition time $T_{\mathrm{O_2}}^{\mathrm{start}}$ 63
3.24 Scanning electron microscopy images of SOI [5 µm] active layer. Preserved active layer in the interior of the sample (left), active layer deterioration on the exterior edge (right). 65
3.25 Quantum yield of Silicon photocathodes. Least-squares fit provides an estimation of B and L_e. The measurements performed on all the samples are shown. The observed quantum yield is very similar for all the three samples analyzed in the present work. 67
3.26 $V_{\mathrm{cath}}^{\mathrm{LE}}$ and $V_{\mathrm{cath}}^{\mathrm{HE}}$ for measurements under continuous excitation (left). Example of threshold shift for different measurements at $h\nu = 1.95\,\mathrm{eV}$ (right). The data shown were measured on bulk Silicon at $T = 300\,\mathrm{K}$. 69
3.27 Position of thresholds versus excitation energy for all measurements on all the three samples 69
3.28 Illustration of spikes removal procedure on EDC (SOI [5 µm], $h\nu = 1.93\,\mathrm{eV}$, $T = 300\,\mathrm{K}$) 71
3.29 Low energy threshold determination (SOI [5 µm], $h\nu = 1.93\,\mathrm{eV}$, $T = 300\,\mathrm{K}$) 71
3.30 Decreasing part of an EDC (left), constructed histogram $(x(i), n(i))$ (center) and its zoom (right) (SOI [5 µm], $h\nu = 1.93\,\mathrm{eV}$, $T = 300\,\mathrm{K}$) 72
3.31 Piecewise linear interpolation for the determination of high-energy threshold (SOI [5 µm], $h\nu = 1.93\,\mathrm{eV}$, $T = 300\,\mathrm{K}$). The determined HE threshold is marked with the square. 73
3.32 EDCs before (left panel) and after alignment (right panel) of HE threshold for the same $h\nu$ (all samples, $h\nu = 1.95\,\mathrm{eV}$, $T = 300\,\mathrm{K}$) 74
3.33 HE thresholds of EDCs for different excitation energies (some of the measurements on SOI samples, $T = 300\,\mathrm{K}$) 74
3.34 Series of EDCs versus temperature measured on bulk Silicon under $h\nu = 1.95\,\mathrm{eV}$. The observed increase is 0.23 eV and 0.1 eV for LE and HE thresholds respectively. 76
3.35 Dependence of EDC rising width on the electron affinity for the measurements made at different spectrometer resolutions (V_{res} is indicated in legend). Straight lines are the guide for eyes. The measurements for all the excitation energies are represented. 77
3.36 Typical decomposition of an EDC with $h\nu \gtrsim \epsilon_{g,\Gamma}$ into the contributions from L valley and the vicinity of zone center, which are superimposed on the main part of the photoemission spectrum. 78
3.37 Determination of features on an EDC (left), the detected feature is located in the interval $0.6 - 1.1\,\mathrm{eV}$ (right) (SOI [5 µm], $h\nu = 3.28\,\mathrm{eV}$, $T = 300\,\mathrm{K}$) 79
3.38 Characteristic EDC (blue curve) and PEDC (red errorbars) under UV excitation (SOI [5 µm], $h\nu = 3.33\,\mathrm{eV}$, $T = 114\,\mathrm{K}$) 80
3.39 Estimation of error on the polarization (SOI [5 µm], $h\nu = 3.28\,\mathrm{eV}$, $T = 300\,\mathrm{K}$) 84

3.40 Estimation of the polarization near high-energy threshold (SOI [5 µm], $h\nu$ = 3.33 eV, T = 114 K). A combined value of all the three estimation is used for the analysis of the polarization. 86

4.1 Light interference in SOI [5 µm] 92

4.2 Maximum of an EDC at $h\nu$ = 1.7 eV as a function of temperature (left), light interference in SOI [2 µm] (right) 92

4.3 Comparison of calculated light interference in SOI [5 µm], T = 115 K, based on different datasets of Silicon absorption coefficient 93

4.4 Polarization at high-energy threshold versus photon energy starting close to the indirect band gap $\epsilon_{g,X}$. $\epsilon_{g,X}(300\,\mathrm{K}) = 1.125\,\mathrm{eV}$ and $\epsilon_{g,X}(115\,\mathrm{K}) = 1.16\,\mathrm{eV}$ are shown with red and blue lines respectively. 94

4.5 Spectra of σ^- (blue image) and σ^+ (red image) components of photoluminescence under σ^+-circularly polarized excitation (left). The peak polarization of hot photoluminescence is denoted with A (right). The inelastic scattering of the incident photons on an optical phonon at Γ of energy 64 meV is denoted with O_Γ. The negative contribution at the energy of 1.24 eV is also likely to be attributed to Raman scattering. ($h\nu$ = 1.24 eV, T = 77 K, bulk Silicon) [Roux2008] 95

4.6 EDC-averaged polarization in IR region. Only the results with statistical error less than 2×10^{-3} are shown. The cumulative error on each individual point, which can be estimated from the scattering, is about 4×10^{-3}. The solid lines are the running average interpolations, which account for the relative error of each measurement. $\epsilon_{g,X}(300\,\mathrm{K}) = 1.125\,\mathrm{eV}$ and $\epsilon_{g,X}(115\,\mathrm{K}) = 1.16\,\mathrm{eV}$ are shown with red and blue lines respectively. 97

4.7 Calculated initial polarization under near indirect gap excitation along $\boldsymbol{e}_z$ [Cheng2011a]. The electrons photoexcited to the longitudinal (located on $\boldsymbol{e}_z$ axis) condition valleys are +10 %-spin polarized, whereas the electrons photoexcited to the transverse with respect to $\boldsymbol{e}_z$ valleys are −25 %-spin polarized. The predicted angular-averaged polarization is around −10 %. 98

4.8 Polarization in BBR under IR excitation (left) and UV excitation (right). The measurements for the temperatures and samples are shown. 100

4.9 First derivative of the EDCs (denoted by $N'(\epsilon)$) for $h\nu \approx \epsilon_{g,\Gamma}$, (1 1 1) (SOI [2 µm]) and 115 K. High energy threshold is represented with black line. Dot-dashed line locates the L valley emission (situated at ϵ = 1.12 eV), dashed line locates the emission from the first direct gap (situated at ϵ = 2.22 eV). 102

4.10 Two processes leading to the accumulation of electrons in L valley of Γ_4^- conduction band. 103

4.11 The amplitude of the first derivative minimum ($N'(1\,\mathrm{eV})$) from fig. 4.9 for different excitation energies. The minimum of the derivative allows to estimate $3.2\,\mathrm{eV} \lesssim \epsilon_{g,L}^{\mathrm{direct}} \lesssim 3.44\,\mathrm{eV}$. 104

4.12 Temperature dependence of features: (1 0 0)-oriented bulk Si (left) and (1 1 1)-oriented SOI [2 µm] (right). Multiples EDCs are shown in order to illustrate the uncertainty in the feature thresholds. Features are represented with bold lines. Dot-dashed lines locate the L valley emission (1.07 eV and 1.12 eV at room and low temperatures respectively), dashed lines locate the emission from the first direct gap (2.175 eV and 2.2 eV). 104
4.13 Comparison of features at 115 K for different samples). The structures are found for excitation energies $h\nu = 1.95 - 3.53$ eV. The indirect (i.e. phonon-assisted) transition to the minimum of the conduction band and a direct transition to L valley are shown. Black line on the top panel represents the high-energy threshold dependence on excitation energy $\epsilon_{\mathrm{HE}} = h\nu - \epsilon_{g,X}$ 105
4.14 High-energy threshold (HE) of the features detected in EDCs. The size of each marker is proportional to the amplitude of the detected feature. 106
4.15 Low-energy threshold of the features detected in EDCs. The size of each marker is proportional to the amplitude of the detected feature. 106
4.16 Histograms of feature $(\epsilon^f_{HE} + \epsilon^f_{LE})/2$ from figs. 4.14 and 4.15 107
4.17 Typical EDC (blue curve) and PEDC (red errorbars) under UV excitation (SOI [5 µm], $h\nu = 3.33$ eV, $T = 114$ K) (left). PEDCs with $h\nu \approx \epsilon_{g,\Gamma}$ (right). 108
4.18 Polarization at the EDC's high-energy threshold versus photon energy in visible and near UV range. The solid lines are the running average interpolations, which account for the relative error of each measurement. 109
4.19 Polarization at the EDC's high-energy threshold in the vicinity of the first direct band gap. The solid lines are the running average interpolations, which account for the relative error of each measurement. 110
4.20 PEDC measurements where the negative contribution on HE threshold was observed for 300 K (left) and 115 K (right). Measurements on all the three samples are shown. 111
4.21 Energy, corresponding to a change of sign on PEDC. Electron kinetic energy values giving change in sing of the polarization in PEDCs. The solid line is the running average interpolation, which accounts for the relative error of each measurement. 112
4.22 Mean polarization of hot electrons in the electron kinetic energy range $0.5 - 1$ eV. The solid lines are the running average interpolations, which account for the relative error of each measurement. The bulk sample measurements are performed with Kr+ laser, whereas SOI samples are measured with Ti:Sapphire laser except some measurements at $h\nu = 3.282$ eV, which are performed with UV diode laser. 113
4.23 The sets of data points from fig. 4.22 plotted separately for ambient (left panel) and low (right panel) temperatures. 114
4.24 Energy- and angle-integrated spin polarization. The arrows indicate the photothresholds from which the polarization was energy-integrated [Bona1985]. 115
4.25 Dependence of the EDC-averaged polarization $\langle P \rangle$ on the electron affinity. The solid lines are the running average interpolations, which account for the relative error of each measurement. 116
4.26 EDC-averaged polarization $\langle P \rangle(h\nu)$, integrated from: onset of absorption (left), from $\epsilon = 1.82$ eV (right) 116

4.27 EDC-averaged polarization, energy-integrated in the limits where L feature on EDCs is observed. 117
4.28 Typical EDC and PEDC acquired with THG (SOI [2 µm], $h\nu = 4.29\,\mathrm{eV}$, $T = 309\,\mathrm{K}$) 117
4.29 Polarization at high-energy threshold in far UV. A large $\pm 0.15\%$ scatter is explained by the incertitude at the HE threshold of PEDCs. 118
4.30 EDC-averaged polarization integrated from $\epsilon = 2.56\,\mathrm{eV}$ 118
4.31 Spin polarization of electrons, photoemitted from gaseous Cesium under σ^+ circularly polarized light [Heinzmann2012] 119

5.1 Broadening of EDCs and decrease in the polarization due to saturation of electron optics by high photoemitted currents under continuous excitation (SOI [5 µm], $h\nu = 3.31\,\mathrm{eV}$, $T = 300\,\mathrm{K}$) 123
5.2 EDC and the corresponding PEDC for pulsed measurement at $h\nu = 3.29\,\mathrm{eV}$, $T = 300\,\mathrm{K}$, SOI [2 µm] (left), same data with rescaled x-axis superposed onto continuous measurements with similar photon energy, temperature and sample (right). 124
5.3 Pulsed (left) and continuous (right) EDCs at $h\nu = 1.4\,\mathrm{eV}$ and spectrometer resolution 40 meV. The power in the right panel vary from 50 mW (blue curve) to 2.2 W (red curve) (SOI [2 µm], $T = 300\,\mathrm{K}$). The typical peak photon fluxes at 1 W of optical power are 1.6×10^{31} photons/m^2/s and 1.3×10^{26} photons/m^2/s for pulsed and continuous modes respectively. 127
5.4 Optical spectra of femtosecond laser radiation at wavelength $\lambda = 885.6\,\mathrm{nm}$ (i.e. photon energy of $h\nu = 1.4\,\mathrm{eV}$) emitted at different optical powers 127
5.5 Energy width of EDCs deduced from fig. 5.3 128
5.6 Cathode current and the maximum of EDC at $V_{\mathrm{cath}} = -3.5\,\mathrm{V}$ versus optical power 128
5.7 Spectrometer transmission $\int N(\epsilon)d\epsilon / I_{\mathrm{cath}}$ at $h\nu = 1.4\,\mathrm{eV}$ 129
5.8 Linear (left) and logarithmic (right) EDCs for $h\nu = 1.67\,\mathrm{eV}$ (SOI [2 µm], $T = 300\,\mathrm{K}$, 100 fs-pulsed radiation). The HE threshold of PEDCs presumably corresponds to excitation at Γ, whereas the feature at $V_{\mathrm{cath}} \approx -2.3\,\mathrm{V}$ can be associated with L valley. 130
5.9 Zoomed-in feature, corresponding to electrons transported or directly excited by a two-photon absorption process in L valley (zoom of the left panel of fig. 5.8) 130
5.10 Optical spectra measured after quartz optical components in the IR pulsed regime (100 fs pulses at 80 MHz repetition rate) 131
5.11 Photocathode $I_{\mathrm{cath}}(V_{\mathrm{cath}})$ curves (left) and corresponding slopes for different photocurrents (right) (SOI samples, $h\nu = 1.4\,\mathrm{eV}$) 132
5.12 Polarization measurement of 2PA feature at $h\nu = 1.67\,\mathrm{eV}$ (SOI [2 µm], $T = 300\,\mathrm{K}$, 100 fs-pulsed radiation)) 132
5.13 Parabolic dependence of cathode current under femtosecond pulsed excitation in two-photon regime (SOI [2 µm], $T = 300\,\mathrm{K}$) 133
5.14 Photocurrent and EDC width versus average optical power (SOI [2 µm], $h\nu = 3.29\,\mathrm{eV}$, $T = 300\,\mathrm{K}$, 100 fs-pulsed radiation)) 134
5.15 Pulsed EDCs (colored curves) with power $50 - 250\,\mathrm{mW}$ compared with continuous EDC of same $h\nu = 3.29\,\mathrm{eV}$ (black curve). (SOI [2 µm], $T = 300\,\mathrm{K}$) 135

5.16 Spectrometer saturation in picosecond mode (THG, SOI [2 µm], $h\nu = 3.8\,\mathrm{eV}$, $T = 300\,\mathrm{K}$) 135
5.17 Theoretical ratio of the intensities of one- and two-photon absorption. The direct band gaps, represented by vertical lines, are indicated at half of their energy, since the energy of the photoelectron in a two-photon absorption is $h\nu_s 2PA = 2h\nu_{1\mathrm{PA}}$. 137
5.18 Theoretical data on the two-photon cross-section for Si 138

6.1 Silicon band structure along high symmetry directions calculated by non-local pseudopotential method [Chelikowsky1976]. Bands are labeled according to [Koster1963]. The numbers in parentheses indicate the degeneracy of bands. 142
6.2 Calculated initial polarization of indirect transitions for 77 K (left) and 300 K (right) [Cheng2011a] 148
6.3 The initial polarization calculated with LDA and k.p methods (left). Initial polarization separated into contributions from different bands, calculated with LDA (right). The transitions from Γ_7^+ band make a small contribution to the total polarization, and are not shown. 150
6.4 Comparison between the energy of Γ_6^-, shifted by 3 eV ($\epsilon_{\Gamma_6^-} + 3\,\mathrm{eV}$) and the energy of Γ_8^+ band ($\epsilon_{\Gamma_8^+}$) (left). Difference $\epsilon_{\Gamma_6^-} - \epsilon_{\Gamma_8^+}$ (right). $k < 0$ correspond to $\Gamma - L$ direction, $k > 0$ correspond to $\Gamma - X$ direction. The band structure is calculated by 30 band k.p method [Richard2004b]. 151
6.5 Two interfering paths of an indirect transition in the case of phonon emission 153
6.6 Calculated deformation of valence band under compressive stress in [1 1 1] direction 155
6.7 Calculated energies at Γ of valence bands (left) and corresponding longitudinal masses (right) under [1 1 1] compressive stress 155
6.8 Spin lifetime in n-type Silicon extracted from Hanle measurements, combined together with ESR data on bulk Si. Silicon with different dopants (Sb, As and P) and dopant density were used, as indicated. [Jansen2012] 160
6.9 T_1 in undoped bulk Silicon estimated from transport properties [Huang2007]. The experimental ESR values are compared to Yafet's $T^{-5/2}$ power law for indirect gap semiconductors (left). Calculation of T_1 [Cheng2010]. The inset shows the contour plot of $1/T_1(T, \epsilon)$ of hot electrons, as a function of their kinetic energy ϵ and lattice temperature T (right). 161
6.10 Dependence of initial polarization at $z = 0$ versus excitation energy for different sample thicknesses. The polarization of thermalized electrons is modeled with $V_r^0 = 10^3\,\mathrm{m/s}$ (left), whereas the polarization of ballistic electrons is modeled by higher recombination velocity $V_r^0 = 10^{10}\,\mathrm{m/s}$ (right). 164
6.11 Profile of carrier concentration $n(z)$ (solid lines) and spin concentration $s(z)$ (dashed lines) for the absorption near the fundamental band edge. $V_r^0 = 10^3\,\mathrm{m/s}$, $V_r^d = 10^4\,\mathrm{m/s}$. 164
6.12 Profiles of carrier concentration $n(z/d)$ (solid lines) and spin concentration $s(z/d)$ (dashed lines) for different excitation energies. $V_r^0 = 10^3\,\mathrm{m/s}$, $V_r^d = 10^4\,\mathrm{m/s}$. 165

7.1 Sample introduction chamber 172

B.1 Symbolical representation of the practical solution of the Hedin's system of equations 183

B.2 Commonly used approaches for the calculation of properties of many-electron systems 185

C.1 Comparison of band structure, calculated directly by DFT or interpolated with MLWF (HGH pseudopotential) 189
C.2 Combination of GW pseudopotential and a pseudopotential accounting for SO coupling: 14-Si.nlcc.fhi and Si-LDA.paw (left), 14si.pspgth and 14si.4.hgh (right) 190
C.3 Combination of GW pseudopotential and a pseudopotential accounting for SO coupling: 14si.pspnc and si.ps.736.lda (left), Si-LDA.paw and Si-LDA.paw (right) 190
C.4 Convergence in cutoff used for planewave basis (`ecut`) 191
C.5 Comparison of convergence with respect to number of k-points in BZ for shifted (`nshiftk 4`, curves on the left) and non-shifted (`nshiftk 1`, curves on the right) Monkhorst-Pack grids 192
C.6 Convergence as function of number of self-consistent GW cycles 194

List of Tables

2.1 Most important symmetry points of the reciprocal lattice. Degeneracy is the number of equivalent directions in which these points are found. $k_0 = \frac{2\pi}{a}$ 24
2.2 Calculated parameters of lowest band gaps in Silicon [Richard2004b] 25
2.3 Experimental measurements of Silicon band structure parameters 28
2.4 Energies of phonon modes at Γ 34

3.1 Maximum conversion efficiency of high-harmonic generator 39
3.2 The direction of the polarization vector of the electron in the moment of contact with the screen. θ is the angle in $(\boldsymbol{e}_y, \boldsymbol{e}_z)$ plane, Φ is the angle between polarization vector and its projection on $(\boldsymbol{e}_y, \boldsymbol{e}_z)$ plane. 51
3.3 Values of the Sherman function for different V_{foil} and V_b 53
3.4 Optimal retarding potential V_b for different high voltages V_{foil} 55
3.5 Sample parameters 56
3.6 Steps of surface preparation procedure 61
3.7 Quantum yield-based estimation of escape probability and diffusion length 66

4.1 EDC- and $h\nu$- averaged polarization near the fundamental gap 95
4.2 Estimated in the present work parameters of Silicon band structure 120

6.1 Wave functions symmetries at Γ for a crystal belonging to O_h point group [Fishman2010] 143
6.2 Analytical model for the polarization of transitions in vicinity of the first direct gap $\epsilon_{g,\Gamma}$ (left) and second direct gap $\epsilon^2_{g,\Gamma}$ (right) 156

C.1 Pseudopotentials from ABINIT distribution which were considered in the present convergence study. 188
C.2 Converged values of `ecut` 191
C.3 Converged parameters of screening part of GW calculation 193
C.4 Converged parameters of quasiparticle part of GW calculation 193

Bibliography

[Allain2013] P. Allain et al. "Large initial compressive stress in top-down fabricated silicon nanowires evidenced by static buckling". In: *Journal of Micromechanics and Microengineering* 23.1 (2013), p. 015014 (cit. on p. 66).

[Allen1962] F. Allen and G. Gobeli. "Work function, photoelectric threshold, and surface states of atomically clean silicon". In: *Physical Review* 127.1 (1962), p. 150 (cit. on p. 171).

[Allen1966] F. Allen and G. Gobeli. "Energy structure in photoelectric emission from Cs-covered silicon and germanium". In: *Physical Review* 144.2 (1966), p. 558 (cit. on pp. 59, 60, 135).

[Allenspach1984] R. Allenspach, F. Meier, and D. Pescia. "Spin polarized photoemission from GaAs and Ge: Temperature dependence of the threshold polarization". In: *Applied Physics Letters* 44.12 (1984), pp. 1107–1109 (cit. on pp. 100, 146).

[Anderson1959] P. A. Anderson. "Work Function of Gold". In: *Physical Review* 115 (3 Aug. 1959), pp. 553–554 (cit. on p. 69).

[Appelbaum2007] I. Appelbaum, B. Huang, and D. J. Monsma. "Electronic measurement and control of spin transport in silicon". In: *Nature* 447.7142 (2007), pp. 295–298 (cit. on p. 17).

[Arapkina2011] L. V. Arapkina et al. "Phase transition on the Si (001) clean surface prepared in UHV MBE chamber: a study by high-resolution STM and in situ RHEED". In: *Nanoscale Research Letters* 6.1 (2011), pp. 1–13 (cit. on p. 60).

[Aspnes1972] D. Aspnes and A. Studna. "Direct observation of the E0 and E0+delta0 transitions in silicon". In: *Solid State Communications* 11.10 (1972), pp. 1375–1378 (cit. on p. 28).

[Bagraev1976a] N. T. Bagraev, L. S. Vlasenko, and R. A. Zhitnikov. "Influence of the depth of location of donor levels on the degree of optical orientation of ^{29}Si nuclei in silicon". In: *JETP Letters* 24 (Oct. 1976), p. 401 (cit. on p. 158).

[Bagraev1978] N. Bagraev and L. Vlasenko. "Optical polarization of nuclei in silicon subjected to optical pumping in weak magnetic fields". In: *JETP Letters* 48.5 (1978), pp. 878–884 (cit. on p. 31).

[Bagraev1976b] N. Bagraev, L. Vlasenko, and R. Zhitnikov. "Determination of the Spin Relaxation Time of Electrons in Si by the Method of Dynamic Polarization of 29-Si Nuclei Under Optical Pumping Conditions". In: *Soviet Physics-Semiconductors* 10.10 (1976), pp. 1199–1200 (cit. on p. 160).

[Becke1993] A. D. Becke. "Density-functional thermochemistry. III. The role of exact exchange". In: *The Journal of Chemical Physics* 98 (1993), p. 5648 (cit. on p. 181).

[Bensoussan1983] M. Bensoussan and J. Moison. "Non linear photoemission from silicon". In: *Physica B+ C* 117 (1983), pp. 404–409 (cit. on pp. 122, 136, 173).

[Bensoussan1981] M. Bensoussan et al. "Photoemission yield under two-quantum excitation in Si". In: *Physical Review B* 23.3 (1981), p. 992 (cit. on p. 133).

[Binnig1983] G. Binnig et al. "7 x 7 reconstruction on Si/111/resolved in real space". In: *Physical Review Letters* 50 (1983), pp. 120–123 (cit. on pp. 60, 87).

[Bir1975] G. Bir, A. Aronov, and G. Pikus. "Spin relaxation of electrons due to scattering by holes". In: *Soviet Journal of Experimental and Theoretical Physics* 42 (1975), p. 705 (cit. on pp. 20, 158).

[Blöchl1994] P. E. Blöchl. "Projector augmented-wave method". In: *Physical Review B* 50.24 (1994), p. 17953 (cit. on p. 182).

[Bludau1974] W. Bludau, A. Onton, and W. Heinke. "Temperature dependence of the band gap of silicon". In: *Journal of Applied Physics* 45.4 (1974), pp. 1846–1848 (cit. on pp. 27, 149).

[Bona1985] G. Bona and F. Meier. "Observation of the spin-orbit splitting at the valence band edge of silicon by spin-polarized photoemission". In: *Solid State Communications* 55.9 (1985), pp. 851–855 (cit. on pp. 31, 115–117, 124, 157).

[Bottegoni2011] F. Bottegoni et al. "Spin polarized photoemission from strained Ge epilayers". In: *Applied Physics Letters* 98.24 (2011), pp. 242107–242107 (cit. on pp. 31, 171).

[Boulanger2011] P. Boulanger. "Etudes ab initio des effets de la température sur le spectre optique des semi-conducteurs". PhD thesis. 2011 (cit. on pp. 26, 33, 157).

[Briggs1983] D. Briggs and M. P. Seah. *Practical surface analysis: by auger and X-ray photoelectron spectroscopy*. Wiley New York, 1983 (cit. on p. 30).

[Bringuier1999] E. Bringuier. "Augmented Fokker–Planck equation for electron transport in arbitrary electric fields". In: *Journal of Applied Physics* 86.12 (1999), pp. 6847–6851 (cit. on p. 166).

[Bristow2007] A. D. Bristow, N. Rotenberg, and H. M. Van Driel. "Two-photon absorption and Kerr coefficients of silicon for 850–2200". In: *Applied Physics Letters* 90.19 (2007), pp. 191104–191104 (cit. on pp. 121, 137, 138).

[Brunetti1989] R. Brunetti et al. "A many-band silicon model for hot-electron transport at high energies". In: *Solid-state electronics* 32.12 (1989), pp. 1663–1667 (cit. on p. 166).

[Bruneval2008] F. Bruneval and X. Gonze. "Accurate GW self-energies in a plane-wave basis using only a few empty states: Towards large systems". In: *Physical Review B* 78.8 (2008), p. 085125 (cit. on p. 192).

[Brust1965] D. Brust. "Band-Theoretic Model for the Photoelectric Effect in Silicon". In: *Physical Review* 139.2A (1965), A489 (cit. on p. 165).

[Busch1972] G. Busch et al. "Photon Energy Dependence of Spin Polarization of Photoelectrons from Cesiated Co". In: *Physical Review Letters* 28.13 (1972), pp. 869–869 (cit. on pp. 100, 117).

[Cagnac1971] B. Cagnac and J. C. Pebay-Peyroula. *Physique atomique: introduction à la physique quantique et structure de l'édifice atomique*. Vol. 1. Dunod, 1971 (cit. on p. 51).

[Cai2001] Z. Cai. "Weighted nadaraya–watson regression estimation". In: *Statistics & probability letters* 51.3 (2001), pp. 307–318 (cit. on p. 85).

[Campbell1985] D. Campbell et al. "A compact cylindrical Mott electron polarimeter operating with accelerating voltage in the range 20-100 kV". In: *Journal of Physics E: Scientific Instruments* 18.8 (1985), p. 664 (cit. on pp. 53, 54).

[Chelikowsky1976] J. R. Chelikowsky and M. L. Cohen. "Nonlocal pseudopotential calculations for the electronic structure of eleven diamond and zinc-blende semiconductors". In: *Physical Review B* 14.2 (1976), p. 556 (cit. on pp. 24, 25, 32, 142).

[Cheng2011a] J. Cheng et al. "Theory of optical spin orientation in silicon". In: *Physical Review B* 83.16 (2011), p. 165211 (cit. on pp. 34, 94, 97, 98, 100, 101, 120, 132, 148, 149, 152, 156, 157, 167, 169, 170).

[Cheng2011b] J. Cheng, J. Rioux, and J. Sipe. "Full band structure calculation of two-photon indirect absorption in bulk silicon". In: *Applied Physics Letters* 98.13 (2011), pp. 131101–131101 (cit. on p. 157).

[Cheng2011c] J. Cheng, J. Rioux, and J. Sipe. "Two-photon indirect optical injection and two-color coherent control in bulk silicon". In: *Physical Review B* 84.23 (2011), p. 235204 (cit. on pp. 131, 132, 149, 157, 173).

[Cheng2010] J. Cheng, M. Wu, and J. Fabian. "Theory of the spin relaxation of conduction electrons in silicon". In: *Physical Review Letters* 104.1 (2010), p. 016601 (cit. on pp. 96, 157, 161, 167).

[Cricenti1995] A. Cricenti, D. Purdie, and B. Reihl. "Temperature dependent photoemission studies of Si (100) 2× 1". In: *Surface Science* 331 (1995), pp. 1033–1037 (cit. on p. 61).

[Daunois1978] A. Daunois and D. Aspnes. "Electroreflectance and ellipsometry of silicon from 3 to 6 eV". In: *Physical Review B* 18.4 (1978), p. 1824 (cit. on p. 28).

[Diederich1998] L. Diederich et al. "Photoelectron emission from the negative electron affinity caesiated natural diamond (100) surface". In: *Diamond and related materials* 7.2 (1998), pp. 660–665 (cit. on p. 59).

[Dovesi2005] R. Dovesi et al. "CRYSTAL: a computational tool for the ab initio study of the electronic properties of crystals". In: *Zeitschrift für Kristallographie* 220.5/6/2005 (2005), pp. 571–573 (cit. on p. 184).

[Drouhin1982] H.-J. Drouhin. "Sélection en énergie à très haute résolution des électrons émis par une photocathode d'arséniure de gallium en état d'affinité négative". PhD thesis. Université Paris-Sud, 1982 (cit. on p. 43).

[Drouhin1986] H.-J. Drouhin and M. Eminyan. "Simple concepts in the measurement of the energy distribution and spin polarization of an electron beam". In: *Review of Scientific Instruments* 57.6 (1986), pp. 1052–1060 (cit. on p. 43).

[Drouhin1985] H.-J. Drouhin, C. Hermann, and G. Lampel. "Photoemission from activated gallium arsenide. II. Spin polarization versus kinetic energy analysis". In: *Physical Review B* 31.6 (1985), p. 3872 (cit. on pp. 30, 99, 152).

[Dyakonov1986] M. Dyakonov and V. Y. Kachorovskii. "Spin relaxation of two-dimensional electrons in noncentrosymmetric semiconductors". In: *Sov. Phys. Semicond* 20.1 (1986), pp. 110–112 (cit. on p. 23).

[Dyakonov1971] M. Dyakonov and V. Perel. "Spin orientation of electrons associated with the interband absorption of light in semiconductors". In: *Soviet Journal of Experimental and Theoretical Physics* 33 (1971), p. 1053 (cit. on pp. 20, 158).

[Dyakonov2008] M. I. Dyakonov. *Spin physics in semiconductors*. Vol. 157. Springer, 2008 (cit. on pp. 21, 22, 158, 159).

[Dymnikov1976] V. Dymnikov, M. Dyakonov, and V. Perel. "Anisotropy of momentum distribution of photoexcited electrons and polarization of hot luminescence in semiconductors". In: *Zhurnal Eksperimentalnoi I Teoreticheskoi Fiziki* 71.12 (1976), pp. 2373–2380 (cit. on p. 96).

[Ebina1972] A. Ebina, T. Sakaue, and T. Takahashi. "Effect of Secondary Infrared Irradiation on the Photoelectron Energy Distribution Curve of Cesiated Silicon". In: *Journal of Applied Physics* 43.5 (1972), pp. 2181–2184 (cit. on p. 31).

[Efanov1983] A. Efanov and M. Entin. "Optical orientation and polarized luminescence in silicon". In: *physica status solidi (b)* 118.1 (1983), pp. 63–72 (cit. on p. 96).

[ElkSoftware] ElkSoftware. URL: `http://elk.sourceforge.net/` (cit. on p. 184).

[Elliott1954] R. J̃. Elliott. "Theory of the effect of spin-orbit coupling on magnetic resonance in some semiconductors". In: *Physical Review* 96.2 (1954), p. 266 (cit. on pp. 20, 158).

[Fabian2007] J. Fabian et al. "Semiconductor spintronics". In: *Acta Physica Slovaca. Reviews and Tutorials* 57.4 (2007), pp. 565–907 (cit. on pp. 17, 159).

[Favorskiy2010] I. Favorskiy et al. "Circularly polarized luminescence microscopy for the imaging of charge and spin diffusion in semiconductors". In: *Review of Scientific Instruments* 81.10 (2010), pp. 103902–103902 (cit. on p. 161).

[Filatov1998] M. Filatov and W. Thiel. "Exchange-correlation density functional beyond the gradient approximation". In: *Physical Review A* 57.1 (1998), p. 189 (cit. on p. 181).

[Fischetti1988] M. V. Fischetti and S. E. Laux. "Monte Carlo analysis of electron transport in small semiconductor devices including band-structure and space-charge effects". In: *Physical Review B* 38.14 (1988), p. 9721 (cit. on p. 166).

[Fishman1974] G. Fishman. *Pompage optique dans l'arséniure de gallium et application du formalisme de l'opérateur densité à l'analyse de la polarisation de la luminescence dans les semiconducteurs*. Université de Paris XI, 1974 (cit. on p. 143).

[Fishman2010] G. Fishman. *Semi-conducteurs : les bases de la théorie k.p.* École polytechnique: Physique. Ecole Polytechnique, 2010 (cit. on pp. 140, 141, 143).

[Fomenko1966] V. Fomenko and G. V. Samsonov. *Handbook of Thermionic Properties: Electronic Work Functions and Richardson Constants of Elements and Compounds*. Plenum Press, 1966 (cit. on pp. 44, 69).

[Garwin1974] E. Garwin, D. Pierce, and H. Siegmann. "Polarized photoemission from optically magnetized semiconductors". In: *HELVETICA PHYSICA ACTA* 47.4 (1974), p. 393 (cit. on pp. 17, 19, 21, 140).

[Gay1992] T. J. Gay and F. Dunning. "Mott electron polarimetry". In: *Review of Scientific Instruments* 63.2 (1992), pp. 1635–1651 (cit. on p. 53).

[Ghiringhelli1999] G. Ghiringhelli, K. Larsson, and N. Brookes. "High-efficiency spin-resolved and spin-integrated electron detection: Parallel mounting on a hemispherical analyzer". In: *Review of Scientific Instruments* 70.11 (1999), pp. 4225–4230 (cit. on p. 54).

[Giannozzi1991] P. Giannozzi et al. “Ab initio calculation of phonon dispersions in semiconductors”. In: *Physical Review B* 43.9 (1991), p. 7231 (cit. on p. 34).

[Giannozzi2009] P. Giannozzi et al. “QUANTUM ESPRESSO: a modular and open-source software project for quantum simulations of materials”. In: *Journal of Physics: Condensed Matter* 21.39 (2009), p. 395502 (cit. on p. 184).

[Glassbrenner1964] C. Glassbrenner and G. A. Slack. “Thermal conductivity of silicon and germanium from 3 K to the melting point”. In: *Physical Review* 134.4A (1964), A1058 (cit. on p. 64).

[Gobeli1964] G. Gobeli, F. Allen, and E. Kane. “Polarization Evidence for Momentum Conservation in Photoelectric Emission from Germanium and Silicon”. In: *Physical Review Letters* 12.4 (1964), p. 94 (cit. on pp. 104, 106, 107, 112, 120).

[Gobeli1966] G. Gobeli, J. Lander, and J. Morrison. “Low-Energy Electron Diffraction Study of the Adsorption of Cesium on the (111) Surface of Si”. In: *Journal of Applied Physics* 37.1 (1966), pp. 203–206 (cit. on pp. 60, 174).

[Gonze2009] X. Gonze et al. “ABINIT: First-principles approach to material and nanosystem properties”. In: *Computer Physics Communications* 180.12 (2009), pp. 2582–2615 (cit. on p. 184).

[Gross1995] E. K. Gross and R. M. Dreizler. *Density functional theory*. Vol. 337. Springer, 1995 (cit. on p. 179).

[Grover1974] J. W. Grover and P. Handler. “Electroreflectance of silicon”. In: *Physical Review B* 9.6 (1974), p. 2600 (cit. on p. 28).

[Hanbicki2012] A. Hanbicki et al. “Electrical injection and detection of spin accumulation in Ge at room temperature”. In: *Solid State Communications* 152.4 (2012), pp. 244–248 (cit. on p. 17).

[Hanle1924] W. Hanle. “Über magnetische Beeinflussung der Polarisation der Resonanzfluoreszenz”. In: *Zeitschrift für Physik* 30.1 (1924), pp. 93–105 (cit. on p. 22).

[Hartwigsen1998] C. Hartwigsen, S. Gœdecker, and J. Hutter. “Relativistic separable dual-space Gaussian pseudopotentials from H to Rn”. In: *Physical Review B* 58.7 (1998), p. 3641 (cit. on p. 154).

[Hedin1965] L. Hedin. “New method for calculating the one-particle Green’s function with application to the electron-gas problem”. In: *Physical Review* 139.3A (1965), A796 (cit. on p. 182).

[Heinz2010] F. O. Heinz and L. Smith. “Ab-initio calibration of the empirical pseudopotential method for strained silicon”. In: *Computational Electronics (IWCE), 2010 14th International Workshop on*. IEEE. 2010, pp. 1–4 (cit. on p. 187).

[Heinzmann2012] U. Heinzmann and J. H. Dil. "Spin–orbit-induced photoelectron spin polarization in angle-resolved photoemission from both atomic and condensed matter targets". In: *Journal of Physics: Condensed Matter* 24.17 (2012), p. 173001 (cit. on p. 119).

[Hermann1977] C. Hermann and C. Weisbuch. "k.p perturbation theory in III-V compounds and alloys: a reexamination". In: *Physical Review B* 15.2 (1977), p. 823 (cit. on p. 22).

[Hohenberg1964] P. Hohenberg and W. Kohn. "Inhomogeneous electron gas". In: *Physical Review* 136.3B (1964), B864 (cit. on p. 179).

[Holzwarth1964] G. Holzwarth and H. Meister. "Elastic scattering of relativistic electrons by screened gold and mercury nuclei". In: *Nuclear Physics* 59.1 (1964), pp. 56–64 (cit. on p. 53).

[Howorth1978] J. R. Howorth and P. J. Pool. "Photocathodes". Patent US 4099198 (US). July 4, 1978 (cit. on p. 60).

[Howorth1972] J. Howorth et al. "CsO negative-electron-affinity surfaces on silicon". In: *Applied Physics Letters* 21 (1972), p. 316 (cit. on p. 60).

[Huang2007] B. Huang, D. J. Monsma, and I. Appelbaum. "Spin lifetime in silicon in the presence of parasitic electronic effects". In: *Journal of Applied Physics* 102.1 (2007), pp. 013901–013901 (cit. on p. 161).

[Ishii2010] S. Ishii, S. Iwata, and K. Ohno. "All-Electron GW Calculations of Silicon, Diamond, and Silicon Carbide". In: *Materials Transactions* 51.12 (2010), p. 2150 (cit. on p. 33).

[Jaccodine1966] R. Jaccodine and W. Schlegel. "Measurement of Strains at Si-SiO 2 Interface". In: *Journal of Applied Physics* 37.6 (1966), pp. 2429–2434 (cit. on p. 65).

[Jansen2012] R. Jansen. "Silicon spintronics". In: *Nature Materials* 11.5 (2012), pp. 400–408 (cit. on pp. 17, 58, 160).

[Jellison1983] G. Jellison and F. Modine. "Optical functions of silicon between 1.7 and 4.7 eV at elevated temperatures". In: *Physical Review B* 27.12 (1983), p. 7466 (cit. on pp. 26, 28, 108).

[Jonker2007] B. T. Jonker et al. "Electrical spin-injection into silicon from a ferromagnetic metal/tunnel barrier contact". In: *Nature Physics* 3.8 (2007), pp. 542–546 (cit. on p. 32).

[Jost1981] K. Jost, F. Kaussen, and J. Kessler. "Efficient low-energy Mott analyser in comparison with other methods for polarisation analysis". In: *Journal of Physics E: Scientific Instruments* 14.6 (1981), p. 735 (cit. on p. 43).

[Kaplyanskii1976] A. Kaplyanskii et al. "Selective optical valley pumping in silicon and germanium". In: *Solid State Communications* 20.1 (1976), pp. 27–29 (cit. on p. 171).

[Kessler1985] J. Kessler. *Polarized electrons*. Vol. 1. Springer, 1985 (cit. on pp. 51, 83).

[Kirschner1981] J. Kirschner, R. Feder, and J. Wendelken. "Electron Spin Polarization in Energy-and Angle-Resolved Photoemission from W (001): Experiment and Theory". In: *Physical Review Letters* 47.8 (1981), p. 614 (cit. on p. 173).

[Kondo1976] K. Kondo and A. Moritani. "Symmetry analysis and uniaxial-stress effect on the low-field electroreflectance of Si from 3.0 to 4.0 eV". In: *Physical Review B* 14.4 (1976), p. 1577 (cit. on p. 28).

[Koopmans1934] T. Koopmans. "Über die zuordnung von wellenfunktionen und eigenwerten zu den einzelnen elektronen eines atoms". In: *Physica* 1.1 (1934), pp. 104–113 (cit. on p. 182).

[Koster1963] G. F. Koster et al. *Properties of the thirty-two point groups*. Vol. 424. MIT press Cambridge, 1963 (cit. on pp. 24, 142).

[Krasovskii1999] E. Krasovskii and W. Schattke. "Local field effects in optical excitations of semicore electrons". In: *Physical Review B* 60.24 (1999), R16251 (cit. on p. 33).

[Krasovskii2010] E. Krasovskii et al. "Dielectric screening and band-structure effects in low-energy photoemission". In: *Physical Review B* 82.12 (2010), p. 125102 (cit. on p. 33).

[Kresse1996] G. Kresse and J. Furthmüller. "Software VASP, Vienna (1999)". In: *Physical Review B* 54.11 (1996), p. 169 (cit. on p. 184).

[Krieger1992] J. Krieger, Y. Li, and G. Iafrate. "Systematic approximations to the optimized effective potential: Application to orbital-density-functional theory". In: *Physical Review A* 46.9 (1992), p. 5453 (cit. on p. 181).

[Lampel1968a] G. Lampel. "Nuclear dynamic polarization by optical electronic saturation and optical pumping in semiconductors". In: *Physical Review Letters* 20.10 (1968), pp. 491–493 (cit. on pp. 17, 94, 158, 160, 170).

[Lampel1968b] G. Lampel. "Relaxation nucléaire dans le silicium à 77K et polarisation dynamique par pompage optique". PhD thesis. Université de Paris, 1968 (cit. on pp. 140, 148).

[Lassailly1990] Y. Lassailly et al. "Experimental photoemission results on the low-energy conduction bands of silicon". In: *Physical Review B* 41.2 (1990), p. 1266 (cit. on p. 31).

[Lautenschlager1987] P. Lautenschlager et al. "Temperature dependence of the dielectric function and interband critical points in silicon". In: *Physical Review B* 36.9 (1987), p. 4821 (cit. on pp. 26, 33).

[Lax1961] M. Lax and J. Hopfield. "Selection rules connecting different points in the Brillouin zone". In: *Physical Review* 124.1 (1961), p. 115 (cit. on p. 153).

[Lee1988] C. Lee, W. Yang, and R. G. Parr. "Development of the Colle-Salvetti correlation-energy formula into a functional of the electron density". In: *Physical Review B* 37.2 (1988), p. 785 (cit. on p. 181).

[Lepine1970] D. J. Lepine. "Spin resonance of localized and delocalized electrons in phosphorus-doped silicon between 20 and 30 K". In: *Physical Review B* 2.7 (1970), p. 2429 (cit. on p. 160).

[Levine1973] J. D. Levine. "Structural and electronic model of negative electron affinity on the Si/Cs/O surface". In: *Surface Science* 34.1 (1973), pp. 90–107 (cit. on pp. 60, 174).

[Li2010] P. Li and H. Dery. "Theory of spin-dependent phonon-assisted optical transitions in silicon". In: *Physical Review Letters* 105.3 (2010), p. 037204 (cit. on pp. 34, 93–95, 147, 149, 167, 170).

[Lin1963] S.-R. Lin, N. Sherman, and J. K. Percus. "Elastic scattering of relativistic electrons by screened atomic nuclei". In: *Nuclear Physics* 45 (1963), pp. 492–504 (cit. on p. 53).

[Luber2006] D. Luber et al. "Imaging transport for the determination of minority carrier diffusion length". In: *Applied Physics Letters* 88.16 (2006), pp. 163509–163509 (cit. on pp. 19, 21).

[Ma2012] P.-W. Ma, S. Dudarev, and C. Woo. "Spin-lattice-electron dynamics simulations of magnetic materials". In: *Physical Review B* 85.18 (2012), p. 184301 (cit. on p. 166).

[Macfarlane1959] G. Macfarlane et al. "Exciton and phonon effects in the absorption spectra of germanium and silicon". In: *Journal of Physics and Chemistry of Solids* 8 (1959), pp. 388–392 (cit. on pp. 57, 91, 121).

[Marini2003] A. Marini and R. Del Sole. "Dynamical excitonic effects in metals and semiconductors". In: *Physical Review Letters* 91.17 (2003), p. 176402 (cit. on p. 33).

[Martin2004] R. M. Martin. *Electronic structure: basic theory and practical methods*. Cambridge university press, 2004 (cit. on p. 179).

[Martinelli1970] R. U. Martinelli. "Infrared photoemission from silicon". In: *Applied Physics Letters* 16 (1970), p. 261 (cit. on pp. 30, 59, 60, 66, 67).

[Maruyama1992] T. Maruyama et al. "Electron-spin polarization in photoemission from strained GaAs_ {1-x} P_ {x}". In: *Physical Review B* 46.7 (1992), p. 4261 (cit. on p. 100).

[Marzari1997] N. Marzari and D. Vanderbilt. "Maximally localized generalized Wannier functions for composite energy bands". In: *Physical review B* 56.20 (1997), p. 12847 (cit. on p. 182).

[Meier1984] F. Meier and B. Zakharchenya. *Optical Orientation*. Modern Problems in Condensed Matter Sciences. Elsevier Science, 1984 (cit. on p. 171).

[Miah2009] M. I. Miah. "Two-Photon Spin-Polarization Spectroscopy in Silicon-Doped GaAs". In: *The Journal of Physical Chemistry B* 113.19 (2009), pp. 6800–6802 (cit. on pp. 22, 132, 172).

[Milne2012] J. Milne et al. "Piezoresistance in silicon at uniaxial compressive stresses up to 3 GPa". In: *Physical Review Letters* 108.25 (2012), p. 256801 (cit. on pp. 155, 171).

[Nastos2007] F. Nastos et al. "Full band structure LDA and k.p calculations of optical spin-injection". In: *Physical Review B* 76.20 (2007), p. 205113 (cit. on pp. 34, 109, 119, 145, 149, 151, 167, 170, 171).

[Nilsson1972] G. Nilsson and G. Nelin. "Study of the homology between silicon and germanium by thermal-neutron spectrometry". In: *Physical Review B* 6.10 (1972), p. 3777 (cit. on pp. 34, 35).

[Nishikawa1995] Y. Nishikawa et al. "All-optical picosecond switching of a quantum well etalon using spin-polarization relaxation". In: *Applied Physics Letters* 66.7 (1995), pp. 839–841 (cit. on p. 160).

[Nishino1974] T. Nishino, M. Takeda, and Y. Hamakawa. "Direct observation of split-off exciton and phonon structures in absorption spectrum of silicon". In: *Solid State Communications* 14.7 (1974), pp. 627–630 (cit. on pp. 24, 27, 28, 34, 35, 110).

[Oh2009] E. Oh et al. "Carrier lifetime and spin relaxation time study for electrical spin injection into GaAs". In: *Journal of Applied Physics* 106.4 (2009), pp. 043515–043515 (cit. on p. 17).

[Onida2002] G. Onida, L. Reining, and A. Rubio. "Electronic excitations: density-functional versus many-body Green s-function approaches". In: *Reviews of Modern Physics* 74.2 (2002), p. 601 (cit. on p. 182).

[Ortega1993] J. Ortega and F. Himpsel. "Inverse-photoemission study of Ge (100), Si (100), and GaAs (100): Bulk bands and surface states". In: *Physical Review B* 47.4 (1993), p. 2130 (cit. on pp. 27, 28).

[Pakhnevich2004] A. Pakhnevich et al. "Energy distributions of photoelectrons emitted from p-GaN (Cs, O) with effective negative electron affinity". In: *Journal of Experimental and Theoretical Physics Letters* 79.10 (2004), pp. 479–483 (cit. on pp. 76, 173).

[Parsons1969] R. Parsons. "Band-to-band optical pumping in solids and polarized photoluminescence". In: *Physical Review Letters* 23 (1969), pp. 1152–1154 (cit. on pp. 17, 19, 22).

[Payne1992] M. C. Payne et al. "Iterative minimization techniques for ab initio total-energy calculations: molecular dynamics and conjugate gradients". In: *Reviews of Modern Physics* 64.4 (1992), pp. 1045–1097 (cit. on p. 179).

[Perdew1985] J. P. Perdew. "Density functional theory and the band gap problem". In: *International Journal of Quantum Chemistry* 28.S19 (1985), pp. 497–523 (cit. on p. 182).

[Petrov2003] V. Petrov et al. "New compact classical 40 kV Mott polarimeter". In: *Review of Scientific Instruments* 74.3 (2003), pp. 1278–1281 (cit. on p. 54).

[Phillips1959] J. C. Phillips and L. Kleinman. "New method for calculating wave functions in crystals and molecules". In: *Physical Review* 116.2 (1959), p. 287 (cit. on p. 182).

[Pi2000] T.-W. Pi et al. "Surface photoemission from Si (100) and inelastic electron mean-free-path in silicon". In: *Journal of Electron Spectroscopy and Related Phenomena* 107.2 (2000), pp. 163–176 (cit. on p. 30).

[Pierce1975] D. Pierce, F. Meier, and P. Zürcher. "Direct observation of spin dependent electronic structure of GaAs using spin polarized photoemission". In: *Physics Letters A* 51.8 (1975), pp. 465–466 (cit. on p. 17).

[Reitze1990] D. Reitze et al. "Two-photon spectroscopy of silicon using femtosecond pulses at above-gap frequencies". In: *JOSA B* 7.1 (1990), pp. 84–89 (cit. on pp. 121, 137, 138).

[Richard2004a] S. Richard. "Modélisation physique de la structure électronique, du transport et de l'ionisation par choc dans les matériaux IV-IV massifs, contraints et dans les puits quantiques". PhD thesis. Université Paris Sud-Paris XI, 2004 (cit. on p. 33).

[Richard2004b] S. Richard, F. Aniel, and G. Fishman. "Energy-band structure of Ge, Si, and GaAs: A thirty-band k.p method". In: *Physical Review B* 70.23 (2004), p. 235204 (cit. on pp. 25, 27, 33, 119, 145, 151).

[Rikken2011] G. L. Rikken. "A new twist on spintronics". In: *Science* 331.6019 (2011), pp. 864–865 (cit. on p. 171).

[Rioux2012] J. Rioux and J. Sipe. "Optical injection processes in semiconductors". In: *Physica E: Low-dimensional Systems and Nanostructures* (2012) (cit. on p. 22).

[Rohlfing1993] M. Rohlfing, P. Krüger, and J. Pollmann. "Quasiparticle band-structure calculations for C, Si, Ge, GaAs, and SiC using Gaussian-orbital basis sets". In: *Physical Review B* 48.24 (1993), p. 17791 (cit. on p. 20).

[Rose1983] H. Rose and R. Spehr. "Energy broadening in high-density electron and ion beams: The Boersch effect". In: *Advances in Electronics and Electron Physics, Supplement C* 13 (1983), pp. 475–530 (cit. on p. 125).

[Roux2008] F. Roux. "Etude du pompage optique du silicium par photoluminescence polarisée et photo-émission à basse énergie résolue en spin". PhD thesis. Ecole Polytechnique X, 2008 (cit. on pp. 31, 32, 43, 53, 56, 60–62, 95, 121, 140, 144, 145, 148, 160, 161, 163, 167).

[Savitzky1964] A. Savitzky and M. J. Golay. "Smoothing and differentiation of data by simplified least squares procedures." In: *Analytical Chemistry* 36.8 (1964), pp. 1627–1639 (cit. on p. 78).

[Shishkin2007] M. Shishkin, M. Marsman, and G. Kresse. "Accurate quasiparticle spectra from self-consistent GW calculations with vertex corrections". In: *Physical Review Letters* 99.24 (2007), p. 246403 (cit. on pp. 33, 190).

[Smith1978] R. A. Smith and R. A. Smith. *Semiconductors*. Vol. 173. Cambridge University Press Cambridge, 1978 (cit. on pp. 161, 167).

[Sze2006] S. Sze and K. Ng. *Physics of Semiconductor Devices*. Wiley, 2006 (cit. on pp. 57, 91).

[Talman1976] J. D. Talman and W. F. Shadwick. "Optimized effective atomic central potential". In: *Physical Review A* 14.1 (1976), p. 36 (cit. on p. 181).

[Tao2003] J. Tao et al. "Climbing the density functional ladder: Nonempirical meta–generalized gradient approximation designed for molecules and solids". In: *Physical Review Letters* 91.14 (2003), p. 146401 (cit. on p. 181).

[Tekker2001] L.-B. Tekker et al. "Systematic oscillation of peak positions in photoemission spectra during alternating caesium and oxygen exposures of silicon surfaces". In: *Applied Surface Science* 177.1 (2001), pp. 122–128 (cit. on p. 60).

[Tereshchenko2004] O. E. Tereshchenko, V. L. Alperovich, and A. S. Terekhov. "Decrease in the bond energy of arsenic atoms on the GaAs (100)-(2× 4)/c (2× 8) surface due to the effect of adsorbed cesium". In: *Journal of Experimental and Theoretical Physics Letters* 79.3 (2004), pp. 131–135 (cit. on p. 61).

[Tochihara1985] H. Tochihara et al. "Cs on Si (111) 2× 1: Si surface state and Cs valence state". In: *Surface Science* 158.1 (1985), pp. 497–504 (cit. on p. 60).

[Toropetsky2008] K. Toropetsky, O. Tereshchenko, and A. Terekhov. "Energy threshold of Cs-induced chemisorption of oxygen on a GaAs(Cs, O) surface". In: *JETP Letters* 88.8 (2008), pp. 520–523 (cit. on p. 63).

[Tyagi1983] M. Tyagi and R. Van Overstraeten. "Minority carrier recombination in heavily-doped silicon". In: *Solid-State Electronics* 26.6 (1983), pp. 577–597 (cit. on p. 57).

[Tyryshkin2005] A. Tyryshkin et al. "Spin manipulation of free two-dimensional electrons in Si/SiGe quantum wells". In: *Physical Review Letters* 94.12 (2005), p. 126802 (cit. on p. 159).

[Ulrych1995] I. Ulrych et al. "Electronic structure of the laser-annealed Si (111) 1x1 surface". In: *Surface Science* 327.3 (1995), pp. 233–240 (cit. on p. 122).

[Van Laar1965] J. Van Laar and J. Scheer. "Fermi level stabilization at semiconductor surfaces". In: *Surface Science* 3.2 (1965), pp. 189–201 (cit. on p. 59).

[Vanderbilt1990] D. Vanderbilt. "Soft self-consistent pseudopotentials in a generalized eigenvalue formalism". In: *Physical Review B* 41.11 (1990), p. 7892 (cit. on p. 182).

[Verhulst2004] A. S. Verhulst. "Optical pumping experiments to increase the polarization in nuclear-spin based quantum computers". PhD thesis. stanford university, 2004 (cit. on pp. 32, 140, 145, 148).

[Verstraete2005] M. Verstraete, X. Gonze, and J.-C. Charlier. "Ab initio calculation of the structural, electronic, and superconducting properties of nanotubes and nanowires". PhD thesis. UCL., 2005 (cit. on p. 179).

[Weber2005] C. Weber et al. "Observation of spin Coulomb drag in a two-dimensional electron gas". In: *Nature* 437.7063 (2005), pp. 1330–1333 (cit. on p. 161).

[Weisbuch1974] C. Weisbuch and G. Lampel. "Spin-dependent recombination and optical spin orientation in semiconductors". In: *Solid State Communications* 14.2 (1974), pp. 141–144 (cit. on pp. 140, 170).

[Wepfer1971] G. Wepfer, T. Collins, and R. Euwema. "Calculated spin-orbit splittings of some group iv, iii-v, and ii-vi semiconductors". In: *Physical Review B* 4.4 (1971), p. 1296 (cit. on pp. 24, 110).

[Yoshida2012] H. Yoshida. "Near-ultraviolet inverse photoemission spectroscopy using ultra-low energy electrons". In: *Chemical Physics Letters* 539 (2012), pp. 180–185 (cit. on p. 31).

[Young1997] C. Young et al. "Electron paramagnetic resonance of conduction-band electrons in silicon". In: *Physical Review B* 55.24 (1997), p. 16245 (cit. on p. 160).

[Zakharchenya1971] B. Zakharchenya et al. "Effect of optical orientation of electron spins in a GaAs crystal". In: *JETP Letters* 13 (1971), pp. 195–197 (cit. on p. 19).

[Zakharchenya1977] B. Zakharchenya, V. Zemskii, and D. Mirlin. "Polarization Dependences in Spectrum of Hot Photoluminescence in Semiconductors of Gaas-Type and Its Relation with Processes of Impulse and Spin Relaxation". In: *Fizika Tverdogo Tela* 19.6 (1977), pp. 1725–1732 (cit. on p. 96).

[Zemskii1976] V. Zemskii, B. Zakharchenya, and D. Mirlin. "Polarization of hot photoluminescence in semiconductors of the GaAs type". In: *JETP Letters* 24.2 (1976), pp. 82–85 (cit. on p. 96).

[Zerrouati1988] K. Zerrouati et al. "Spin-lattice relaxation in p-type gallium arsenide single crystals". In: *Physical Review B* 37.3 (1988), p. 1334 (cit. on p. 21).

[Zucca1970] R. R. Zucca and Y. Shen. "Wavelength-modulation spectra of some semiconductors". In: *Physical Review B* 1.6 (1970), p. 2668 (cit. on p. 28).